Nonlinear Refraction and Reflection Traveltime Tomography

by

Jie Zhang

Submitted to the Department of
Earth, Atmospheric, and Planetary Sciences
in partial fulfillment of the requirements
for the degree of
Doctor of Philosophy in Geophysics

at the

MASSACHUSETTS INSTITUTE OF TECHNOLOGY

February, 1997

Signature of Author ....
Department of Earth, Atmospheric, and Planetary Sciences
January 10, 1997

Certified by .. ..
Professor M. Nafi Toksöz
Director, Earth Resources Laboratory
Thesis Advisor

Accepted by ....
Professor Thomas H. Jordan
Department Chair

Nonlinear Refraction and Reflection Traveltime Tomography

by

Jie Zhang

Submitted to the Department of Earth, Atmospheric, and Planetary Sciences
on January 10, 1997, in partial fulfillment of the requirements
for the degree of
Doctor of Philosophy

Abstract

We develop three traveltime imaging techniques that utilize refraction/reflection data recorded on the surface. They include nonlinear refraction traveltime tomography, joint refraction traveltime migration and tomography, and joint nonlinear refraction and reflection traveltime tomography. These techniques are applicable to a large range of geological investigation problems, from imaging the shallow earth structure to deep crustal soundings. We implement these techniques on a regular velocity grid, which can well represent any complex velocity structure in the earth.

We first describe a wavefront raytracing algorithm for calculating the first-arrival refractions and later reflections, and for downward continuing the traveltime curves for the refraction migration purpose. The method simulates wave propagation by expanding a wavefront in terms of traveltimes, accounting for various wave effects. In addition, it is more accurate and efficient than several existing methods.

We develop a nonlinear refraction traveltime tomography method that accounts for several fundamental physical issues in the refraction problem. The inversion jointly minimizes the misfits of the *average slownesses* (ratios of traveltimes to the corresponding ray lengths) and the *apparent slownesses* (derivatives of traveltimes with respect to distance). We apply the Tikhonov regularization method to obtain a stable solution. To measure the reliability of the solution, we perform uncertainty analysis and calculate its posterior model covariance by way of nonlinear Monte Carlo inversions.

To enhance resolution of the tomographic image when large velocity contrasts occur in the Earth, we conduct joint refraction traveltime migration and tomography.

Refraction traveltime migration that downward continues the forward and reverse traveltimes reconstructs the location (image) of a refractor for a given velocity model, while traveltime tomography resolves a velocity structure with a curvature constraint constructed from the migration image. We present two algorithms to solve this joint imaging problem. Numerical experiments and real cases prove that both methods are useful for reconstructing a velocity model with sharp interfaces.

We also develop a joint nonlinear refraction and reflection traveltime tomography method on a regular-velocity grid. Similar to the nonlinear refraction traveltime tomography, we explicitly invert the average-slowness and the apparent-slowness data that are converted from the refraction and reflection traveltimes. The approach is beneficial to this joint inverse problem, because it modifies traveltimes associated with long rays and short rays in the refractions and reflections to the same order of magnitude, and combines two types of data on the basis of their physical information rather than using an arbitrary weighting factor. We show that the inclusion of the first-arrival refractions can be very helpful to reduce the undetermined features in the slowness field in the reflection traveltime problem.

For imaging the shallow earth, utilizing the first-arrival traveltimes is practical and reliable. Nonlinear refraction traveltime tomography is useful for imaging complex velocity variations. For cases with sharp refraction interfaces, the joint refraction traveltime migration and tomography proves more applicable. When we image the deep earth structure for which the deep reflections can be readily identified, performing joint refraction and reflection traveltime tomography appears to be more attractive.

We demonstrate applications to three real cases. The first case in South Boston, Massachusetts is to determine the bedrock topography in a complex near-surface area for an engineering project. The second real case is to image the shallow velocity structure surrounding the Bala Kimberlite which is partially exposed at the surface in Riley County, Kansas. Our interest is to understand the structure of the kimberlite plug in the subsurface. We apply nonlinear refraction traveltime tomography and joint refraction traveltime migration and tomography techniques to both cases. The results are consistent with other geophysical information. The third case is to image the crustal structure of California Borderland using marine OBS data and joint refraction and reflection traveltime tomography technique. The results show that most of the anomalous variations seen in the traveltimes are due to the shallow complex velocity structure. The deep crust is relatively simple, and the Moho at the depth of about 23 km with slightly lateral variation is found along two survey lines.

Thesis supervisor: M. Nafi Toksöz
Title: Professor of Geophysics

Acknowledgment

I have encountered so much kindness and invaluable support from so many people in the course of researching and writing this dissertation that I cannot possibly thank everyone. I would, however, like to single out a few people here. I would like to express my deepest gratitude to my advisor, Nafi Toksöz, who has encouraged me to develop a broad range of research interests and offered me necessary guidance when I met challenges in both science and life. Over the years, Nafi's ceaseless efforts have brought together a unique group of researchers, the best computational facilities and great academic freedom to pursue a large range of research topics. Needless to say, I have benefited very much from this environment during past four and a half years.

I am also indebted to Randy Mackie and Ted Madden who supervised my research in 3D d.c. resistivity tomography, which is as important as my thesis work. Working with Randy was a great learning experience. His teaching skill and ability to listen and to address scientific issues contributed greatly to the development of the work. Ted's insights on inverse theory and a number of other areas in geophysics helped me quickly identify many research topics. I would like to thank Bill Rodi, another great mentor at Earth Resource Laboratory whose extensive knowledge in inverse theory is a great access to the students here. He helped me understand a number of important issues in inversion, which became critical for developing my thesis work and several other research projects. I am also grateful to Dale Morgan, who always encouraged me to develop state-of-the-art imaging techniques and offered his philosophical views and guidance on the importance in environmental geophysics.

At ERL, Joe Matarese helped me use nCube and also discussed with me on various issues in seismic traveltime tomography. Rick Gibson taught me to use ProMax. Roger Turpening convinced me of the value of my research and helped me look for potential research market. Arthur Cheng provided me with the computer equipment I needed. Chuck Doll gave his reviews on my papers. John Olsen and Shirley Rieven Danke helped me improve my presentation skill.

My research trip to Antarctica in the austral summer 1993-1994 gave me an unforgettable experience. I am grateful to Uri ten Brink, my supervisor at USGS, who made great efforts to support me during this project as well as the LARSE project. Uri's deep insights on tectonics and crustal seismology contributed greatly to several topics that we worked together. I would also like to thank Allan Cooper at USGS for his support in my research on the Antarctic project. My friends Bruno Della Vedova and Giulio Pellis at the University of Trieste, Italy, deserve special recognition for their help and support in my research. During the summer of 1994, I took an internship at Shell Development Company. I thank Drs. T. Padhi and Peter Wills in the Seismic Imaging Department for teaching me prestack depth migration and many other skills. The provision of the data sets used in one of the chapters in this thesis must be greatly acknowledged - many thanks to Brian Macy and Don Steeples at University of Kansas. I would also like to thank Doria Kutrubes and Jutta Hager for their unconditional support in several environmental field experiments. Doria has been a great friend to me. Her constant encouragement is much appreciated.

I would also like to take this opportunity to express my gratitude to Professors Roy Greenfield, John Louie, Shelton Alexander, and Chuck Langston for their help and advice during my M.S. studies at the Pennsylvania State University. Special thanks to Dale and Suzanne Beeson, whose warmth and unfailing encouragement helped me survive the most challenging stage in my life when I first came to the United States.

I would like to thank Prof. Rinaldo Nicolich and Dr. Bruno Della Vedova for inviting me to visit University of Trieste, Italy twice to give a series of seminars in Geophysics. Prof. Richard Carlson invited me to be a guest speaker in the Department of Geology and Geophysics at Texas A&M. Prof. Norman Gray and Prof. Lanbo Liu invited me to be a guest speaker at University of Connecticut.

My thesis committee members, Drs. Robert Langan and Uri ten Brink, Profs. Chris Marone, Rob van der Hilst, Dale Morgan and Nafi Toksöz, offered many valuable comments and suggestions for this thesis work. Dr. Joe Stefani at Chevron, Dr. John Queen at Conoco, and Dr. Bill Rodi also read a draft of the thesis and gave many insights. I am also thankful for the OYO Corporation and the United States Environmental Protection Agency whose fellowships have funded my thesis research.

Scientific achievements at the Earth Resources Laboratory involve efforts of more than just scientists. I wish to thank Sara Brydges, Naida Buckingham, Liz Henderson, Sue Turbak, Jane Maloof and Lori Weldon for the kindness they have shown me over the years and for keeping the Lab in great shape. I also benefited greatly from discussions with my fellow students and staff on geophysics, sports, politics, and life in general. They include Wei Chen, Ningya Cheng, Chantal Chauvelier, Shirley Rieven Danke, Wenjie Dong, Yingping Li, Matthijs Haartsen, Xiaojun Huang, Matthias Imhof, Antonio De Lilla, Oleg Mikhailov, Bertram Nolte, Maria Auxiliadora Perez, Chengbin Peng, Delaine Thompson Reiter, Weiqun Shi, Craig Schultz, Feng Shen, Guo Tao, Xiaomin Zhao, Zhenya Zhu, and Xiang Zhu.

My greatest debt of gratitude is to my parents, who have instilled into me the confidence in attaining any goal I set my mind to. I am grateful to my wife Ling Xiao for her encouragement over the years. Without her constant support, I would not even be able to come to MIT.

Contents

Chapter 1

Introduction

1.1 Objectives

In this thesis we develop and apply three traveltime imaging techniques to reconstruct seismic velocity structures from data recorded on the surface. These three techniques include:

- nonlinear refraction traveltime tomography
- joint refraction traveltime migration and tomography
- joint nonlinear refraction and reflection traveltime tomography

Seismic tomography techniques have been extensively applied to image the earth. Almost all seismic tomographic images are based on the spatial distribution of seismic wave velocity. However, even with dense sources and receivers, solving a seismic traveltime tomography problem can be a very complicated problem. Because the seismic energy associated with a traveltime measurement may follow a complicated path, both raypath and physical properties along the raypath need to be reconstructed. If sources and receivers are both placed on the surface, the seismic traveltime tomography problem becomes more difficult than the transmission geometry, from the forward traveltime calculation to the solution of the nonlinear inverse problem. Consequently, traveltime linearization and model simplification are widely adopted in the surface tomography problem. In this thesis, we shall explore *how* we incorporate the unique physical properties in the refraction and reflection wave propagation into the tomography treatment and conduct tomographic inversion on a regular velocity grid.

1.2 Background

Difficulties in conducting refraction/reflection traveltime tomography arise for many reasons. First of all, for the surface sources and receivers, we are not even sure if we can always simulate the forward traveltime modeling with sufficient accuracy for any velocity structures. Two-point raytracing algorithms may suffer from the problem of converging to a local minimum traveltime path, and occasionally missing the global minimum (Vidale, 1988; Moser, 1991; Lees and Shalev, 1992; Fischer and Lees, 1993). The applications of these methods require smooth velocity structure in terms of slowness gradient (Julian and Gubbins, 1977; Červený *et al.*1977). Vidale (1988, 1990) presented a finite-difference appproach to solve the eikonal equation for traveltime calculation. His scheme can quickly fill in traveltimes in a regular velocity grid, and is by far the fastest method of computing traveltime. However, several authors pointed out that the finite-difference solution to the eikonal equation (Vidale, 1988, 1990) might violate causality for moderate to large velocity contrasts because of expanding a square wavefront (Qin *et al.*, 1992; Aldrige and Oldenburg, 1992; van Trier and Symes, 1991; Schneider *et al.*, 1992). Undoubtedly, to calculate refraction traveltimes accurately for tomography purposes is a challenge, since it may involve many wave effects, such as diffractions, head waves, and paths through shadow zones, for which ray theory breaks down. On the other hand, we cannot solve a wave equation for the purpose of traveltime calculation, because it requires intensive computation and subsequent "picking" of times. Wavefront raytracing methods that simulate wave propagation using traveltimes seem very promising. But accurate wavefront raytracing methods may require vast computer memory and intensive computational effort. Therefore, the first research topics in this thesis are to develop an accurate and efficient wavefront raytracing method that can be ideally suited for the refraction/reflection tomography problem.

We also find that little effort has been made to identify implicit and explicit information in the traveltime data associated with the type of wave propagation for the tomography formulation. The difference among several types of existing seismic tomography (i.e., crosswell, refraction, and reflection) lies only in the source/receiver geometry, rather than in the consideration of the wave propagation. For any survey geometry, when we construct a model and minimize the misfit between the predicted traveltimes and data with an l_2 norm, we qualitatively know that the physical information associated with the traveltimes is utilized in some way. However, nature does not have to obey a least-squares criterion. Conducting a least-squares inversion, We do not know how to measure the true data information. After having identified this problem in the existing seismic tomography methods, we attempt to convert implicit physics in the traveltime data to be explicit with some quantitative criteria. This leads to the tomography problem that inverts *average-slowness* data (traveltimes divided by the ray lengths) and *apparent-slowness* data (derivatives of traveltimes with respect to distance).

In the world of seismic imaging, *migration* and *tomography* represent two major techniques. Migration maps interfaces in the subsurface by reconstructing physical raypaths in a downward continuation process, while tomography reconstructs a slowness model by inverting recorded data. The idea of migration can be applied to both reflection and refraction data, in terms of either wave fields or traveltimes, although their imaging conditions differ. Theoretically, it would be ideal if one can combine migration and tomography in a simultaneous imaging process, since they constrain the model in two very unique ways. However, it is difficult to establish same meaningful criteria for evaluating both migration image and tomography solutions owing to their different sensitivity to properties. Clayton and McMechan (1981) demonstrated a 1-D joint refraction migration and inversion method, which was interactive. To our knowledge, there has been no better method proposed so far. To solve this problem, we adopt French's (1975) probability concept for explaining the migration image, and introduce two algorithms that automatically link migration and tomography by way of regularization.

For deep earth soundings, refraction and reflection methods can be applied to estimate both velocities and the reflector horizons. Because of intensive computation required, all existing joint refraction and reflection methods simplify the problem by using coarse model parameters (e.g., Zelt and Smith, 1992; Wang and Braile, 1996). On the other hand, nonlinear traveltime method on a regular velocity grid is applied to solve refraction or reflection problem only (Pullammanappallil, 1994). This motivates us to study several issues in the joint refraction and reflection problem and propose a practical nonlinear method. In addition, Bube *et al.*(1995) theoretically derived that the depths of reflectors are determined, but the slowness field has some undetermined features in the reflection traveltime problem. The inclusion of the first-arrival refraction data can help constrain the slowness field.

In all three imaging methods, we apply the Tikhonov regularization (Tikhonov and Arsenin, 1977). Although the method was applied in solving geophysical inverse problem long time ago, the true essence of the approach has been recognized only recently. The method can serve several purposes:

1. To produce a minimum-structure solution which does not have unnecessary features to fit the data to a predetermined misfit level (Constable *et al.*, 1987).

2. To perform a global inversion in the sense of reconstructing the whole model (Matarese, 1993).

3. To avoid solving an ill-posed inverse problem, and find an effective regularization criterion in the class of the Tikhonov method so that the inverse problem is valid for continuum and the solution is independent of the model parameterization (Delprat-Jannaud and Lailly, 1993; Zhang *et al.*, 1996; Zhang and Toksöz, 1996).

Therefore, the purpose of applying the Tikhonov method is already beyond the initial motivation, i.e., for obtaining a "smooth" solution only. We attempt to further extend its concept and demonstrate that the use of Tikhonov method allows to combine migration and tomography in one joint process and resolve sharp features.

1.3 Outline

This thesis focuses on developing new techniques in many aspects, and studying the applicability of the new techniques in solving real problems. Chapter 2 introduces an improved wavefront raytracing approach on a regular slowness grid which is designed to avoid particular problems in the minimum-traveltime (shortest path raytracing) methods. This new method is applied to all three imaging techniques presented in this thesis. In Chapter 3, a nonlinear refraction traveltime tomography method is formulated. Several issues have been discussed, including physical information in the traveltime data, Tikhonov regularization, nonlinear inversion algorithms, and comparison of linearized and nonlinear uncertainty analyses. Chapter 4 presents a joint refraction traveltime migration and tomography method. This new method simultaneously reconstructs interfaces associated with wavefront systems by way of migration, and inverts model parameters from traveltimes. Two algorithms for conducting joint migration and tomography are developed. Chapter 5 introduces joint nonlinear refraction and reflection traveltime tomography. Numerical examples demonstrate that combining refraction and reflection traveltime tomography in one joint algorithm can better resolve reflector depths and the slowness field. In Chapter 6, we show applications of the nonlinear refraction traveltime tomography and the joint refraction traveltime migration and tomography methods to two shallow imaging problems. One is to image bedrock at a coastal site in eastern Massachusetts, and the other is to image the Bala Kimberlite in Riley County, Kansas. Chapter 7 presents application of the joint refraction and reflection traveltime tomography method to the crustal structure of the California Borderland using marine data from Ocean Bottom Seismometers. The data were collected during the Los Angeles Region Seismic Experiment (LARSE) in 1994. Three Appendices are included to detail the numerical computation in terms of both the forward modeling and inversion. Appendix A compares traveltime accuracy using two finite-difference eikonal solvers (Vidale, 1988; Hole and Zelt, 1995), a conventional minimum-traveltime method (Saito, 1989; Moser, 1989, 1991) and a proposed method in this study. Appendix B discusses the differences between two inversion schemes, *creeping* and *jumping* methods. Appendix C demonstrates how the regularization trade-off parameter influences the inversion results, and how one should choose a proper trade-off parameter for an optimal solution.

Chapter 2

Wavefront Raytracing Method

Abstract

We develop a wavefront raytracing technique using graph theory. The method is based on the minimum-traveltime raytracing approach proposed by Saito (1989, 1990) and Moser (1989, 1991), but significant improvement has been made to enhance the accuracy and efficiency of the numerical calculation. The fundamental goal of this new development is to provide a sophisticated traveltime calculation approach for performing nonlinear refraction traveltime tomography, joint refraction traveltime migration and tomography, and joint refraction and reflection traveltime tomography. Therefore, our method is designed to deal with a point source in any complex medium for tomography purpose, line-source downward continuation for migration problem, and calculation of both the first and the later arrivals on a regular slowness grid for joint refraction and reflection traveltime tomography. To apply this method, one expands a wavefront with a graph template following the Huygens' principal. We optimize node distribution by two steps in a given slowness model prior to the raytracing. First, we apply an iso-angle node distribution in the graph template to reduce traveltime errors associated with angle sampling. Second, we avoid the zig-zag raypath problem by removing nodes in smooth or homogeneous areas in the model. Numerical examples demonstrate that this new method is accurate and efficient.

2.1 Introduction

During last five years, geophysicists have focused on developing wavefront raytracing methods for serving several purposes in the seismic interpretation. Particularly in the exploration context, traditional two-point raytracing approches are nearly abandoned. For seismic modeling purposes, it is not necessary to calculate exact traveltimes for a given velocity model. Even with a modern parallel computer, exact traveltime calculations for an arbitrary velocity model can be very costly. Instead, geophysicists hope to develop numerical algorithms that are efficient enough and can yield required traveltime accuracy for the seismic survey geometries. In addition, raytracing methods are often applied to serve as a tool for conducting tomography and migration. Therefore, one must account for the integrity of the entire modeling problem when deriving a raytracing algorithm. It appears that wavefront raytracing methods have the best suitability in most circumstances (Vidale, 1988, 1990; Saito, 1989, 1990; Moser, 1989, 1991; Schneider *et al.*, 1992; Coultrip, 1993).

Historically, *Raytracing* has referred to two-point raytracing algorithms (Julian and Gubbins, 1977; Um and Thurber, 1987; Červený, 1987). In the geophysics community, this term is now extensively used for any traveltime calculation that involves *ray*. To distinguish between different methods, we define any method using a two-point raytracing algorithm as a *ray method*, and any method applying a wavefront expansion algorithm as a *wavefront method.* Ray methods are based on the concept that seismic energy of infinitely high frequency follows a trajectory determined by the rayrtracing equations. Physically, these equations describe how energy continues in the same direction until it is refracted by velocity variations. In "shooting" methods, a fan of rays is shot from one point in the general direction of the receiver. The correct path and traveltime to connect the two points may then be approached with successively more accurate guesses (e.g., Julian and Gubbins, 1977; Červený *et* *al.*, 1977). "Bending" methods start with an initial, probably incorrect guess for the ray path. The raypath is bent by a perturbation method until it satisfies a minimum traveltime criterion (Um and Thurber, 1987; Thurber, 1987). However, the ray methods suffer from the problem of converging to a local minimum traveltime path, and occasionally missing the global minimum (Moser, 1989, 1991). When travel paths to many points from a source are needed, one has to conduct raytracing calculations for many times. Therefore, they are impractical for tomography and migration purposes which generally deal with the common-shot data. In addition, they require the use of a continuous model parameterization and cannot be easily applied to a grid model without some form of reparameterization (Lees and Shalev, 1992; Fischer and Lees, 1993).

We should point out that the raytracing methods that we address in this thesis only calculate traveltimes and solve traveltime equations which have no amplitudes involved. For example, finite-difference traveltime methods solve the eikonal equation rather than the elastic or acoustic wave equation. Wave propagation in media, in high frequency asymptotics, can be described by the WKBJ Green's function, which consists of both traveltimes and amplitudes (Chapman, 1978). We should also point out that two-point raytracing methods or wavefront methods all can be used to calculate the later refractions and reflections. For wavefront raytracing methods (*e.g.*, the finite-difference and the minimum-traveltime methods), the later arrivals can be calculated following a Huygens' principle (Moser, 1989, 1991).

In fact, we cannot afford solving a wave equation for the purpose of traveltime calculation because intensive computational work may be required. However, ideally we do want to account for all the wave effects in the traveltime calculation, such as raypaths through the shadow zones, head waves, and diffractions. This provides motivation for the development of wavefront raytracing methods that use rays locally and expand minimum-traveltime wavefronts. In this study, we separate existing wavefront raytracing methods into three groups: applying finite-difference method to solve the eikonal equation (Vidale, 1988, 1990; van Trier and Symes, 1991; Schneider *et al.*, 1992); applying an analytical solution to expand a wavefront (Vinje *et al.*, 1993); and using graph theory to find minimum-traveltime paths by expanding a wavefront (Saito, 1989, 1990; Moser, 1989, 1991; Mandal, 1992; Fischer and Lees, 1993; Klimes and Kvasnicka, 1993; Weber, 1995). Moser (1991) called the last approach as a shortest path raytracing method based on the original Dijkstra's (1959) algorithm. However, in seismic traveltime problem, we calculate the minimum traveltimes. Therefore, throughout this thesis, we shall call Saito's (1989, 1990) and Moser's (1989, 1991) approach as a "minimum-traveltime raytracing method".

Wavefront methods are attractive because they can simulate wave propagation in the entire model. However, they are by no means able of simulating all the wave effects. For example, they cannot account for frequency responses to the structure. At this point, wavefront raytracing methods employ rays at infinitely high frequency, as with any other ray methods. In Figure 2-1, we show an example where a wavefront is expanded in a complex medium from a surface source using a 5th-order minimum-traveltime raytracing algorithm of Saito (1989, 1990) and Moser (1989, 1991). Although the model has of strong heterogeneities, the wavefront is continuous through high- and low-velocity zones.

The performance of the wavefront raytracing algorithms is uneven. Using an analytical ray solution to expand a wavefront requires locally smooth velocity structure. Qin *et al.*(1992) showed that the finite-difference approach by Vidale (1988, 1990) violates causality for moderate to large velocity contrasts. On the other hand, the minimum-traveltime raytracing method by Saito (1989, 1990) and Moser (1989, 1991) also requires local smooth velocity structure, but may produce zig-zag raypath problem if the velocity structure is too smooth. Nevertheless, several authors showed the flexibility of the minimum-traveltime method and its potential for better performance

(Mandal, 1992; Fischer and Lees, 1993; Klimes and Kvasnicka, 1993; Weber, 1995). In this study, we improve the conventional minimum-traveltime method by using a sparse and iso-angle node distribution in a graph template so that it is more accurate and efficient for traveltime calculations in any velocity medium. In Appendix A, a detail of comparison between finite-difference methods and minimum-traveltime methods in theory and numerical performance is presented.

2.2 Graph Theory

Graph theory and shortest paths in networks are an abstract formulation of problems that appear in many different branches of science. For a finite number of objects involved, the exact solution of the problem can be found in a finite number of steps. For example, a traveling salesman wants to find the shortest route from one city to another in order to minimize his time spent on traveling. Saito (1989, 1990) and Moser (1989, 1991) independently introduced this network approach for calculating seismic traveltimes. They all demonstrated the expansion of a wavefront with a graph template in which local straight rays may cross several square cells, although Saito (1989, 1990) attributed his method to the use of Huygens' principle. Indeed, the necessary physics for adopting graph theory to seismic modeling is succinctly contained in Huygens's secondary source principle. The application of Huygens' principle to networks yields the efficient Dijkstra's (1959) algorithm. Mandal (1992) implemented the same algorithm on a triangular grid. Subsequently, several authors applied the minimum-traveltime method in various seismic imaging and earthquake modeling problems, such as crosswell traveltime tomography (Saito, 1991; Matarese, 1993), reflection migration (Moser, 1994), earthquake location problem (Moser *et al.*, 1992; Nolet and Moser, 1991).

Following notation given by Moser (1991), we will illustrate the application of graph theory in the seismic traveltime calculation. A graph is a set of nodes with a weight function that assigns a real number to each connection arc (slowness). A path is a sequence of nodes and connections succeeding each other. The traveltime along a path from one node to another is defined as the sum of the weights of the connections of the path. A shortest path is a path with the smallest possible traveltime. There will be one and only one way to reach a node from the source node through the network and there are no loops. The procedure to time nodes depends on a graph template which fixes a number of ray directions for sampling a wavefront. Figure 2-2 shows a 4th-order graph template that was used by Saito (1989, 1990) and Moser (1989, 1991). Each square represents a slowness cell which may or may not have the same slowness with the neighbors. Local straight rays cross cells up to four rings in the 4th-order template. For higher accuracy, one needs to apply higher-order templates which can better sample angles of an expanding wavefront, but it will require more computation time. For the 4th-order template as shown in Figure 2-2, it samples 32 directions around the central point which may be the original source or a secondary source. Matarese (1993) showed graph templates at several orders with the concept by Saito (1989, 1990) and Moser (1989, 1991).

Applying graph theory to trace the shortest (minimum) traveltime path, one needs to repeat a three-step algorithm. For simplicity, we demonstrate this procedure using a 2nd-order graph template as shown in Figure 2-3. The exact Dijkstra's (1959) algorithm behind this procedure is given in Appendix A. We can extrapolate traveltimes from the source to all the other nodes in the model using graph theory. At the first step, we time the neighbor nodes that are connected by the graph template using straight rays. For local traveltime calculations, one can integrate over constant slowness cells or average the slowness over a line segment connecting the grid point to the source. After timing the candidate nodes, in the second step, we determine a minimum time point among the candidate nodes and take it as a secondary source. In the third step, we exclude the previous source from the candidate list and re-time all candidates in the neighborhood of the secondary source. The procedure is repeated until the nodes in the whole model are timed with the minimum-time criteria. During this process, we use a vector to store a record of the "parent" sources simultaneously, which are the raypath connections for each node. The raypath information gives cell sensitivities to the receiver traveltimes which are needed for tomography inversion. This simultaneous storage of raypaths during raytracing differs from the use of a finite-difference eikonal solver which needs to estimate raypaths from the traveltime gradients after the completion of traveltime calculation.

The most time-consuming step during this process is the second one, finding the minimum-traveltime points among candidate nodes. Moser (1989, 1991) suggested sorting the candidate times in a "heap". Given a set of arbitrary numbers in a random order, the HEAP algorithm is a fast one for selecting the minimum. If the number of nodes is n, the selection by comparison needs n operations. Using HEAP algorithm, one only needs $\log n$ operations. However, the HEAP algorithm is a general approach for sorting any arbitrary numbers, and it does not account for any particular process in the seismic traveltime calculation. Recently, Klimes and Kvasnicka (1994) introduced an INTERVAL algorithm which is about five times faster than the use of HEAP algorithm. This algorithm separates nodes into intervals of length d_{min} according to their traveltimes. When updating traveltimes for candidate nodes, the updated nodes belong to intervals higher than the current minimum node i. The nodes in the lowest non-empty interval are not affected. Thus, one can select a node from the lowest non-empty interval to be the minimum. Figure 2-4 shows a comparison of the computation speed by using HEAP and INTERVAL algorithms for a series of nodes.

2.3 Improved Wavefront Raytracing Algorithm

A major concern about the minimum-traveltime method is with the accuracy of its result. The accuracy of the minimum-traveltime method depends on the number of connections per node, because with more connections, the minimum-traveltime method can sample more directions. As pointed out by Moser (1991), the traveltime errors in the minimum-traveltime method are due to space discretization and angle discretization. These two errors are independent, *i.e.*, decreasing the grid size does not reduce the error due to a finite angle coverage. As a result, using a low-order graph template yields zig-zag raypaths in smooth parts of the velocity model. On the other hand, computer time increases linearly with the number of node connections. It is not practical to apply a graph template consisting of a large number of node connections. Fischer and Lees (1993) showed an improvement that applies a correction after the raytracing. They perturbed the rays at interfaces according to Snell's Law. Weber (1995) presented another posterior correction method to remove zig-zag raypaths. If a raypath changes its direction at a node, it has a breakpoint at that node. If the elimination of a breakpoint makes the traveltime shorter, the breakpoint is removed. We point it out that the new generation of minimum-traveltime method that Fischer and Lees (1993) and Weber (1995) presented applies local straight rays only within a slowness cell in a graph template, which will be illustrated in the following.

In this study, we improve the minimum-traveltime method by two steps prior to the raytracing calculation. The basic idea is to sample a wavefront more evenly and also determine a minimum computational effort needed for a given velocity model. The first improvement is made by optimizing node distribution at cell interfaces so that the angle coverage can be more even. Figure 2-5 shows placement of nodes in the new version of the minimum-traveltime method that we propose. Suppose that we employ two nodes at each cell interface. If we place nodes with $a_1 = 0.29289dx$,

$a_2 = 0.41421dx$, and $a_3 = 0.29289dx$ (where dx is the length of a slowness cell), then the angles that these local rays sample are equal, 22.5°. In this case, the equal-angle distribution becomes obvious when we draw a circle passing all these nodes as shown in Figure 2-5. With the selection of these particular a_1, a_2, and a_3, each arc between two local rays is 22.5°. Figure 2-6 displays two different graph templates on the same network, one with regular node distribution on cell interfaces (Moser, 1991; Fischer and Lees 1993; Weber, 1995), the other with the optimized node distribution that we proposed. Notice that the differences of local raypaths are not large, but they are very significant for the global accuracy. Meanwhile, this modification does not alter any computation time, because we only need to define a_1, a_2, and a_3 with a different set of numbers in the calculation. If the number of nodes on each grid boundary is more than two, then the optimized propagation angles cannot be exactly equal, but they can be optimized to have a minimum difference.

Further node optimization is made by analyzing the velocity model prior to the raytracing. This step is more important. Instead of timing all the network nodes with the same graph template, the traveltime nodes in the areas where velocity gradients are smaller than a given tolerance are eliminated. This results in a sparse node network. When a wavefront is expanded into this area, a path record will be kept and updating time will not take place until reaching another node. The use of this sparse-node model avoids the zig-zag raypath problem and also enhances computation speed. Therefore, the computation time of our approach is structure-dependent. The computation time for a model without any node elimination represents an upper run-time bound of our approach, which occurs only when the model is extremely complex, every cell velocity is unique.

2.4 First-Arrival Refraction Traveltimes

In this section, we shall demonstrate four numerical examples for calculating the first-arrival refractions. Applying the minimum-traveltime method, one can calculate the global-minimum traveltimes from a source to any point in the model. Therefore, the method can be directly applied in the cross-well traveltime tomography and the first-arrival refraction traveltime tomography.

Figure 2-7 illustrates the raypaths calculated for the first-arrival traveltimes using three different graph templates. The model consists of two layers with a graben interface. A source is placed at the surface, and our interest is to examine the first-arrival refractions. With both 4th-order and 5th-order Saito-Moser graph templates, the results show zig-zag raypaths in the constant velocity medium. Under the refractor interface, apparently the calculated raypaths are much longer than what they should be. Over the refractor, deviations from straight rays mainly occur near the diffraction points. These problems are introduced due to the use of Dijkstra's (1959) algorithm in a network with a finite number of nodes. With discrete paths and few node connections in a graph template, there are often several equally short paths between two nodes, especially where the velocity structure is homogeneous or smooth. Some of these equally short paths are good approximations of the ray, but most are not, and Dijkstra's (1959) algorithm does not differentiate between them, often choosing a ray not close to the true one. As shown in Figure 2-7(c), the approach that optimizes node distribution as we proposed can accurately construct the refraction raypaths. Before raytracing, it removes nodes in the constant velocity areas by checking the gradients of the velocity structure. With an iso-angle distribution for the remaining nodes on the interface, the method can find an accurate critical point for generating the refraction, and construct accurate raypaths as well. Figure 2-8 displays the traveltimes corresponding to the above calculated raypaths. It shows that the lower-order graph template produces larger refraction traveltimes. Increasing the number of nodes in the graph template helps to reduce the problem, but meanwhile it requires more intensive computation. Proposed graph template appears performing well, results in the shortest raypaths and minimum traveltimes.

In a tomography inversion, raypaths are taken as the model sensitivity. For migration, raypaths along with the traveltimes determine the image locations. Therefore, correctly estimating raypaths for a given model is important for imaging purpose. In refraction imaging, two well-known problems associated with raypaths are the hidden-layer structure and the low-velocity zone. Thidden-layer problem is one whose the velocity in an intermediate layer is higher than those above and lower than the over layers it overlies. But its velocity is not high enough to generate any first-arrival refraction, it only influences the absolute traveltimes of those refracted from the deep layers. Accurately calculating raypaths through the hidden layer is important for reconstructing this structure from the limited information. Figure 2-9 shows a three-layer model and the first-arrival raypaths from a source at the surface. Using a 4th-order Saito-Moser graph template produces nearly straight paths across the hidden layer. With a 5th-order graph template the raypaths are improved, but the bending points due to the hidden layer occur slightly above the physical interface. Another difficulty for refraction imaging is the low-velocity zone problem in which refraction does not occur along its upper interface at all. Figure 2-10 shows a three-layer model, and the intermediate layer has the lowest velocity (1000 m/s). Again, correctly constructing physical raypaths through the layer is very important for conducting tomography inversion. However, similar problems occur for this model as shown in Figure 2-10 when using the 4th- and 5th-order Saito-Moser templates. The 4th-order graph template produces straight paths across the low-velocity layer, while the 5th-order graph template places the bending points above the velocity interface. As one can see, for both hidden-layer and low-velocity models, our proposed graph template can correctly calculate the raypaths. This is because of two reasons. First, the local straight rays in our graph template do not cross cell interface. Second, we do not place traveltime nodes in homogeneous or smooth velocity zones. Figure 2-11 and Figure 2-12 show the calculated traveltimes using three different graph templates for the two models. Only the results for the refractions are displayed for comparison. In any cases, Saito-Moser graph templates result in larger traveltimes.

We will show another comparison of the traveltime modeling results using the second generation of the graph templates in which local rays do not cross cell interfaces. Figure 2-13 displays absolute traveltime accuracy for three solutions. The model consists of two layers and is gridded into 200 by 50 uniform cells (spacing interval 1.0 m). In this example, we show results using only two nodes on each cell boundary as shown in Figure 2-5. In modeling real data, we usually use four or five nodes for higher accuracy. Regular nodes produce large errors in some areas including refraction in this case due to uneven angle sampling. Without additional computation effort, simply adjusting the node distribution according to Figure 2-5 reduces the error by nearly 50% for refraction traveltimes. Further optimizing the nodes by eliminating those in the smooth-velocity areas gives results with negligible errors.

2.5 Reflection Traveltimes

Because we shall perform a simultaneous refraction and reflection traveltime tomographic inversion, we need to modify the minimum-traveltime method to calculate both the first arrivals and the later arrivals. This modification is based on our new version of the minimum-traveltime method. To calculate the reflection traveltimes, we first expand a wavefront from the point source, and time the nodes in the slowness network which are on and above a given reflector. After this step, the first-arrival refraction traveltimes and the minimum traveltimes from the source to a given reflector are determined. In the next step, we keep a copy of the calculated travel times and raypaths, and assign all the network nodes with traveltime infinity except for those along the reflector. Then we continue to expand a wavefront from the reflector (line source) back to the receivers. During this process, traveltimse at any point along the line source are not allowed to be updated by any other point. This restricts the calculation to a reflection raypath rather than a refraction. If we want to calculate the later refraction, we simply remove this restriction and allow the traveltime at a point along the line source (refractor) to be updated by any other point along the line source, if such an update makes a minimum.

Figure 2-14(a) shows a synthetic model of the axial magma chamber in the crust. We apply the wavefront method that we introduced to calculate the first-arrival refraction (Pg) and the reflection from the Moho (PmP). Later we shall demonstrate tomographic inversions for the same model. The model consists of sea water (1.5 km deep), large velocity gradients in the shallow earth, and a central low-velocity zone. It is parameterized by 300 $\times$ 100 grids covering a 2-D profile of 30 km by 10 km. The Moho is about 8.4 km in average depth with lateral and depth variation. We simulate an OBS experiment and display the calculated traveltimes from an OBS on the seafloor. For efficient numerical modeling, we apply reciprocity, and take the OBS as a "source" and calculate the traveltimes from the OBS to a dense receiver array (shooting locations) at the sea surface. In fact, for modeling the OBS problem that one needs to calculate a large number of traveltimes from the same source, wavefront methods are more efficient and convenient than the two-point raytracing approaches. They only need a single forward computation. Figure 2-14(b) shows the downward incident traveltimes from the OBS including the first-arrival refraction (recorded at the sea level) and the minimum traveltimes from the OBS to the Moho. After this step, we place a *line source* along the reflector (the Moho) and continue to expand the wavefront for reflection calculation. Figure 2-14(c) shows the contoured reflected traveltimes from the Moho. In Figure 2-15, the absolute refraction and reflection traveltimes are displayed. At long offset distance, the wide-angle reflection traveltimes nearly have the same moveout as the refractions. The influence of the central low-velocity zone can be seen in both the near-offset refraction and reflection traveltimes, but the changes are not dramatic.

Figure 2-16 shows another numerical model which consists of a curved reflector and lateral velocity variations. This model also presents the velocity structure in a crustal scale. For a source near the right edge on the surface, one can see that the reflections from the curved interface propagate to the surface with an uniform wave pattern, and reach all of the receivers. For this type of structure, conventional two-point raytracing algorithms may fail to find ray connections for some receivers due to large raypath error associated with very curved interfaces (Moser, 1991). In Figure 2-17, reflection traveltimes for 11 sources equally distributed on the surface are displayed. Because of lateral velocity variations and the reflector geometry, it turns out that the fastest reflection always appears to the receiver in the left side of the model, where is above the top of the reflector.

2.6 Conclusions

Application of a wavefront raytracing method to the seismic modeling problem is appealing, because it simulates a wave propagation process, thus it can handle effects due to waves, such as diffraction, head waves, and paths to shadow zones. This avoids the breakdown of ray theory for certain complex velocity structures, and ensures the traveltime calculation in the tomography and migration problems to be reliable. Among various wavefront methods, it seems that the minimum-traveltime has the great potential to honor well the physics in the traveltime problem. Another popular approach includes finite-difference method to solve the eikonal equation. However, the eikonal equation describes the magnitude of the traveltime gradient only, not its direction. Differentiating the eikonal equation, we can derive as high-order derivatives of traveltime along the ray as we select, but no information on the behavior of the traveltime in other directions may be derived from it directly. In preferring the direction of a ray to other directions in a finite-difference scheme, in order to increase the accuracy and stability in strongly heterogeneous media, the resulting algorithm needs to include a sorting procedure in a much similar way as in the minimum-traveltime method (Podvin and Lecomte, 1991). In Appendix A, we analyze several theoretical aspects of wavefront raytracing methods and point out that a finite-difference eikonal solver is useful only when it closely follows the strategies in the minimum-traveltime methods.

We identified two major problems in the existing minimum-traveltime methods, i.e., nonuniform angle sampling, and zig-zag raypaths. Therefore, we proposed a two-step procedure to improve the minimum-traveltime method. These two steps include applying an iso-angle node distribution, and eliminating unnecessary nodes in smooth velocity areas prior to the raytracing. Notice that all these problems are associated with a regular grid slowness model. However, we chose to stay with this type of slowness parameterization rather than a continuous functional or a few interfaces, because this type of model is essential for performing high-resolution seismic imaging and tomography. Therefore, our fundamental goal is to improve the performance of the traveltime calculation method on a regular velocity grid. It appears that our new method is successful.

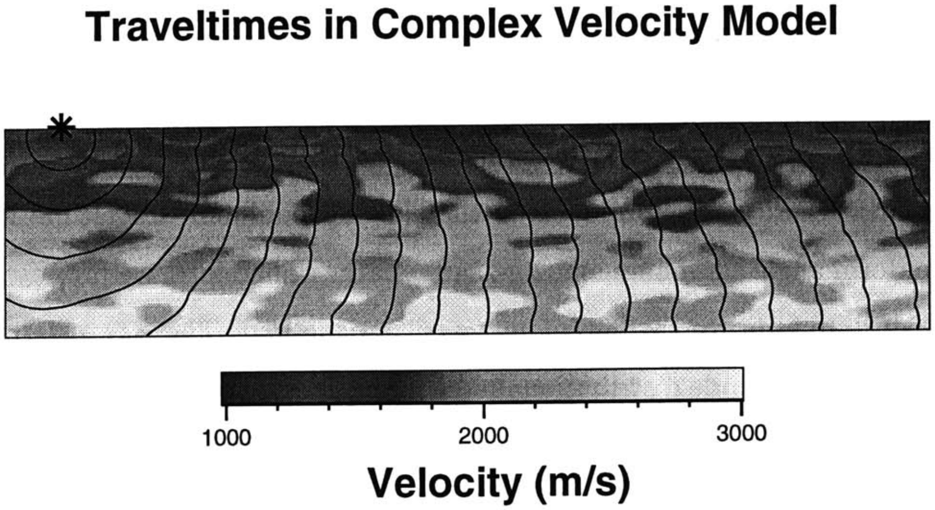

Figure 2-1: Expanding a wavefront in a complex velocity model. A 5th-order Saito-Moser graph template is applied. After raytracing is completed, traveltimes and raypaths in the entire model are calculated.

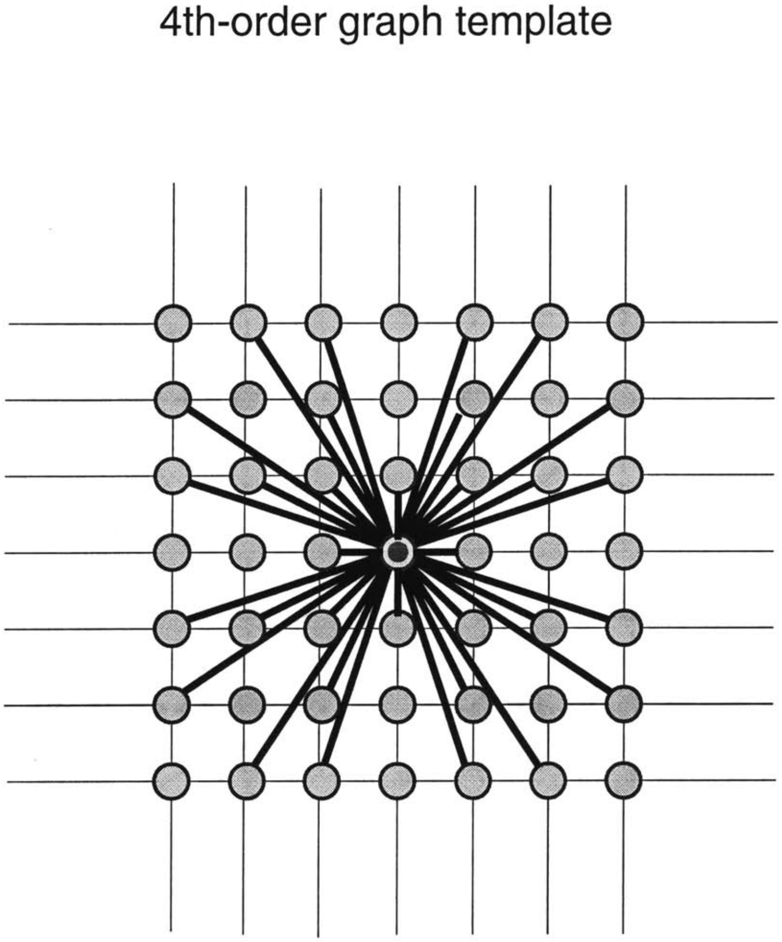

4th-order graph template

Figure 2-2: A 4th-order graph template for extrapolating traveltimes from a source. Each circle is a traveltime node, and each square cell may have one slowness. Local straight rays are used to time neighbor nodes.

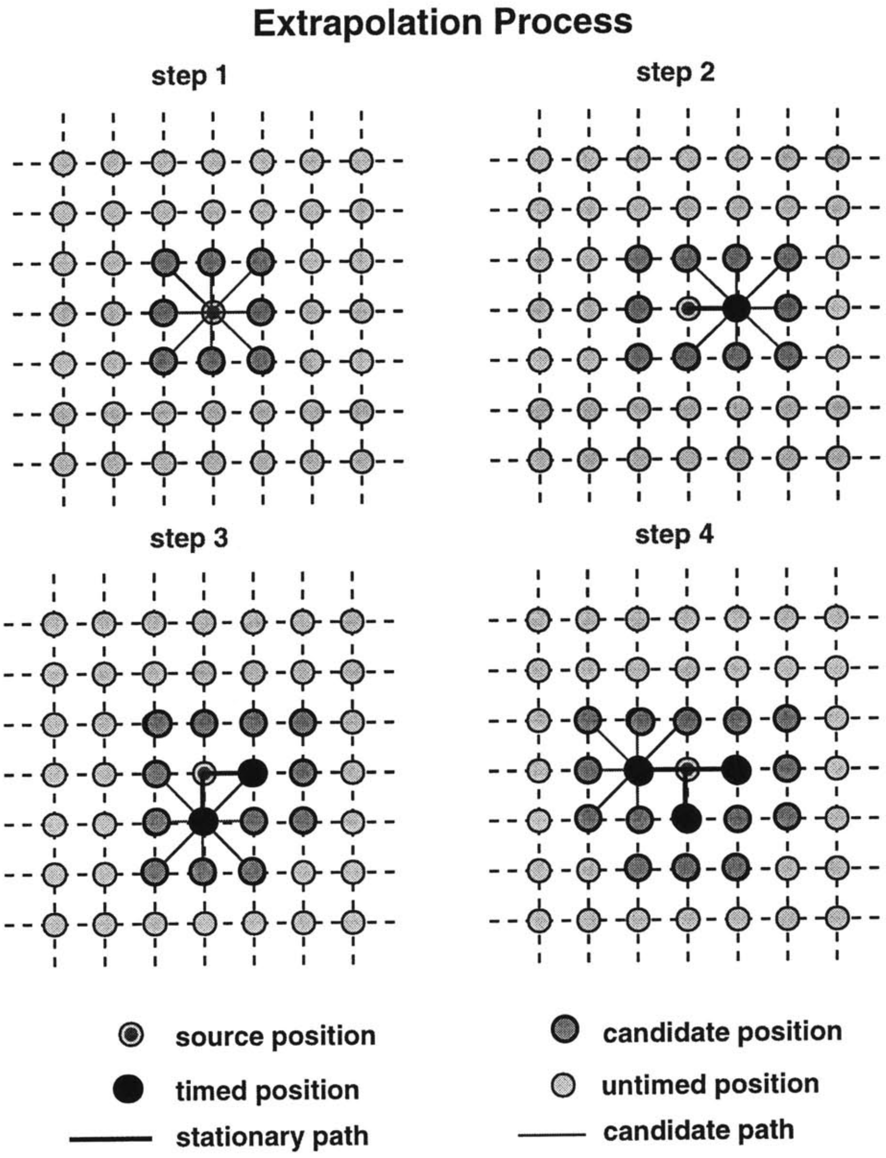

Figure 2-3: Wavefront extrapolating procedure using graph theory. A 2nd-order graph template is applied for demonstration. See text for details.

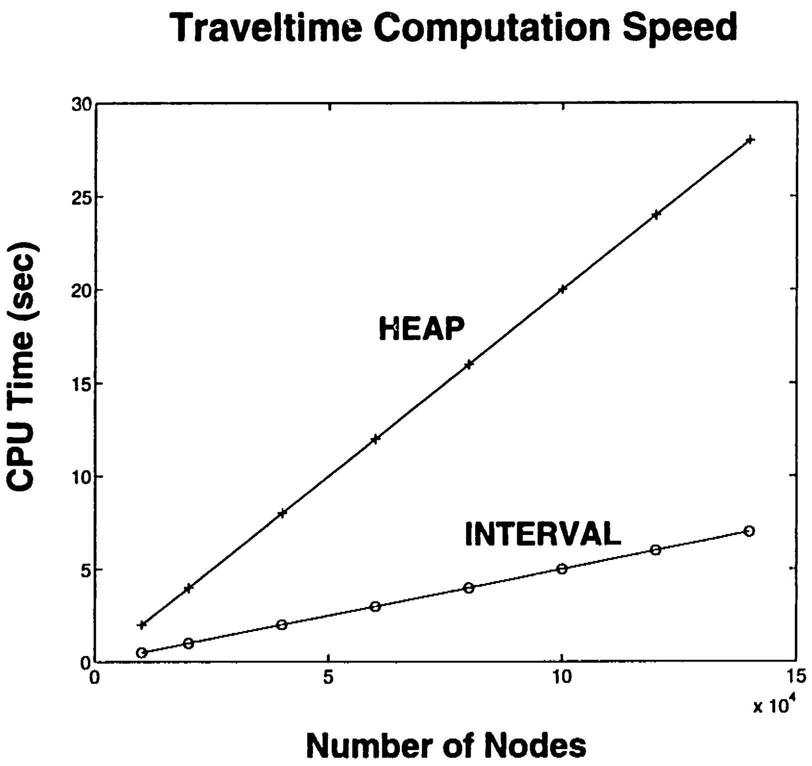

Figure 2-4: A comparison of computation time for using HEAP and INTERVAL algorithm in the minimum-traveltime raytracing method.

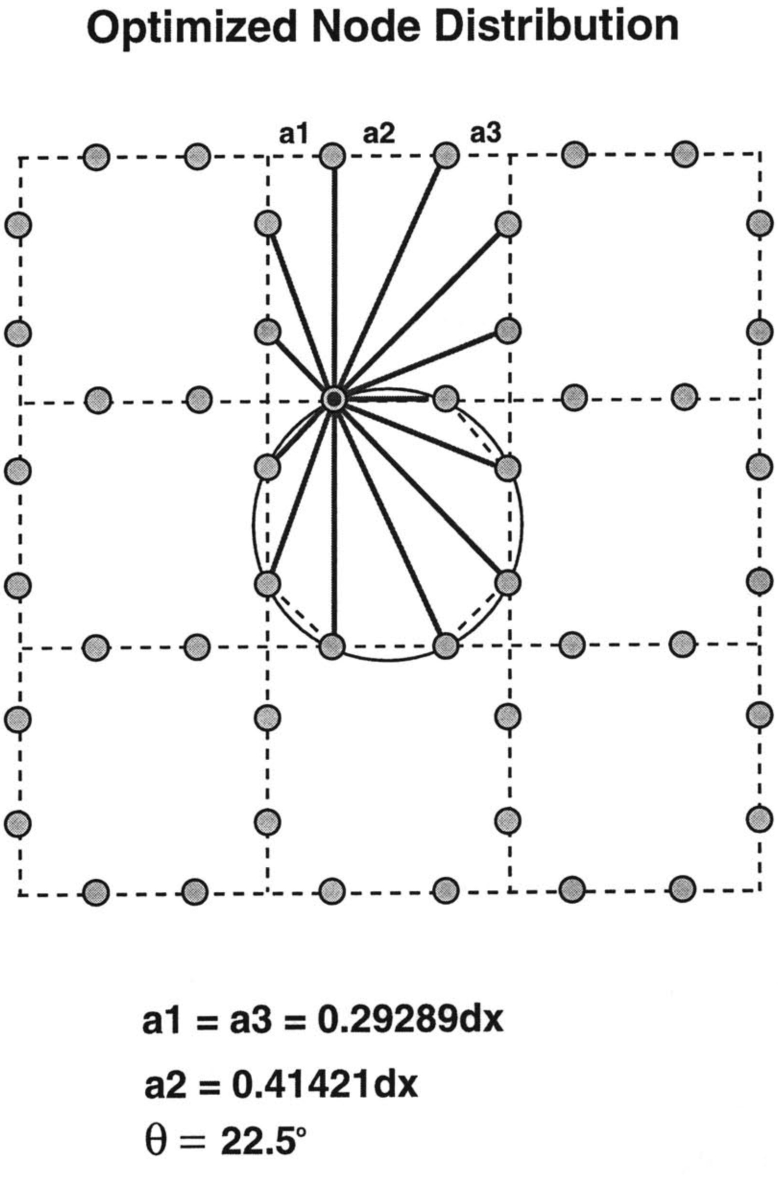

Figure 2-5: A proposed graph template of the shortest raypath method for traveltime calculation. Traveltime nodes are placed on the cell interfaces in a slowness network based on a_1, a_2 and a_3. We select optimal a_1, a_2 and a_3 so that the angles of the expanded wavefront are equally sampled

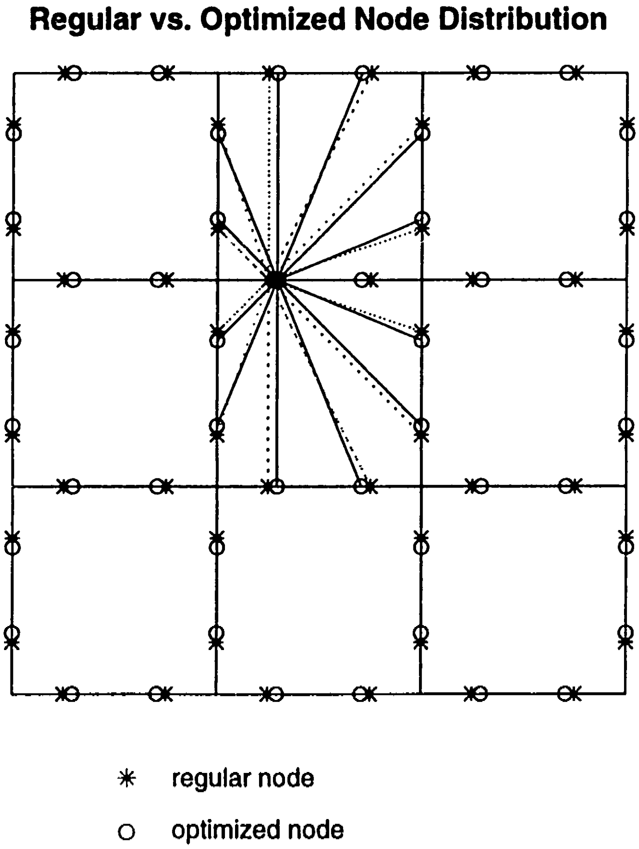

Figure 2-6: A comparison of graph templates for the shortest path raytracing method. Star denotes regular node that samples grid interface equally; the open circle represents the iso-angle node that we propose. Slightly shifting nodes along the grid interface so that rays evenly sample angles can reduce raytracing error due to the angle discretization.

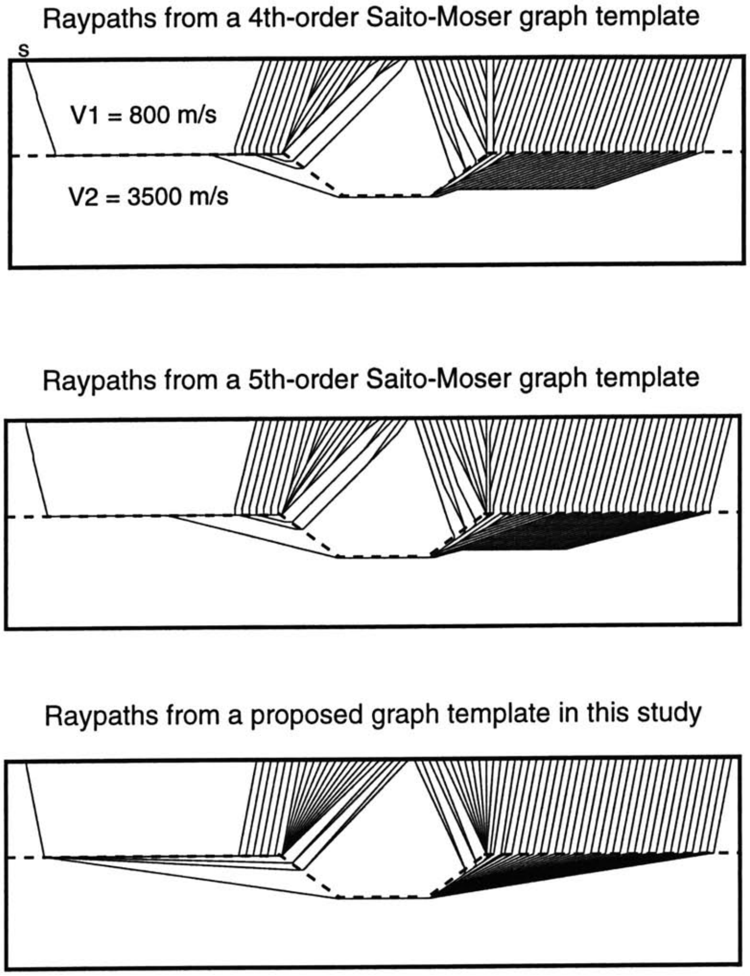

Raypaths from a 4th-order Saito-Moser graph template

Raypaths from a 5th-order Saito-Moser graph template

Raypaths from a proposed graph template in this study

Figure 2-7: A comparison of raypath accuracy for a two-layer model with a graben interface for using three graph templates. The 4th-order and 5th-order Saito-Moser templates introduce large raypath errors, while the proposed new graph template can accurately construct raypaths.

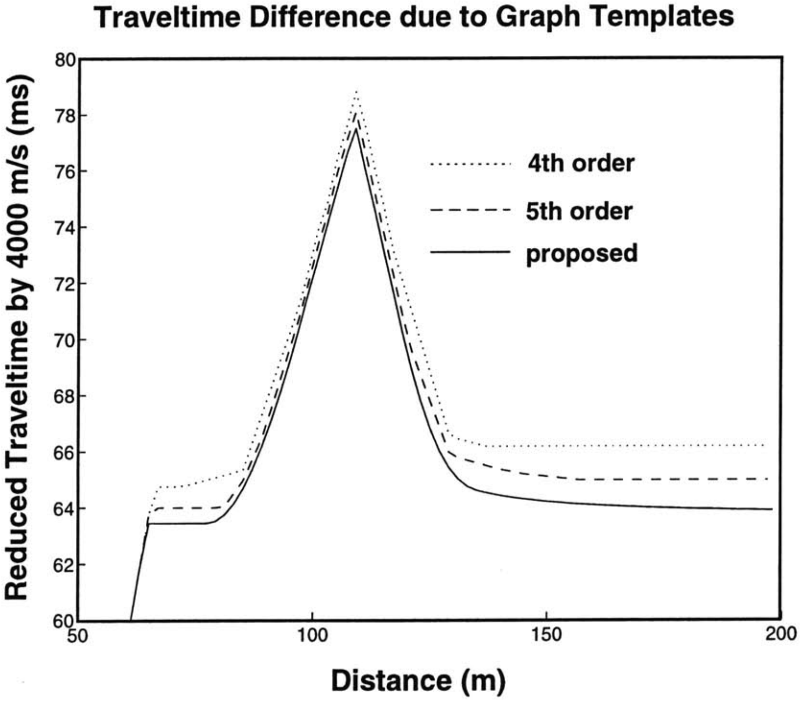

Figure 2-8: Refraction traveltimes calculated using the 4th-order and 5th-order Saito-Moser templates and the proposed graph template for the graben model. A velocity reduction by 4000 m/s is applied. Notice that the traveltimes from the 4th-order and 5th-order Saito-Moser templates are larger due to longer raypaths. Higher-order results are more accurate, but also require more computation time.

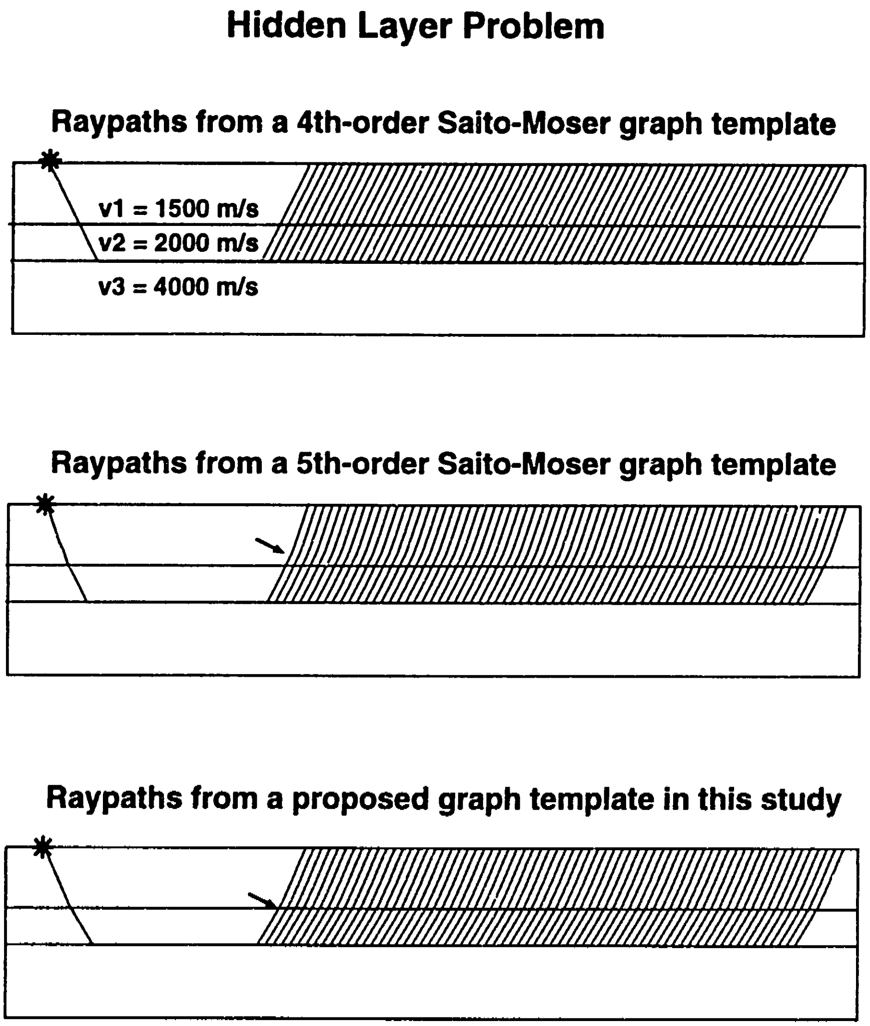

Figure 2-9: Three-layer velocity model and raypaths using the 4th-order and 5th-order Saito-Moser templates and the proposed graph template. The second layer velocity is not sufficiently high, causing a hidden layer problem in the first-arrival traveltimes. Notice that the use of the 4th-order and 5th-order Saito-Moser templates is unable to calculate the raypaths in the hidden layer correctly.

Low-Velocity Layer Problem

Raypaths from a 4th-order Saito-Moser graph template

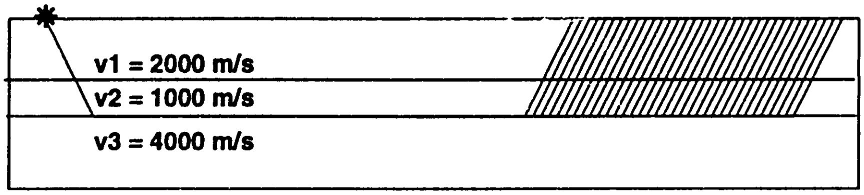

Raypaths from a 5th-order Saito-Moser graph template

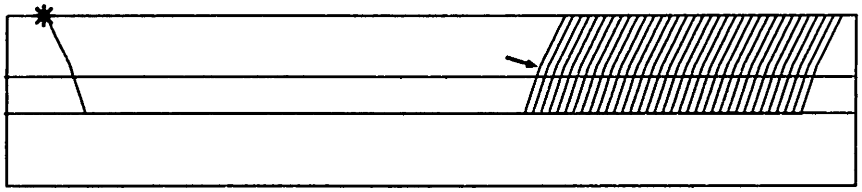

Raypaths from a proposed graph template in this study

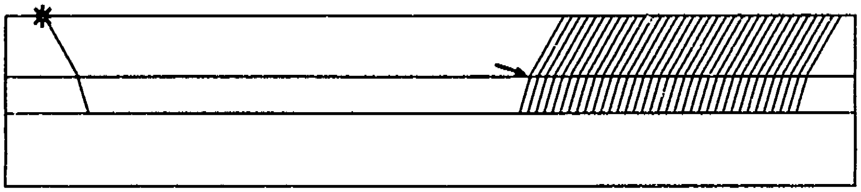

Figure 2-10: Three-layer velocity model and raypaths using the 4th-order and 5th-order Saito-Moser templates and the proposed graph template. The second layer velocity is the lowest, causing bending raypaths. Notice that the use of the 4th-order and 5th-order Saito-Moser templates is unable to compute the raypaths in the low-velocity layer accurately.

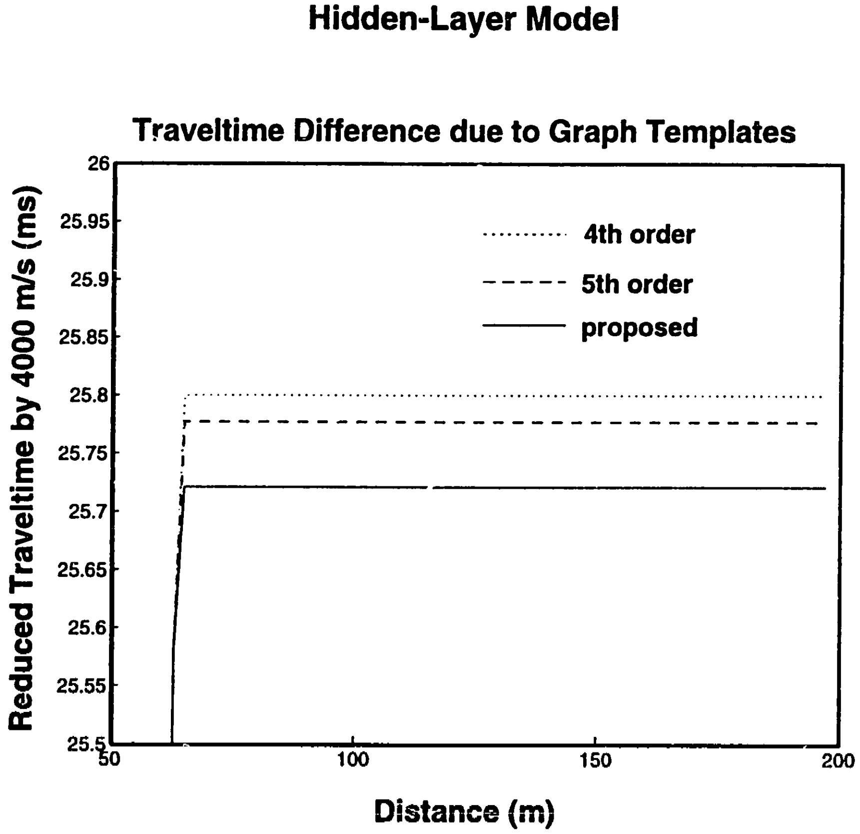

Figure 2-11: Calculated traveltimes using three different graph templates for the hidden-layer model. Only the results at the range between 50 m to 200 m are displayed to show the first-arrival refractions. Velocity reduction 4000 m/s is applied.

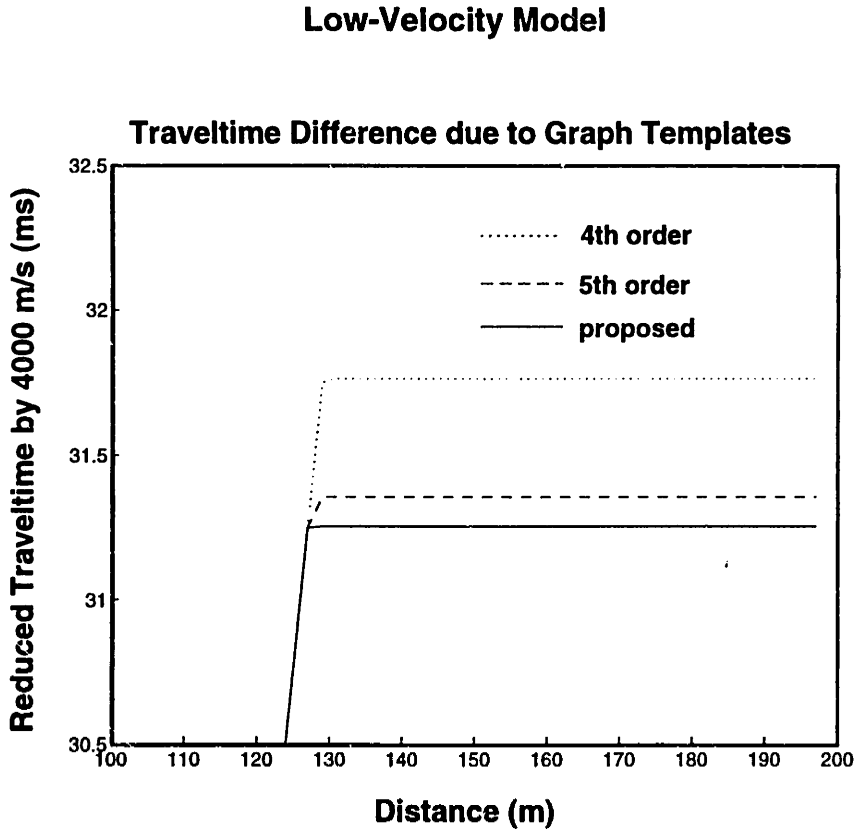

Figure 2-12: Calculated traveltimes using three different graph templates for the low-layer model. Only the results at the range between 100 m to 200 m are displayed to show the first-arrival refractions. Velocity reduction 4000 m/s is applied.

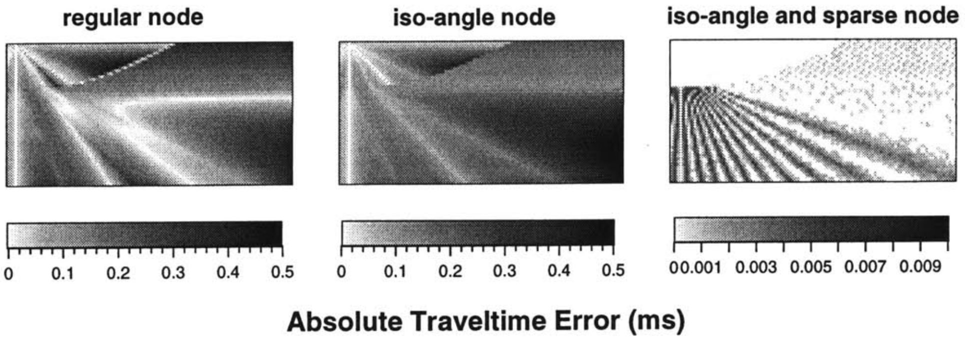

Figure 2-13: A comparison of raytracing accuracy due to two different graph templates shown in Figure 2-3. A two-layer model (200 m by 50 m) is discretized with grid size 1.0 m. The upper-layer velocity is 2500 m/s and the lower-layer velocity is 4500 m/s. Using two regular nodes on each cell interface produces refraction traveltime error up to 0.4 ms; shifting these two nodes for equal angles (22.5°) reduces refraction traveltime error down to 0.2 ms; further eliminating nodes in the homogeneous areas reduces error to be eligible.

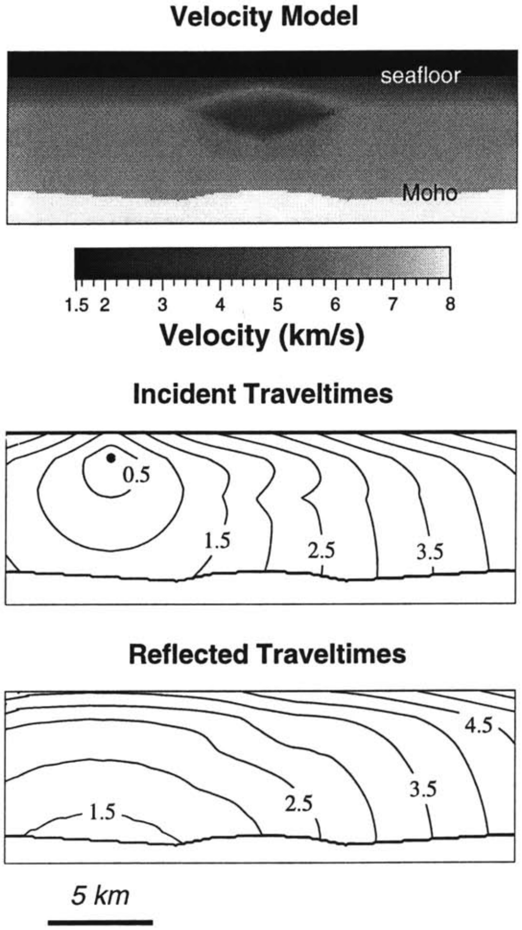

Figure 2-14: Traveltime calculation for a mid-ocean ridge model: a) P-wave velocity model; b) incident traveltime contour from a source on the seafloor; c) reflected traveltime contour back from the Moho.

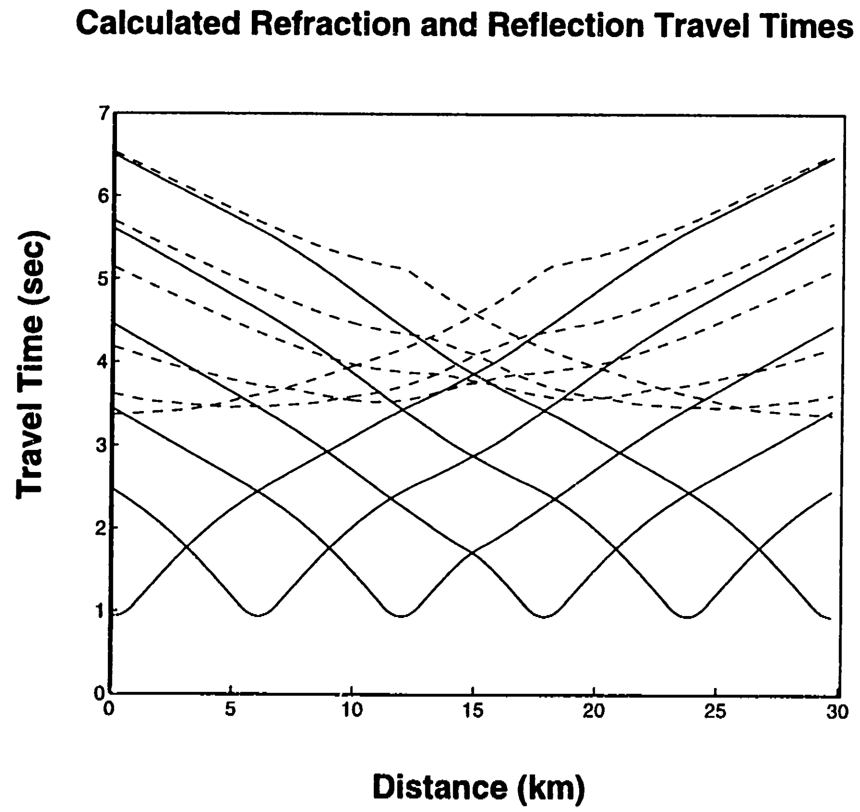

Figure 2-15: Refraction and reflection traveltimes from six OBSs on the seafloor. Solid curve represents refraction traveltimes and dashed line denotes reflection traveltimes.

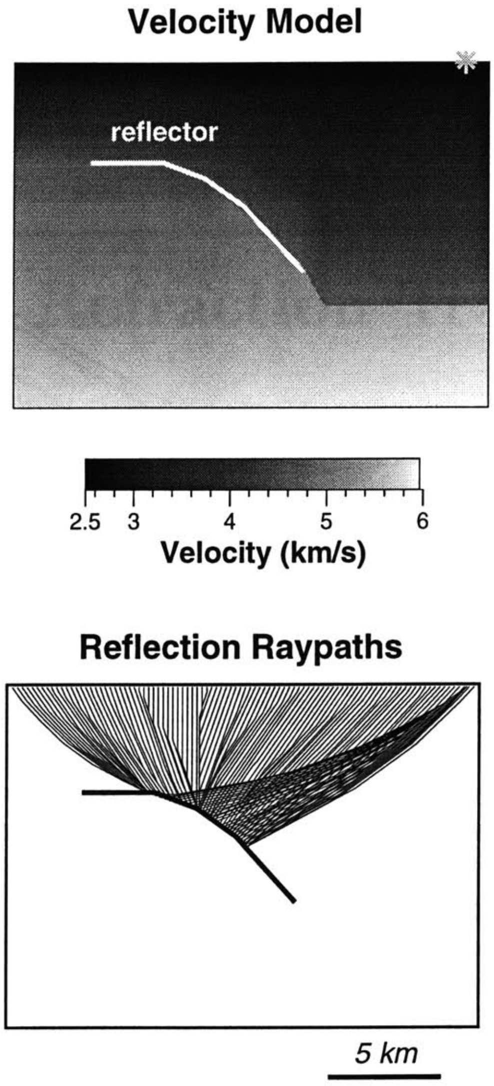

Figure 2-16: A crustal structure model consisting of a curved reflector and strong lateral and vertical velocity variations. Raypaths of reflections from a source near the model edge.

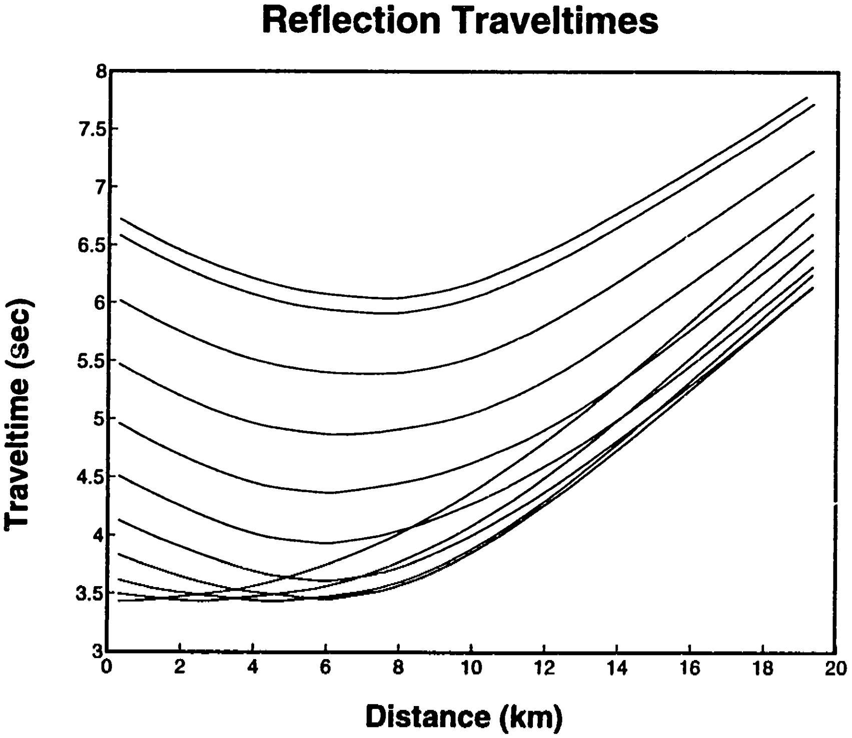

Figure 2-17: Reflection traveltimes from 11 sources on the surface with even distribution. Because of large lateral velocity variations and curved reflector shape, the reflection traveltimes are not symmetric to the source locations.

Chapter 3

Nonlinear Refraction Traveltime Tomography

Abstract

We have identified a few important issues for performing nonlinear refraction traveltime tomography. These include the information content of the refraction traveltime curves, characteristics of the refraction traveltime errors, and ill-posedness of the inverse problem. Consequently, we have developed a regularized nonlinear refraction traveltime tomography method that explicitly honors the physics of the refraction traveltime problem. Aside from an accurate raytracing approach needed to calculate the first-arrival refractions, we find that structure ambiguity due to short and long rays in the seismic refraction problem may significantly influence the inversion results. In addition, minimizing the misfit of the absolute traveltimes with a least-squares criterion does not account for the whole meaning of a refraction traveltime curve. Therefore, with the new raytracing approach that we developed, we chose to solve a tomography problem that explicitly minimizes the misfits of the *average slownesses* (ratios of traveltimes to the corresponding ray lengths) and the *apparent slownesses* (derivatives of traveltimes with respect to distance). As a result, we enhance the resolution as well as the convergence speed. We regularize our inverse problem with the Tikhonov method. The use of the Tikhonov regularization avoids solving an ill-posed inverse problem and allows us to invert an infinite number of unknowns. We characterize errors in refraction traveltimes in terms of a *common-*

shot error, a constant deviation for recordings from the same shot, and a relative *traveltime-gradient error* with zero mean with respect to the true gradient of the traveltime curve. Correspondingly, we measure the uncertainty of our tomographic solution using a nonlinear Monte Carlo approach and compute the posterior model covariance associated with two different types of random data vectors and one random model vector. The nonlinear uncertainty analysis indicates that the resolution of a tomographic solution may not correspond to the ray coverage in some areas in the model.

3.1 Introduction

Utilizing seismic refraction traveltime data for imaging the subsurface has long been a standard technique. It is appealing because of its low-cost field operation and easy data interpretation. Dobecki and Romig (1985) predicted that the seismic reflection survey would "replace the refraction survey as the most common seismic tool for engineering and groundwater studies", while Lankston (1989) argued that "the reflection method offers some capabilities that the refraction method cannot offer; but the converse is also true". Indeed, from a physical point of view, refraction methods rely on the heterogeneity of the medium to turn seismic energy back to receivers, providing velocity information independent from that in reflection methods. However, conventional processing of refraction data falls short of showing the true strength of this technique with oversimplified geometry and media, although they do attempt to develop unique physical concepts from refraction traveltimes. On the other hand, modern tomography methods seem to ignore the value of physical concepts that have been already established for the refraction problem. They simply match the absolute traveltimes using a least-squares criterion like any other tomographic problem (*e.g.*, reflection and crosshole tomography). Consequently, the unique physical information in the seismic refraction data has not been fully or properly utilized, and certain statements have often been made about the effectiveness of the refraction method without appropriate qualifications. In this study, we investigate a few fundamental issues in the refraction traveltime problem and perform numerical modeling in several ways. As a result, we have developed a new refraction tomography technique that combines both conventional concepts and recently developed inversion techniques.

Seismic refraction data are conventionally acquired with "forward" and "reverse" shots, and their interpretation is often made using reciprocity. These include the Generalized Reciprocal Method (GRM) (Palmer, 1980), the wavefront reconstruction method (Aldrige and Oldenburg, 1992), and the wavefield extrapolation method (Clayton and McMechan, 1981; Hill, 1987). All of these methods assume that seismic velocity structures are simple, and primarily attempt to map a refractor. Tomography methods, using some approach to calculate traveltimes and raypaths on a regular grid and applying an inversion technique to reconstruct the seismic velocities, have been extensively studied and developed for crosshole and reflection geometry. However, little has been done for refraction problems. White (1989) developed a refraction traveltime tomographic method that applies a two-point raytracing algorithm and solves a damped least-squares problem for both velocities and refractor depths. The inverse problem is regularized with a gradient smoothing operator in a *creeping* manner (for definition and concept, see Appendix B). Zhu and McMechan (1989) performed refraction tomography using an analytic traveltime solution, and their tomographic approach is same for the crosswell geometry (McMechan *et al.*, 1987) and requires the initial model to have positive velocity gradients. Stefani (1995) showed a turning-ray tomography which is similar to White's (1989) but he inverted the velocities only. Using a finite-difference approach to solve the eikonal equation without rays involved, Ammon and Vidale (1993) developed a refraction traveltime tomography regularizing the inverse problem with second-order model derivatives in a *jumping* fashion (for definition, see Appendix B). Because they explicitly construct a sensitivity matrix by repeating the forward calculation for each perturbed slowness cell, their approach is limited to a small number of model grids. In Appendix A, we show that the relative errors in the traveltime calculation for a two-layer model using Vidale's (1988) algorithm can be extremely large due to expanding a square wavefront. The error is up to 8.7% when the velocity contrast is 1:2.5.

It appears that existing techniques for refraction traveltime tomography have some numerical shortcomings due to either the raytracing approach used or to the ill-posed inverse problem encountered or both. In the previous chapter, we addressed issues of traveltime calculation, now we focus on the nonlinear inverse problem. We have to deal with an ill-posed inverse problem, where the number of unknowns is greatly more than the number of data points. An ill-posed inverse problem must be properly regularized in order to obtain a stable solution, which is independent of the model discretization (Delprat-Jannaud and Lailly, 1993; Zhang *et al.*, 1996). Rodi (1989) and Zhang *et al.* (1996) showed that regularizing the model update (*creeping*) rather than the model itself (*jumping*) cannot ultimately avoid the difficulties associated with solving an ill-posed inverse problem (a detailed discussion of *creeping* and *jumping* inversions is presented in Appendix B). Further, not all regularization approaches perform well, and an appropriate criterion for refraction traveltime tomography must be defined. It also appears that existing refraction tomography methods have not sufficiently considered the physical properties inherent in the refraction problem. As a result, all of these refraction tomography techniques are not much different from those for crosswell or reflection geometry.

In this study, we shall improve the performance of refraction traveltime tomography in terms of both the forward raytracing calculation and the inversion techniques. Moreover, our numerical treatment will account for several issues that are uniquely associated with the physical properties in the seismic refraction. Our method includes several new developments. First, instead of using traditional two-point raytracing algorithms (Julian and Gubbins, 1977; Um and Thurber, 1987; Červený, 1987), we apply a new version of the minimum-traveltime raytracing approach (Saito, 1989, 1990;

Moser, 1989, 1991) which can expand a wavefront in a regular grid model from its source. Second, we view seismic refraction traveltimes as continuous "curves" rather than uncorrelated data points. Therefore, we solve an inverse problem that takes traveltimes in two different forms, *i.e.*, minimizing the misfit of *average slownesses* (traveltimes divided by the ray lengths) and the misfit of *apparent slownesses* (derivatives of traveltimes with respect to distance). Third, we view model parameters as correlated and realize that a meaningful tomography solution should not depend on the model parameterization. Therefore, we apply Tikhonov regularization (Tikhonov and Arsenin, 1977) to perform a global inversion in the sense of reconstructing the whole model as opposed to applying *ad hoc* posterior smoothing constraints to keep the inversion stable. We will show that not all the smoothing criteria in the Tikhonov method can perform well for the refraction tomography. Fourth, we conduct uncertainty analysis to quantify the resolution and variance of the solution. We view the errors in the refraction traveltime data in terms of a *common-shot error*, a constant shift from the "true traveltimes" of the same shot, and a relative *traveltime-gradient error*. We construct two data vectors with random errors and one random model vector, and apply a nonlinear Monte Carlo approach to estimate the posterior model covariance.

3.2 Characterizing the Refraction Traveltime Problem

Seismic refraction contains both lateral and vertical subsurface information due to its variety of raypaths. This variety is attractive because rays from a small number of shots may cover a large area of the subsurface. However, it can also be potentially dangerous because there may be too many possibilities of model solutions to produce the same traveltime curves due to the variety allowed. Although using Tikhonov regularization to find a solution with minimum structure can eliminate those results with extreme roughness (Constable *et al.*, 1987), there may still be many solutions that *look* physically reasonable and fit data equally well due to insufficient physical constraints inherently occuring in the refraction problem. For instance, deep refraction raypaths are always poorly constrained but significant to our solution. If we can characterize a refraction traveltime problem with sufficient physical concepts, we may be able to constrain our solution to be more physically meaningful under quantitative criteria. This leads to the discussion of the following issues, which governs our philosophy for further numerical implementation:

(1) Unlike crosshole or reflection problems, ray lengths in the refraction problem may range over two orders of magnitude. Short rays constrain the velocity more tightly than do long rays, structure ambiguity increases with ray length. Therefore, inverting the absolute traveltimes with the least-squares criterion would be potentially dangerous because it tends to update the deep structure first for fitting long-ray traveltimes due to their large misfit magnitude. We chose to minimize the misfit of "average slownesses" (the ratios of traveltimes to the ray lengths) instead of "integrated slownesses" (absolute traveltimes). This conversion modifies the traveltimes to be of the same order, and allows for constraining the shallow structure more tightly. It also allows one to characterize the data misfit in terms of a physical measure, *i.e.*, average slowness. The drawback of this approach is that the long-ray traveltimes cannot be fit to the same variance with the short-ray traveltimes when using the least-squares criterion for inversion. Consequently, the deep structure cannot be resolved well. However, this problem can be solved by additionally inverting the traveltime derivatives.

(2) Refraction data are conventionally utilized in the form of absolute traveltimes and traveltime derivatives with respect to distance. Both types of data provide inde-

pendent information of the subsurface, alternatively, independent constraints on the raypaths. The latter gives a local *apparent slowness* of a refractor, which is conceptually similar to the *apparent resistivity* in the electrical problem. Refraction traveltime tomography method should also incorporate this type of data in the inversion and explicitly minimize the misfit of traveltime derivatives. Although minimizing traveltime misfit with the least-squares criterion tends to reduce the misfit of traveltime derivatives as well, it does not explicitly specify a variance for the apparent-slowness misfit. In terms of ray traveltime tomography, inverting traveltime derivatives also ensures continuity of a wavefront across receivers, thus the solution maintains a wave resolution as the traveltime curves imply.

Figure 3-1 shows several possibilities of calculated traveltimes that give the same rms traveltime misfit but may correspond to different models if one uses the least-squares criterion. The calculated traveltime at the receiver R_0 is assumed to be fixed. If the next receiver is placed at R_1 or R_2 and the rms traveltime misfit remains same, then the apparent-slowness (traveltime gradient) misfits for R_1 and R_2 from R_0 are different, implying two different models. Therefore, one must account for the receiver spacing when measuring the traveltime misfit in terms of least-squares criterion. For the same receiver location (R_2 and R'_2), the same rms traveltime misfit may also correspond to two different traveltime gradients because of the use of the least-squares criterion. Jointly inverting average-slowness data and apparent-slowness data, one can reconstruct a model that fits the traveltime *curves* rather than the data points only.

Bube and Langan (1989) addressed the problem with the least-squares criterion from a different aspect: least-squares solutions of seismic inversion problems tend to be very sensitive to data points with large errors. Using L^p minimization with $1 \leq p < 2$ gives more robust solutions, but usually with higher computation cost. Bube and Langan (1989) thus proposed to apply an iteratively reweighted least squares approach with reasonable efficiency and solve a hybrid L^1/L^2 minimization problem. The hybrid L^1/L^2 data fitting behaves like an L^2 fit for small residuals and like an L^1 fit for large residuals. They obtained favorable results when testing synthetic crosswell tomography inversion. In this study, as an alternative approach, we keep the simplicity of the L^2 minimization, but we convert one L^2 minimization problem of the absolute traveltime misfit into two simultaneous L^2 minimizations. One is the L^2 minimization of the average slowness misfit, the other is the L^2 minimization of the apparent slowness misfit. We shall demonstrate that this alternative approach also gives reliable results.

(3) Characterizing data error is important for us to understand issues of uncertainty in the refraction traveltime problem. Errors in refraction traveltime data are not arbitrarily "random", and generally do not have a zero mean to the "true traveltimes" from a statistical point of view. From our experience with numerous field experiments, we found it often difficult to determine an accurate zero time even with a modern recording system for the large crustal imaging projects, or an electronic trigger system for the small-scale survey purpose. For instance, in the latter case, a constant trigger threshold under different near-surface geological conditions may lead to different trigger delays (Zhang *et al.*, 1996). Further, the primary data from a seismic experiment are the waveform records, and the traveltimes are picked from the primary data in one way or another. Random noise does not influence the picked traveltimes explicitly. In fact, picking traveltimes from controlled-source records is a process that relies in part on the phase moveout. Therefore, we define two types of errors, *common-shot error*, a random shift for traveltimes at all the receivers from the same shot, and a *traveltime-gradient error* which is mainly due to the traveltime-picking uncertainty.

3.3 Minimizing A Physically Meaningful Objective Function

We solve a regularized nonlinear inverse problem. Starting from an initial model constructed using a conventional analytical refraction approach (e.g., GRM method), we iteratively update traveltimes and raypaths without assuming any interfaces or velocity functionals in the model. The refraction traveltime problem is highly nonunique. If inversion algorithms are properly applied, one may easily find many solutions that can predict the data equally well. However, not all these solutions are physically meaningful. To obtain an optimal solution, our strategy is to establish quantitative criteria for *meaningful* data fit and *meaningful* model correlation when sufficient physical concepts are involved. Instead of inverting absolute traveltimes, we minimize the misfit of the *average slownesses* and the misfit of the *apparent slownesses*. We apply Tikhonov regularization (Tikhonov and Arsenin, 1977) to explicitly constrain the model roughness as opposed to applying *ad hoc* posterior smoothing for keeping the inversion stable. Specifically, we minimize the following objective function,

$$\begin{aligned} \Phi(m) &= (1-\omega)\|C_l(d-G(m))\|^2 + \omega\|D_x(d-G(m))\|^2 + \tau\|Rm\|^2 && (3.1)\\ &= (1-\omega)\|\bar{d}-\bar{G}(m)\|^2 + \omega\|\hat{d}-\hat{G}(m)\|^2 + \tau\|Rm\|^2 && (3.2)\\ &= (1-\omega)S_1 \;+\; \omega S_2 \;+\; \tau S_3 && (3.3) \end{aligned}$$

$$\begin{aligned} \bar{d} &\overset{def}{=} \frac{d}{l} : \; \textit{average}-\textit{slowness data}, && (3.4)\\ \hat{d} &\overset{def}{=} \frac{\partial d}{\partial x} : \; \textit{apparent}-\textit{slowness data}, && (3.5) \end{aligned}$$

where d is the traveltime data; $G(m)$ is the calculated traveltime data for the current model m; C_l is an operator that scales a traveltime with the corresponding ray length l and returns an average slowness $\bar{d}$ along the raypath. Here, the ray length $l(m)$ is a variable parameter, and it is updated iteratively in the tomographic inversion.

Later we will show that using the shot-receiver distance to replace l in the inversion plays the same role as l. D_x is a differential operator for traveltime with respect to distance, and $\hat{d} = D_x d$ returns the gradients of the traveltime-distance curves (apparent slownesses); R is a regularization operator; τ is a smoothing trade-off parameter; and ω is a weighting factor between the average-slowness misfit norm and the apparent-slowness misfit norm. As one can see, the objective function (3.1) contains three terms all associated with slownesses in one way or another, *i.e.*, the misfit of *average slownesses*, the misfit of *apparent slownesses*, and the roughness of slowness derivatives.

3.3.1 Inversion algorithm

Efficiency of numerical computation is important for performing a nonlinear traveltime tomography. In addition to the fast raytracing approach that we described, we also want to develop an efficient inversion procedure so that a large inverse problem can be rapidly solved on a workstation. For this purpose, a critical strategy is to avoid explicitly dealing with the sensitivity matrix in inversion, *i.e.*, one should implicitly account for the effects of sensitivity matrices rather than constructing or storing the sensitivity matrix itself for inversion (Mackie and Madden, 1993; Zhang *et al.*, 1995). For example, using the Gauss-Newton (GN) method to linearize the stationarity equation associated with minimizing the objective function (3.1) and then applying a Conjugate Gradient (CG) approach to solve the inversion for each iteration (Scales, 1987) is one of these approaches. Directly minimizing the objective function using a CG method (Nolet, 1987) is another. Both techniques do not require the storage of any matrix, but only the results of a matrix multiplying a vector or its transpose multiplying a vector. We take the first approach to demonstrate our concepts in inverting refraction traveltime data. This leads to the following equation,

$$((1-\omega)A_k^T A_k + \omega B_k^T B_k + \tau R^T R + \epsilon_k I)\Delta m_k =$$
$$(1-\omega)A_k^T(\bar{d} - \bar{G}(m_k)) + \omega B_k^T(\hat{d} - \hat{G}(m_k))) - \tau R^T R m_k, \qquad (3.6)$$

$$A \overset{def}{=} \frac{\partial \bar{G}}{\partial m} = \frac{1}{l} \cdot \frac{\partial G}{\partial m}, \qquad (3.7)$$

$$B \overset{def}{=} \frac{\partial \hat{G}}{\partial m} = \frac{\partial^2 G}{\partial m \partial x}, \qquad (3.8)$$

$$m_{k+1} = m_k + \Delta m_k, \quad k = 1, 2, 3, ..., N, \qquad (3.9)$$

where each non-zero term in A_k (average-slowness sensitivity matrix) contains the length of a local ray across a model cell divided by the entire ray length, and each non-zero term in B_k (apparent-slowness sensitivity matrix) represents the differences of the ray lengths in a cell divided by the receiver spacing when the locations of two adjacent receivers are used to calculate derivatives. In fact, *apparent slowness* can be defined more robustly by giving different receiver combination. In this study we take the simplest combination for the purpose of showing this concept.

Linearizing a nonlinear inverse problem in an iterative fashion may be highly efficient for numerical computation. Linearization does not necessarily lead to a "poor" solution or miss the "global" solution. In fact, it is a matter of question *how* a nonlinear function is linearized and for *what* scale the linearization is applied rather than linearization itself. We account for nonlinearity by adding a variable damping parameter in the GN method as suggested by Morgan (1981). Because we explicitly minimize model roughness as described by equation (1), large nonlinearity occurs only in the early inversion stage due to a poor starting model, and the objective function approaches a quadratic form when the data misfits (S_1 and S_2 in equation (1)) are small and the model roughness (S_3) becomes dominant. Following a procedure described by Morgan (1981), we add a variable damping term $\epsilon_k I$ to the left-hand side of equation (6) with $\epsilon_k = \alpha \times rhs$, where α is an empirical parameter (about

0.1) and *rhs* is the rms misfit norm of the right-hand side of equation (6). If the objective function is not minimized well and quite nonlinear, then *rhs* is large, and a large damping ϵ_k is automatically applied and only small model updates are allowed. With the inversion proceeding further and *rhs* decreasing, a smaller ϵ_k drives the convergence speed faster. Several authors applied this approach to solve nonlinear electrical tomography problems (*e.g.*, Mackie and Madden, 1993; Zhang *et al.*, 1995) and demonstrated its effectiveness.

3.3.2 Average-slowness and apparent-slowness data

We chose to minimize the misfit of *average-slowness* data and the misfit of *apparent-slowness* data instead of absolute traveltimes (*integrated slownesses*). There are several advantages to use these concepts. We shall demonstrate the inversion performance with numerical examples.

Figure 3-2 shows a numerical model consisting of 200 × 50 cells with a uniform grid spacing 1.0 m. Its velocities vary from 600 m/s to 4500 m/s, and the structure consists of a near-surface low-velocity zone, and a deep graben refractor. A total of 12 shots are assumed with 48 surface receivers at a 4.0 m spacing. Figure 3-2 also illustrates the first-arrival raypaths for this survey, and Figure 3-3 displays calculated traveltimes for the model. We first estimate the upper-bound velocities using a GRM type velocity analysis function (Palmer, 1980) and construct a 2-layer starting model. Figure 3-4 demonstrates tomography results obtained by inverting different types of data, *i.e.*, *integrated slowness*, *average slowness*, and jointly *average slowness* and *apparent slowness.* A third-order derivative operator (R in equation (1)) is applied in all three inversions for regularization, and appropriate parameters are selected so that all these inversions converge to the same rms traveltime misfit (0.1 ms). It appears that inverting the absolute traveltimes tends to overestimate the features in the deep structure. Given an initial guess of the model, a larger misfit almost always occurs for the longer-range traveltimes. Therefore, inverting the absolute traveltimes attempts to produce deep features before the shallow structure is well reconstructed, and it quickly reduces the misfit variance mostly associated with long rays. On the other hand, inverting *average slowness* constrains the shallow velocities well, but cannot precisely reconstruct the deep structure due to a larger misfit variance allowed for the longer rays. Finally, this example shows that an optimal solution can be obtained only by jointly inverting the *average slownesses* and the *apparent slownesses.* Figure 3-6 and Figure 3-5 show the progressive reconstruction of the models when inverting absolute traveltimes and traveltime curves, respectively. One can see that inverting traveltime curves more tightly constrains the slowness structure at every inversion iteration. The traveltime derivative data give independent structure information.

Figure 3-7 illustrates the progress of the inversion in terms of rms *average-slowness* misfit, rms *apparent-slowness* misfit, and the objective function. Two experiments are conducted, one, inverting average-slowness data only, the other, inverting average-slowness data during the first 6 iterations and jointly inverting apparent-slowness data from the 7th iteration. It appears that the misfit of traveltime gradients rapidly decreases after the inversion starts to explicitly minimize the misfit of *apparent slowness.* An appropriate weighting factor (ω in equation (1)) is selected so that the rms misfit of the average slowness and the apparent slowness converge to the similar variance, corresponding to the compatible resolving capability. Figure 3-7 shows that one can also invert *pseudo* average slownesses (traveltimes divided by shot-receiver distances) instead of "true" average slownesses (traveltimes divided by ray lengths). In terms of misfit measurements, they are nearly identical, but inverting pseudo average slownesses avoids tracking exact ray lengths and thus saves computation time.

Figure 3-8 shows the traveltime fit for the noise-free data at iteration 4 (inverting *average slowness* only) and at iteration 25 (jointly inverting *average slowness* and *apparent slowness* from the 7th iteration). At an early inversion stage (iteration 4), traveltimes associated with short rays are preferentially fitted. With the inversion proceeding, traveltimes associated with long rays are also fitted well due to inverting the traveltime gradients (apparent slowness) until the misfit of the traveltime curves becomes negligible (iteration 25). Although we eventually fit the absolute traveltimes, inverting the traveltime curves with two separate data vectors gives different misfit criteria and requires a different inversion procedure that progressively reconstructs a model in a physically meaningful way. It also defines a physically meaningful measure of the data misfit.

Traveltime calculation is the most time-consuming step of nonlinear traveltime tomography. As we described earlier, our traveltime calculation method defines a node distribution on the basis of the model complexity. Therefore, the CPU time for each inversion iteration is nonuniform. Figure 3-9 presents CPU time for the tomography experiment inverting both average-slowness data and apparent-slowness data. Given a simple 2-layer starting model, the inversion is fast at the beginning, but slow down when the detailed features appear in the model, and eventually becomes stable when the whole model is reconstructed. This calculation was conducted on a DEC 3000 workstation.

3.3.3 Tikhonov regularization

When an inverse problem is ill-posed, no matter how sophisticated the optimization approach is, there can be no definitive "solution" solely on the basis of fitting the data. In other words, minimizing only the data misfit (even including the traveltime gradient data) does not have one "global solution". Of course, one could increase the grid size up to the point where the number of grids is equal to the rank of the least-squares matrix. But such a coarse model would not be sufficient to produce accurate forward solutions. For refraction traveltime tomography, most methods attempt to apply *ad hoc* constraints to keep the inversion stable. These include filling areas between rays with nonzero sensitivity (Hole, 1992; Cai and Qin, 1994), applying model gradient derivatives to damp the model stepsize in a creeping manner (White, 1989), or using a posterior low-pass filter to smooth the model itself after each iteration (Zhu and McMechan, 1989). We chose to solve an inverse problem that explicitly minimizes data misfit as well as model roughness using the Tikhonov regularization. The use of Tikhonov regularization avoids solving an ill-posed inverse problem and validates an inverse problem for an infinite number of unknowns (Delprat-Jannaud and Lailly, 1993; Zhang *et al.*, 1996).

Applying Tikhonov regularization involves the use of model derivative operators, and may produce a "smooth" solution. However, when we say "model smoothness" or "model roughness", we must answer, "by what criterion?" In fact, we found that not all smoothness criteria of the Tikhonov method perform well for the refraction traveltime problem. We will study the following four criteria:

$$first-order\ smoothing: \quad R = \nabla,\ S_3 = \int (\nabla m(\mathbf{x}))^2\, d\mathbf{x}, \tag{3.10}$$

$$second-order\ smoothing: \quad R = \nabla^2,\ S_3 = \int (\nabla^2 m(\mathbf{x}))^2\, d\mathbf{x}, \tag{3.11}$$

$$third-order\ smoothing: \quad R = \nabla^3,\ S_3 = \int (\nabla^3 m(\mathbf{x}))^2\, d\mathbf{x}, \tag{3.12}$$

$$fourth-order\ smoothing: \quad R = \nabla^4,\ S_3 = \int (\nabla^4 m(\mathbf{x}))^2\, d\mathbf{x}. \tag{3.13}$$

Each of these derivatives yields one criterion of smoothness. One can also apply a higher-order derivative operator and define a different smoothness criterion for inversion. Figure 3-10 shows a comparison of the inversion results for smoothness at three different criteria, *i.e.*, the first-order smoothing, the second-order smoothing, and the fourth-order smoothing. All these numerical experiments are performed by inverting both average-slowness data and apparent-slowness data. We select appropriate parameters to allow them to converge to the same misfit level. The application of a third-order smoothing operator is given in Figure 3-4.

The results show that the use of the first-order smoothness criterion for smoothing (gradient smoothing) produces nonphysical smoothness because the true model contains nonlinear velocity variations. The second-order smoothness criterion (curvature smoothness) can effectively regularize the inverse problem. One can observe the evidence that the resolution increases with the solution uncertainty. Applying higher-order smoothness criteria yields oscillating near the structure interfaces where the deep rays pass. Our experience shows that it is not necessary to apply a derivative operator higher than the fourth order. When we applied the fourth-order smoothing operator, we actually had to enforce the highest velocity in the model to be less than 4800 (m/s), which was estimated using the GRM method (the highest true velocity is 4500 (m/s)). This constraint helps to reduce the oscillation. Similar to the performance of spline interpolation/extrapolation (Press *et al.*, 1992), we found that minimizing the second- or third-order model derivatives is more stable and has less possibility of nonphysical oscillation. Figure 3-11 illustrates inversions with the 1st- and 2nd-order derivative operators for a complex velocity model. The model consists of random velocity variations with an Gaussian distribution. With 12 sources and 48 receivers on the surface, we test synthetic traveltime tomography inversions. As shown in Figure 3-11, the 1st-order smoothing operator tends to construct linear features in the model, while the 2nd-order smoothing operator allows nonlinear variations in the velocity model.

We notice that some authors chose a regularization operator with different tradeoff parameters for vertical and lateral constraints or different derivative operators for vertical and lateral regularization (e.g., Cai and Qin, 1994). This approach assumes that the lateral velocity variations are smaller than the vertical variations in the refraction problem. However, this assumption is not always true, particularly when an undulating refraction boundary occurs.

3.4 Measuring Nonlinear Uncertainty

A complete solution to any inverse problem must address issues of uncertainty. Two important approaches in geophysics are the Backus-Gilbert method (Backus and Gilbert, 1968, 1970), measuring uncertainty in terms of spread, and Bayesian inference (Tarantola, 1987), characterizing uncertainty completely through the posterior covariance operator. We apply Monte Carlo methods to measure variance and resolution from the posterior model covariance associated with our regularized inverse problem. Monte Carlo methods require inverting data vectors with random errors starting from models with random perturbation for many realizations until the posterior model covariance can be well approximated. We shall compare the performance of nonlinear and linearized Monte Carlo methods in dealing with the refraction traveltime problem.

Unlike waveform problems, noise influences traveltime data implicitly. Although numerical algorithms can be applied to pick traveltimes automatically, the user often has to determine where the first-break energy starts. In many cases, the user may need to pick all of the traveltimes manually because of noise. As we addressed earlier, we characterize refraction traveltime variance in terms of "common-shot error" and "traveltime-gradient error". Figure 3-12 displays noise-free synthetic traveltimes (solid curve) from the numerical experiment that we described and "picked" traveltimes with some assumed error patterns (dash curves). It seems unlikely that one would pick or take such rough traveltimes for inversion as those shown in Figure 3-12(a). In other words, assuming Gaussian errors for the absolute traveltimes is not realistic even at a first look and inclusion of additional random shooting-time errors is not realistic either (see Figure 3-12(b)). In fact, in most cases, one would pick traveltimes by identifying the moveout of the first-break waves other than solely based on a single trace. This leads to the possible picked traveltime curves that one may determine as shown in Figure 3-12(c), which contains "common-shot error" and "traveltime-gradient error". Therefore, for uncertainty analysis with the Monte Carlo methods, we need to construct two random vectors for data errors, and one random vector for model perturbation with uncorrelated normal Gaussian distribution:

$$\begin{aligned}
\hat{d}_k &= \hat{d} + e_k^{(1)}, \quad e_k^{(1)} \sim N(0, \sigma_1^2), && (3.14)\\
d_k &= (d + e_k^{(2)}) + \hat{d}_k \Delta x, \quad e_k^{(2)} \sim N(0, \sigma_2^2), && (3.15)\\
m_k &= m_\infty + e_k^{(3)}, \quad e_k^{(3)} \sim N(0, \sigma_3^2), && (3.16)\\
k =&\ 1, 2, ..., K,
\end{aligned}$$

where, d is a data vector and $\hat{d}$ is a data-gradient vector, $e_k^{(1)}$ is the traveltime-gradient error, $\hat{d}_k$ is the perturbed data-gradient vector with error $e_k^{(1)}$; $e_k^{(2)}$ is the shooting-time error, and d_k is a perturbed data vector by both the shooting-time error and the traveltime-gradient error, Δx is the receiver spacing for which we consider the traveltime gradient; m_∞ is the solution of our nonlinear tomography inversion, and m_k is a perturbed model vector by error $e_k^{(3)}$. Because of our objective function definition, we can directly take the rms apparent-slowness misfit to be the variance of the traveltime-gradient error σ_1^2, and use the rms average-slowness misfit for the variance of the model perturbation σ_3^2. The variance of shooting times can be estimated using the near-shot traveltimes or simply half a period of the refracted wave to account for the variance of trigger responses.

After solving K realizations, we compute the posterior covariance matrix (Matarese, 1993),

$$C_m = \frac{1}{K} \sum_{k=1}^{K} (\hat{m}_k - m_\infty)(\hat{m}_k - m_\infty)^T, \qquad (3.17)$$

where $\hat{m}_k$ is the solution of the *kth* realization. In practice, we estimate a convergence criterion S_0 for the objective function and only accept those realizations with the value of the objective function less than S_0.

We measure variance and resolution of our regularized nonlinear solution from C_m

matrix. The square roots of the diagonal elements in C_m can be interpreted as "error bars" describing the uncertainties on the posterior values of the model parameters. More importantly, model correlation tells how well each point is resolved (Tarantola, 1987). For a point i, its correlation with the entire model is given by,

$$\begin{aligned} \rho_i(n) &= \frac{C_m(i,n)}{(C_m(i,i))^{1/2}(C_m(n,n))^{1/2}}, \\ n = &\quad 1, 2, ...N, \end{aligned} \tag{3.18}$$

where N is the total number of the model parameters. If the posterior correlation is close to zero, the posterior uncertainty are uncorrelated. If the correlation is close to +1, the uncertainties are highly correlated, indicating that the parameters have not been independently resolved by the data set, but only some linear combination of the parameters. If the correlation is close to -1, the uncertainties are highly anti-correlated.

For the numerical experiment that we performed, we show uncertainty measurements using a nonlinear Monte Carlo approach (250 realizations), *i.e.*, allowing raypath perturbed in each realization (see Figure 3-13). The solution is obtained by minimizing misfit of the average-slowness and apparent-slowness data, and the inversion is regularized by the third-order Tikhonov method. We found that common-shot error primarily influences the near-surface structure, particularly near the shot locations. The traveltime-gradient error mainly produces uncertainty along the deep rays. Model correlation results from the nonlinear realizations show that two particular points that we select are fairly well resolved.

It is interesting to see that a better resolution is shown for the deep point right above the graben bottom where rays actually do not pass. This estimate is correct, because nonlinear traveltime tomography would not allow the velocities above the graben refractor arbitrary. If the velocities are too high, the deep rays would move up and reduce the velocities. If they are too low after the random model perturbation, regularized inversion would remove the low-velocity features which are not required for fitting the data. Therefore, areas where rays do not pass may not be poorly resolved. Meanwhile, we also performed linearized Monte Carlo inversions to measure uncertainty by fixing the raypaths for each realization (see Figure 3-14), which are much faster than the nonlinear approach. For the selected model point in the shallow low-velocity zone, applying linearized Monte Carlo method yields a resolution estimate similar to the result obtained by using the nonlinear approach. This is because many rays pass through the area, and the fixed raypaths are sufficient to constrain the whole area in the model. On the other hand, linearized Monte Carlo inversions fail to delineate the resolution of the second model point where rays do not pass. Since insufficient ray coverage often occurs in the refraction traveltime problem, applying nonlinear Monte Carlo inversions are necessary for measuring uncertainty.

3.5 Conclusions

After identifying a few important issues in the refraction problem, we speculate on possible improvements in performing nonlinear refraction traveltime tomography. These include developing an approach for accurate and efficient traveltime calculation, defining data correlation and model correlation with physically meaningful concepts, performing the inversion efficiently and effectively, and measuring uncertainty of the regularized nonlinear solution. All these issues are important in conducting complete refraction traveltime tomography. Therefore, we develop a new version of the SPR method with sparse and iso-angle node distribution which is particularly useful for refraction calculation. We take traveltimes into the inversion with two separate data vectors, *i.e.*, average slowness and apparent slowness. As a result, we invert the entire traveltime *curves* rather than uncorrelated traveltimes. Because we deal with an ill-posed inverse problem, we cannot obtain an unique and stable solution solely on the basis of fitting the data. It is necessary to apply additional constraints. The approach that we have taken is to employ a smoothness operator (2nd, 3rd or 4th order) to find the simplest or a minimum-structure solution that fits the data to a given tolerance. Not only do we obtain a solution, but we also measure the variance and resolution of the solution. We found it important to apply a nonlinear Monte Carlo method for measuring the uncertainty of the regularized solution in the area where rays do not pass. Finally, our tomography techniques prove effective in both numerical experiments and two real cases that will be shown later.

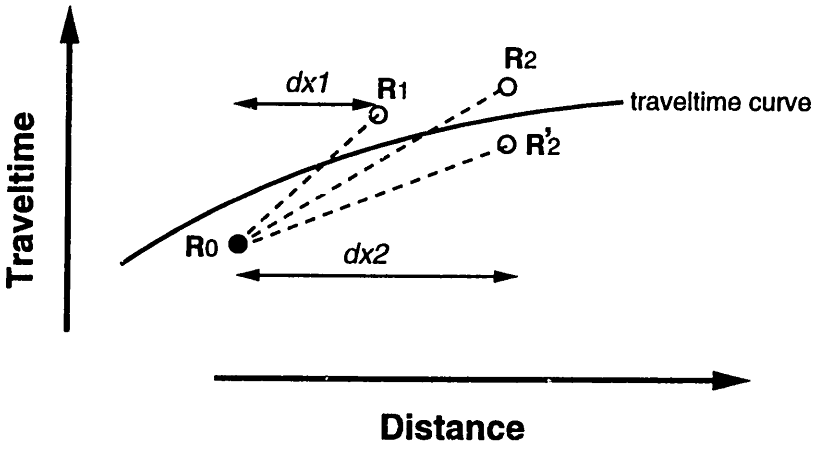

Figure 3-1: A demonstration of the limitation on the least-squares criterion for measuring traveltime fit. The calculated traveltimes at R_1, R_2 and R_2' all have the same rms misfit in terms of a least-squares criterion, but their traveltime gradients relative to R_0 fit the data gradients differently, thus corresponding to different model solutions. Therefore, a meaningful solution must fit the traveltimes as well as their gradients which are associated with the receiver spacing.

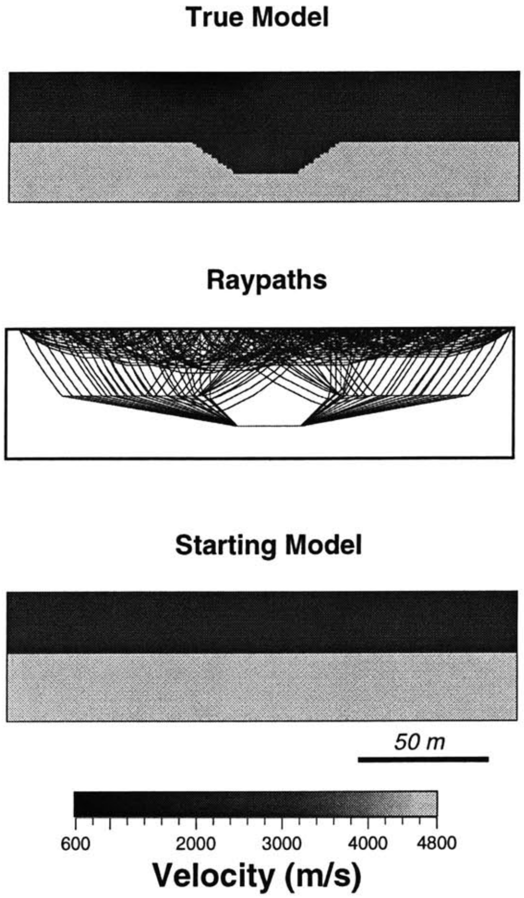

True Model

Raypaths

Starting Model

Figure 3-2: Numerical experiment for resolving a graben model containing a near-surface low-velocity zone. A "true" velocity model (200 m by 50 m) is gridded into 200 by 50 cells. raypaths for 12 sources and 50 receivers on the surface, and an estimated starting model for inversion are presented.

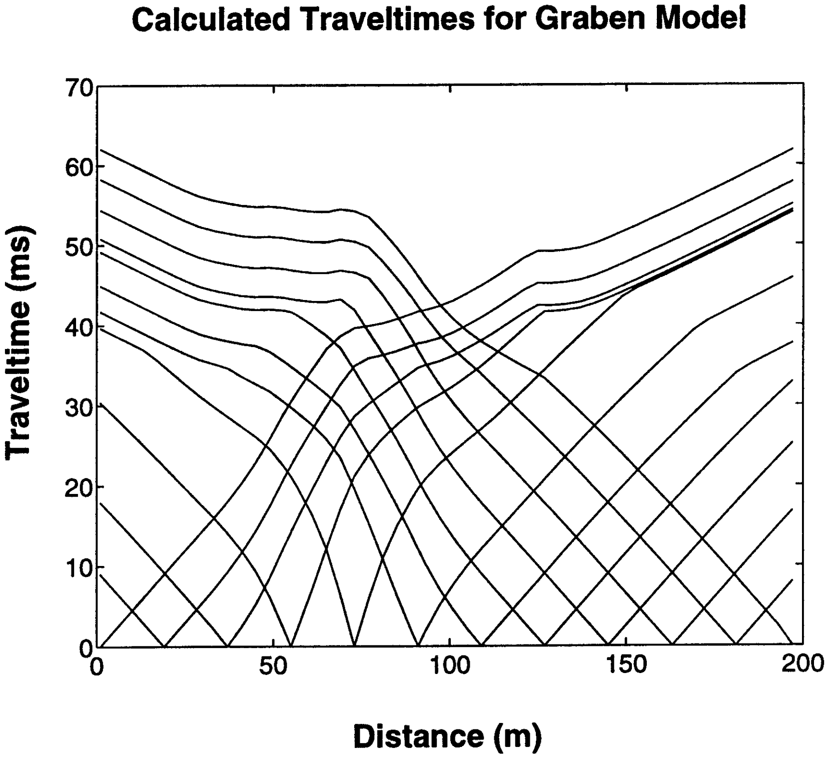

Figure 3-3: Calculated traveltime curves for the graben model. Twelve shots and fouty-eight receivers are applied for the inversion problem.

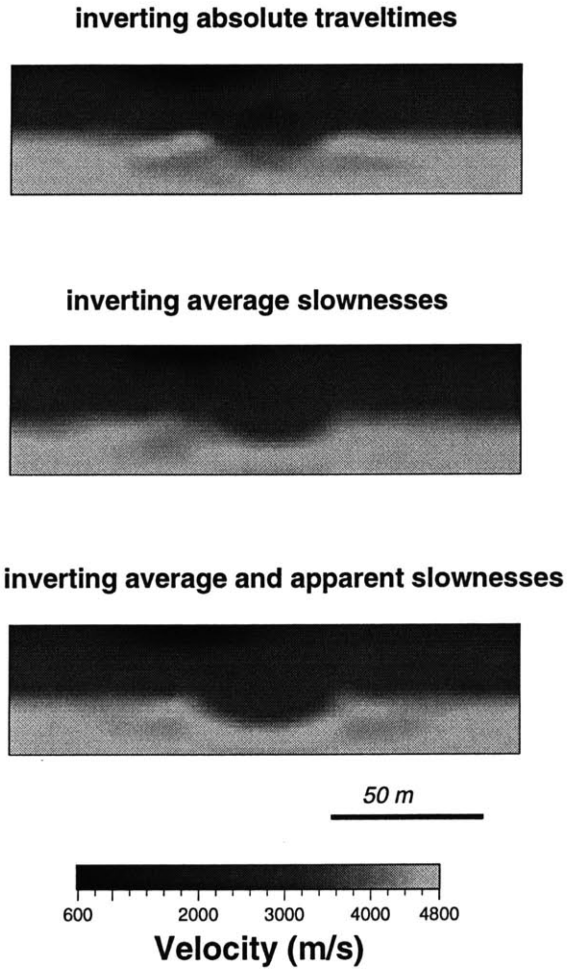

Figure 3-4: With a 3rd-order derivative regularization, inversion results from inverting traveltime data only; average slownesses only (ratios of traveltimes to the ray lengths), or both average slownesses and apparent slownesses (traveltime gradients); the last one shows the best performance for resolving graben shape and velocities.

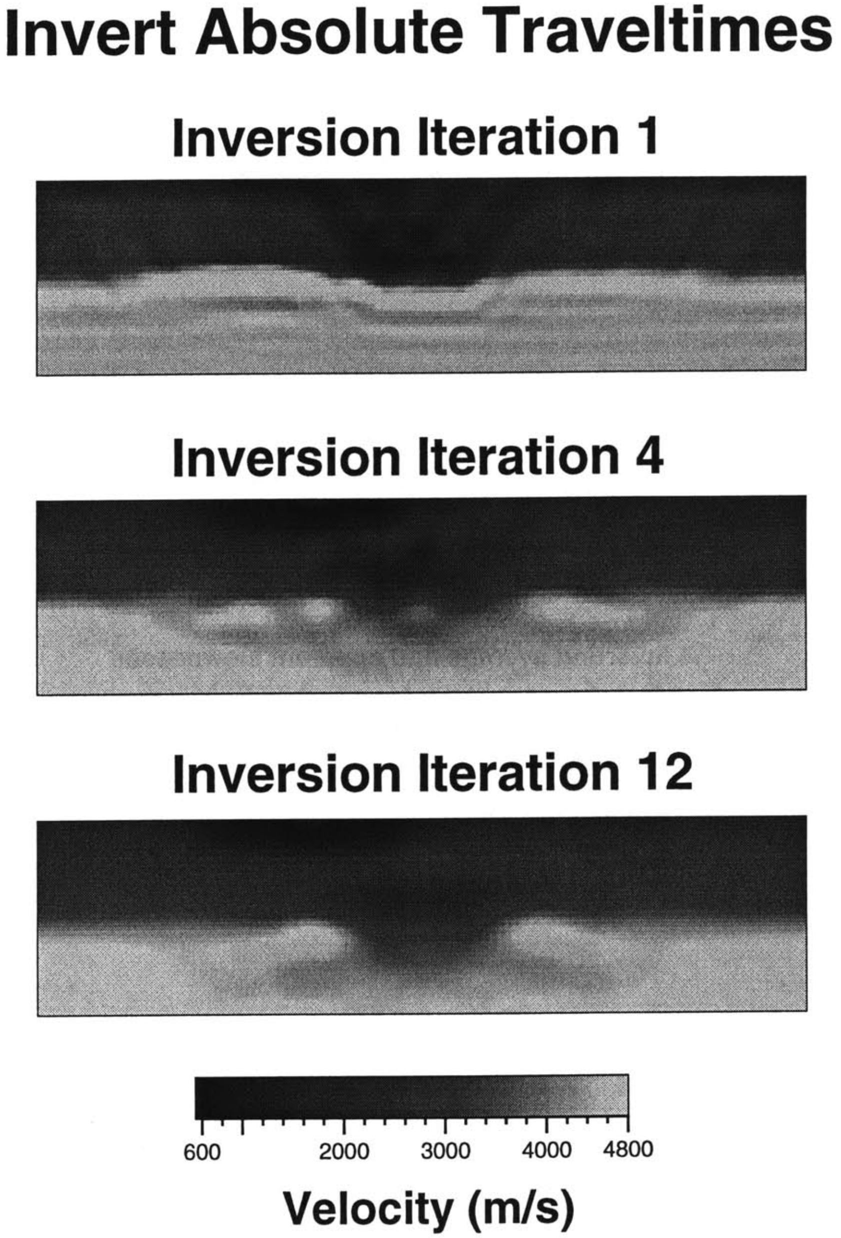

Figure 3-5: Iterative solutions by inverting absolute traveltimes.

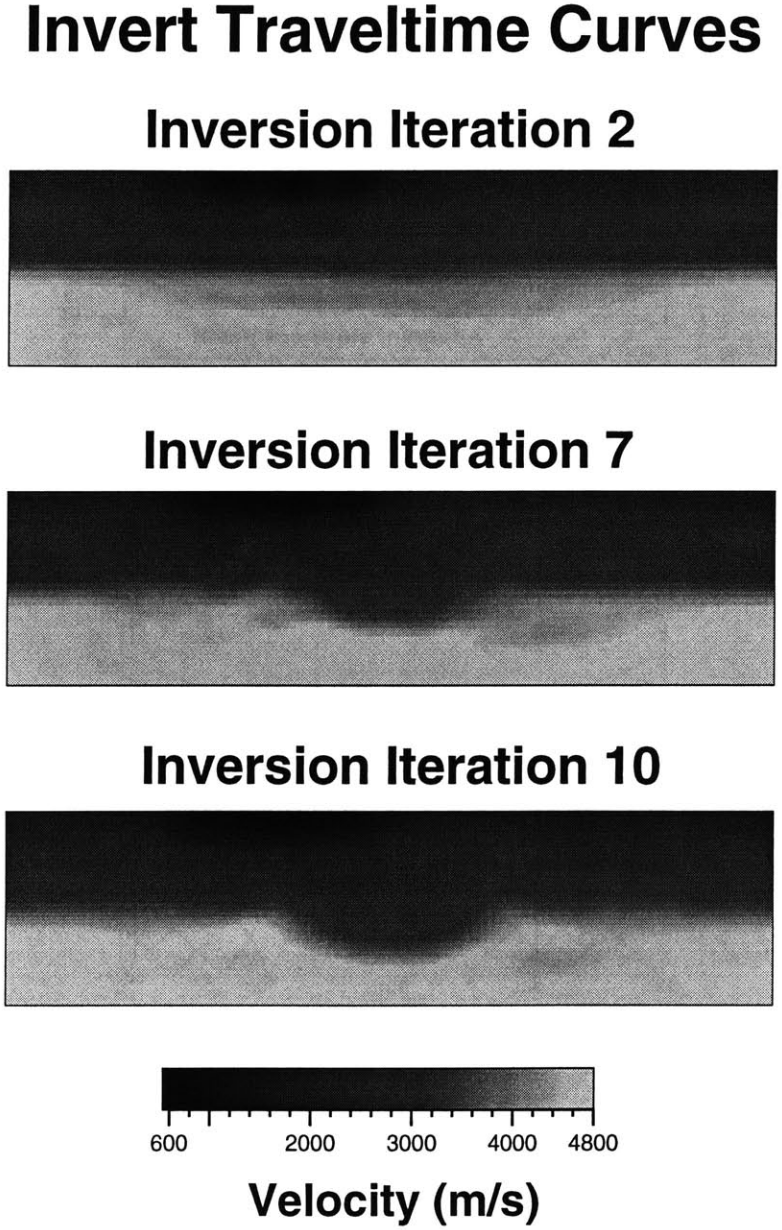
Invert Traveltime Curves

Inversion Iteration 2

Inversion Iteration 7

Inversion Iteration 10

Figure 3-6: Iterative solutions by inverting traveltime curves.

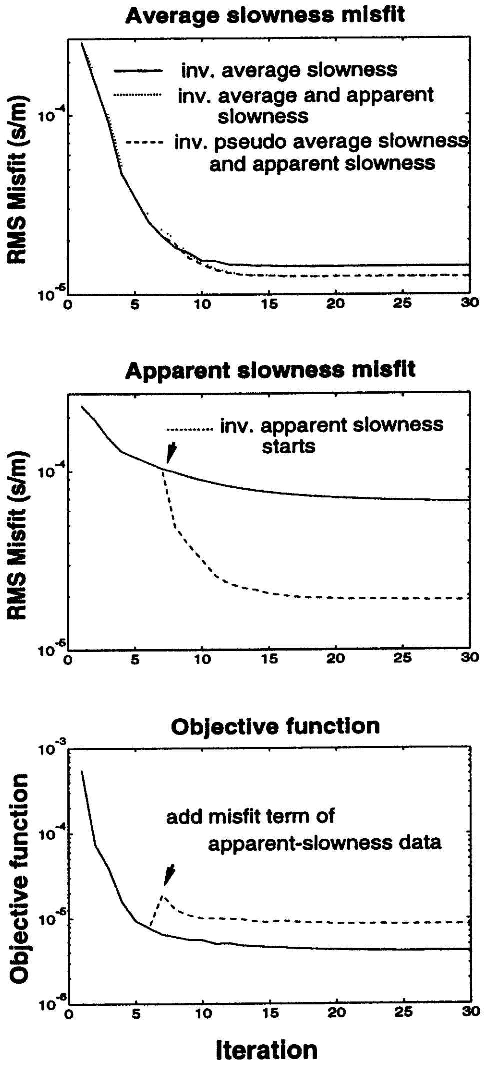

Figure 3-7: Two inversions using a 3rd-order derivative operator for regularization but different data are conducted for the model shown in Figure 3. One inversion (solid curve) takes average slowness data only in all 30 iterations; the other (dash curve) starts to explicitly minimize misfit of traveltime gradients (apparent slownesses) from the 7th iteration. Right from here, a rapid decrease of *rms* misfit is shown for both average and apparent slowness. The objective function becomes slightly larger due to the sudden inclusion of an l_2 norm of the traveltime gradient misfit.

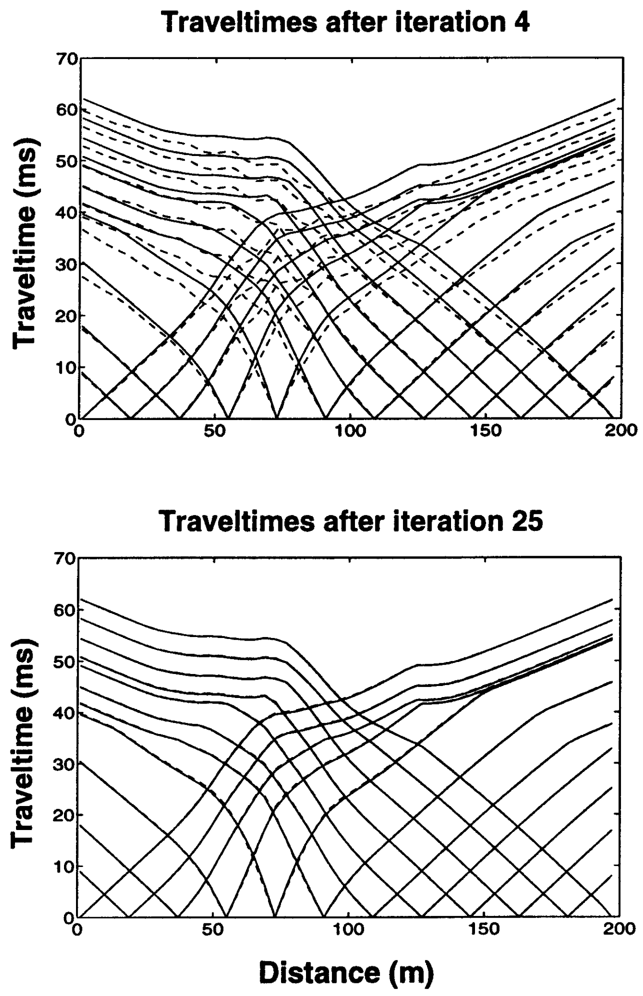

Figure 3-8: Traveltime data fit at iteration 4 and iteration 25. It demonstrates that tomography tends to invert near-shot traveltimes in the early inversion stage, later fits the long-offset traveltimes.

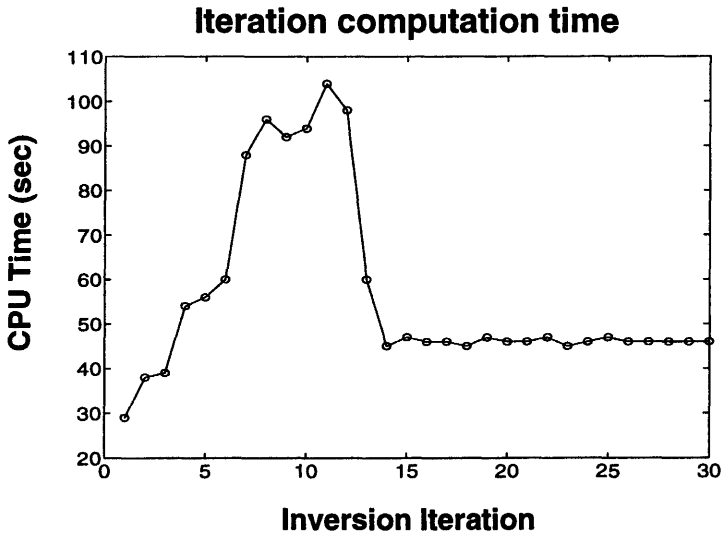

Figure 3-9: CPU run time for each inversion iteration. Note they are not equal because our forward traveltime calculation depends on model heterogeneity, and also because inverting apparent slowness data starts at the 7th inversion.

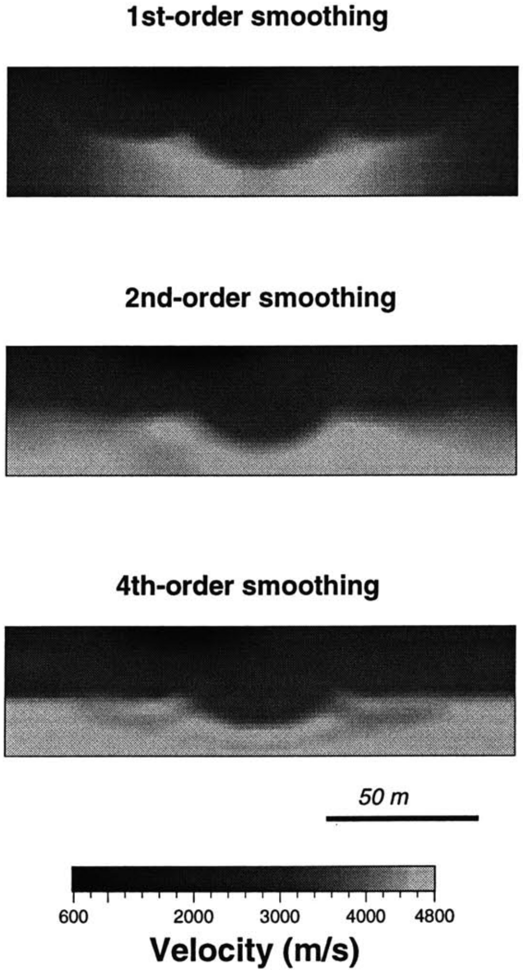

Figure 3-10: Inverting average-slowness and apparent-slowness data, tomography results using 1st-order derivative operator (over-smoothed), 2nd- and 4th-order derivative operators for regularization.

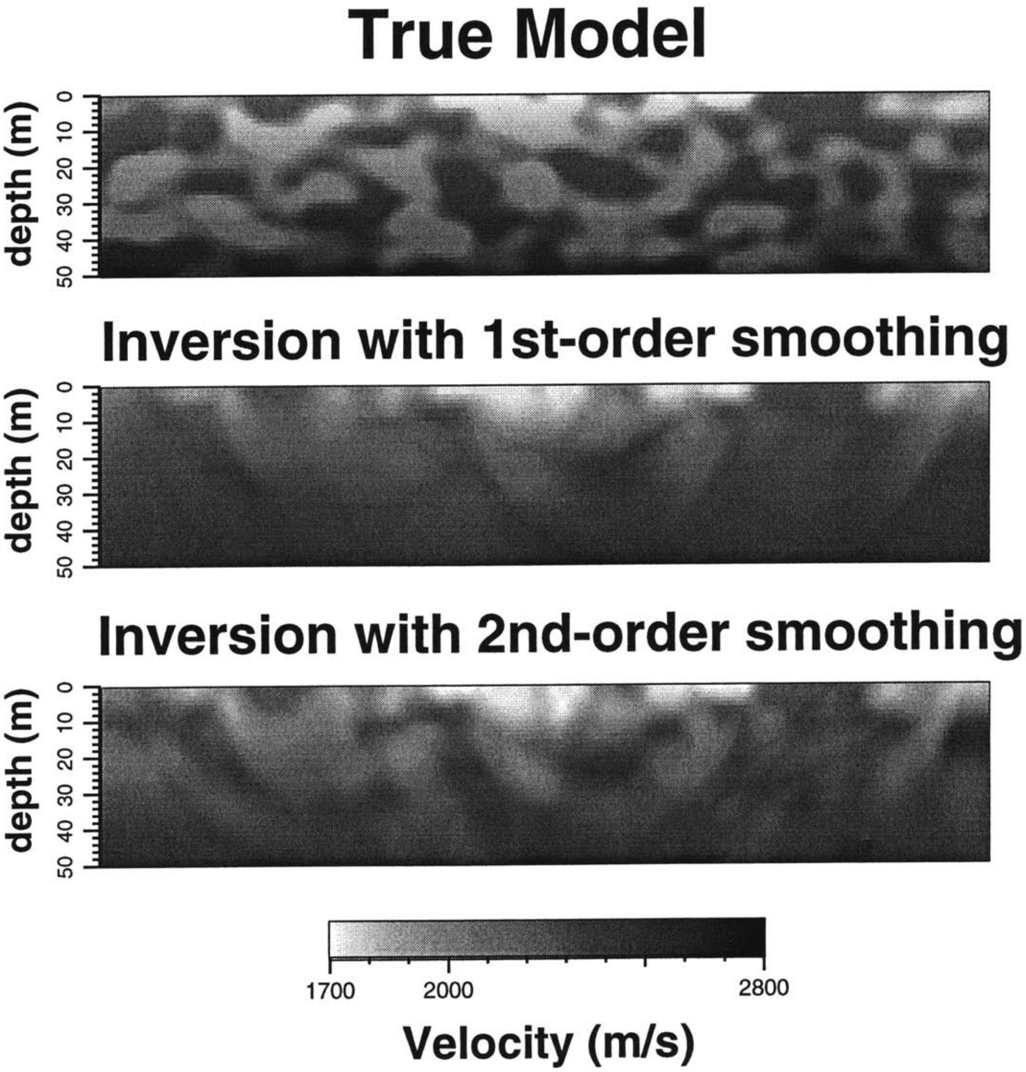

Figure 3-11: Inverting complex velocity model with 1st- and 2nd-order smoothing operators.

a) adding random data-point noise

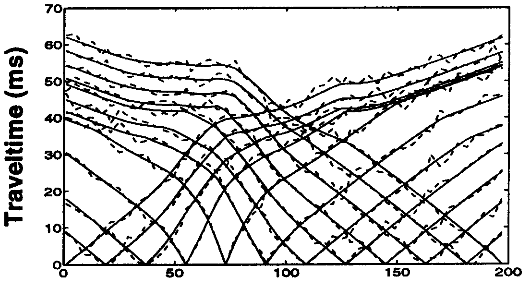

b) adding random data-point noise
and shooting-time noise

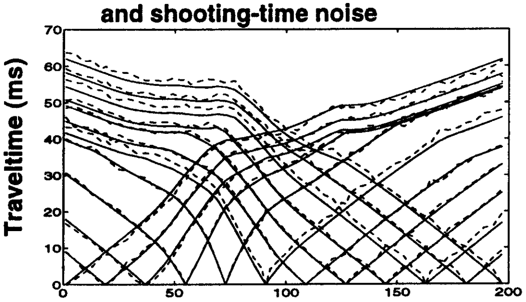

c) adding random gradient noise
and shooting-time noise

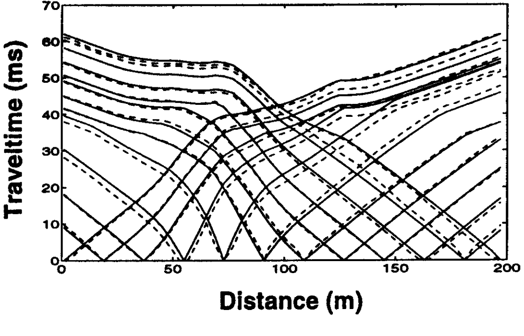

Figure 3-12: noise-free synthetic traveltimes and "picked" traveltimes with assumed noise pattern: a) adding random Gaussian noise to the absolute traveltimes; b) adding random Gaussian noise to the absolute traveltimes and to each shot record; c) adding random Gaussian noise to the traveltime gradients and also adding random Gaussian noise to each shot record. Pattern c) is realistic for refraction problem.

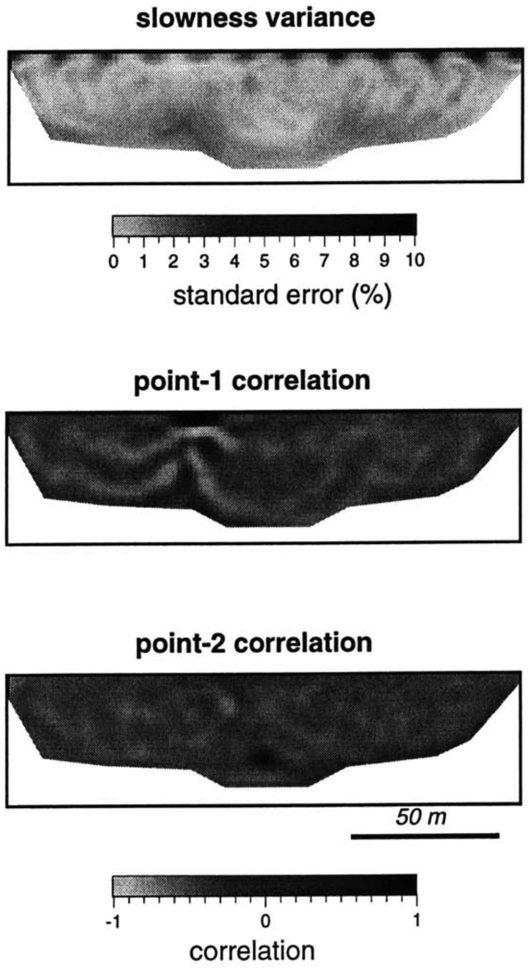

Figure 3-13: Uncertainty analysis using a nonlinear Monte Carlo method: it shows % standard error in the reconstructed slowness values as a function of position, and model correlation at two selected points. Both are well resolved.

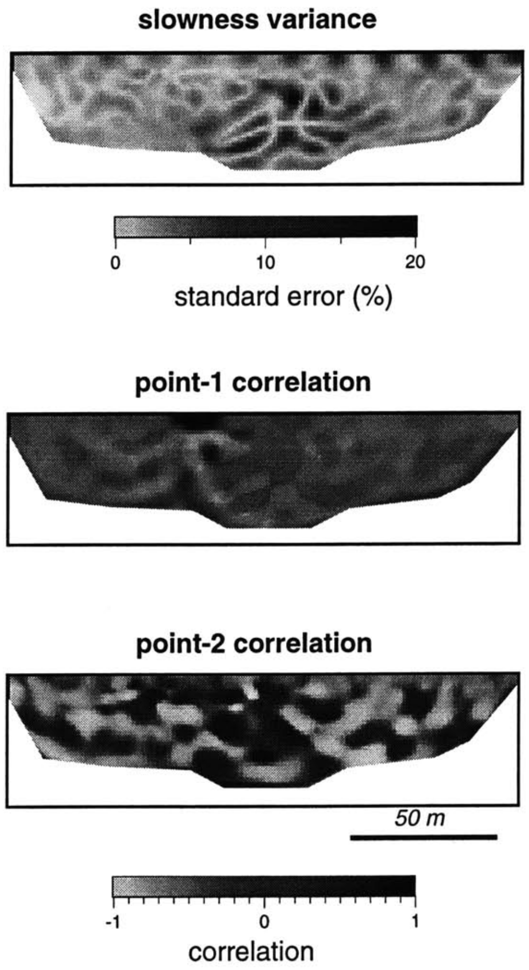

Figure 3-14: Uncertainty analysis using a linearized Monte Carlo method by fixing raypaths of the final solution. For the second point that is not covered by any rays, linearized method fails to estimate its resolution, while for the first one where many rays pass, the correlation estimate is similar to that from nonlinear method.

Chapter 4

Joint Refraction Traveltime Migration and Tomography

Abstract

Migration and tomography represent two major methods in state-of-the-art seismic imaging technology. Migration maps interfaces in the subsurface by reconstructing physical raypaths from a downward continuation process, while tomography reconstructs a physical model by inverting recorded data. For interpreting refraction traveltimes, we present two new approaches that combine migration and tomography in one joint imaging process in an iterative manner. The slowness parameters on a regular grid can be updated on the basis of fitting traveltimes as well as defining interfaces associated with the migrated traveltime image. The first method, *model-interface method*, assumes that a slowness discontinuity corresponds to the entire migration image. Therefore, a reference curvature constraint is emplaced at the image location by way of Tikhonov regularization. The second approach places a discontinuity in the regularization (Laplacian) operator according to the location of the migration image, thus we call it *derivative-interface method.* The first method gives a stronger model constraint, while the second one relies more on the data. We demonstrate that both methods are capable of reconstructing sharp features.

4.1 Introduction

Although imaging the shallow earth using the seismic refraction methods has long been a standard approach, reconstructing reliable and high-resolution image from traveltimes is still a challenge. Conventional traveltime approaches (e.g., GRM method, plus-minus method) are efficient, but they are only applicable to simple problems because of the many structural assumptions required for interpretation. Inverting a large number of traveltimes from many shots, in a fashion of the tomographic imaging, has recently become a more attractive tool, because tomography methods can potentially deal with more complex media (White, 1989 ; Zhu and McMechan, 1989; Ammon and Vidale, 1993; Stefani, 1995; Pullammanappallil, 1994). However, many studies showed that sharp interfaces in the subsurface generally are not necessary features for fitting the refraction traveltimes (Zhu and McMechan, 1989; Stefani, 1995). Subsequently, turning-ray tomogarphy methods are developed, and applied to obtain a smooth velocity structure. In Chapter 3, we presented a nonlinear refraction traveltime tomography approach that explicitly accounts for the physical context of the refraction traveltimes and applies Tikhonov regularization to obtain a stable solution. In this chapter, we show a further improved technique that combines refraction traveltime migration with nonlinear refraction traveltime tomography in one joint algorithm which is capable of reconstructing a reliable velocity model with a sharp interface. This joint process updates a slowness model associated with the physical raypaths of refractions derived from a traveltime migration.

Refraction traveltime migration consists of two steps: wavefront reconstruction and the application of an imaging condition. The wavefront reconstruction method is one of the earliest of the many techniques for interpreting refraction traveltimes. Thornburgh (1930) demonstrated that subsurface wavefronts could be reconstructed from surface arrival times by applying Huygens's principle in reverse. Subsequently, Hagedoorn (1959) elucidated an imaging condition for delineating a refracting horizon. Reconstructing wavefronts of the surface arrival times and then applying imaging condition yields the spatial image of the refractor. The physical concepts of this procedure are similar to those in the prestack reflection depth migration. Aldridge and Oldenburg (1992) implemented a refraction traveltime migration method using a finite-difference approximation to the solution of the eikonal equation for traveltime calculation. They called it "wavefront reconstruction method". Since the wavefront reconstruction is really only the first step in the method, we view the two-step imaging approach that they described as "migration". In fact, the wavefront reconstruction is equivalent to the process of the downward continuation in the reflection migration method, and applying the imaging condition yields a migrated traveltime system. We point out that refraction migration methods can be also applied to the seismic wavefield data as demonstrated by Clayton and McMechan (1981) and Hill (1987).

Although the application of refraction migration method may yield a clear image of the refractor, the imaging process requires an accurate velocity input in the same way as in the reflection migration problem. Unlike reflection problem, the refraction wavefront reconstruction is a wide-angle process. It requires an accurate raytracing approach for the traveltime downward continuation. We shall apply a new version of the minimum-traveltime method (Zhang and Toksöz, 1996). The method is far more accurate than the finite-difference approach which expands a "square wavefront", and also more accurate and efficient than the minimum-traveltime method by Saito (1989, 1990) and Moser (1989, 1991). We present two algorithms that jointly perform refraction traveltime migration and tomography. In an iterative manner, nonlinear refraction traveltime tomography reconstructs a velocity model to be used by migration, while the migrated image in turn helps locate sharp interfaces associated with refractions for the tomographic imaging. In principle, we simultaneously reconstruct velocities and wavefront systems by such a joint process.

4.2 Refraction Traveltime Migration

Before we introduce refraction traveltime migration, we will first recall what reflection migration is about. Although interpretation procedures in the way of "migration" was really first started in the refraction problem (Thornburgh, 1930; Hagedoorn, 1959), the full concept of migration was later completed in the reflection problem as a general approach to interpret seismic reflection data. Among many contributors, Claerbout (1971) established a fundamental framework for reflection wavefield migration. Since then extensive applications of migration techniques on computers have been developed for petroleum exploration (Gardner *et al.*, 1974; French, 1975; Stolt, 1978; Gazdag, 1978).

Seismic reflection migration involves reconstructing the subsurface image from the surface wavefield recordings. Instead of inverting the entire wavefield data to reconstruct a large number of physical parameters in the earth, migration simplifies the imaging problem by mapping seismic events back into the subsurface on the basis of reversing a forward wave propagation process. Therefore, migration is believed to be more efficient and practical than wavefield tomography. We should point out that migration and tomography are two completely different imaging techniques, according to the physics and mathematics that they rely on. One cannot view migration as one iteration of the tomographic inversion, or linearized tomography. In practice, reflection migration and tomography need different forward modelers for simulating wave propagation, for example, one-way wave equation for migration, but full (accoustic or elastic) wave equation for tomography. Tomography attempts to fit the recorded data by reconstructing a physical model, while migration downward continues the data without any effort to fit them but reconstructing a wavefront system instead. Both reconstruction processes are nonlinear to the seismic velocities, thus requiring sophisticated numerical techniques.

Refraction traveltime migration is an unique approach. Two oppositely propagating wavefront systems are reconstructed from the arrival times recorded on a forward and reverse spread, respectively. Then, pairs of these subsurface wavefronts intersect on or slightly below the refracting interface when the sum of their times equals the known reciprocal time. The downward continuation of two wavefront systems are separately completed by activating a line source at the receiver array each time. The line source is activated sequentially with an initiation function $T_s(X)$ derived from the recorded refraction arrival times $T(X)$:

$$T_s(X) = T_r - T(X) \tag{4.1}$$

where T_r is the reciprocal time. To properly image both edges of refractor where they are not covered by the forward and reverse raypaths, one needs to construct phantom arrival times from the traveltimes of offset shots (Rockwell, 1967; Ackermann *et al.*, 1986). The direct arrival times from the forward and reverse shots are replaced by the corresponding offset data with parallel moveout (see Figure 4-1). The downward continuation of a wavefront system is straight-forward using the minimum-traveltime method, which can expand a wavefront from any source. With the recent improvement made by Zhang and Toksöz (1996), the method is fairly accurate for complex velocities. Figure 4-2 depicts downward continuation of the forward and reverse arrival times for a two-layer graben model. Constant layer velocities 800 m/s and 3500 m/s are given in the model. Downward continuation of surface arrival times with the overburden velocity 800 m/s in the entire model results in reconstructed traveltimes $t_f(x, z)$ and $t_r(x, z)$, corresponding to the forward and reverse data, respectively. Then, according to Hagedoorn's imaging principle, the refracting interface is implicitly defined by the relation,

$$t_f(x, z) + t_r(x, z) = T_r. \tag{4.2}$$

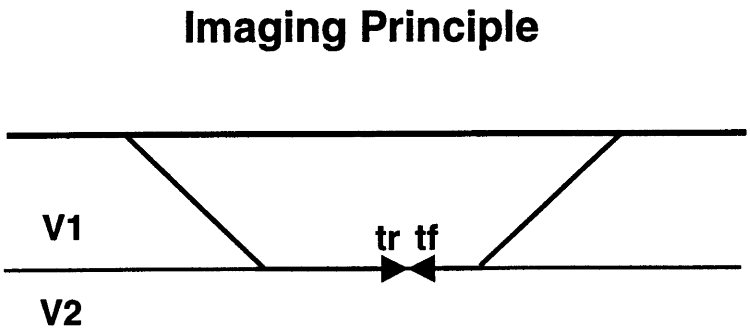

Therefore, we sum two downward continued wavefront systems, and locate grid points where the imaging condition (4.2) is satisfied. Figure 4-2c illustrates the superposition of the two reconstructed wavefront systems shown above and the migration image (solid line). The resulting depth is an accurate spatial image of the original refracting horizon.

Figure 4-3 shows the forward, reverse, and offset traveltimes for the graben model that we studied in Chapter 3 (see Figure 3-2). It has variable overburden velocities. A shallow low-velocity zone is in one side of the model, making the model asymmetric. Thus the arrival times vary with offset due to the shallow complex velocity structure. Figure 4-4 displays the downward continued wavefronts and the migration results using the exact overburden velocities. Again, the graben geometry can be well imaged.

The refraction migration procedure that we described above is similar to the prestack depth migration in reflection seismology. In prestack depth migration, one needs to downward continue a wavefront system from a shot impulse and a wavefront system from the recorded data, and apply an imaging condition. However, there are some differences between two procedures. Two downward propagators in the refraction migration are same, while the reflection migration employs a down-going propagator for shot and a up-going propagator for the data. In the refraction migration, the imaging condition is applied only once after downward continuation is completed in the entire model; but in the prestack reflection migration, after each depth step of the downward continuation, the imaging condition needs to be applied once to determine possible image. On the other hand, refraction imaging condition yields the correct refracting horizon only if the earth consists of constant velocity layers bounded by plane dipping interfaces, but the reflection imaging condition is correct for any velocity model in theory as long as it is dealing with the reflected events.

Refraction imaging condition is a good approximation in general as demonstrated by several authors (Hagedoorn, 1959; Rockwell, 1967; Schenk, 1967; Hill, 1987; Aldrige and Oldenburg, 1992). Note that the refraction imaging condition is only approximately valid in the two examples above, because raypaths of the forward and reverse shots are not coincident with the entire refracting horizon due to graben geometry. The migration results, however, are fairly accurate. This is because unrefracted wavefronts still cross near the interface when the reciprocal raypath associated with the refracted wavefronts is off the interface (Hill, 1987).

Refraction migration can yield an accurate image of refractor, but it requires detailed knowledge of the near-surface velocity structure. Therefore, the true strength of this technique can be achieved only when a tomography method is applied to obtain an accurate velocity model. In this study, we will solve a joint migration and tomography problem. Because the migration output is the image of a refractor, and the tomography output is a velocity structure, the immediate question is, how do we automatically tie two different processes together? We shall present two algorithms to answer the question.

4.3 Joint Migration and Tomography Algorithms

In Chapter 3, we described a nonlinear refraction traveltime tomography method that inverts traveltimes in a physically meaningful way. We converted refraction traveltimes into average slownesses and apparent slownesses for inversions, and regularized the inverse problem with the Tikhonov method. Therefore, the objective function consists of three terms. Using a conjugate gradient (CG) approach or a combined Gauss-Newton (GN) and conjugate gradient method (Scale, 1987; Mackie and Madden, 1993; Matarese, 1993; Zhang *et al.*, 1995), one can minimize the objective function (3.1) without constructing or storing any sensitivity matrices. Therefore, the tomographic inversions can be very efficient. In this study, we apply GN-CG method to solve a joint imaging problem iteratively.

Our objective is to combine migration and tomography in one joint imaging process. The approaches that we take are to apply constraints derived from the migration to the Tikhonov regularization for the tomography inversions. The Tikhonov method has been extensively applied in the geophysical tomography inversions to serve several purposes:

1. To produce a minimum-structure solution which does not have unnecessary features or roughness to fit the data to a predetermined misfit level (Constable *et al.*, 1987). From a statistical point of view, such a solution has the highest probability for the available data.

2. To perform a global inversion in the sense of reconstructing the whole model (Matarese, 1993).

3. To avoid solving an ill-posed inverse problem by defining effective regularization criterion in the class of the Tikhonov method so that the inverse problem is valid for

continuum and the solution is grid-independent (Delprat-Jannaud and Lailly, 1993; Zhang *et al.*, 1996; Zhang and Toksöz, 1996).

The use of the Tikhonov method involves applying a derivative operator. A Laplacian (second-order derivative) operator is a favorite one (Constable *et al.*, 1987; Smith and Booker, 1988; Rodi, 1989). In the following, we will show that regularization does not always produce a "smooth" solution as one may expect. When we say "smoothness", in fact, we must have an explicit criterion for it. This leads to the two methods for performing joint imaging studies.

4.3.1 Model-Interface Method

If we can construct a curvature constraint from the migration result, we may obtain a slowness model with sharp features by using a new form of the Tikhonov regularization. Suppose that $i_m(k)$ is a traveltime migration image (impulse response), and we assume a constant magnitude of a slowness change Δs at the interface associated with the migration image, and m is the slowness model, then we rewrite the third term in the objective function (3.3) with the inclusion of the migration image,

$$S_3 = ||\Delta s(D_1(i_m)) - D_2(m)||^2 \tag{4.3}$$

where D_1 is a first-order derivative operator, and D_2 is a second-order derivative operator.

The regularization term as defined in the equation (4.3) places a model curvature constraint with reference to the migration image. Figure 4-5 illustrates how it works. Considering a 1-D slowness structure, for a step change of the slownesses at a refraction interface with Δs $(s_{i+1} - s_i)$, the slowness gradient across the interface is a delta function with a finite magnitude Δs. The curvature of the model slownesses across the interface can be evaluated by calculating the gradient of the delta function. Because the traveltime migration image is like an impulse, and corresponds to the refraction interface, we can view the image as the gradient of a reference slowness model which consists of one interface separating two constant-slowness areas. Therefore, applying a first-order derivative operator on the migration image associated with the current model produces a curvature constraint for the nonlinear tomography inversion in the same iteration. We call this technique "model-interface method", because it assumes that the slowness interface coincides with the migration image.

Migration imaging is a process that needs accurate velocity information. Therefore, it is not necessary to conduct migration when the shallow velocities have not been reconstructed sufficiently well. In practice, we conduct tomographic inversions for a few iterations until the traveltime misfit is less than a predetermined criterion, then we start to perform joint migration and tomography. Hereafter, the migration image and the slowness parameters are simultaneously updated after each subsequent iteration. During this joint process, a significant raypath update may appear although there may not be much change in the traveltime misfit. Note that the slowness change magnitude Δs in the equation (4.3) has to be provided for conducting joint migration and tomography. However, we shall show that the imaging results are not very sensitive to this parameter. Inverting the data will eventually reconstruct a proper slowness jump when the location of the jump is correct.

Figure 4-6 demonstrates the application of the joint migration and tomography algorithm to the graben model experiment. At early inversion stage, the major concern is to reconstruct a reasonable velocity model before migration is applied. Therefore, during the first 5 iterations, only tomography inversions are conducted. But the migration results (solid line) using the corresponding velocity models are also plotted in the figure. Starting from the 6th iteration, the joint traveltime migration and tomography algorithm is applied. Figure 4-6 shows the final solution at iteration 10, which reconstructs both velocities and interface well.

4.3.2 Derivative-Interface Method

Applying a Laplacian operator for regularizing the inverse problem as in equation (4.3), we assume that the model parameters are correlated, and we conduct inversions to reconstruct the whole model with the same correlation. In seismic refraction problem, however, we often deal with the earth structure that consists of different geological units, namely, overburden low-velocity zone, high-velocity refractor. Physically, the elastic parameters in one geological zone may not be correlated with those in the other geological zone. If we can construct an interface between two zones by way of migration, we may correlate model parameters in the same zone only and allow tomography inversion to determine any possible slowness jump across the interface. This motivates the second approach for doing joint migration and tomography: constructing an image driven regularization operator which has a derivative discontinuity along the migration image. Specifically, we rewrite the regularization term in equation (3.1) for joint migration and tomography:

$$S_3 = ||R_i m||^2 \tag{4.4}$$

where R_i is an image driven operator, which varies with iteration when joint migration and tomography is activated. In Figure 4-5, we illustrate derivative discontinuity across cell i and $i+1$ along z axis (depth). In numerical implementation, a difference operator is applied instead of a differential operator for the regularization purpose (e.g., Constable *et al.*, Ammon and Vidale, 1993, Zhang *et al.*, 1996). An uniform Laplacian operator connects three cells and returns a roughness residual, $s_{i-1} - 2s_i + s_{i+1}$ for point i, and $s_i - 2s_{i+1} - s_{i+2}$, for point $i+1$, except at model edges. When a migration image is derived, i.e., it is located between cell i and cell i+1, we design an operator R_i such that it has a derivative discontinuity across the image, returning $s_{i-1} - s_i$ for point i, and $-s_{i+2} + s_{i+1}$ for point $i+1$, and the same three-point formula for cells elsewhere except for the model edges. Therefore, there is no connection between cells i and $i+1$. In other word, the slowness change across the image

$s_i - s_{i+1}$ is not constrained at all, inversion will determine this value on the basis of fitting data and correlating model parameters in each individual zone.

We take a similar procedure to the first method, i.e., conducting nonlinear refraction traveltime tomography for a few iterations, then activating joint migration and tomography until the rms traveltime misfit is acceptable. One may choose different regularization parameters for each correlated parameter zone, say, τ_1 for the upper zone, and τ_2 for the lower zone. In general, a smaller τ_1 may be selected for the overburden medium, because large velocity variations may occur in the shallow structure. A smaller τ_1 allows larger model roughness. In theory, there should be one unique set of τs that allows a model to fit data to a predetermined noise level. However, one may not be able to find the exact τs needed without conducting any inversion, because such optimal regularization parameters are associated with data residuals and model residuals. Therefore, trial-and-error experiments are required. Numerical examples will be demonstrated.

4.3.3 Comparison of Two Algorithms

Two different approaches can be applied to accomplish same goal, i.e., jointly conducting migration and tomography on the basis of regularizing the model parameters. The first approach, which places an *a priori* curvature constraint, seems to apply a stronger penalty on the model slownesses than the second one. When the migration image is taken into the tomography inversion as a curvature constraint in certain iteration, a slowness interface must appear at the image location. When the second approach is applied and the model correlation is disconnected for areas above and below the image location, the migration image only implies a possible interface in the model. Whether the interface is true and how large the slowness jump is, it will be further determined by the nonlinear tomography inversion. In other words, during the joint process, our first approach completely trusts the migration result, while the second one leaves the image reliability to tomography. As we addressed earlier, the imaging condition in the refraction migration problem is not exact, but approximate. The situation that the migration image does not correspond to a refractor could happen, where the second approach can be more applicable. On the other hand, the first approach can be more useful if the deep rays cannot sufficiently constrain the refractor in the way of the tomographic inversion, and if the refractor geometry is not too complex. We shall show that both approaches can well reconstruct the graben model. For a model that consists of a discontinuous refractor, however, only the second (derivative-interface) method works well.

Figure 4-6 shows a model consisting of a shallow low-velocity zone, and a deep refractor with sharp horizontal interface and lateral discontinuities. The model scale is exactly same with the graben model, and we actually take the calculated traveltimes for the same shots and receivers as for the graben model and investigate the resolving capabilities of the two joint imaging approaches. Figure 4-7 displays forward, reverse, offset traveltimes and phantomed traveltimes. In comparison to the traveltimes shown in Figure 4-3 for the graben model without the lower layer discontinuity, a systematic delay occurs for all far receivers. This suggests velocity ambiguity for the overlain discontinuity.

In the following tomography and joint migration and tomography imaging processes, we start from a homogeneous initial model. The image resulted from nonlinear refraction traveltime tomography shows a major shape of the graben with relatively large velocity contrast near the edges of graben. It also shows evidence that under the central graben bottom, velocity is low, but it does not show sharp lateral contrast owing to the nearly horizontal raypaths. Joint migration and tomography methods, however, accurately reconstruct sharp horizontal interface. In Figures 4-6c and 4-6d, migration images are also displayed over the velocity solution for illustration. Both model-interface and derivative-interface methods show evidence of low velocity under the central graben. In fact, their solutions are nearly identical.

It is also important to know how the solutions of the two joint imaging methods are sensitive to the choices of the a priori parameters, for example, slowness variance Δs in the model-interface method, and the trade-off parameters τ_1 and τ_2 in the derivative-interface method. We will repeat joint migration and tomography for a range of these parameters and demonstrate their sensitivities to the solutions.

The true velocity change at the refractor interface is 1500 m/s (from 3000 m/s to 4500 m/s) in the graben model. Figure 4-8 illustrates that the model-interface method is capable of imaging structure when an approximate estimate of this parameter is used, for example, 1000 m/s and 2000 m/s, respectively. As we learned in Chapter 3, one may find many global solutions from conducting nonlinear refraction traveltime tomography fitting data equally well. The role of Δs in the model-interface method is to direct the joint migration and tomography imaging to obtain one global solution that has an interface associated with the migration image. Therefore, this parameter need not be exact. In fact, one can estimate this parameter reasonably well based on velocity analysis from the traveltime curves prior to imaging.

When applying the derivative-interface method, we need select the regularization trade-off parameters τ_1 and τ_2. Matarese (1993) showed the general role of the regularization parameter in nonlinear traveltime tomography. With τ increasing, the rms traveltime misfit increases and the model solution becomes smoother. In contrast, with τ decreasing, the rms traveltime misfit also decreases, and the model tends to be rougher. The idea is to choose a proper τ so that the rms traveltime misfit converges to a predetermined noise level when dealing with real data, and the solution is geologically meaningful. Using the derivative-interface method for joint imaging, we may need to select two different trade-off parameters as we addressed earlier. Figure

4-9 shows that the graben model can be well reconstructed if we take τ_1 and τ_2 to be 20.0 and 200.0, respectively. But the results also show that they are not too sensitive to these parameters. With the change of τ_1 or τ_2 by a factor of 2, the solutions are still acceptable.

4.4 Low Velocity Zone Problem

Joint migration and tomography proves to be very useful for imaging the graben model. It combines the advantages of migration and tomography, and allows to resolve a sharp interface and smooth velocity structure. However, it by no means solves all the difficulties in the refraction traveltime problem. In this section, we shall show that the joint method does not help to improve the low-velocity zone image in the subsurface. The low-velocity zone problem has long been a difficult one for the application of the refraction traveltime method (Zanzi, 1990).

We start from a two-layer model with dipping interfaces as shown in Figure 4-11. At very short offset distance, the first-arrivals are the direct waves, then the refractions from the first interface. At long offset distance, the refractions from the second interface come first. In Figure 4-12 we show a modified model and place a low-velocity zone (Vp: 1700 m/s) in the second layer (average P-wave velocity 2300 m/s). In this case, many rays pass above or beneath the low-velocity zone, but few pass through the zone. The first-arrival traveltimes for both models are presented in Figure 4-13 for a comparison. The influence of the low-velocity zone is small, showing low sensitivity. We apply both tomography and joint migration and tomography method to the synthetic traveltimes for the two models, and reconstruct them from a homogeneous starting model (P-wave velocity 3200 m/s). In these cases, we apply the model-interface method in the joint imaging approach.

In Figure 4-14, we show the results of imaging the two-layer model by way of traveltime tomography and joint migration and tomography methods. Similar to the graben model that we demonstrated earlier, joint method can better reconstruct the image than the tomography method, resolving a sharp interface associated with the forward and reverse traveltimes. For the second model consisting of a low-velocity zone, Figure 4-15 shows that the tomography method roughly resolves a low-velocity zone in the second layer, but the geometry of the interface between the second and the third layers apparently trades off the velocities in the zone, resulting in a biased solution. The joint method does not improve the solution, and the interface beneath the low-velocity zone is incorrectly placed due to the incorrect overburden velocities. However, both solutions give traveltimes to fit "data" equally well with rms misfits less than 0.1 ms.

This experiment suggests that the joint imaging method may still suffer from nonuniqueness although it reduces the number of possible solutions because of the additional data information that is utilized. This problem occurs due to the limited physical information in the data. As we can see in Figure 4-13, the signature of the low-velocity zone in the subsurface is very small for receivers on the surface. Therefore, it is easy to find many solutions to explain the data. Among those, the easiest one, a minimum-structure solution, may not approximate the true model well if sharp boundary exists around the low-velocity zone. Possible approaches for solving such a problem in the future may include method that accounts for the first-arrival amplitude and its attenuation in some way, or that applies *a priori* low-velocity constraints in the tomography inversion.

4.5 Conclusions

In this chapter, we introduce two new imaging approaches that combine refraction traveltime migration and tomography in one joint process. Two methods proposed both on the basis of regularizing model parameters, are, model-interface method and derivative-interface method. The model-interface method completely trusts the migration result and assumes a slowness discontinuity along the entire image. The derivative-interface method, on the other hand, suggests a possible interface at the image location, allowing the tomography inversion to update slownesses in both sides of the image and further determine whether an interface should stay. From a first look, it seems that the second method should be more flexible. Nonetheless, when the ray coverage in the subsurface is not sufficient, the first method may be more useful, with a stronger constraint, provided that the refractor geometry is not too complex.

Finally, when we evaluate the performance of joint migration and tomography approaches, we have to admit that the results are fairly good for general structures. All these tests started with an initial homogeneous slowness model, but the slowness structure was well reconstructed after about 10-15 iterations. Remember that we used only the first-arrival refraction traveltimes recorded on the surface. On the other hand, we also demonstrated some difficulties of the methods when imaging the low-velocity zone in the subsurface.

Why does a joint migration and tomography imaging method work better than the tomography alone? The answer is simple: because the sufficient physics context of the seismic wave propagation has been accounted for in the joint imaging methods. Migration and tomography represent two different perspectives on the seismic data, the earth model, and their relationship. The former tries to reverse the wave propagation process (forward modeler) and uses the data as an initial condition; the latter attempts to reverse the input (model parameters) and the output (data) in the seismic wave propagation. When two approaches are combined, it presents a maximum resolving power.

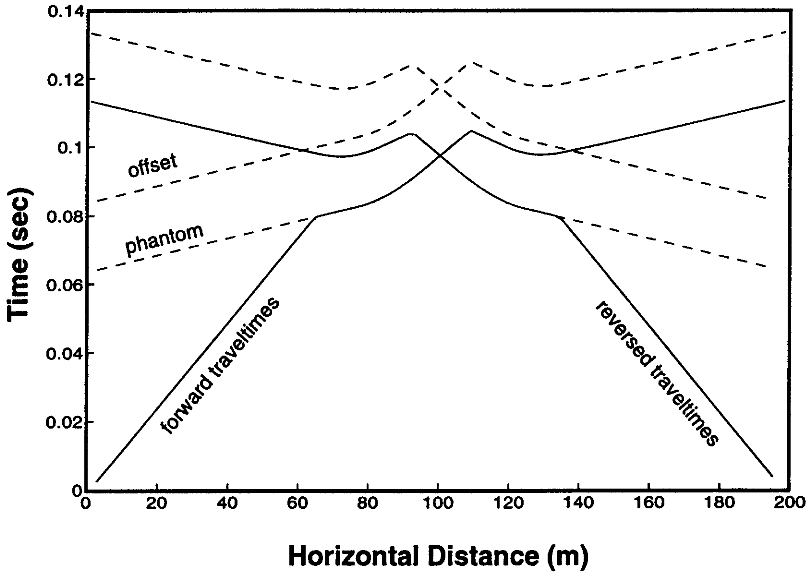

Figure 4-1: Forward, reverse, and offset traveltimes for a simple two-layer graben model. The forward and reverse traveltimes are phantomed with the offset data for the purpose of migration.

a) Downward continuation of the forward traveltimes

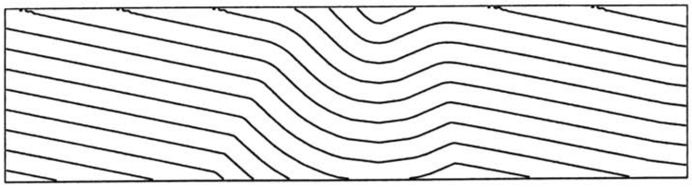

b) Downward continuation of the reverse traveltimes

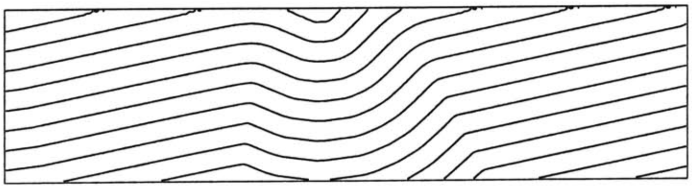

c) Superposition of the two reconstructed wavefronts

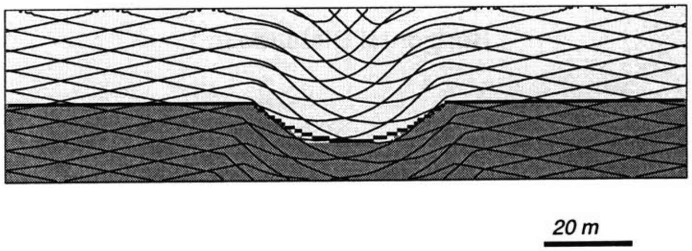

Figure 4-2: Downward continuation of the phantomed forward and reverse traveltimes with the overburden velocity constructs two wavefront systems. Summing up two wavefront systems and applying an imaging condition yields an migration image.

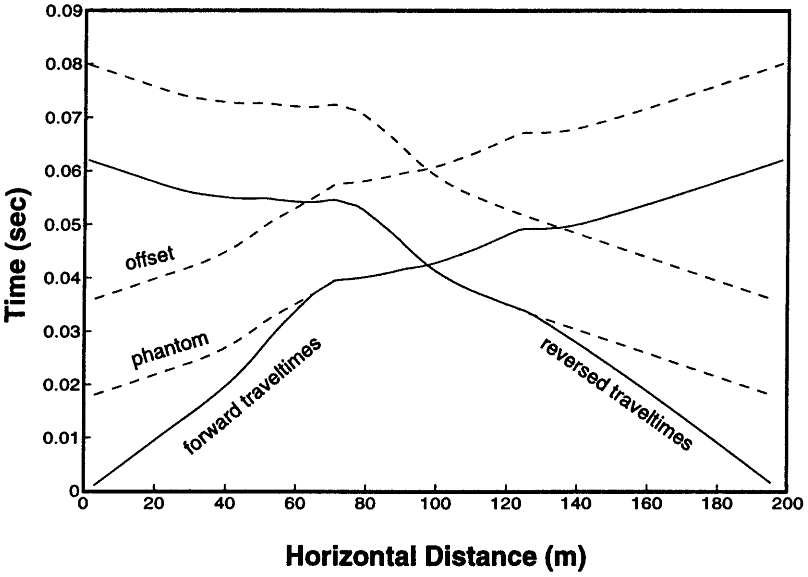

Figure 4-3: Forward, reverse, and offset traveltimes for a graben structure with variable overburden velocities. Notice asymmetric traveltime curves due to a low velocity zone in the left side of the model.

a) Downward continuation of the forward traveltimes

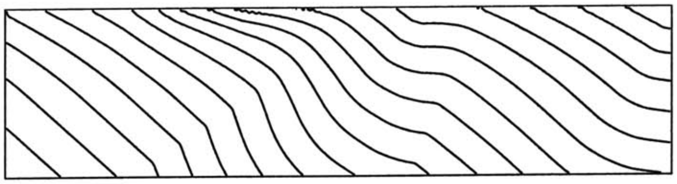

b) Downward continuation of the reverse traveltimes

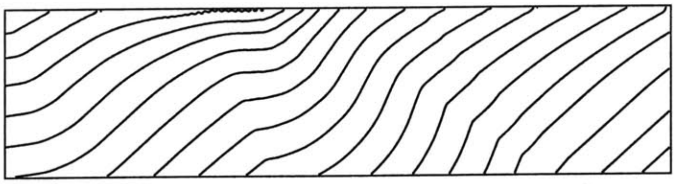

c) Superposition of the two reconstructed wavefronts

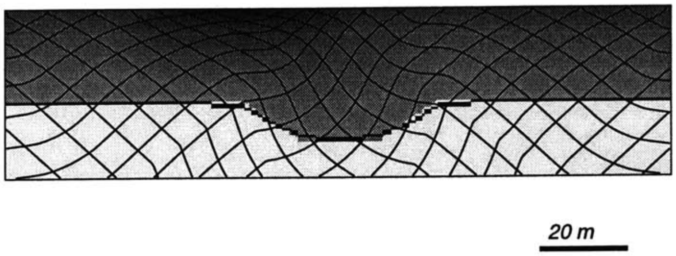

Figure 4-4: Downward continuation of the phantomed forward and reverse traveltimes with the overburden velocity constructs two wavefronts systems. Applying an imaging condition yields migration result which is fairly close to the model interface.

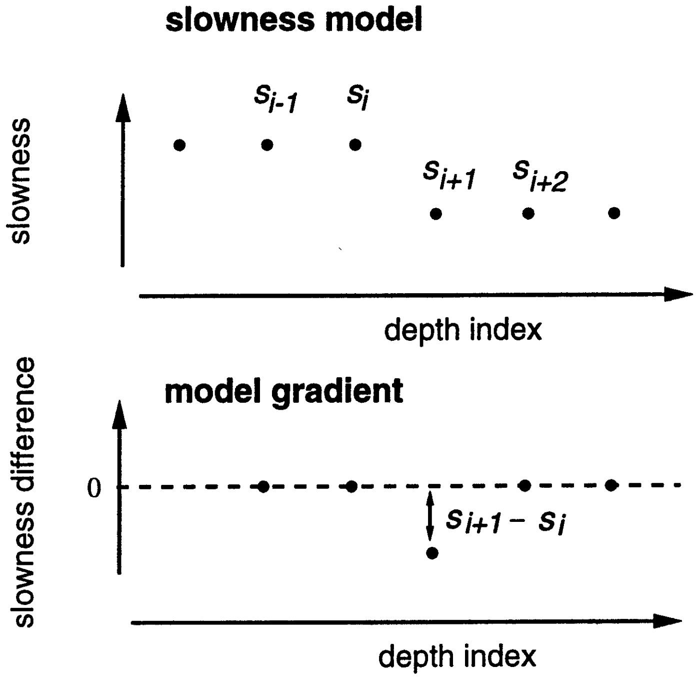

Figure 4-5: a) 1-D slowness cells; 2) taking derivatives of a) results in an impulse response. If we use the migration image to correspond to this interface, a curvature constraint can be constructed by taking derivative of the image. See text for details.

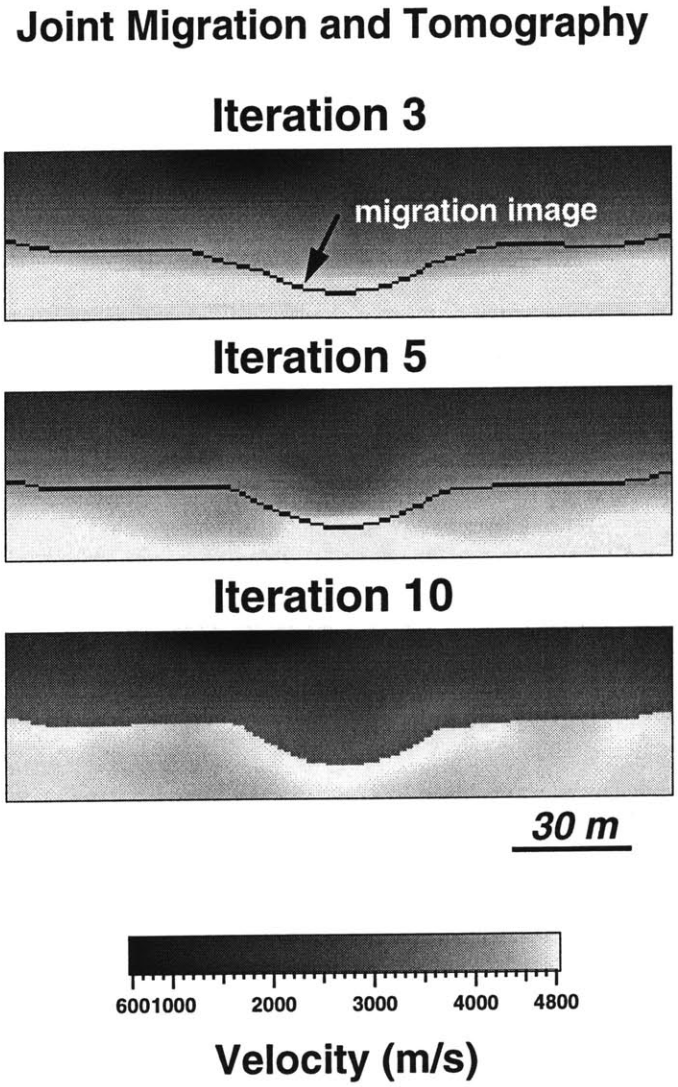

Figure 4-6: Iterative solutions using a model-interface algorithm for joint traveltime migration and tomography. During first 5 iterations, only tomography inversions are conducted. From the 6th iteration, joint algorithm is applied.

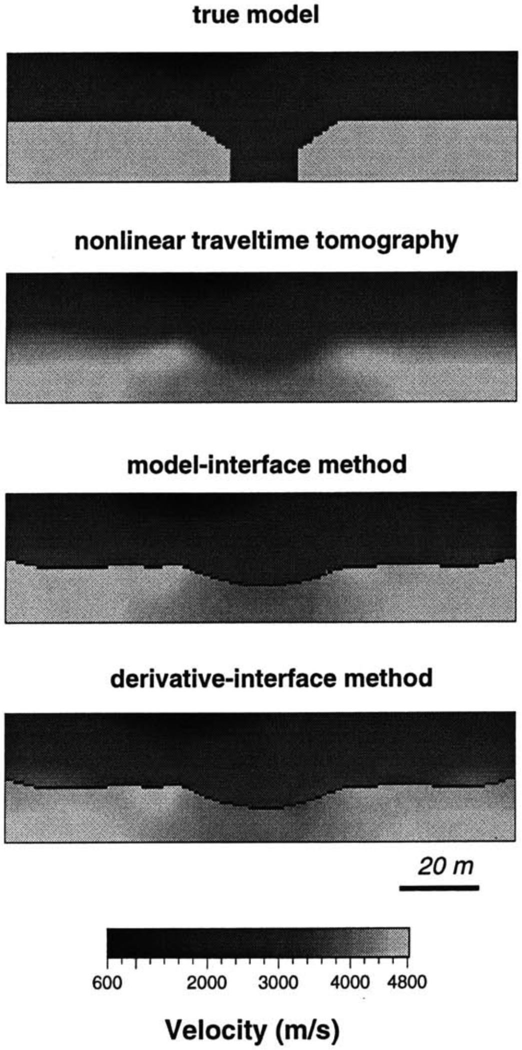

Figure 4-7: a) a graben model with overlain discontinuity; b) nonlinear refraction traveltime tomography; c) solution of joint migration and tomography by model-interface method (migration image displayed); d) solution of joint migration and tomography by derivative-interface method (migration image displayed).

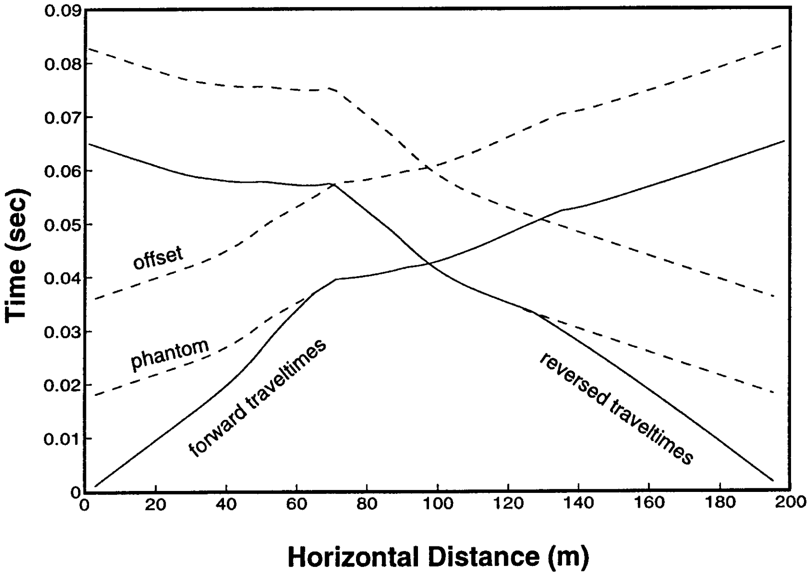

Figure 4-8: Forward, reverse, and offset traveltimes for the model shown in Figure 4-6. Forward and reverse traveltimes are phantomed for migration imaging.

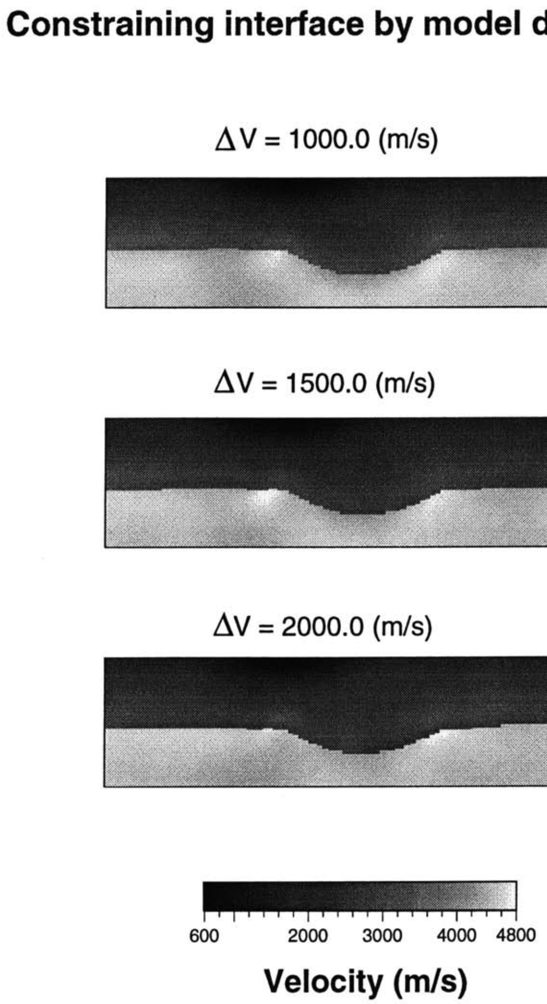

Figure 4-9: Imaging graben structure by model-interface method with a range of assumed velocity change at interface. Solutions show little sensitivity to the choices of these parameters.

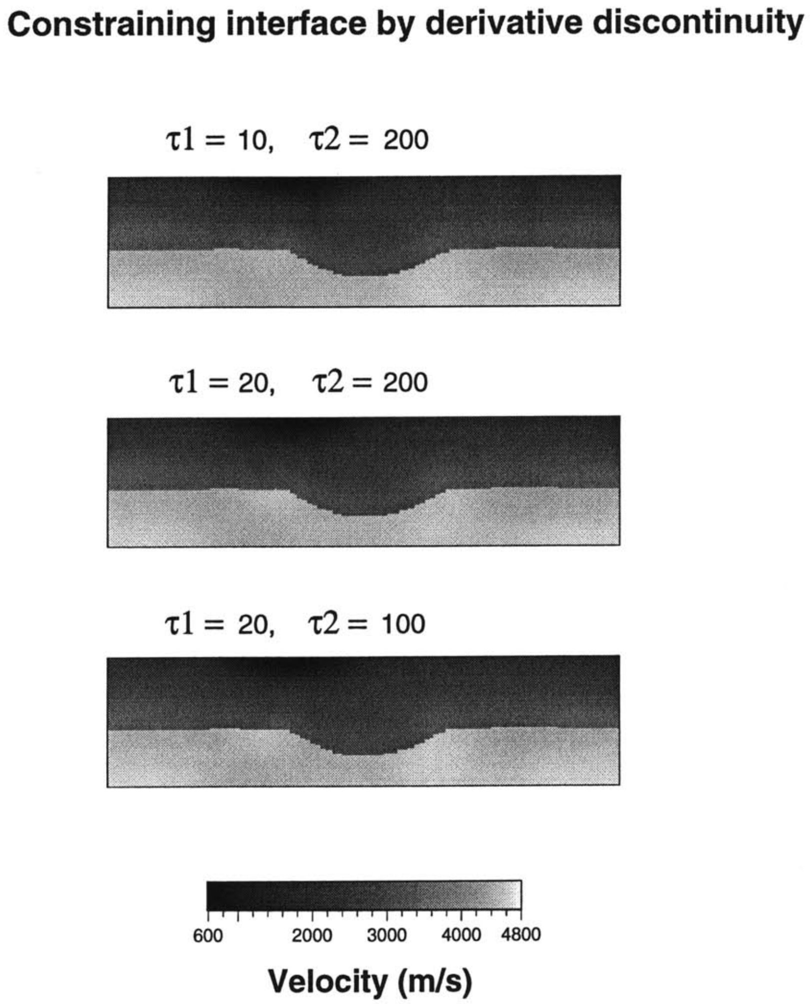

Figure 4-10: Imaging graben structure by derivative-interface method with a range of regularization trade-off parameters. Solutions show little sensitivity to the choices of these parameters.

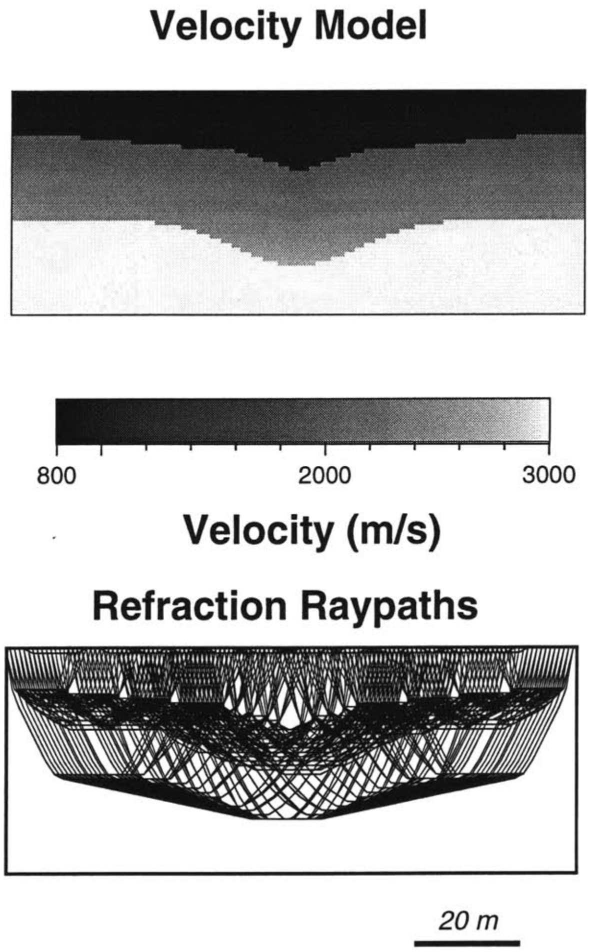

Figure 4-11: A two-layer velocity model, and raypaths of the first arrivals from 15 sources to 96 receivers on the surface.

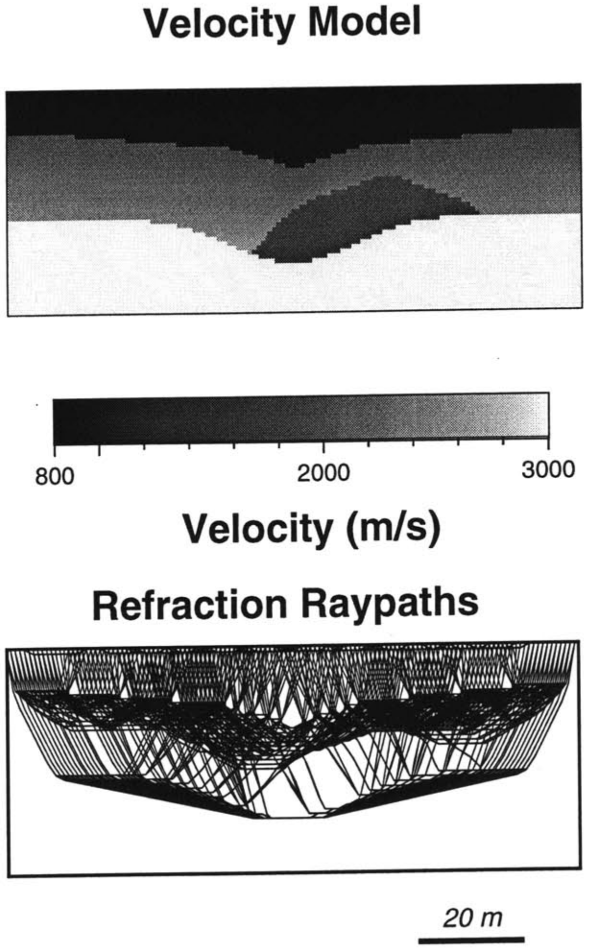

Figure 4-12: A two-layer velocity model with a low-velocity zone in the second layer, and raypaths of the first arrivals from 15 sources to 96 receivers on the surface.

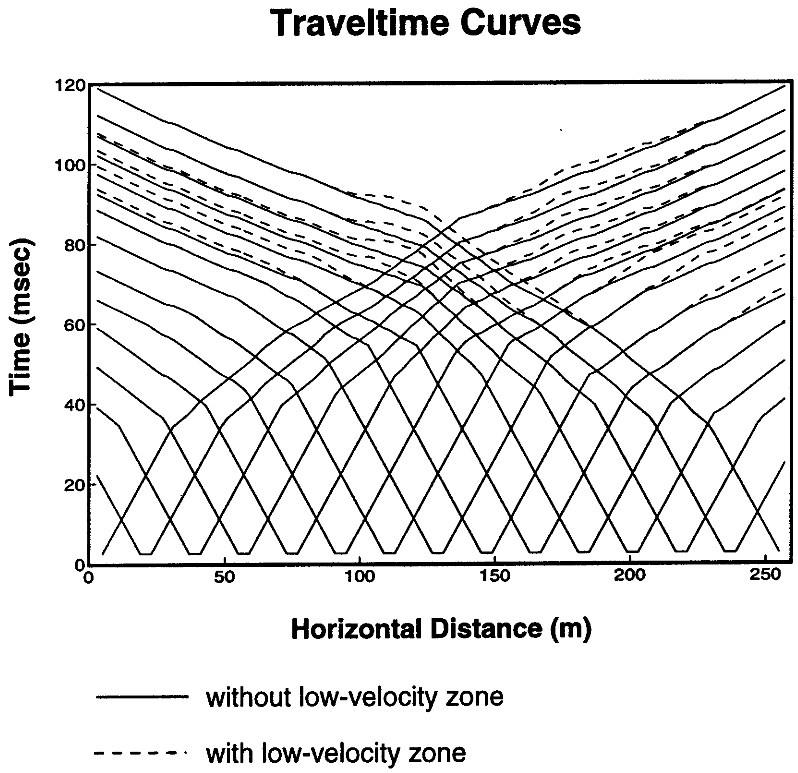

Figure 4-13: The first-arrival traveltimes for the two-layer model (solid line), and for the two-layer model with a low-velocity zone in the second layer (dashed line).

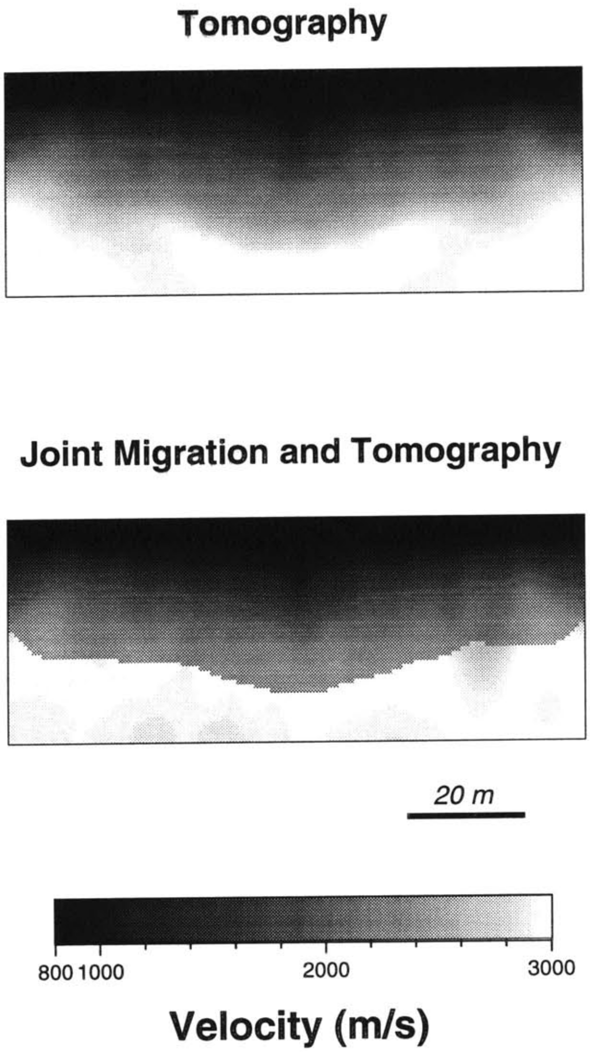

Figure 4-14: Tomography and joint migration and tomography solutions for the two-layer model.

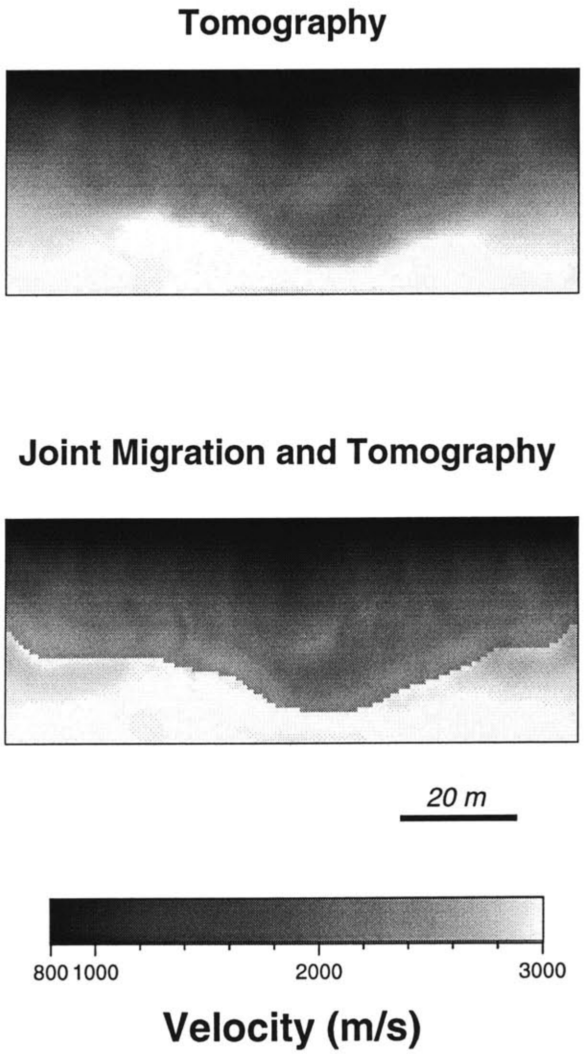

Tomography

Joint Migration and Tomography

Figure 4-15: Tomography and joint migration and tomography solutions for the two-layer model with a low-velocity zone.

Chapter 5

Joint Nonlinear Refraction and Reflection Traveltime Tomography

Abstract

We develop a rapid nonlinear traveltime tomography method that simultaneously inverts refraction and reflection traveltimes on a regular velocity grid. For traveltime and raypath calculation, we employ the new wavefront method that we introduced in Chapter 2. The first-arrival traveltimes are calculated on the basis of cell velocities, and the later refraction and reflection traveltimes are computed using both cell velocities and given interfaces. We solve a regularized nonlinear inverse problem. The model parameters (cell slownesses and reflector geometry) are regularized by a Laplacian operator in order to solve a valid inverse problem for a *continuum.* The traveltimes are also regularized such that we invert traveltime curves rather than uncorrelated traveltime points. A conjugate gradient method is applied to minimize the nonlinear objective function. After obtaining a solution, we perform nonlinear Monte Carlo inversions for uncertainty analysis and compute the posterior model covariance. In a numerical experiment, we demonstrate that combining the first-arrival refraction with the reflection can better constrain the slowness field. This is particularly important for inverting crustal structures where large velocity variations occur in the upper crust.

5.1 Introduction

Seismic tomography techniques have been rapidly developed since Aki's first demonstration in 1974 (Aki *et al.*, 1974). The concept of traveltime tomography was originally from medical science, however, seismologists have been dealing with very different problems in which the seismic traveltimes are nonlinear to the medium and the inversion solution is nonunique due to ill-posedness or insufficient medium information in data. Seismologists apply tomography to many experimental geometries and different type of data (*i.e.*, reflection, refraction, crosshole and earthquake data). Among those, tomography using refraction and reflection data is the one that can provide a much broad range of angular ray coverage of the subsurface and has become a popular technique for imaging crustal and upper mantle structure with controlled sources. The basic idea of refraction and reflection tomography is to use a large number of traveltimes for non-coincident sources and receivers located at the Earth's surface to determine velocity distribution and reflector locations. To solve a reflection traveltime tomography problem, Nercessian *et al.*(1984) assume reflector depth and shape *a priori* and perform a tomographic inversion for velocity alone. Lutter and Nowack (1990) use velocities from a previous inversion and then invert reflector shape alternatively. Bishop *et al.* (1985), Stork and Clayton (1986) and Farra and Madariaga (1988) simultaneously invert for reflectors and velocities with an arbitrary weighting parameter. Recently, Bube *et al.*(1995) found that the depths of the reflectors are determined in theory except for edge effects, but the slowness field has some undetermined features.

Because the undetermined features of the slownesses inherently exist in the reflection traveltime problem, one cannot solve this problem with any advanced numerical techniques unless additional physical information is provided. Performing a joint tomographic inversion of refraction and reflection data can better constrain the slowness field. Refraction implicitly relies on the heterogeneity of the medium to turn seismic energy back up to receivers, which provides independent velocity information. Methods of joint inversions of refraction and reflection data to obtain interfaces and velocity parameters are given by Chiu *et al.* (1986), Huang *et al.* (1986), Lutter and Nowack (1990), Zelt and Smith (1992), and Wang and Braile (1996). However, all these methods oversimplify the forward traveltime calculation and the inverse problem by parameterizing interfaces and velocities using some functionals with few parameters. On the other hand, nonlinear traveltime tomography methods that iteratively reconstruct raypaths and update a model on a regular velocity grid have been developed, but only applied to the first-arrival refraction traveltimes (Zhu and McMechan, 1989; Hole, 1992; Cai and Qin, 1994; Stefani, 1995; Zhang and Toksöz, 1996) or reflection traveltimes (Pullammanappallil and Louie, 1993) separately.

Existing traveltime methods are also limited in several other ways. The use of the two-point raytracing algorithms is valid for smooth velocity structure only (Červený *et al.*, 1977; Julian and Gubbins, 1977; Um and Thurber, 1987). The finite-difference method by Vidale (1988, 1990) violates causality for moderate to large velocity contrasts (Qin *et al.*, 1992). Its accuracy is reasonably good for transmission and reflection calculation, but extremely poor for refractions when large velocity contrasts exist (see Appendix A for details). Other finite-difference methods either also suffer from the same problem though some improvements are made (e.g., Hole and Zelt, 1995), or require a large amount of CPU time (Podvin and Lecomte, 1991; Qin *et al.*, 1992). For inversion, current refraction and reflection methods solve ill-posed inverse problems, and obtain a numerical solution dependent to the model parameterization. Although the refraction and reflection traveltime problem is nonlinear, linearized uncertainty analyses (e.g., sensitivity and raypath analyses) are often used to estimate variance and resolution of the tomography solution. Therefore, they cannot measure nonlinear uncertainty beyond what is implied in the raypaths of the solution.

Recent developments in accurate and efficient raytracing techniques (Saito, 1989; Moser, 1991; Fischer and Lees, 1993; Klimes and Kvasnicka, 1993; Weber, 1995; Zhang and Toksöz, 1996) and understanding of the regularized tomographic inversions (Rodi, 1989; Delprat-Jannaud and Lailly, 1993; Matarese, 1993; Zhang *et al.*, 1996) should yield improved tomographic techniques. In this chapter, we report a new method of joint refraction and reflection tomography that can accurately and efficiently reconstruct velocities and reflector geometry in a model with a large number of grids. Our approach includes several new developments:

1) We develop a new version of the minimum-traveltime raytracing method based on Saito (1989, 1990) and Moser (1989, 1991), which can rapidly expand a wavefront in the entire velocity network from its source and calculate refraction and reflection traveltimes. This method can correctly handle diffraction, headwaves, and paths to shadow zones.

2) We solve a regularized nonlinear inverse problem that is valid for a *continuum* problem, *i.e.*, the solution is independent to the model parameterization (Delprat-Jannaud and Lailly, 1993; Zhang *et al.*, 1996). This is achieved by applying Tikhonov method (Tikhonov and Arsenin, 1977) to perform a global inversion in the sense of reconstructing the whole model.

3) We also regularize traveltime data and invert traveltime *curves* rather than uncorrelated *points*. Jointly inverting *average-slowness* data (traveltimes divided by the ray lengths) and *apparent-slowness* data (traveltime derivatives with respect to distance), we convert the refraction and reflection traveltimes to be in the same order of magnitude for better numerical performance, and meanwhile preserve all the structure information in the data.

4) Not only obtaining a meaningful solution, we also measure the variance and resolution of the solution. By applying a nonlinear Monte Carlo approach, we calcu-

late the posterior covariance matrix and quantitatively demonstrate the uncertainty of the nonlinear solution.

5.2 Regularized Nonlinear Inversion Method

We solve a regularized nonlinear inverse problem and reconstruct velocities associated with both refractions and reflections as well as interfaces associated with reflections. Because later refractions are not available in the real data that we shall study in this thesis work, we address interface problem associated with reflections only. Therefore, we invert two types of traveltime data and reconstruct two types of model parameters simultaneously. In addition to the rapid traveltime calculation, successfully performing such a joint tomography also requires properly regularizing traveltimes as well as model parameters. In the early inversion studies, fitting data seems to be the major concern (Marquardt, 1963; Jackson, 1973; Kirkpatrick *et al.*, 1983; Rothman, 1985). A "global" minimum is defined when the data misfit is sufficiently small. However, recent tomography studies show that conducting nonlinear inversions one can fit data to any small misfit magnitude depending on the constraints applied to the model parameters (Matarese, 1993; Thompson, 1993), but the solutions may or may not be physically meaningful. Fitting data primarily trades off with model features. One important question is how to obtain one stable and unique solution that does not have unnecessary structures for the given data. On the other hand, there are many numerical criteria for defining a data misfit. Nature does not have to obey the least-squares criterion (Guillemin, 1954; Lines and Treitel, 1984). In the following, we shall first address the issues of data regularization. We regularize traveltimes such that they can be easily inverted in terms of numerical computation and the complete physical information in the traveltimes can be accounted for. These subjects will be studied in the following.

5.2.1 Regularizing traveltimes

We perform joint refraction and reflection traveltime tomography, which usually involves traveltimes over two orders of magnitude due to long rays and short rays. Numerically, it is difficult to deal with this large data range, because inversions tend to construct structures associated with long rays, and the convergence may be slow. On the other hand, fitting traveltimes with a least-squares criterion does not account for the whole physical meaning of a traveltime curve. For instance, it does not quantitatively account for the *continuum* of traveltimes, though a *continuum* physically occurs when the seismic wave propagates across receivers on the surface. With these considerations, we propose to convert traveltimes into *average slownesses* (traveltimes divided by the ray lengths) and *apparent slownesses* (traveltime derivatives with respect to distance), and jointly invert these two types of data. This approach allows to invert data in the same order and also account for the shapes of the traveltime curves. It avoids weighting reflection and refraction traveltimes with an arbitrary factor. Specifically, we minimize the following nonlinear objective function,

$$\Phi(m) = (1-\omega)\|\bar{d} - \bar{G}(m)\|^2 + \omega\|\hat{d} - \hat{G}(m))\|^2 + \tau\|Rm\|^2 \tag{5.1}$$

where $\bar{d}$ is a regularized refraction and reflection data vector or *average-slowness* vector, $\bar{G}(m)$ is a vector of the calculated *average slownesses*, $\hat{d}$ is a vector of the traveltime derivatives with respect to distance or *apparent-slowness* data, and $\hat{G}(m)$ is a vector of the calculated *apparent slownesses*, ω is a weighting parameter between the misfit of *average slownesses* and the misfit of *apparent slownesses*, R is a Laplacian operator for regularizing model parameters (model slownesses and reflector geometry), and τ is a smoothness trade-off parameter. The factor ω, weights between the misfit of *average-slowness* data and the misfit of *apparent-slowness* data. The criterion for selecting ω is that it must allow the rms misfits of *average slownesses* and *apparent slownesses* to converge to the same order of magnitude, representing one consistent resolving capability. From our numerical experiments, we found that taking ω to be

0.4 to 0.5 seems working well in general.

The first term in the objective function measures the misfit of an average slowness. The inclusion of the second term in the objective function is particularly meaningful for refraction and wide-angle reflection traveltime problem. It gives an l_2 norm of the apparent slowness misfit, which is independent to the information from traveltime itself. In fact, a sophisticated approach for picking reliable traveltimes from seismic records must consider the systematic moveout of a seismic wave across all the traces. As a result, the information of the traveltime gradients is implicitly extracted and included in the picked traveltimes. Although minimizing the traveltime misfit with an l_2 norm tends to minimize the misfit of traveltime gradients as well, it does not quantify the misfit or minimize the misfit to a required tolerance. Therefore, one must explicitly invert the traveltime gradients. A detailed comparison of minimizing traveltime misfit in several ways for refraction tomography was demonstrated in Chapter 3.

5.2.2 Regularizing model parameters

When the number of unknowns is more than the number of data points, no matter how sophisticated the optimization approach is, there can be no definitive "solution" solely on the basis of fitting the data. It is necessary to introduce additional constraints. The approach that we take is to employ a smoothness constraint to find a simplest or minimum-structure solution that fits the data to a given tolerance (Constable *et al.*, 1987; Smith and Booker, 1988; Rodi, 1989). We accomplish this using the method of Tikhonov regularization (Tikhonov and Arsenin, 1977), which is defined as the third term in equation (1). However, as we demonstrated earlier, not all the smoothing criteria in the class of Tikhonov regularization can work well for a geophysical inverse problem. A Laplacian operator is often selected in various inverse problems (Scales *et al.*, 1990; Delprat-Jannaud and Lailly, 1993; Martarese, 1993; Thompson, 1993; Zhang *et al.*, 1996).

In fact, applying a derivative operator to model parameters plays a role more than just smoothing structure or stabilizing inversion. In a reflection traveltime problem, Delprat-Jannaud and Lailly (1993) view a useful regularization as a means to make an inverse problem valid for *continuum* problem, *i.e.*, a well-regularized solution should be independent of model discretization. Zhang *et al.*(1996) demonstrate that 3-D electrical tomography regularized by the second- or the third-order model derivatives can almost produce the same solution for two different model discretizations. From a different philosophical view, Matarese (1993) applies Tikhonov regularization method for performing a global inversion in the sense of reconstructing the whole model. In all these applications, it is important to apply the derivative operators explicitly on the model parameters rather than on the model changes. Smoothing model changes may stabilize inversion in certain stage, but ultimately it cannot avoid solving an ill-posed inverse problem, because it minimizes an objective function requiring to fit data only (Rodi, 1989; Zhang *et al.*, 1996). Appendix B presents a detailed discussion.

Based on these studies, we chose R in equation (1) to be a Laplacian operator for the joint refraction and reflection traveltime tomography. Numerically, this implies that a nonlinear interpolation and extrapolation method is applied in the model space while inverting the data. Considering the fact that the model vector m includes slownesses and reflector geometry, we actually regularize two different types of model parameters with the same derivative operator. The selection of the smoothness trade-off parameter τ is not difficult, but one must conduct the inversions a few times to find an optimal one. This is because an optimal τ is inherently dependent to the physical relationship between the data misfit residuals and the model roughness. Given a parameter τ, the data misfit residuals and the model roughness converge to certain values. With τ increasing, the model roughness increases and the misfit residual decreases. One can follow these rules of thumb to determine an optimal τ.

5.2.3 Nonlinear inversion algorithm

Another major difficulty for solving a joint refraction and reflection traveltime problem is the numerical computational burden. The forward traveltime calculation for refraction and reflection is numerically intensive on a large number of velocity grids. Therefore, the inversion approach must be sufficiently efficient so that the entire nonlinear tomography method is practical. In this study, we apply nonlinear Conjugate Gradient (CG) method to minimize the objective function (1) directly. The advantages of the method include fast convergence rate and efficient vector calculations without any requirement to store matrices in the entire computation. Specifically, the CG algorithm is described in the following:

$$\begin{aligned}
\textit{updated model}: \quad & m_{k+1} = m_k + \alpha_k h_k && (5.2)\\
\textit{search direction}: \quad & h_0 = C_0 g_0 && (5.3)\\
& h_k = C_k g_k + \beta_k h_{k-1} \quad (k > 0) && (5.4)\\
& \beta_k = \frac{g_k^T C_k (g_k - g_{k-1})}{g_{k-1}^T C_k g_{k-1}} && (5.5)\\
\textit{gradient of } \Phi: \quad & g_k = -A_k^T(\bar{d} - \bar{G}(m_k)) - B_k^T(\hat{d} - \hat{G}(m_k)) + \tau R^T R(m_k) && (5.6)\\
\textit{preconditioner}: \quad & C_k = (A_k^T A_k + B_k^T B_k + \tau R^T R)^{-1} && (5.7)
\end{aligned}$$

where the step length α_k is computed so that $\Phi(m_k + \alpha_k h_k)$ is minimized, A_k is the average-slowness sensitivity matrix, each non-zero term in A_k contains the length of a local ray across a model cell divided by the entire ray length, B_k is the apparent-slowness sensitivity matrix, each non-zero term in B_k is the difference of the two ray lengths in a cell divided by the receiver spacing when data from two adjacent receivers are used to calculate derivatives. In these calculations, it is not necessary to explicitly set up matrices of A_k, B_k or C_k. The algorithm only requires the results of these matrices multiplying vectors, therefore, one does not need to compute or store any matrix (Scales, 1987; Mackie and Madden, 1993; Zhang *et al.*, 1995). In fact, the sensitivity information (raypath) is stored in compact vectors during the raytracing calculation. Therefore, this algorithm is efficient for dealing with a large inverse problem.

5.3 Nonlinear Uncertainty Analysis

Several linear (or linearized) uncertainty analysis methods are often applied in the seismic traveltime problems. These include the examination of a resolution matrix (Aki and Richards, 1980), display of the integrated sensitivity of all the traveltimes to each node (*e.g.*, Hole, 1992; Parsons *et al.*, 1996), and calculation of the posterior model covariance matrix using a linearized Monte Carlo method (*e.g.*, Matarese, 1993). All these methods fix the raypaths of the final solution, and attempt to estimate uncertainty along the raypaths by one way or another. Physically, they all assume that good ray coverage corresponds to good resolution. However, as we have shown in the refraction traveltime tomography in Chapter 3, for a nonlinear traveltime problem an area with coarse ray coverage may not necessarily appear to be poorly resolved, it may be essential for fitting the data. An accurate measurement of resolution for a nonlinear problem must account for the raypath uncertainty. Therefore, for the nonlinear refraction and reflection traveltime tomography, we also apply nonlinear Monte Carlo inversions to measure the solution uncertainty as the same way for the nonlinear refraction traveltime problem.

Apparently, performing nonlinear uncertainty analysis for joint refraction and reflection traveltime problem may require intensive computation. Repeating the forward calculations for numerous times is a computational challenge. Nevertheless, we found that the nonlinear inversions in each realization starting from a randomly perturbed model solution can quickly converge to the tolerance given for the tomography solution after about 4 to 5 iterations. The posterior model covariance can be well approximated after about 100 to 200 realizations. On a modern workstation such as DEC 3000, this usually takes 5 to 6 hours for a large inverse problem (300 by 200 slowness cells, 6 sources and 100 receivers).

5.4 Numerical Experiment

We demonstrate a numerical example of nonlinear traveltime tomography inversions using noise-free synthetic data for a model of the axial magma chamber in the crust (see Figure 5-1(a)). A true velocity structure similar to this model has been found across the East Pacific Rise (Vera *et al.*, 1990; Wilcock *et al.*, 1993). Although we are not going to model real data from magma-chamber structure, our interest is to understand the performance of a nonlinear traveltime tomography in solving such a complicated problem. An OBS experiment is simulated with six OBSs on the seafloor (1.5 km below sea level) along a 30 km survey line. A 2-D profile of 30 km by 10 km is sampled by 300 $\times$ 100 grids. The model consists of a low velocity zone in the central area (3.5 km/sec). The upper oceanic crust consists of a high velocity gradient zone, and the velocities in the lower crust vary vertically and laterally. The Moho depth varies across the profile with an average value of about 8.4 km. Using a finite-difference method to study full seismic waveforms, Wilcock *et al.* (1993) found that P_g (refraction from upper crust) and PmP (reflection from the Moho) are the two major phases for a similar model. In Figure 5-1(b), we show the raypaths of these two phases for our experimental model. As described above, we take the average traveltimes (average slownesses) and the traveltime gradients (apparent slownesses) of P_g and PmP as the input data for inversion. As one can see, the central area of the model is not well covered by either reflection or refraction raypaths due to a large low-velocity anomaly. In fact, this insufficient coverage situation may often occur in real surveys due to the physical structure no matter how dense the receivers or sources are. It is our interest to see how well the nonlinear traveltime tomography performs in this situation. Therefore, we conduct three tomography problems separately, *i.e.*, a refraction traveltime tomography, a reflection traveltime tomography, and a joint refraction and reflection traveltime tomography. A 1-D initial model m_1 is constructed for all these inversions, and a flat Moho at a depth of 7.0 km is assumed.

For inverting velocity distribution from OBS data, we would like to incorporate *a priori* information of bathymetry and sediment into the tomography if they are available. One can take two different approaches to constrain velocities in these areas with *a priori* information: enforcing model sensitivities to be zero or constraining model curvatures. We take the latter, because its numerical implementation is more flexible for solving a general problem. Specifically, we slightly modify the objective function (1),

$$\Phi(m) = (1-\omega)\|\bar{d} - \bar{G}(m)\|^2 + \omega\|\hat{d} - \hat{G}(m)\|^2 + \tau\|L(m_0 - m)\|^2, \qquad (5.8)$$

where m_0 is a model containing *a priori* information. However, m_0 may differ from the starting model (m_1) that we use for the first inversion iteration. The purpose of using m_0 is to take its curvature information to constrain inversion, because L is a Laplacian operator and $L(m_0)$ returns the curvature of m_0. For this numerical experiment, we put a water velocity (1.5 km/s) above the seafloor and a homogeneous velocity (2.5 km/s) below the seafloor into m_0. This assumes that we only have *a priori* bathymetry information. Otherwise, we assume a velocity "jump" at the seafloor. For this numerical experiment, taking m_1 as shown in Figure 5-1(c) to be m_0 in the objective function (8) will bias the inversion due to very incorrect curvatures assumed in the initial guess. However, if any reliable curvature information about the subsurface is available, it should be placed in m_0.

Figure 5-2 shows inversion results of the refraction traveltime tomography. Using P_g traveltimes, nonlinear refraction traveltime tomography can reasonably well reconstruct the velocity structure in the upper crust although the initial model in this area is very different from the true model. It can also map the gradient interface between the upper crust and the lower crust and indicate the lateral velocity variations including the low-velocity zone. However, it does not constrain the deep structure due to shallow raypaths. Therefore, the deep structure that is assumed in the initial model remains unchanged. It does not constrain the shape of the magma chamber well because of the lateral velocity ambiguity inherent in the refraction problem.

Reflection traveltime tomography can constrain the lateral velocity changes and delineate the lateral boundaries of the magma chamber reasonably well, but it suffers from a velocity-depth ambiguity (see Figure 5-3). As one can see, the model is fairly well covered by the reflection raypaths, and the raypaths of the wide-angle PmP are actually similar to those of the deep refractions. However, because the large velocity variations occur in the shallow structure, the absence of shallow lateral velocity constraints leads to the structural ambiguity. When the refraction and reflection traveltimes are simultaneously inverted, the entire image can be significantly improved (see Figure 5-4). A large number of near-horizontal raypaths in the shallow structure greatly help to map traveltime residuals due to the deep velocity anomaly.

After solving these three tomography problems, we apply a nonlinear Monte Carlo method to compute the posterior covariance and measure the solution uncertainty. In Figures 5-2, 5-3 and 5-4, it demonstrates the posterior correlation with respect to one selected point beneath the low-velocity zone (magma chamber). If the correlation is close to +1, the uncertainties are highly correlated, indicating that the parameters have not been independently resolved by the data set, and the result represents only some linear combination of the parameters. If the correlation is close to -1, the uncertainties are highly anti-correlated. In the case of refraction traveltime inversion, we see the effect of the solution ambiguity along the deep raypaths for the selected point. For reflection traveltime inversion that incorporates both pre-critical and post-critical reflections, the resolution of the point is greatly enhanced. It also shows that the point is slightly anti-correlated with the shallow structure due to the velocity-depth ambiguity. As in the case of joint inversion, the resolution of the point is the highest due to sufficient vertical and lateral ray constraints.

The above example is performed on a DEC 3000 workstation. Because the forward traveltime approach that we used in this study minimizes computation time for each model by accounting for complexity in the model, the iteration CPU time varies when the inversion proceeds. Figure 5-6 shows this situation, especially for refraction traveltime tomography and joint refraction and reflection traveltime tomography. For reflection calculation, the area in the model that is covered by the raypaths does not vary much, therefore, the computation time is relatively constant when inversion starts from an inhomogeneous initial model. When refraction calculation is included, the computation time of each iteration may increase in the early inversion stage because of structure changes in the model. In the average sense, one iteration of the refraction tomographic inversion takes about 1 min 30 sec; one iteration of the reflection tomographic inversion takes 2 min; and one iteration of the joint tomography needs 3 min 10 sec. Most of the computation time for solving these tomography inversions is owing to the forward traveltime calculation.

For the three inversions starting from the same initial model, Figure 5-5 shows the convergence of the rms traveltime misfits versus iteration. In any of these inversions, we minimize the misfit of traveltime curves and model roughness. However, we output the rms traveltime misfit during the inversions and observe its changes with iteration. Apparently, for the same starting model, the initial rms traveltime misfit for the refraction problem is the smallest, and it quickly reduces to 5 ms after 8 iterations. For the same misfit, reflection traveltime tomography needs about 15 iterations, while joint reflection and refraction tomography needs about 20 iterations.

5.5 Conclusions

In this chapter we demonstrate a nonlinear traveltime tomographic technique that simultaneously inverts both refraction and reflection data on a regular velocity grid. This approach is an integration of recent development of the raytracing algorithms (Zhang and Toksöz, 1996) and the understanding of the performance of the regularized tomographic inversion (Delprat-Jannaud and Lailly, 1993; Zhang *et al.*, 1996). The method is extended from the nonlinear refraction traveltime tomography. Modeling synthetic and real data demonstrates that this approach is practical for imaging large 2-D crustal structures. To understand quantitatively the resolution of our regularized solution, we conduct uncertainty analysis using a Monte Carlo approach. One of the important issues that we must address is the nonuniqueness of the inverse problem, *i.e.*, fitting seismic data does not necessarily suggest that the "true earth structure" can be uniquely imaged. We deal with this problem from a view of data correlation and model correlation. Instead of taking traveltimes as uncorrelated points to invert, we fit "traveltime curves", including both traveltime and traveltime derivative information. Therefore, the tomographic inversion maintains a wave resolution as implied in the traveltime curves. Numerically, this is accomplished by simultaneously inverting *average-slowness* data and *apparent-slowness* data as the same way that we implement the refraction traveltime tomography. This conversion is more beneficial to the joint refraction and reflection traveltime problem, because refractions and reflections are input with their physical meaning rather than an arbitrary weight. On the other hand, we apply Tikhonov regularization to correlate model parameters with the second-order derivatives. The idea is to obtain one stable solution with minimum curvatures and with the only necessary features for the given data. We show a comparison of the performance of the refraction traveltime tomography, the reflection traveltime tomography, and the joint refraction and reflection traveltime tomography for a numerical model. It demonstrates that combining the first-arrival refraction and reflection traveltimes can better constrain the slownesses.

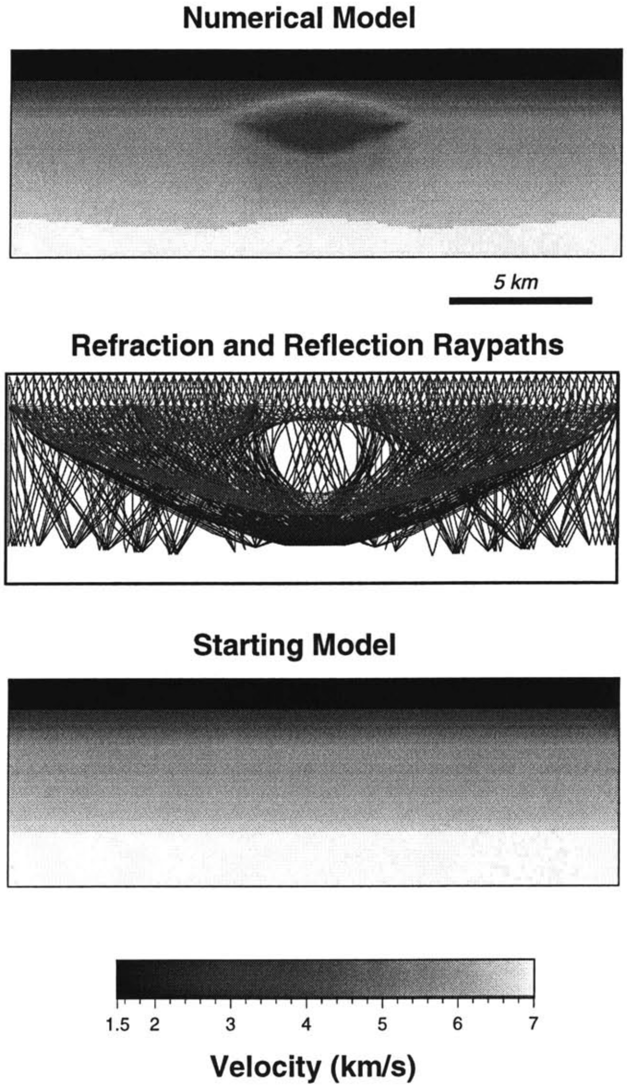

Figure 5-1: An oceanic crust model consisting of sea water, a magma chamber, and variable Moho topography for numerical experiments. It shows velocity up to 7.0 km/s, the actual velocity beneath the Moho is 8.0 km/s. Simulating an OBS experiment, six OBSs are placed on the seafloor, and marine shooting at the sea surface. The raypaths of the first-arrival refractions (P_g) and reflections from the Moho (PmP) are displayed. A 1-D gradient starting model is constructed for tomography inversions with a flat Moho. No vertical exaggeration is applied.

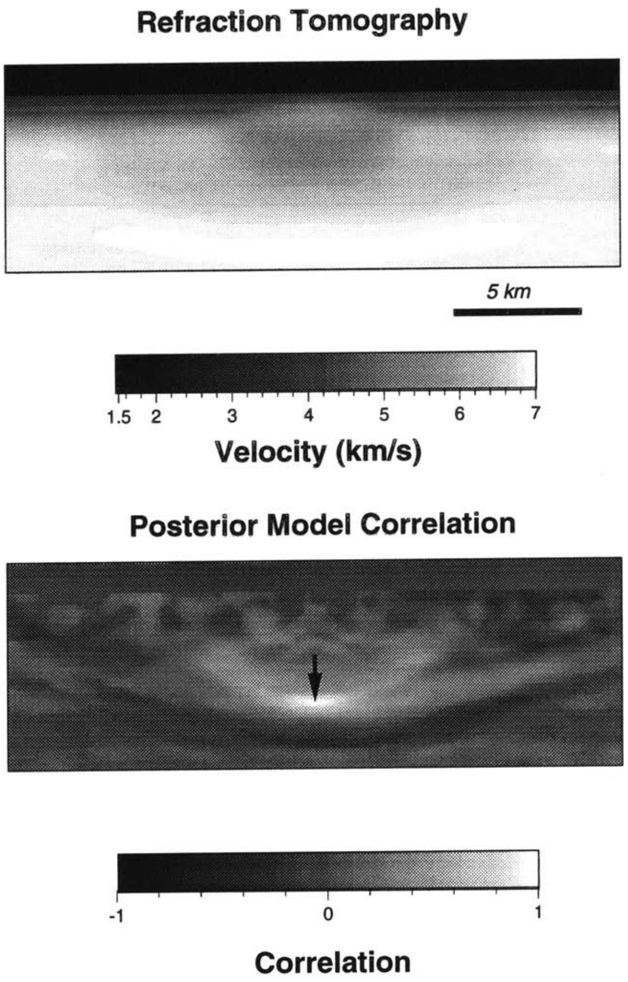

Figure 5-2: Nonlinear refraction traveltime tomography using synthetic refraction data for the above model. The solution indicates a low-velocity zone in the central area, but the detail is not resolvable. Uncertainty analysis using nonlinear Monte Carlo method is conducted. For a point selected in the model (arrow point), it shows large lateral correlation, indicating a trade-off pattern for that particular point in the solution.

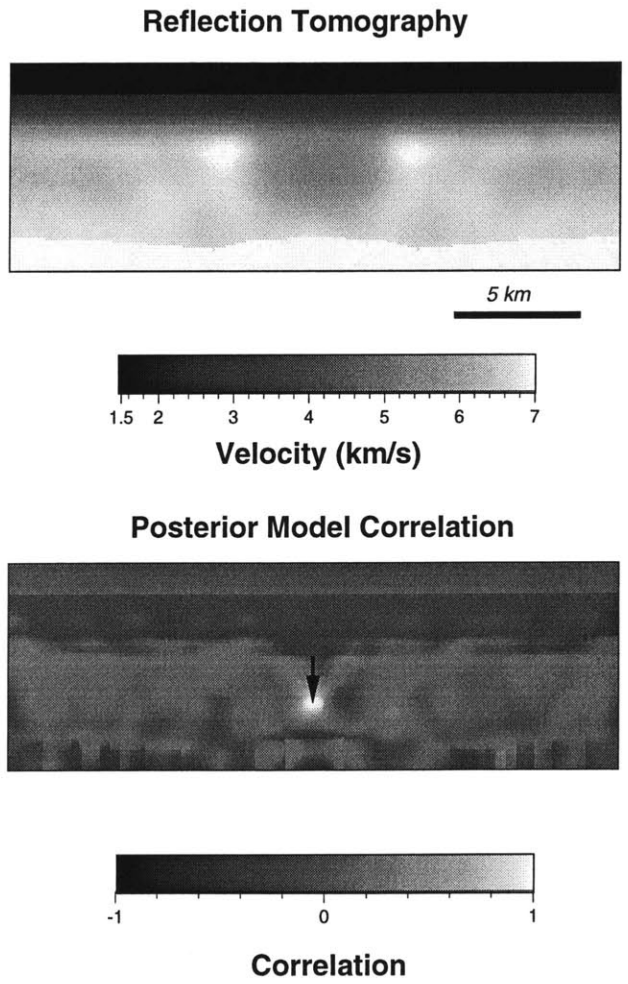
Reflection Tomography

Posterior Model Correlation

Figure 5-3: Nonlinear reflection traveltime tomography using synthetic reflection data for the numerical model. The solution shows some deep lateral velocity changes near the magma chamber, and the Moho topography can be reconstructed reasonably well. But the overall image is poor due to lack of shallow lateral constraints. Uncertainty analysis, however, suggests that the point selected is well resolved due to the use of pre-critical and post-critical reflections. But it also shows certain anti-correlation with the velocities within the sedimentary area.

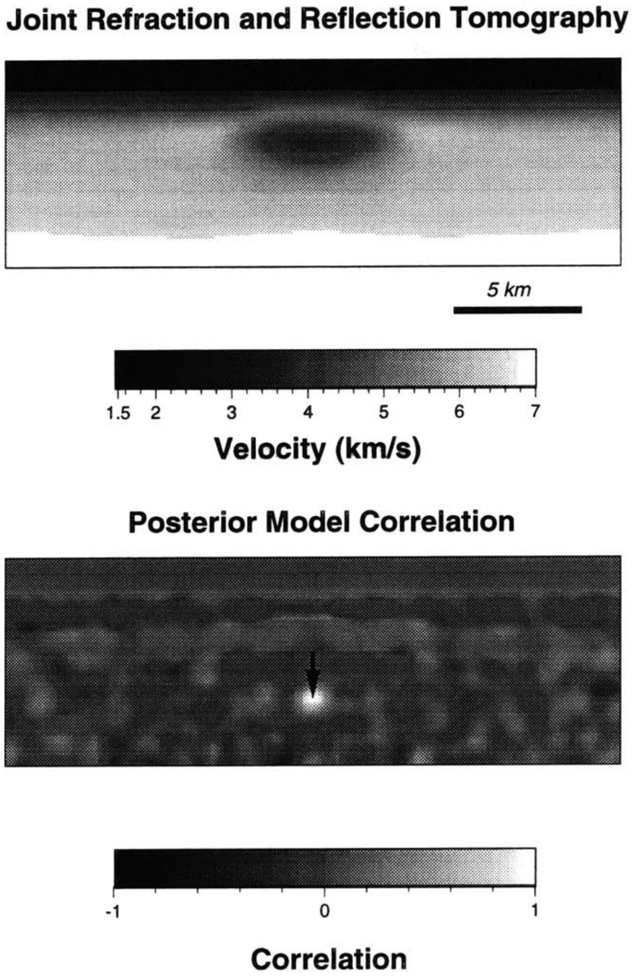

Figure 5-4: Joint refraction and reflection traveltime tomography using both synthetic refraction and reflection data for the same numerical model. It shows that it can reconstruct an optimal solution when both the shallow and deep structures are constrained. Uncertainty analysis shows that the point selected is well resolved.

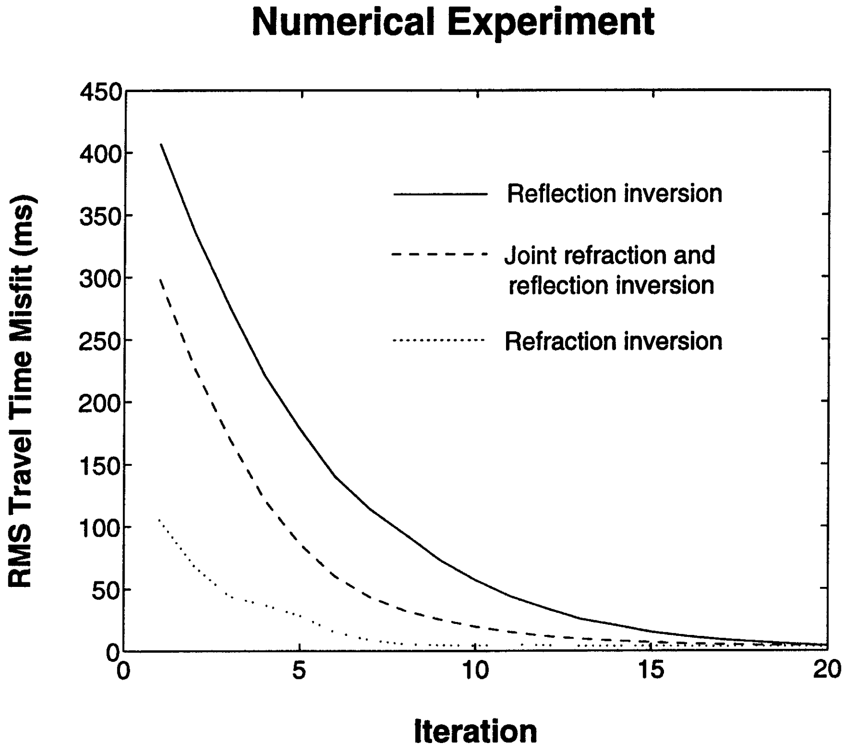

Figure 5-5: The rms misfits of traveltimes versus iterations for three traveltime tomography inversions.

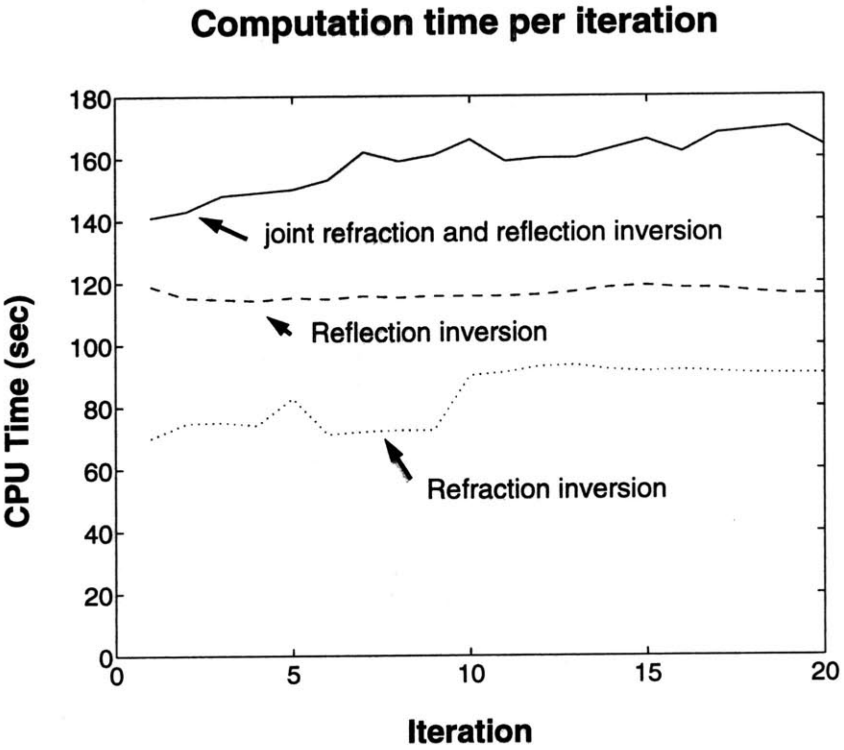

Figure 5-6: Iteration CPU time of three different tomography inversions. Because the traveltime computation speed depends on the model complexity, the CPU time for each inversion iteration varies.

Chapter 6

Imaging the Shallow Earth Structures

Abstract

We apply a nonlinear refraction traveltime tomography method and a joint refraction traveltime migration and tomography technique to two seismic surveys: determining bedrock depth at a coastal site in eastern Massachusetts, and imaging the Bala Kimberlite in northeastern Kansas. The goal of the first survey was to locate areas where the overburden soil thickness above the bedrock is sufficient for the construction of a replacement storm-drainage system. In the second experiment, the goal was to image the Bala Kimberlite in the subsurface and its surrounding structure so that we can better understand its emplacement in the shallow Earth.

For the first survey, we show that nonlinear refraction traveltime tomography can deal with the near-surface variability and accurately reconstruct the bedrock topography. Nonlinear uncertainty analysis for the solutions quantitatively demonstrates its high reliability, which has been verified by drilling. Subsequently, applying a joint migration and tomography technique to the same data set results in a more realistic estimate of the bedrock interface and ultimately more accurate velocity structure. In modeling data from the second experiment in Riley County, Kansas, our nonlinear tomography results delineate a structure of soil, bedrock block, and the sharp discontinuity of the bedrock near the Bala Kimberlite. The fact that the refraction

traveltime migration image consistently corresponds to the structure in the tomography solution implies high reliability of the result. The imaging results suggest that the Bala Kimberlite might be emplaced into a shear fracture zone from the upper mantle during a major tectonic event.

6.1 Imaging Bedrock Topography at Eastern Massachusetts

6.1.1 Introduction

As part of an engineering project in the Boston area, a new storm-drainage system is being constructed to serve several communities in eastern Massachusetts. To reduce project cost, the new service will need to be constructed in tidal areas where bedrock is relatively deep, so that costly blasting can be avoided. A seismic refraction survey was conducted to determine bedrock topography and locate those areas where the overburden is the thickest. Because of complex geological conditions due to glaciation and tectonic activity along the Boston Basin, bedrock topography may have large variability.

Hager GeoScience, Inc. collected approximately 1,300 feet of seismic refraction data along four traverses parallel to, and three traverses perpendicular to, the west shore of the Fore River in Braintree, Massachusetts (Kutrubes *et al.*, 1996). We will show imaging results of the two parallel lines close to the river. Data were collected using an OYO DAS-1 seismograph with 24-channel geophone array. A sampling rate of 0.25 ms was chosen. Geophone spacing of 10 feet was used for the two lines that we study in this thesis. The environment at the working site was quite unusual because the survey area was covered by sea water during the high-tide period, and exposed for only 1 to 2 hours during the low tide each day. Therefore, we used a hammer source in most cases and a Betsgun source if the recordings were too weak in other cases. Surveys along two adjacent short lines (each 230 ft or 70.1 m) were conducted with 12 shots for each line. The field configuration is shown in Figure 6-1.

Figure 6-2 shows the seismic waveforms recorded from a forward shot and a reverse shot on line 1. Data from both shots show delayed first arrivals between receivers 7 and 14, although the topography along line 1 is flat. Moreover, the amplitudes of these delayed first arrivals are relatively small. The evidence suggests that a low-velocity zone with strong seismic attenuation exists beneath receiver 7 to 14. It became obvious when we placed sources (hammer and Betsygun) right at locations between receivers 7 and 14, the seismic energy was observed to be significantly attenuated across all of the receivers. Subsequent drilling revealed organics deposit in this area. Although survey line 2 is adjacent to line 1, a different structural influence was found. Figure 6-3 displays the forward- and reverse-shot records on line 2. They suggest a relatively high-velocity anomaly in the shallow structure. At the surface, we found that weathered sandstone outcrops in the central area on line 2.

6.1.2 Nonlinear refraction tomographic imaging

To precisely map bedrock topography, we conducted nonlinear tomography studies with a model consisting of 250 × 100 square cells for each survey area (71.0 m by 30.5 m). The surface topography is flat, with variations less than 0.3 meter. For each line with 24 receivers, 288 traveltime picks were taken from the recordings. Corrections accounting for reciprocity were made before they were used for modeling. One of the major problems in the data is the inconsistent shot delay due to the near-surface variability. A trigger threshold of 100 mV was set in the recording system, however, different shot locations along survey lines had different responses to it. In fact, similar situation was also found in many other small-scale surveys, i.e., it is difficult to define one accurate shot time for the entire data set. The influence of the shot time perturbation was demonstrated in Chapter 3, mainly affecting the near-shot structure reconstruction.

We design an imaging process with two stages. At the early tomography inversion stage (first 5 iterations), we invert the average-slowness data only. This will give a large weight to the near-shot traveltime misfit, therefore, inversion tends to construct the near-surface structure in this stage. When the near-surface structure is reasonably approximated, we start the second inversion stage that jointly minimizes the misfits of average slownesses and apparent slownesses. As we addressed earlier, this approach is rather conservative, but it is important and essential for solving a refraction traveltime problem because the near-surface variability may introduce many nonunique and nonphysical solutions.

Figure 6-4 presents a tomography solution of line 1 and the corresponding raypaths. It shows a shallow low velocity anomaly which explains the consistent traveltime delays for receivers above it and the strong attenuation effects shown in Figure 6-2. Correctly reconstructing the shallow overburden velocities is critical for accurately mapping bedrock topography. This example at this point demonstrates the importance of the application of nonlinear tomography method for imaging heterogeneity in solving real problems. The interface between the bedrock and overburden layer is deeper under receivers 12 to 19, reaching the depth of about 15 meters. In Figure 6-5, Line-2 tomogram presents a different shallow structure in which a layer with an intermedium velocity (3000.0 m/s) appears above the bedrock and outcrops surface in the central area. Because the velocity in this layer is higher than the soil, and the saturated sand and gravel, it causes relatively early arrivals between receivers 12 and 19. From the field observation, we identified that this outcroped layer is weathered sandstone which is seated on the sedimentary rock in this area.

The process of inversion versus iteration is displayed in Figure 6-6. It shows a transition from preferably reconstructing the shallow media to the deep structure when the apparent-slowness data are subsequently included in the inversion. Figure 6-7 and Figure 6-8 show the corresponding traveltime fits. It appears that poor traveltime fit corresponds to the low-velocity anomaly in line-1 profile. The fact that the waveforms are strongly attenuated in this area makes it difficult to determine accurate first-arrival traveltimes. Therefore, these traveltime picks are unreliable in comparison to those elsewhere.

To quantitatively measure the uncertainty of the solutions, we apply nonlinear Monte Carlo inversions to compute the posterior covariance matrix associated with the final solutions. Therefore, we perturb data and model with random errors, and then reconstruct solutions for each new data set and initial model. Our numerical study indicates that nonlinear uncertainty analysis is essential for refraction problem because insufficient ray coverage often occurs in the media. We select one point in each model solution and display their posterior model correlation in Figure 6-9. The uncertainty analyses certainly yield slowness variance and posterior correlation for cells in the entire model. Physically, we know that the image of the weathered sandstone outcroping the surface on line 2 is true. Therefore, we take a point in the weathered sandstone in line-2 profile for reference, and compare its correlation size with a point on the bedrock in line-1 profile. They all show similar correlation with the neighbors, therefore, the result suggests that the bedrock image in line-1 profile should be very reliable. Subsequent drilling in two locations near line-1 confirmed the estimate fairly accurate.

6.1.3 Joint migration and tomographic imaging

We further conduct joint migration and tomography using the same traveltime data. The motivation for developing this new technique is to reconstruct structure with sharp interface more accurately in a physically meaningful way. Imaging bedrock topography is apparently one of the ideal cases for the application of this new technique. When the joint approach is applied, tomography inversion reconstructs a velocity structure which is needed in the refraction migration, the migration image of the bedrock in turn assists the tomography to better resolve the velocities. Because we have already conducted nonlinear traveltime tomography and obtained some ideas about velocities in the subsurface, we would apply the model-interface method which places an *a priori* velocity change at the migration image.

In Figure 6-10, we show a progressive development of the joint imaging process for reconstruction of the line-1 profile. It displays both the migration image and reconstructed velocities, although the migration image is not applied to constrain tomography until iteration 8 when the velocity structure is accurate enough. However, one can observe the progressive convergence of the migration image and the large velocity variations to the same locations in the subsurface. Similarly, Figure 6-11 demonstrates an imaging process for the reconstruction of line-2 profile. Although these new images suggest very similar estimates of bedrock topography to those derived from tomography inversions alone in these two particular cases, we found that the joint method constructs very different raypaths as shown in Figure 6-12 in comparison to those in Figures 6-4 and 6-5. This is because regularized traveltime tomography on a regular grid always tends to construct turning rays due to the smoothness constraints applied. Only a joint imaging approach can take full advantage of regularization and maintain sharp features as well.

6.1.4 Conclusions

Nonlinear refraction traveltime tomography and joint refraction migration and tomography are two advanced imaging techniques that should be very useful to the shallow environmental investigations. Application of these two methods to the field data from a coastal site in eastern Massachussets demonstrates their resolving capabilities. In the shallow structure imaging problems, near-surface velocity variability often occurs and may introduce large uncertainty in the interpretation. Conventional methods have difficulties to deal with this problem, and they cannot quantitatively measure such uncertainty either. In fact, no matter what seismic techniques are applied and at what depth the object is interested in, one must have sufficient velocity information for making accurate interpretation. In some cases, resolving velocities itself is a purpose for investigating the shallow structure. Nonlinear refraction traveltime tomography is perhaps the most sophisticated approach for reconstructing velocity information. Along with a migration method, it can reconstruct both velocities and interfaces automatically.

6.2 Imaging Bala Kimberlite in Northeastern Kansas

6.2.1 Introduction

At least six kimberlites are found in northern Riley County, Kansas. Five of them, including Bala, Leonardville, Randolph No. 1, Randolph No. 2, and Stockdale crop out, and a sixth, Winkler, has been discovered by drilling. The exposed kimberlites are brecciated masses filled with fragments of country rock and appear as small elliptical outcrops averaging around 100 by 50 ft. More than 90 percent of the kimberlites consist of serpentine and calcite, but no two kimberlites are exactly alike in their mineralogy, bulk chemistry, or texture. Previous geological studies suggested that these six kimberlites might appear as plugs in the subsurface, associated with that segment of the Abilene anticline where the regional joint pattern shows a marked deflection in trend. It has been proposed that the kimberlites crystallized in the upper mantle in the late Precambrian at a minimum depth of 120 km and perhaps as deep as 300 km. The Riley County, Kansas, kimberlites are thought to have been emplaced under explosive conditions resulting from an abrupt tectonic activity about 120 m.y. ago (Brookins, 1970).

It is important to learn the detailed structure of the kimberlites in the subsurface, which should be helpful for the understanding of its geological history in this region. Unfortunately, previous geophysical investigations of the Riley County kimberlites were not very successful in providing detailed information. Surface magnetometer surveys proved unsuccessful as the magnetic anomalies associated with the kimberlites are restricted to an extremely small area, although Dreyer (1972) was able to interpret a general trend of the kimberlite from a magnetic survey. Gravimetric studies were also unsuccessful because the density of the pentinized, carbonated kimberlite is not appreciably different from the surrounding calcareous country rocks. Recently, the Department of Geology at University of Kansas have made great efforts to image the Bala Kimberlite using advanced seismic techniques (Steeples *et al.*, 1995). A seismic refraction/reflection survey was conducted along two perpendicular lines near and above the exposed Bala Kimberlite. In this study, we shall apply a nonlinear refraction traveltime tomography method by Zhang and Toksöz (1996) to reconstruct P-wave velocities in the subsurface and attempt to characterize the geological structures near the Bala Kimberlite.

A seismic refraction survey was conducted across the Bala Kimberlite in Riley County, Kansas. Two seismic lines perpendicular to each other were collected in the field as shown in Figure 6-13. At the interception of the two lines, the Bala Kimberlite is covered by a thin layer of soil at the surface. Topography variations in this area seem associated with the appearance of the Bala Kimberlite, but the details in the subsurface remain unknown.

Along each survey line, 96 geophones were evenly deployed on the surface with a receiver spacing of 4 feet. On line 1 (NW-SE), the first receiver is on the SE end. On line 2 (NE-SW), the first receiver is on the SW end. The NW end of the first line ties with the NE end of the second line. Shots with an 8-gauge shotgun source (Betsy Seisgun) were placed at every geophone location and at a few offset distances as well. We chose data from 19 shots along a survey line. This should be sufficient for the refraction traveltime modeling. The overall data quality is fairly good, clearly showing the significant structural influence in the subsurface. In this section, we show data and modeling results for line 2 only.

Figure 6-14 shows waveform recordings from a forward spread on line 2. One of the striking observations is the rapid traveltime decrease with distance at the end close to the kimberlite. Note that no velocity reduction is applied in the plot. This dramatic traveltime change is quite unusual, it cannot be explained by any simple layered structures. On the other hand, the amplitudes of the wavefield at the longer offsets strongly increase as opposed to the geometrical spreading effect, indicating strong wavepath focusing. Figure 6-15 shows the records of the reverse spread along the same line. Comparing with Figure 6-14, we found that the amplitude focusing effect seems reciprocal, suggesting a true structural influence rather than an instrumental problem. The first-arrival traveltimes from 19 shots are shown in Figure 6-16. It clearly indicates a low-velocity zone near the kimberlite. All these observations indicate a complicated velocity structure near the Bala Kimberlite, which cannot be interpreted with conventional techniques.

6.2.2 Nonlinear Traveltime Tomography and Joint Imaging

Parameterizing a grid model with 195 × 70 square cells and each cell length 2.0 feet, we conduct nonlinear refraction traveltime tomography using data from survey line 2. Topography variations along line 2 (NE-SW) are over 20 feet. The effects are accounted for in the tomographic imaging. Examining traveltimes from the survey line 2 as shown in Figure 6-16, we found a deep flat refractor with velocity about 2850 m/s in the areas away from the exposed kimberlite. It appears that significant structure complexity occurs right near the kimberlite. We first construct a homogeneous initial model with the velocity 2850 m/s for the tomography inversions. From numerical experiments, we found that using a homogeneous initial model for the nonlinear refraction tomography inversion can result in a reliable minimum-structure solution. The solution can help us to understand a major structure pattern due to data in the entire model.

Figure 6-17 presents tomographic images for line 2 (NE-SW) starting form a homogeneous initial model. This initial model gives an rms data misfit residual of about 26.5 ms. A flat bedrock discontinues near the kimberlite. Low-velocity soil fills in the area between the kimberlite and bedrock. The corresponding traveltime fit is shown in Figure 6-18. The solution primarily suggests three major areas with average velocities about 2850 m/s (bedrock), 2000 m/s (kimberlite) and 1300 m/s (near-surface materials), respectively. Therefore, we construct an initial model with these features, i.e., making three velocity blocks in the model as shown in Figure 6-19. This model allows the initial rms data misfit residual to be 11.2 ms. Inversion reconstructs a solution that shows the same structure as the previous one in the shallow areas where sufficient rays are available. In the deep structure, the high-velocity bedrock remains on one side of the model, indicating that the high-velocity structure near the kimberlite in the previous solution is not necessary. The traveltime fit is shown in Figure 6-20. The convergence of the rms data residual is illustrated in Figure 6-21. In Figure 6-22, we show the reconstructed raypaths corresponding to the two tomographic solutions.

The joint refraction traveltime migration and tomography technique that we described in Chapter 4 was applied to the line-2 data (see Figure 6-23) with a homogeneous starting model. During the first 7 iterations, we conduct nonlinear traveltime tomographic inversion. Starting from the 8th iteration, we apply the joint imaging method. One can see that the migration image shows a sharp lateral discontinuity which verifies what has been resolved from the tomographic inversion. After migration joins the imaging process, the smooth velocity transition above the flat bedrock shown in the tomography solution vanishes. Figure 6-24 shows downward continuation of the forward and reverse traveltimes using the velocity solution from the second inversion. The results demonstrate large certainty of the solution, because the migration image corresponds to the velocity features well.

6.2.3 Conclusions

Many researchers studied geology in Riley County, Kansas, and attempted to understand six kinds of kimberlite plugs found in the area (for review, see Brookins, 1970). There may be more kimberlites in the area that are unrecognized or that do not crop out, since kimberlites commonly occur in swarms. For the six kinds of kimberlites that were already found, it is not clear how and why they were emplaced here. Many other questions also remain unanswered. Seismic techniques can well serve the purpose of the investigation. Our seismic tomographic images present a first look of the subsurface structure near the Bala Kimberlite.

Our results show dramatic changes of the bedrock (limestone) topography right near the Bala Kimberlite. Such strong structural variations do not seem associated with a slow surface movement. Rather, they indicate a rapid tectonic activity. The image of the Bala Kimberlite also indicates that it is elongate along line 2 which is transverse to the trend of the Abilene anticline. Fractures transverse to the anticline appear to have controlled the emplacement. Therefore, a strike-slip movement along the nearby Abilene anticline might cause large transverse fractures in the crust where the Bala Kimberlite intruded from an upper-mantle source under explosive condition. The presence of high-pressure kimberlite minerals such as pyrope, as well as the eclogite and pyroxenite indicates an upper-mantle origin for the kimberlites (Brookins, 1970).

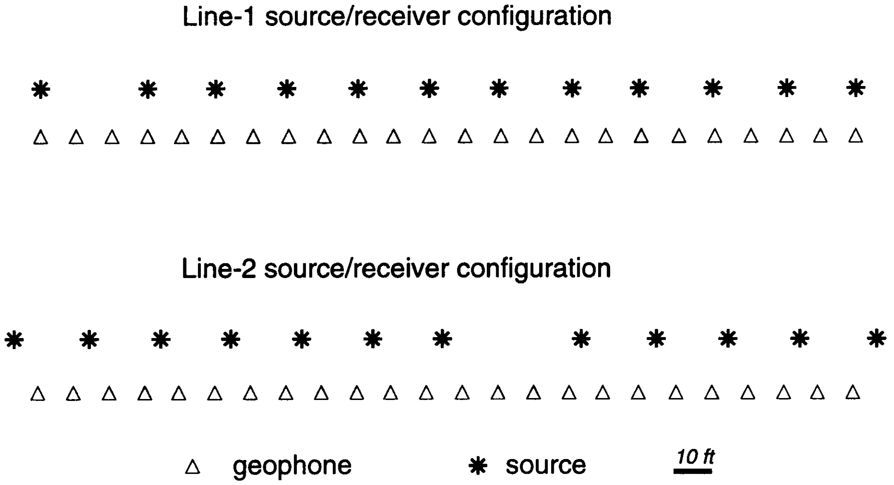

Figure 6-1: Source and receiver configuration applied in the seismic surveys at a coastal site in eastern Massachusetts. Line 1 and line 2 are adjacent to each other. 24 geophones and 12 shots for each line were used. Note that shot locations shift off geophone for half a receiver spacing in line 2 for better estimating near-surface velocities.

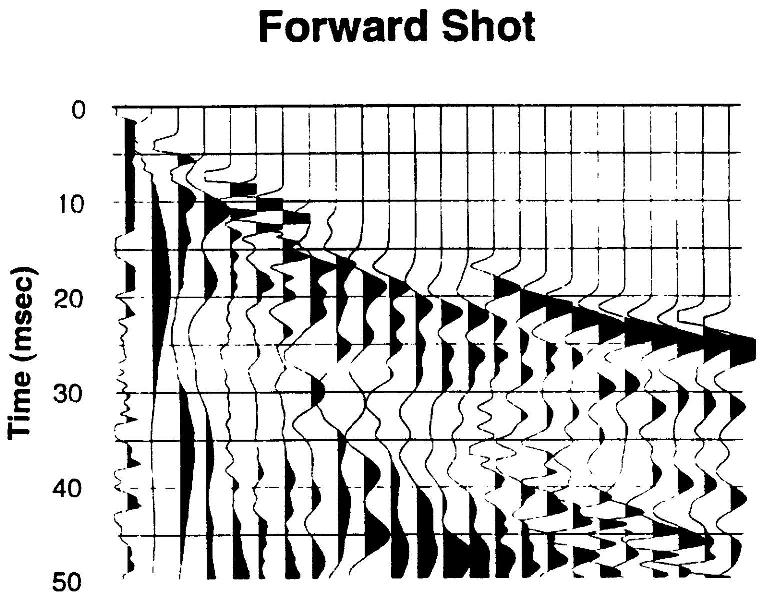

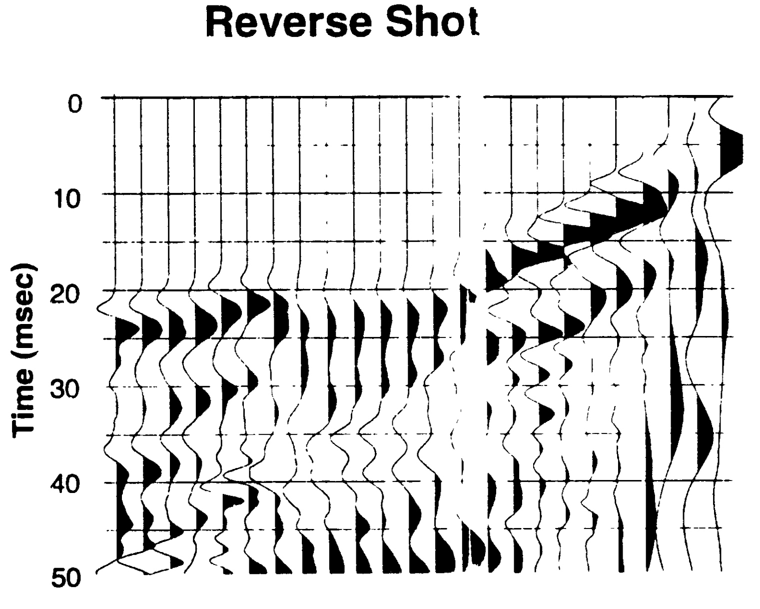

Figure 6-2: Waveform data from forward and reverse shots along line 1. Note the influences due to a shallow low-velocity zone between trace 7 and 14 along line 1.

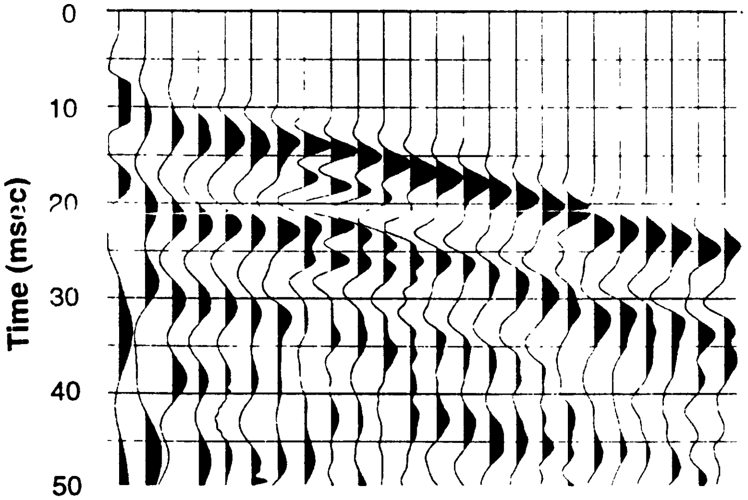

Forward Shot

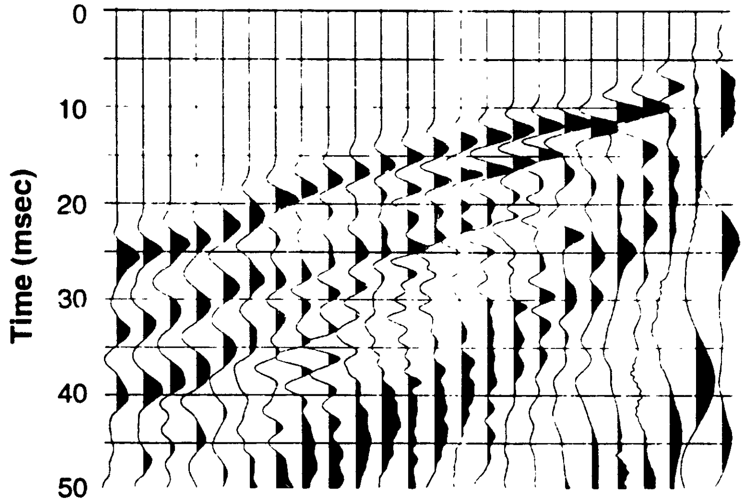

Reverse Shot

Figure 6-3: Waveform data from forward and reverse shots along line 2. Note the influence due to a shallow high-velocity zone along line 2.

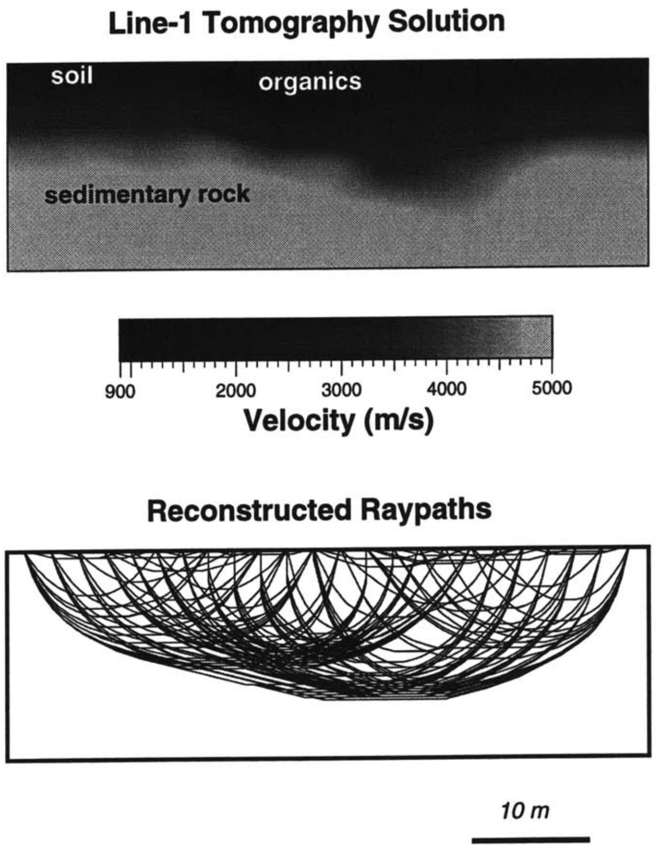

Line-1 Tomography Solution

Reconstructed Raypaths

Figure 6-4: Line-1 tomography solution. It shows a low-velocity zone near the surface where organices was later found by drilling. Bedrock topography deepens slightly off the center toward the right. Reconstructed first-arrival raypaths are also displayed.

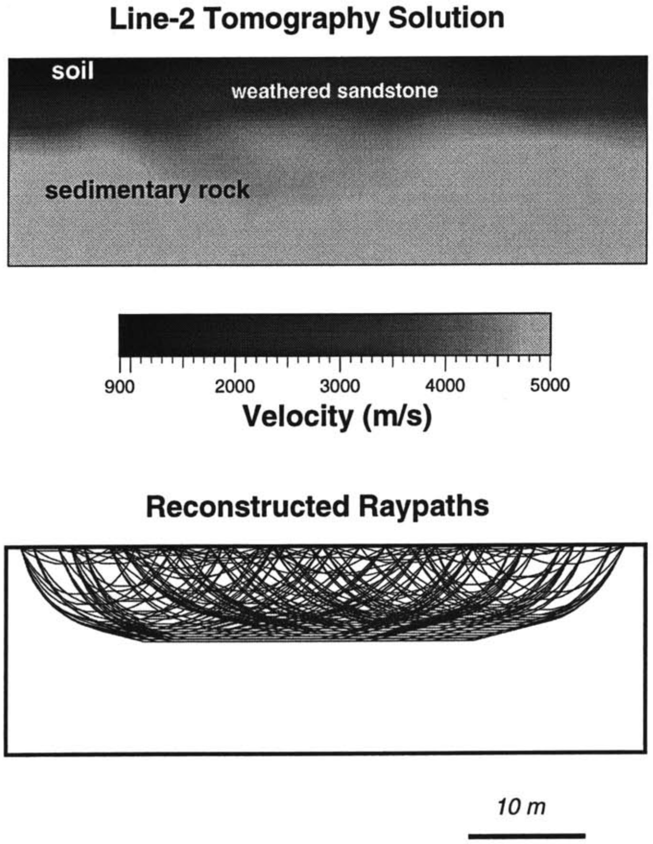

Figure 6-5: Line-2 tomography solution. Bedrock topography is found relatively flat. An intermediate velocity layer is overlain on the bedrock and outcrops the surface. It is identified as weathered sandstone. Reconstructed raypaths are displayed.

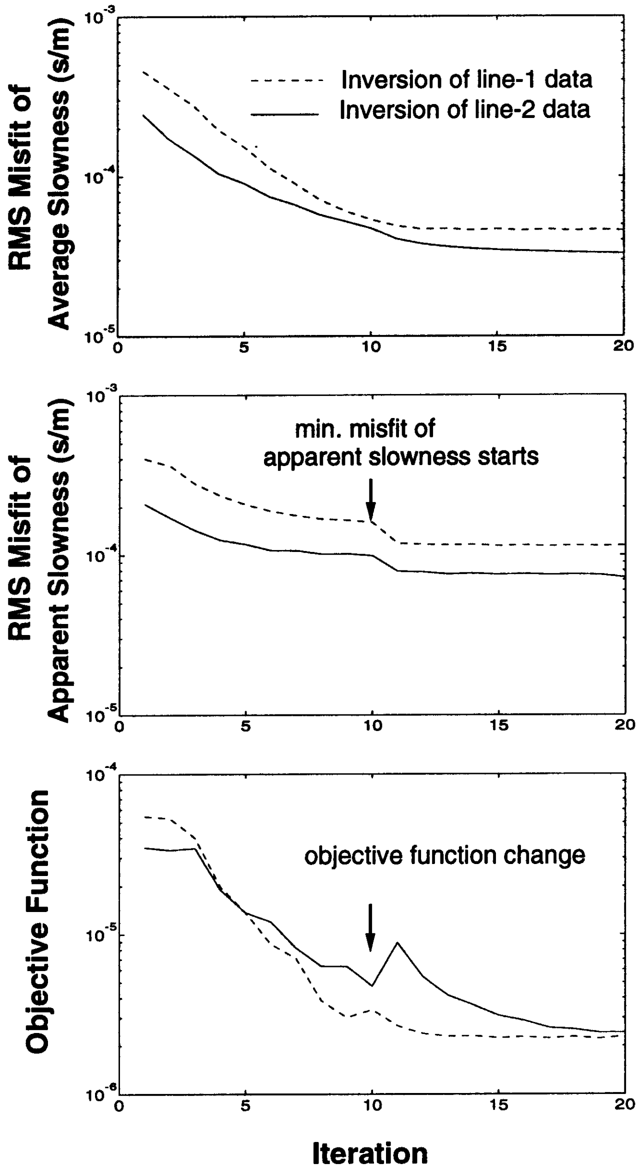

Figure 6-6: Convergence progress of the line-1 and line-2 inversions. Average-slowness data were inverted during the first 10 iterations, then both average-slowness and apparent-slowness data were inverted for another 10 iterations.

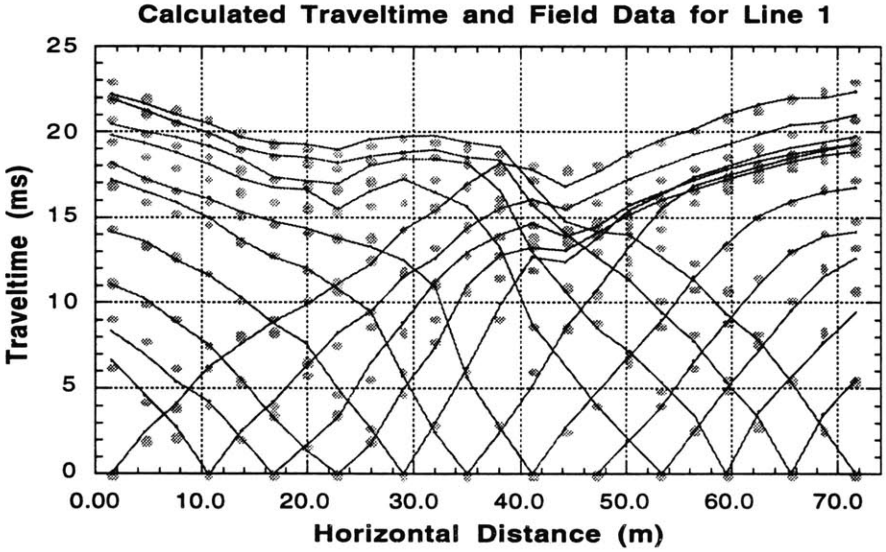

Figure 6-7: Line-1 traveltime fit. Solid curves are the picked traveltime data, dots are the calculated traveltimes for the final model. Large misfit was found at receivers near the low velocity zone due to inaccurate traveltime picks.

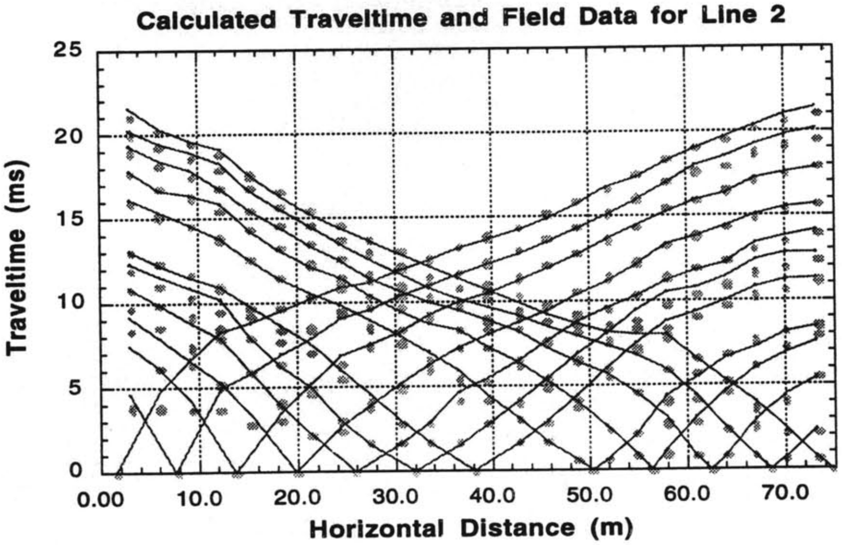

Figure 6-8: Line-2 traveltime fit. Data (solid curve) and calculated traveltimes (dot) are displayed.

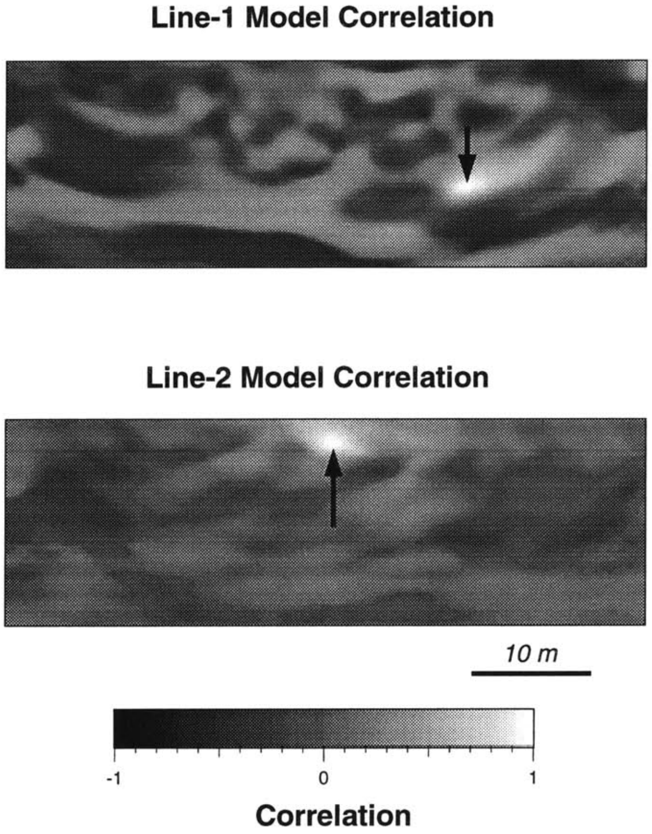

Line-1 Model Correlation

Line-2 Model Correlation

Figure 6-9: Uncertainty analysis using nonlinear Monte Carlo inversions. Posterior model correlation for selected points are displayed, one from each model. Both points are correlated only to a very small area in the neighbors, indicating good resolution.

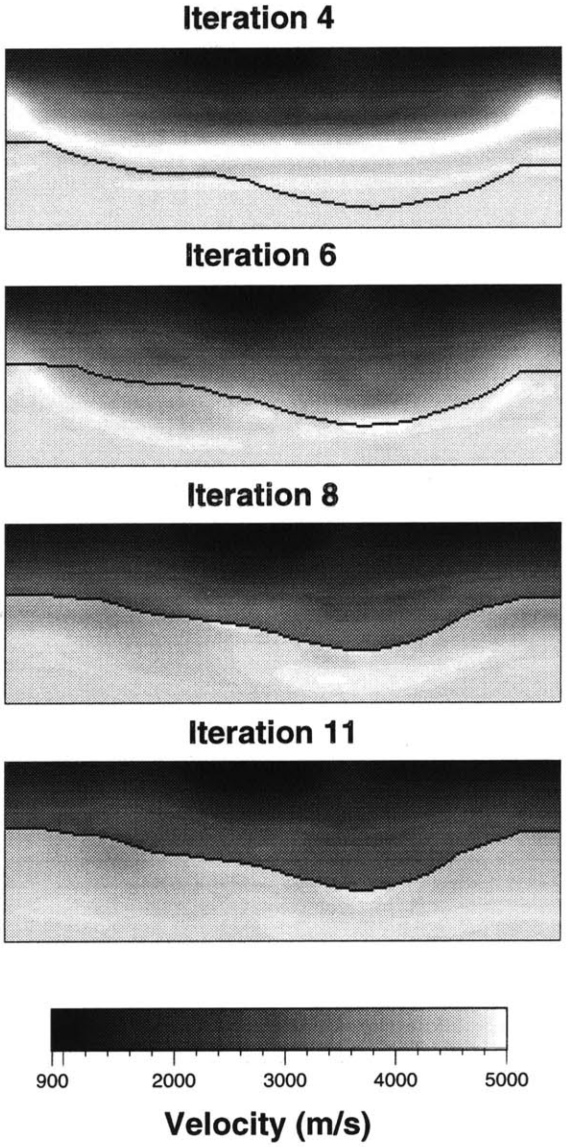

Figure 6-10: Applying joint migration and tomography method to line-1 traveltime data. Migration image and velocity model are superposed for display purpose. During the first 6 iterations, only tomography was conducted to obtain a reasonable velocity estimate. Starting from the 7th iteration, migration and tomography are jointly conducted.

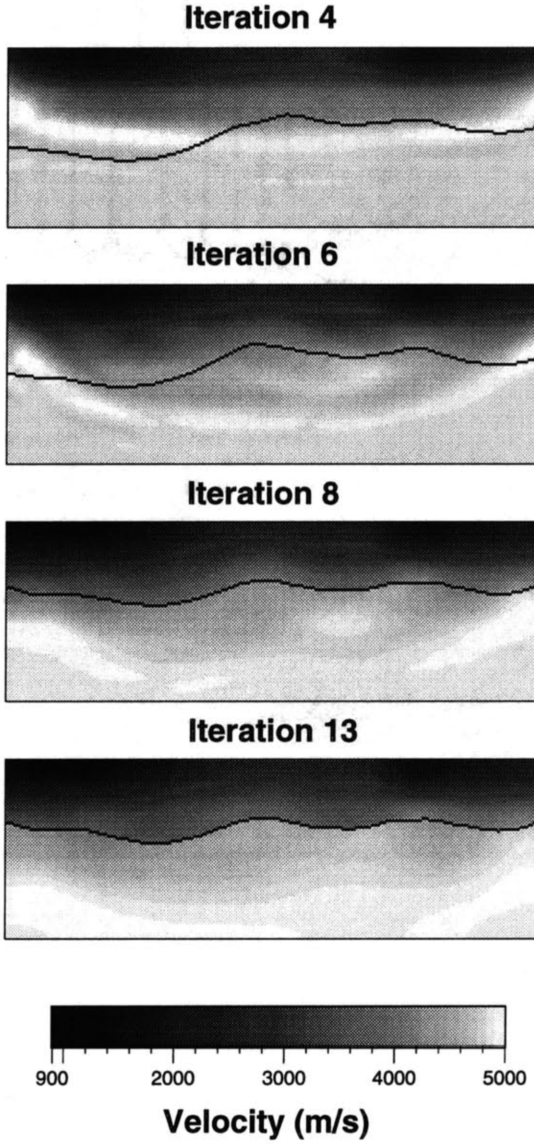

Figure 6-11: Applying joint migration and tomography method to line-2 traveltime data. Similar to line-1 imaging, during the first 6 iterations, only tomography was conducted to obtain a reasonable velocity estimate. Starting from the 7th iteration, migration and tomography are jointly conducted.

Line-1 Raypaths from Joint Migration and Tomography

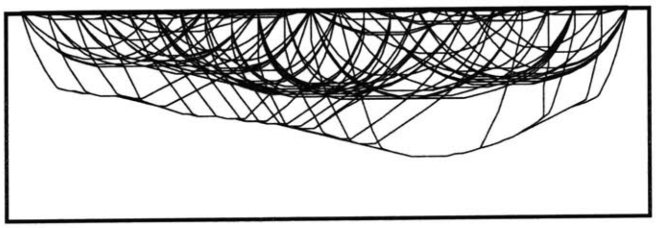

Line-2 Raypaths from Joint Migration and Tomography

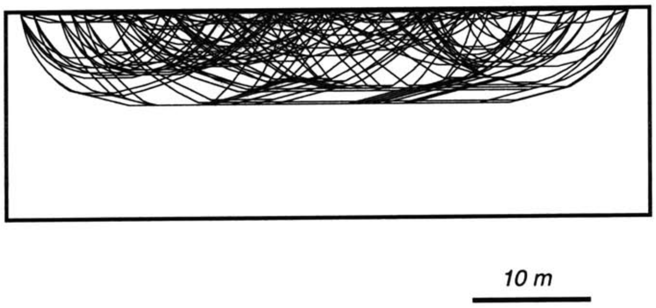

Figure 6-12: Reconstructed raypaths from joint migration and tomography. Note their deep rays differ from those reconstructed from nonlinear refraction traveltime tomography.

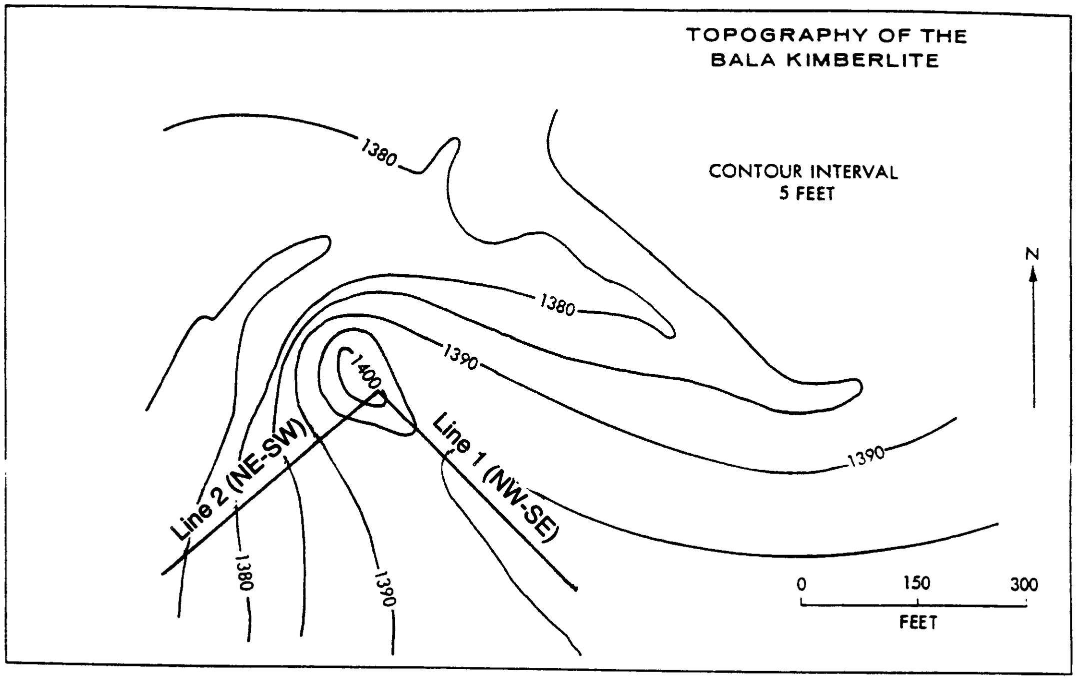

Figure 6-13: Topography of the Bala Kimberlite and the seismic survey locations. Above elevation 1400 feet, a small dome shape of the Bala Kimberlite was exposed at the surface, where two seismic survey lines intercept. Along each line, 96 geophones were deployed, and shots at every receiver locations and also at offset distances were conducted.

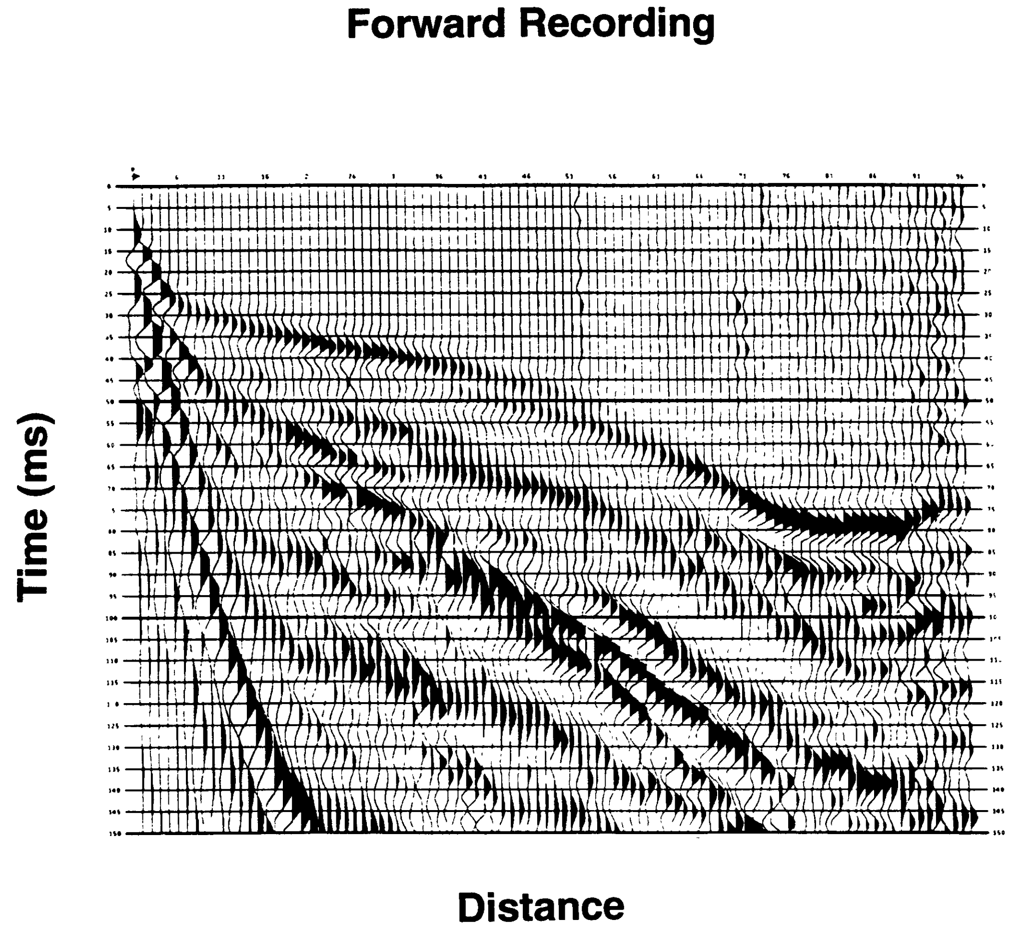

Figure 6-14: Waveform recordings from a forward spread on line 2. Note the rapid traveltime decrease with distance at the end close to the kimberlite. It also shows amplitude focusing effects near the kimberlite.

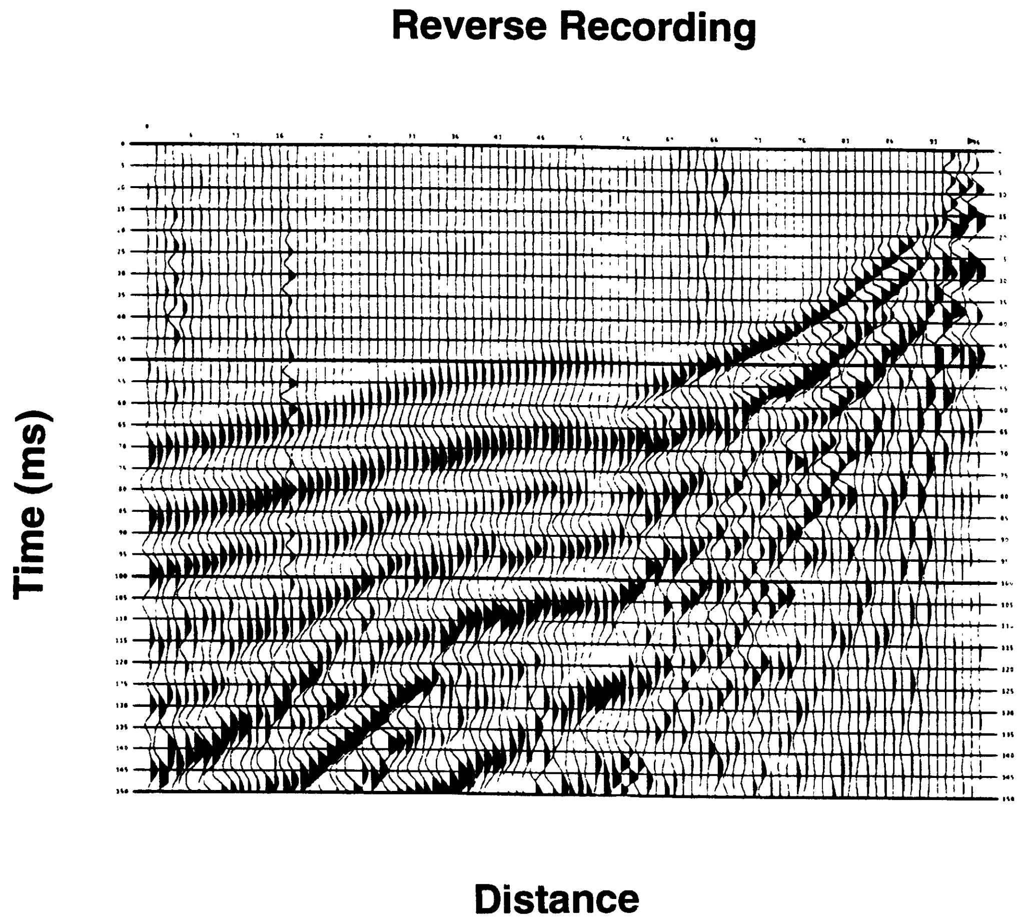

Figure 6-15: Waveform recordings from a reverse spread on line 2. Note the rapid traveltime decrease near the kimberlite and amplitude focusing.

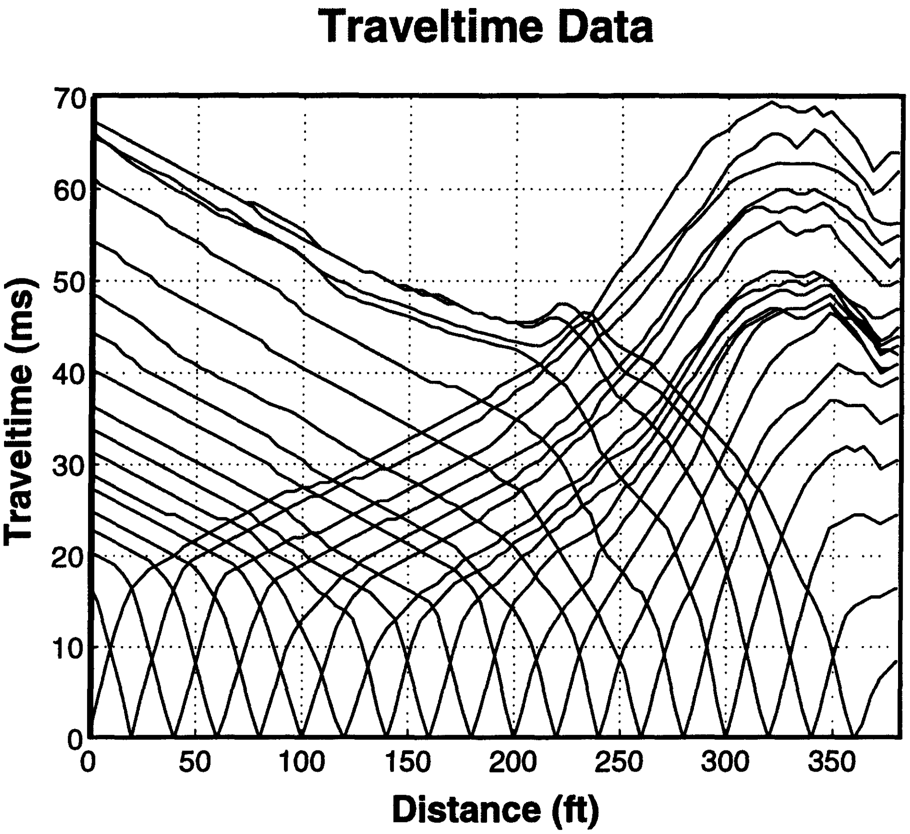

Figure 6-16: The first-arrival traveltimes from 19 shots to 96 receivers. Note the significant traveltime delay near the kimberlite.

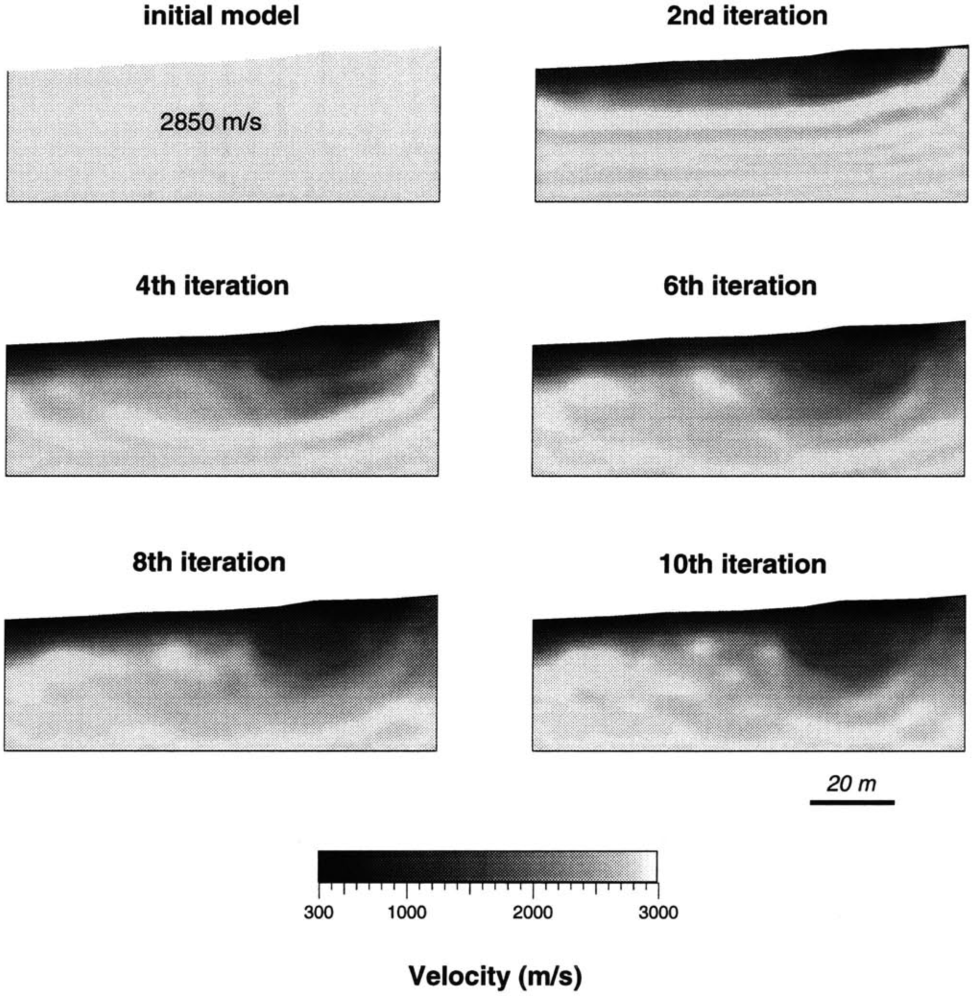

Figure 6-17: Tomography inversions of line-2 traveltimes from a homogeneous starting model (2850 m/s). It shows high-velocity bedrock topography and its lateral discontinuity. The boundary of the Bala Kimberlite is also reconstructed.

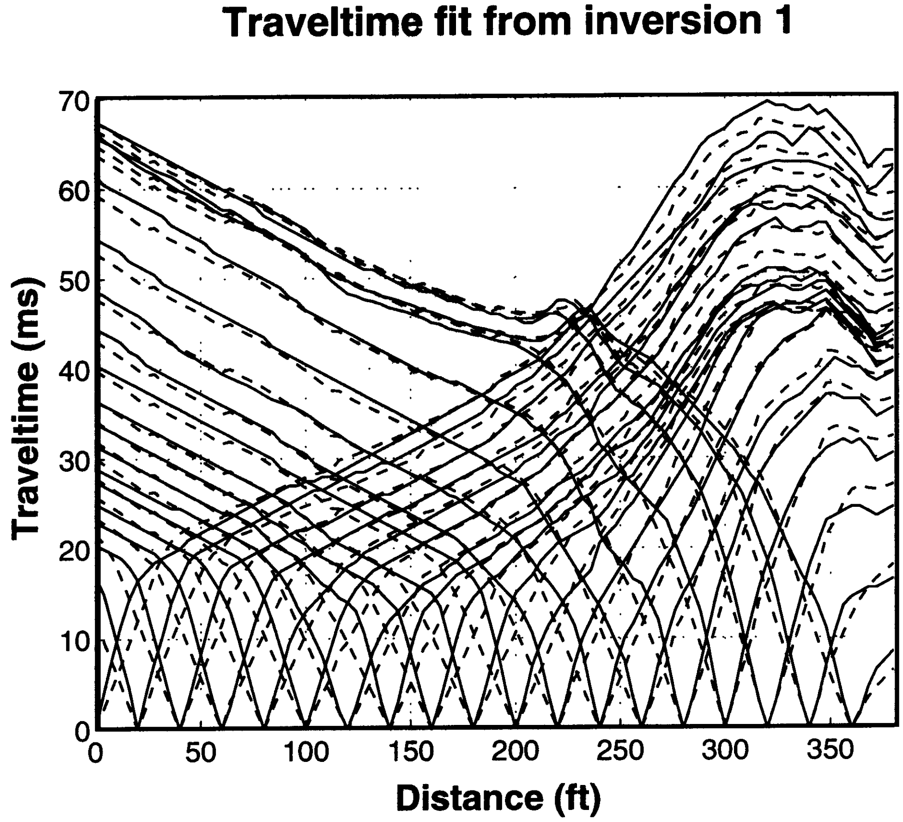

Figure 6-18: Picked traveltimes from real data (solid line) and the calculated traveltimes for the first inversion solution (dashed line).

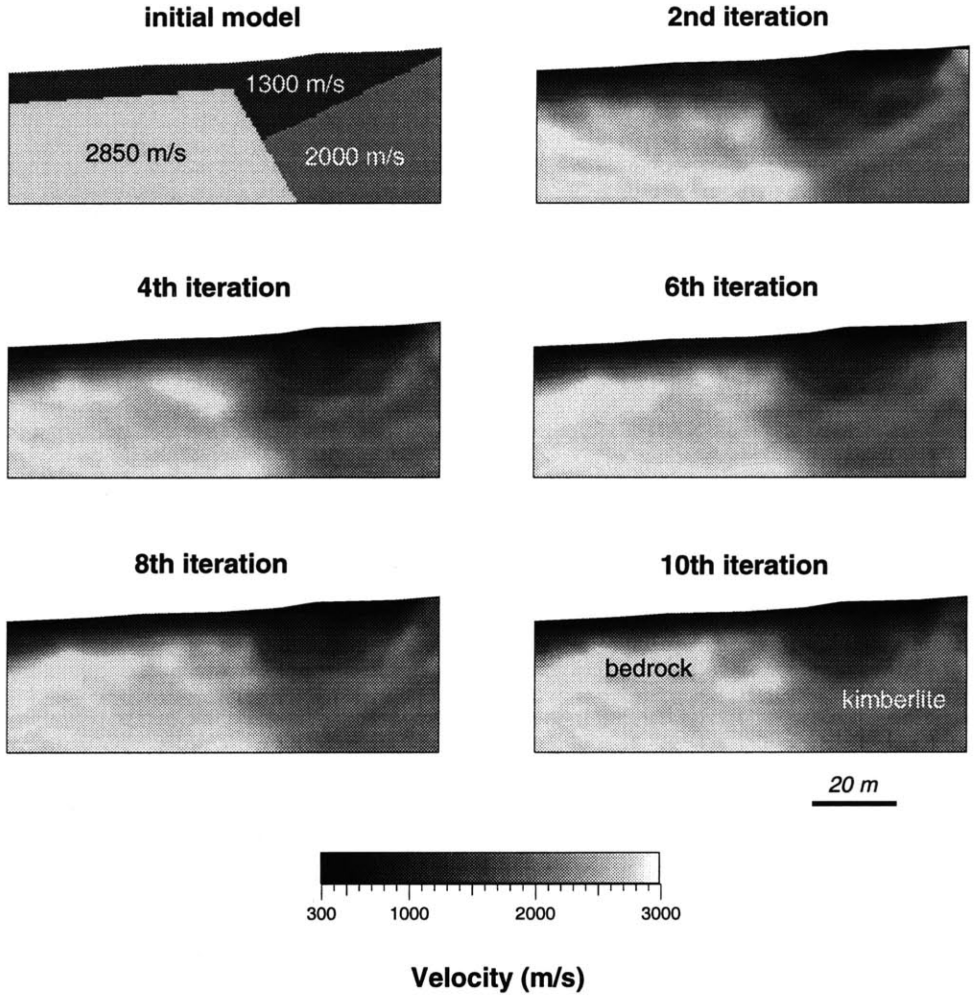

Figure 6-19: Tomography inversions of line-2 traveltimes from a 2D starting model with major features resolved from the first inversion.

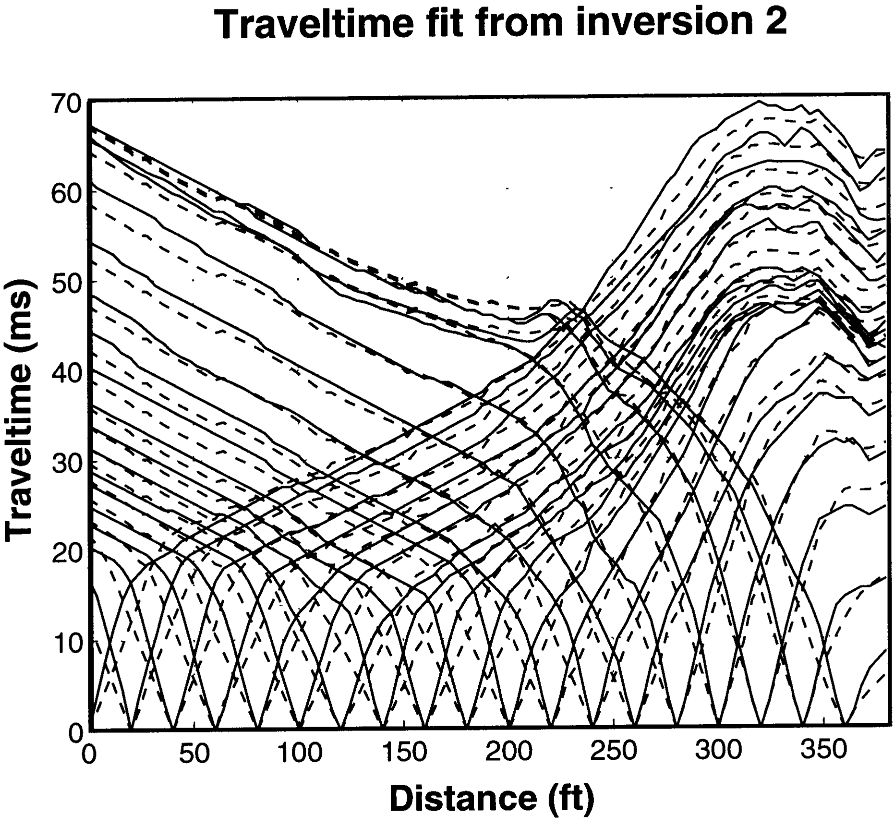

Figure 6-20: Picked traveltimes from real data (solid line) and the calculated traveltimes for the second inversion solution (dashed line).

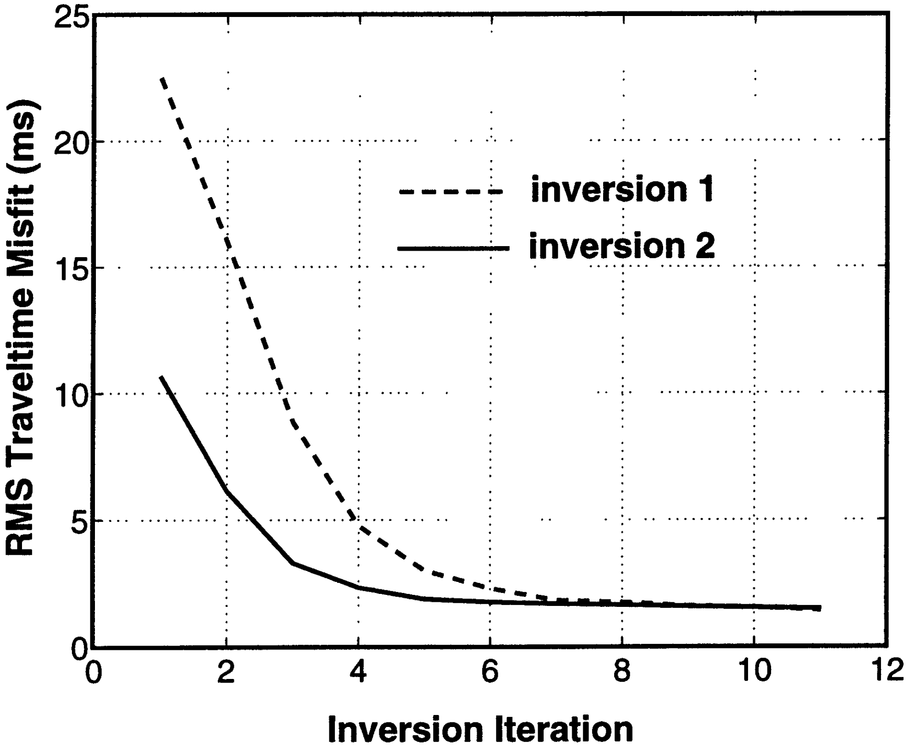

Figure 6-21: RMS traveltime residuals versus inversion iterations for both inversions.

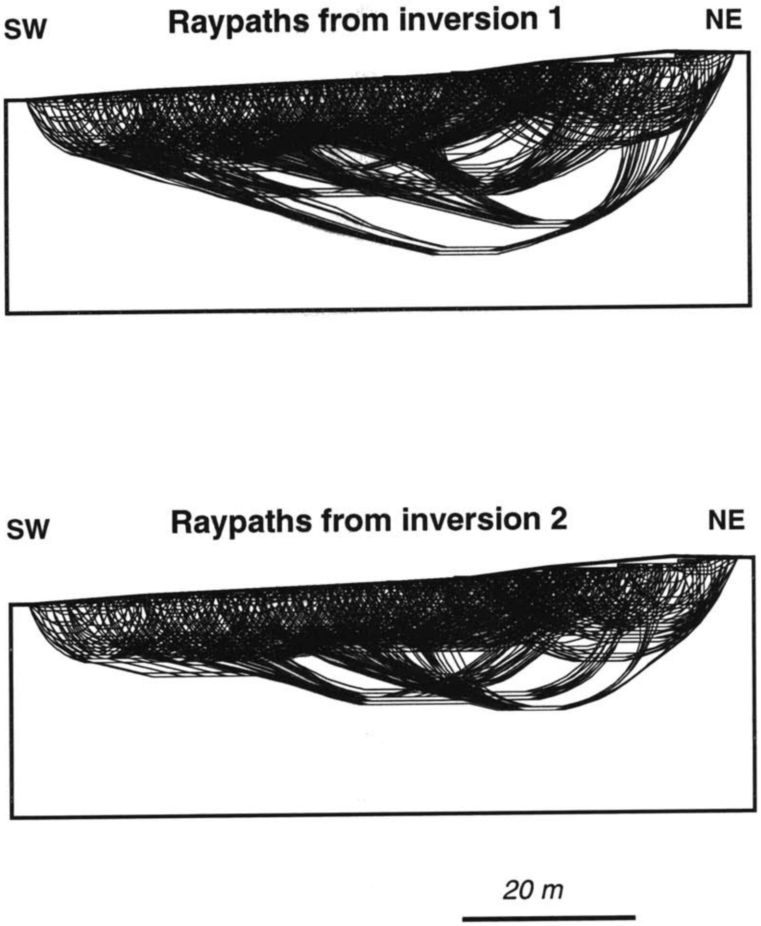

Figure 6-22: Reconstructed raypaths corresponding to the tomography solutions shown in Figure 6-17 and Figure 6-19.

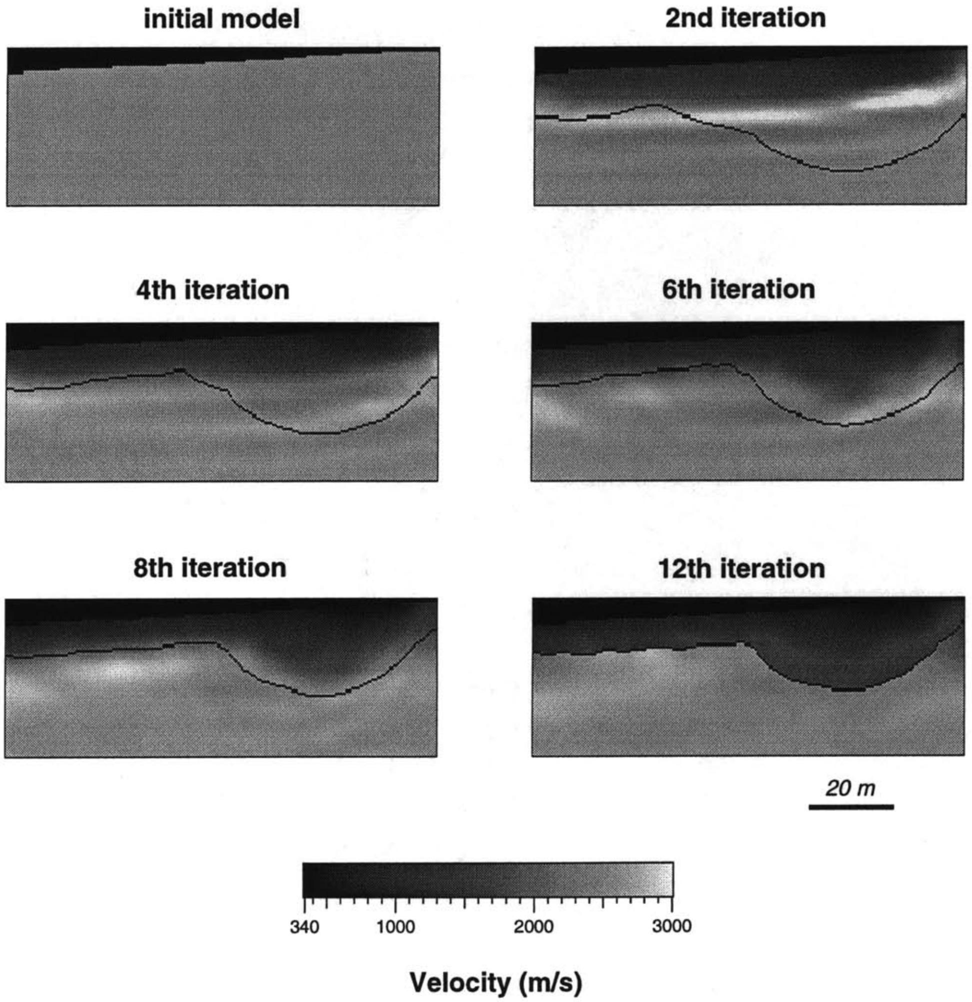

Figure 6-23: Application of joint migration and tomography method to the line-2 data. The migration image and the velocity models are superposed for display. During the first 7 iterations, tomography method was applied to obtain a reasonable well model. Staring from the 8th iteration, the joint method is applied.

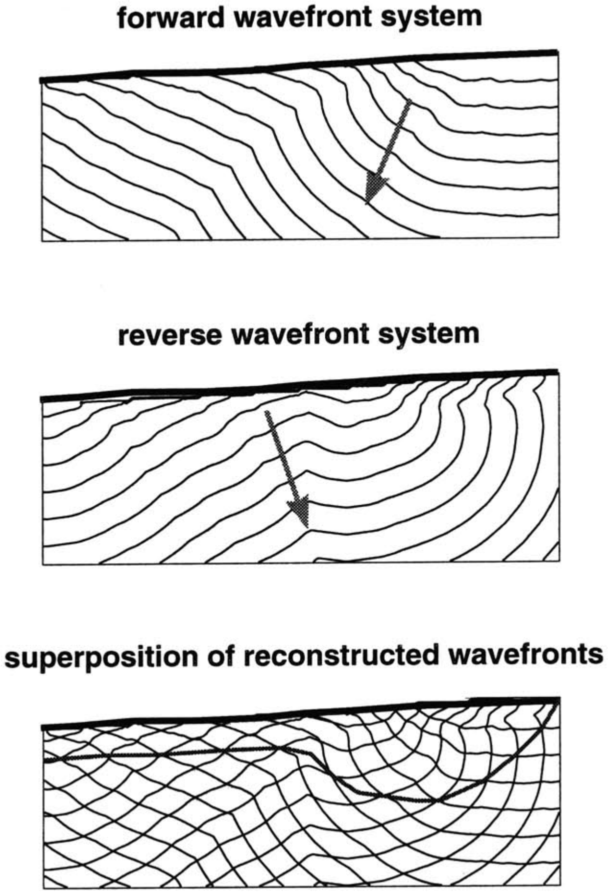

forward wavefront system

reverse wavefront system

superposition of reconstructed wavefronts

Figure 6-24: Downward continuation of the phantomed forward and reverse traveltimes for constructing a line-2 migration image. The velocity model reconstructed from the second inversion was used for migration.

Chapter 7

Imaging Crustal Structure of the California Borderland

Abstract

We apply a joint nonlinear refraction and reflection traveltime tomography method to image the crustal structure of the California Borderland. Ocean Bottom Seismometer (OBS) and land data were collected during the Los Angeles Region Seismic Experiment (LARSE) along two marine survey lines. Along both lines, it shows strong P refractions from the upper crust and wide-angle P-wave reflections from the Moho (PmP). For line 1 from Seal Beach to San Clemente Island, we model a 2-D profile 90.2 km by 24.6 km with 1100×300 grids. Details of our image include a high velocity zone under the Catalina Ridge, but a smooth gradient zone between Catalina Ridge and San Clemente Ridge. The Moho depth is about 23 km with lateral variations. For line 2 from Santa Monica to south 160 km, our model covers a profile of 160.5 km by 25.0 km with 1605×250 grids. We also found the similar high velocity features under both Catalina Ridge and San Clemente Ridge. After tomographic imaging, we measure the uncertainty of the solutions using nonlinear Monte Carlo inversions. The results indicate that the shallow high-velocity features in the solutions are reliable.

7.1 Introduction

Seismic experiments have played a major role in imaging the crustal structure of the earth. To study the crustal structure of the California Borderland province crossing from land to sea, the Los Angeles Region Seismic Experiment (LARSE) was conducted in October, 1994. This project was a cooperative study involving scientists from the U. S. Geological Survey, California Institute of Technology, the University of Southern California, the University of California Los Angeles, and the Southern California Earthquake Center (SCEC). The primary goal of this project was to investigate the crustal structure in the Southern California which can aid the study of earthquake hazard associated with buried faults and amplification of seismic energy due to structural influences. Nine OBSs were deployed off shore along two survey lines and recorded air-gun blasts generated by the R/V Ewing (see Figure 7-1). Land stations were also used to record the marine seismic energy. A detail of the project is given by ten Brink *et al.* (1996) and Fuis *et al* (1996).

As defined by Shepard and Emery (1941) and Moore (1969), the California borderland is bounded on the northwest by Point Arguello and Arguello Canyon; on the southeast by Bahia Sebastian Vizcalino and Cedros Island. Its western edge is marked by the base of the continental slope at the north and by Cedros Deep at the south (Moore, 1969; Vedder, 1987). Previously there was only one large-scale refraction experiment offshore the Los Angeles basin, and only one-dimensional velocity structure was determined from modeling analog data (Shor and Raitt, 1958). From that survey the crust was reported to be 24-km-thick in the area between Catalina and San Clement Islands, increasing to 30 km on shore and decreasing to 18 km under the Patton Ridge where it is close to the continent-ocean boundary.

7.2 Reflection and OBS Data

Because of the geological structure in this region which is characterized as velocity gradients due to Catalina Schist, multi-channel seismic reflection techniques fail to record any information of the deep crust (Bohannon and Geist, 1996). In Figure 7-2 and Figure 7-3, we display single-channel reflection records along two survey lines. They only show the seafloor and sediment reflections and their multiples. Other than these, the wavefields are quite simple. Nevertheless, refraction and wide-angle reflection survey with OBSs and land stations provides traveltimes contraining the lateral and vertical velocity variations in the crust. Figure 7-4 dsiplays the vertical waveform recordings from one of the OBSs along line 1. It shows strong P-wave refractions from the upper crust (Pg) and the wide-angle reflections from the Moho (PmP). Figure 7-5 shows a similar waveform pattern from line 2. Recordings along line 1 and line 2 all show these two phases, Pg and PmP. Therefore, we perform a joint refraction and reflection tomography that inverts Pg and PmP traveltimes simultaneously.

7.3 Nonlinear Traveltime Tomographic Images

For line 1, we discretize a 2-D profile of 90.2 (km) × 24.6 (km) with 1100×300 (330,000) cells and equal grid spacing 0.082 km. The profile starts from the shore close to Long Beach to San Clemente Island, and the shooting ship slightly turns near Catalina Island because of shallow seafloor. Figure 7-6 shows the tomographic image and Figure 7-7 displays the corresponding raypaths. It shows high velocities under the Catalina Ridge, which are constrained by the first-arrival refractions only. Off the Catalina Ridge, the upper crust has been constrained by both refraction and reflection raypaths. A large number of rays penetrate into the deep crust and reflect back to the seafloor from the Moho. A bending Moho topography occurs under the Catalina Ridge. Between San Clemente Island and Catalina Island, the entire crustal structure is smooth and simple, while between Catalina Island and the shore the upper crust displays much complexity. In fact, as shown in Figure 7-1, geological observations on the seafloor also indicate that many faults exist along the profile close to shore, but no faults are found between San Clement Island and Catalina Island except for San Clement fault at the end. Because PmP traveltimes are not asscoiated with any velocities below the Moho, the tomographic image is meaningful only above the Moho.

For modeling the crustal structure along line 2, we construct a model of 160.5 (km) × 25.0 (km) with 1605×250 (401,250) cells and equal grid spacing 0.1 km. This profile starts from Santa Monica to 40 km south of the ridge containing San Clemente Island passing near the NW tips of Catalina and San Clemente Islands. Figure 7-8 shows the tomographic image of the crustal structure with large velocity variations in the shallow earth (< 3.0 km), and simple in the deep crust. The Moho dips away from shore, and its average depth is about 23.0 km. The reconstructed raypaths are shown in Figure 7-9.

After obtaining tomographic solutions, we conduct nonlinear uncertainty analysis to estimate variance and resolution of the solutions. We select one point in each model and compute its posterior model correlation. On line 1, the point is selected at the high velocity structure under Catalina fault. On line 2, the point is also at a high velocity structure under San Clemente fault. We try to estimate how well these high velcoity zones are resolved from the nonlinear tomography studies. Because the point in line-1 profile is covered by refraction only and the point in line-2 profile is covered mostly by refraction, we only take refraction data for their uncertainty analyses. Figure 7-10 shows that the model correlation for each selected point is large only in a small area (slightly along raypaths), indicating that both points are well resolved.

Therefore, the high velocity structures under Catalina fault and San Clemente fault are the necessary features for the traveltime data that we inverted. Figure 7-11 and Figure 7-12 display traveltime fits corresponding to the final solutions. They include both Pg and PmP traveltimes. The convergence of the rms traveltime misfits are presented in Figure 7-13.

7.4 Conclusions

We apply a joint refraction and reflection tomography approach to image crustal structure of the California Borderland along two marine survey lines. Results indicate that the velocity structure is generally complex in the shallow earth (< 3.0 km), smooth in the deep crust. The Moho is about 22.0 km in depth. The structure pattern is also consistent with the waveform records, *i.e.*, they show two major phases only, the first-arrival refractions and the wide-angle reflections from the Moho. These results are important for other seismological studies that need an input of the detailed crustal struture in the California Borderland. Such studies may include earthquake relocation, simulation of the strong ground motion, deep earth structure modeling, and seismic wave propagation. Combining modeling results from other geophysical data in the future, we may also have a better understanding on the tectonics beneath California.

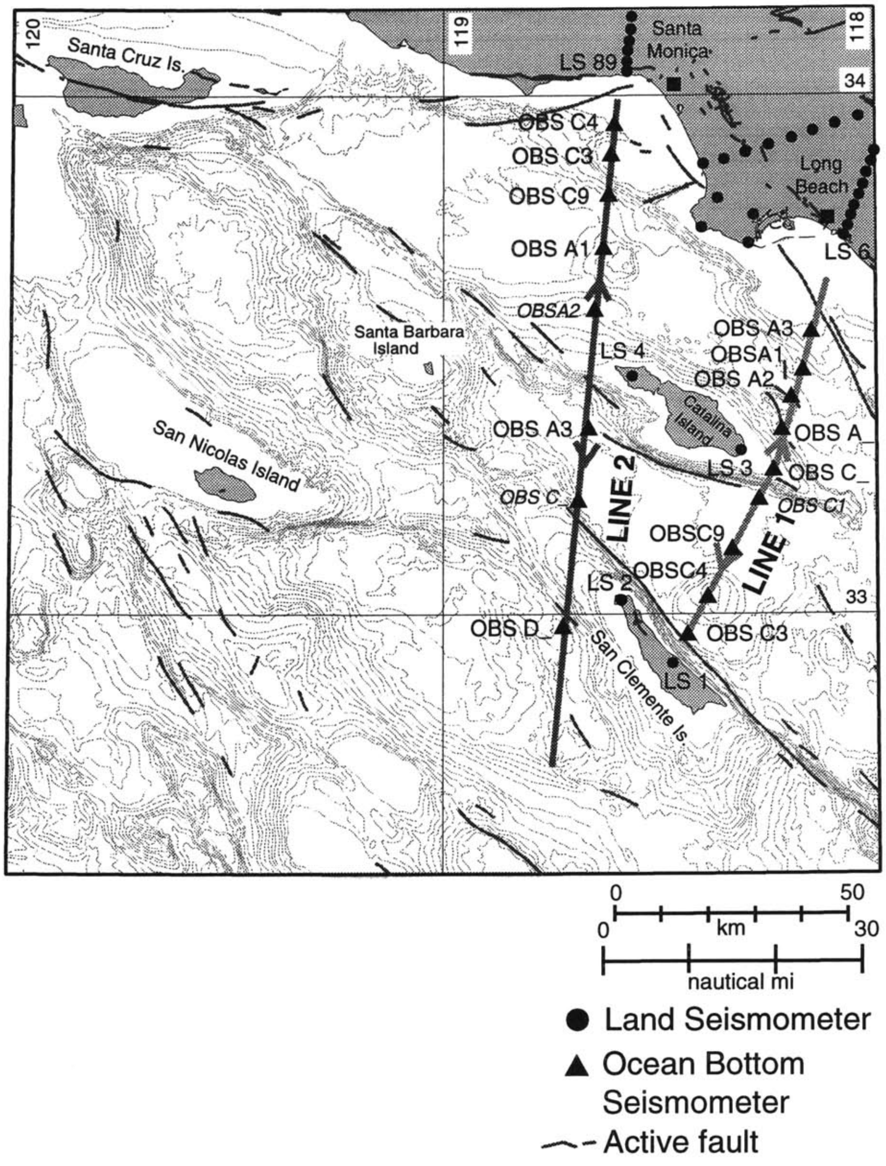

Figure 7-1: Locations of LARSE offshore survey lines. OBSs were deployed along two lines, continuous marine shooting was conducted. Land seismimeters were also used to receive the same shooting signal.

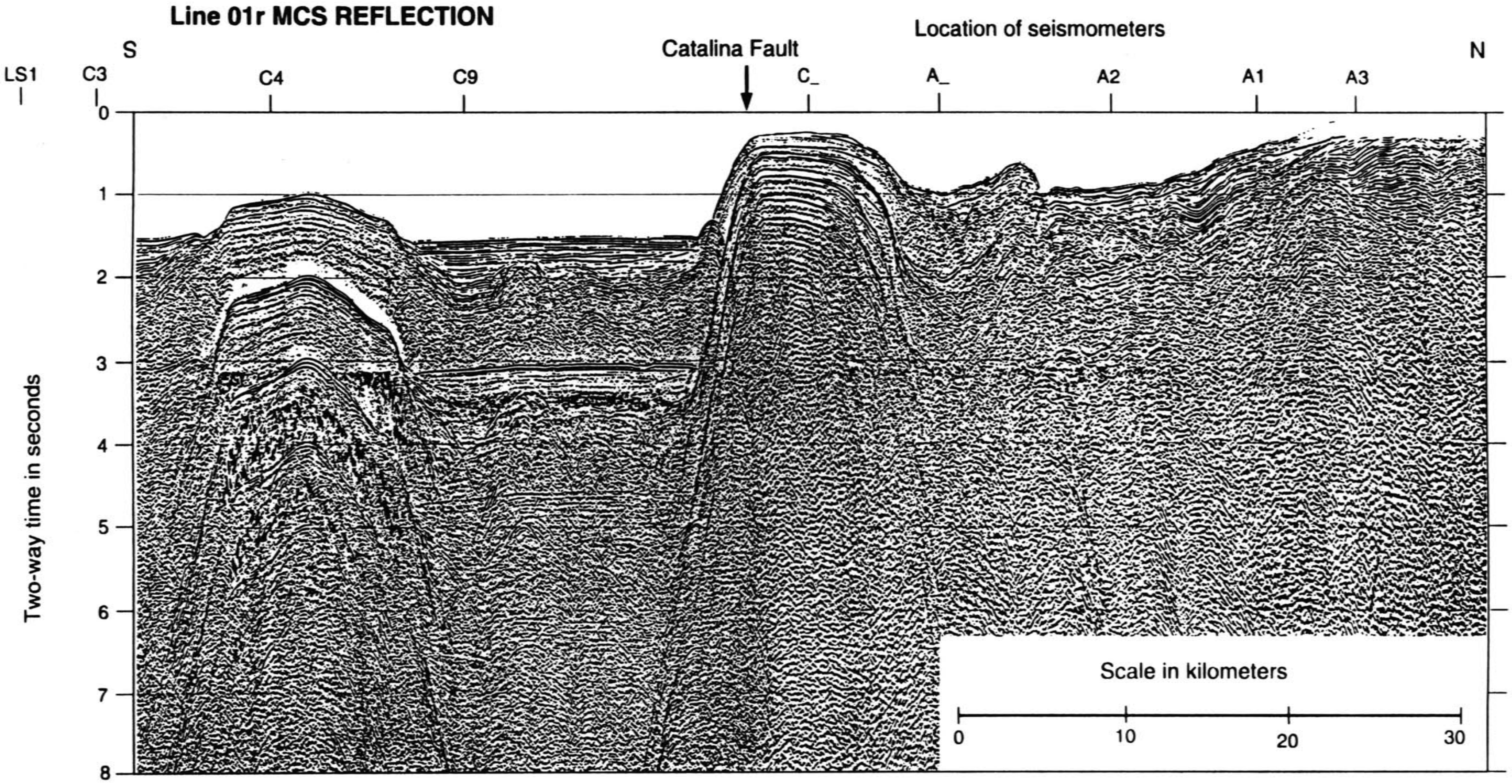

Figure 7-2: Single-channel reflection data following the shooting ship along line 1. It shows reflection from seafloor and sediment, and their multiples. It does not show any deep features. Stronger attenuation in the sea water is found from the Catalina fault to the north.

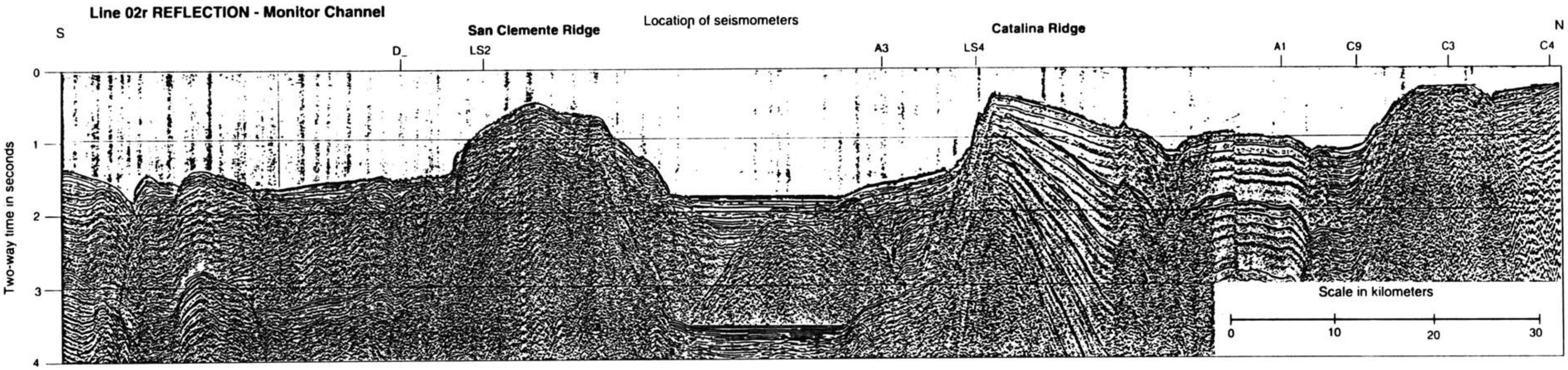

Figure 7-3: Single-channel reflection data following the shooting ship along line 2. Again, it shows seafloor and sediment responses only.

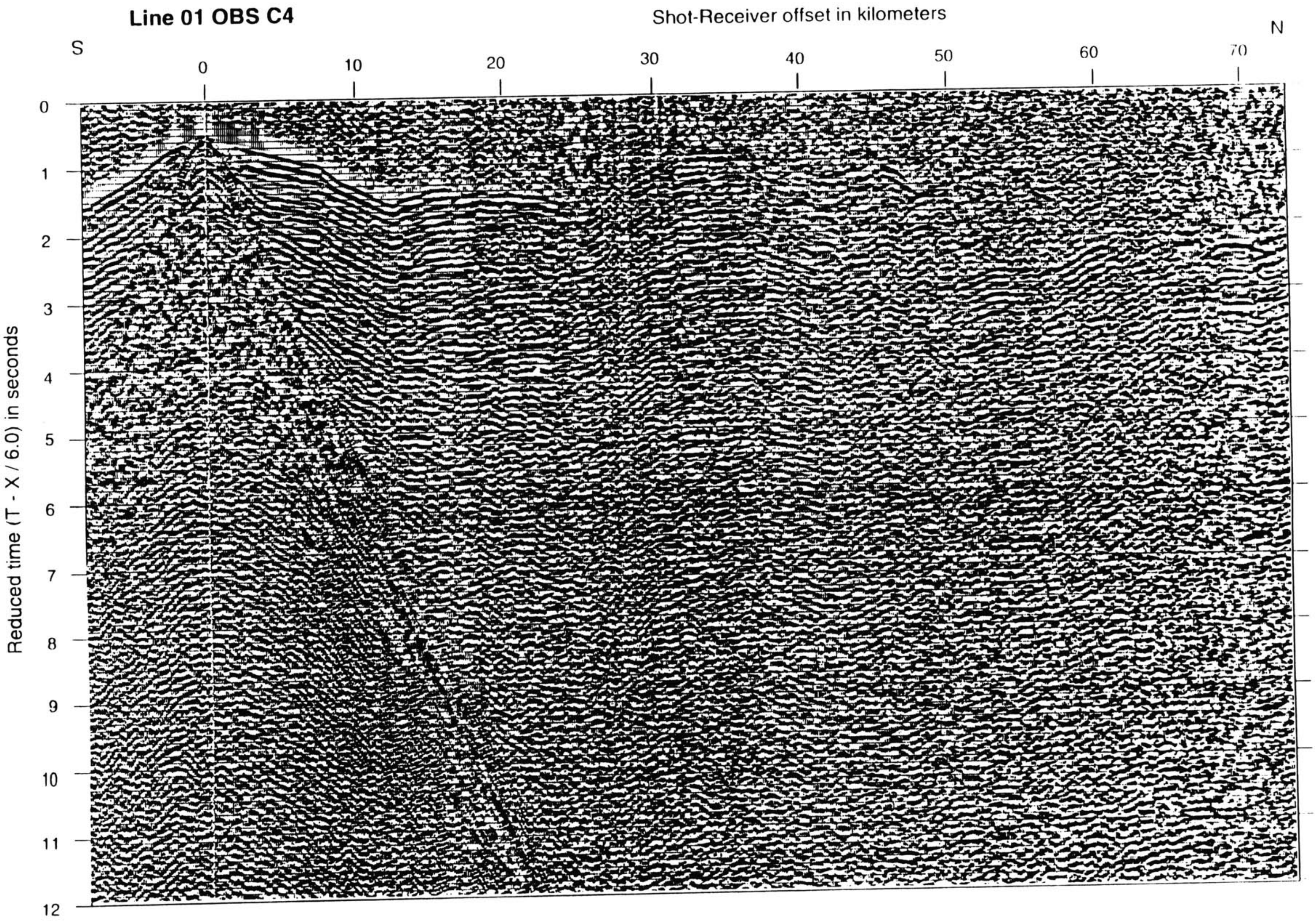

Figure 7-4: Recorded seismic data displayed with a velocity reduction 6.0 km/s from the OBS C4 in line 1. It shows the first-arrival Pg, and PmP 50 km away to the north.

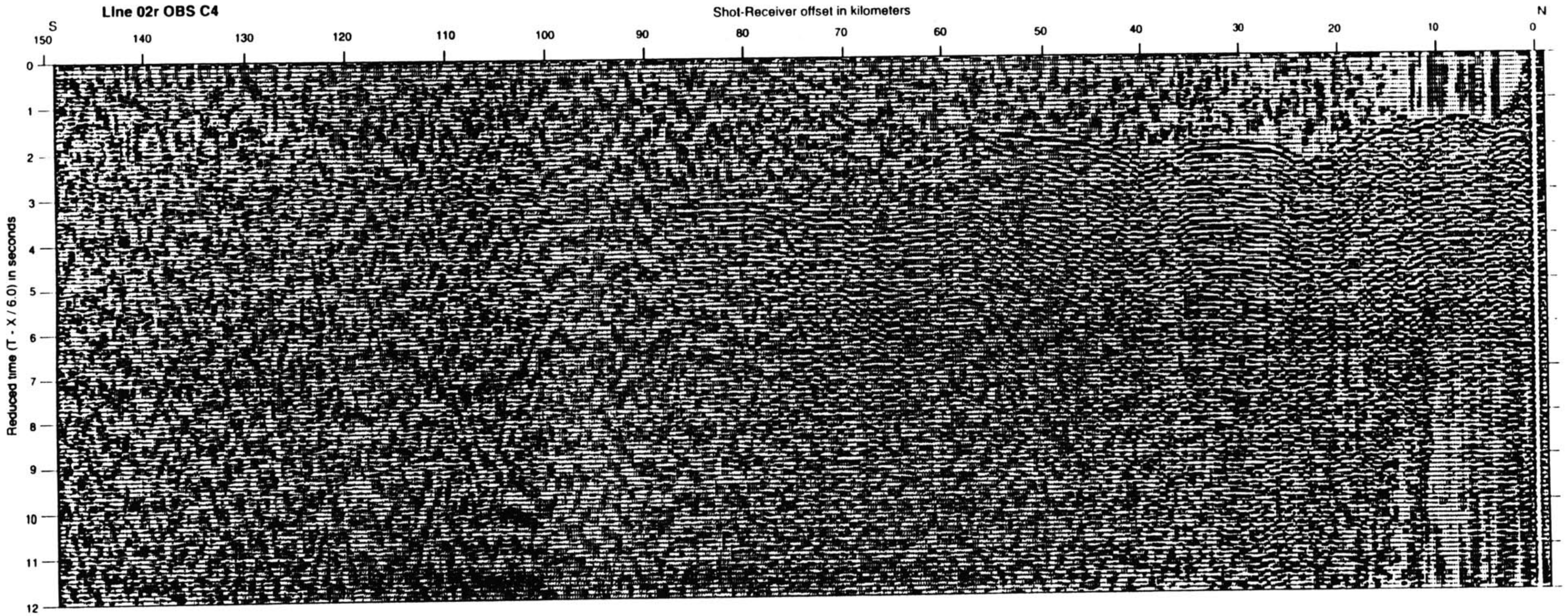

Figure 7-5: Recorded seismic data displayed with a velocity reduction 6.0 km/s from the OBS C4 in line 2. It shows the first-arrival Pg, and PmP at distances 50 km away to the south.

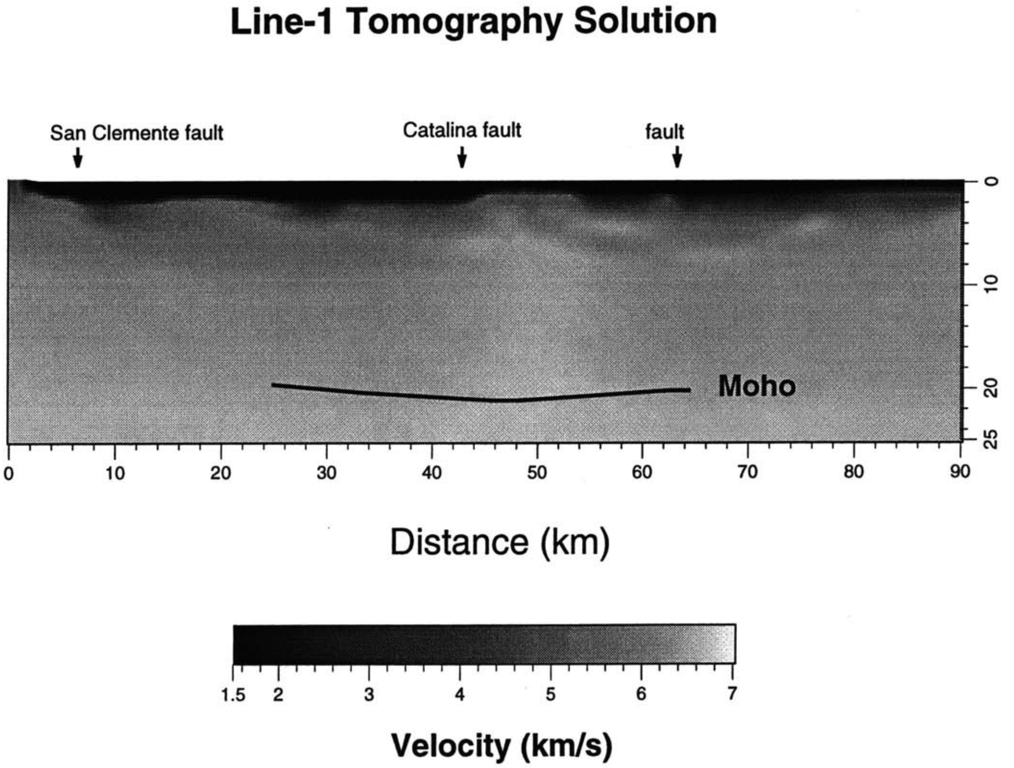

Figure 7-6: Solution of joint nonlinear refraction and reflection traveltime tomography for line 1. Velocity complexity occurs in the shallow structure, particularly near Catalina fault. The Moho depth is about 23 km. The velocity structure is meaningful only above the Moho, because Pg and PmP do not have any information about the velocity beneath the Moho.

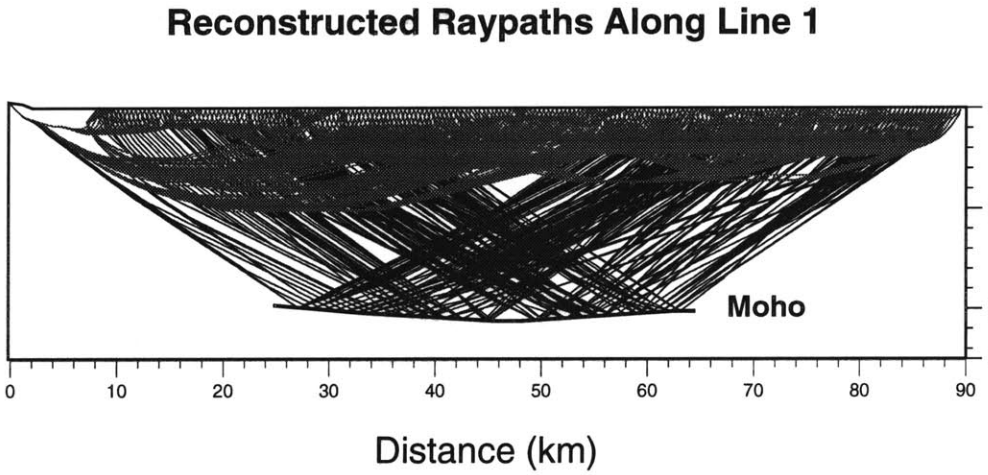

Figure 7-7: Reconstructed refraction and reflection raypaths corresponding to the final tomography solution for line 1.

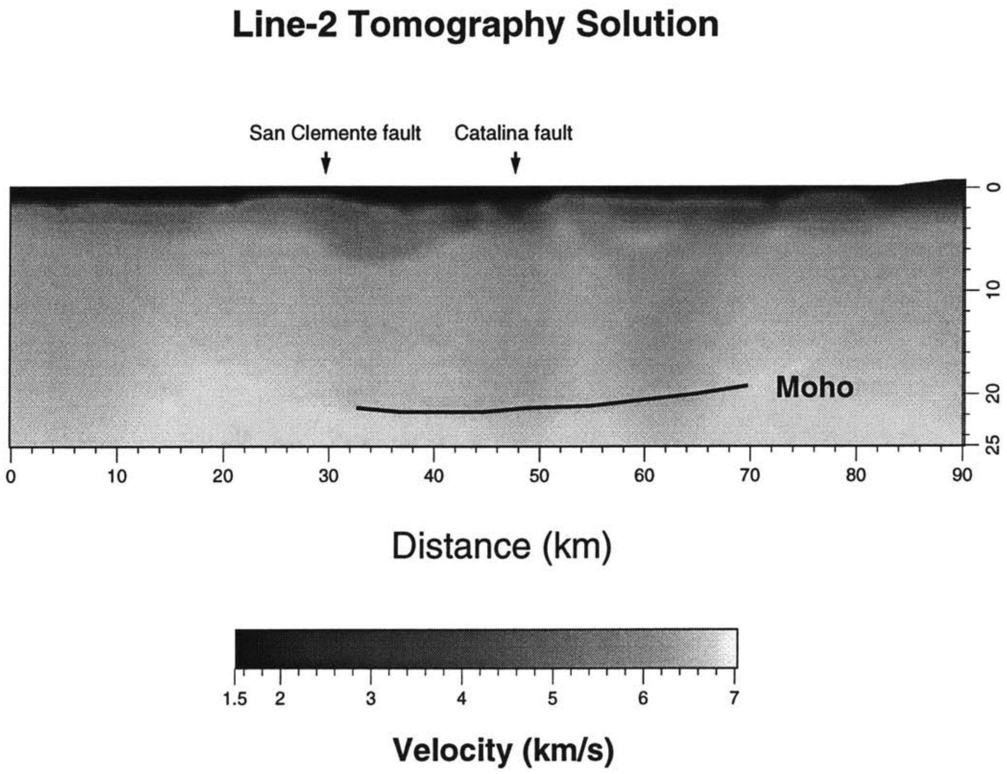

Figure 7-8: Solution of joint nonlinear refraction and reflection traveltime tomography for line 2. Again, large velocity variations occur in the shallow structure. The middle crust is smooth. The Moho is at depth 23 km, dipping away from the shore.

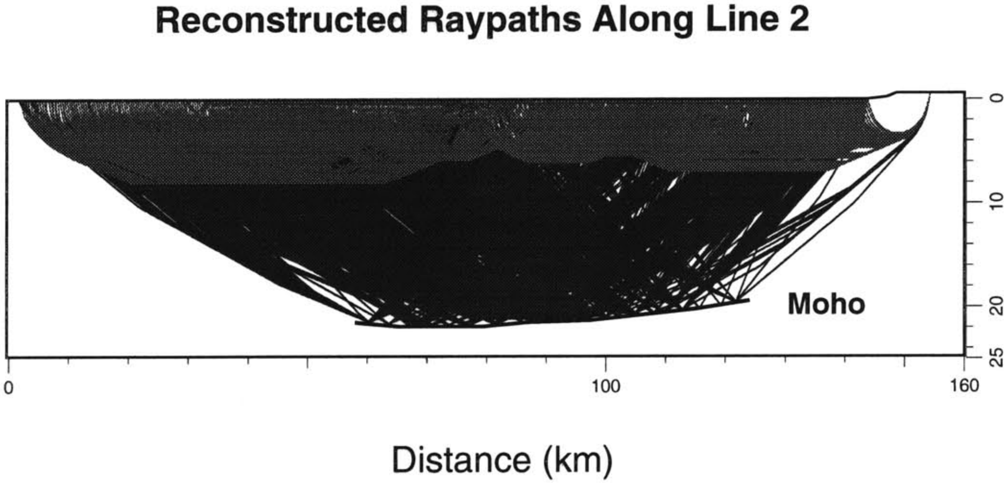

Figure 7-9: Reconstructed refraction and reflection raypaths corresponding to the final tomography solution for line 2.

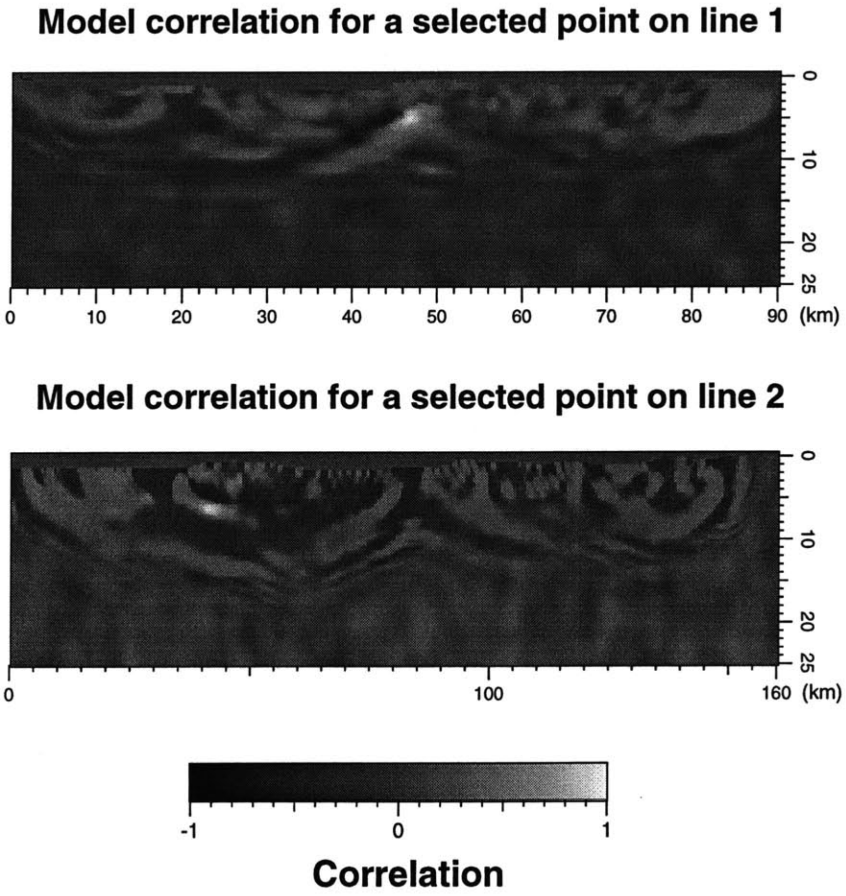

Figure 7-10: Uncertainty analysis of the final solutions. One point in each model is selected for displaying its posterior model correlation. They both show good vertical resolution, but somewhat lateral trade-off (correlation and anti-correlation).

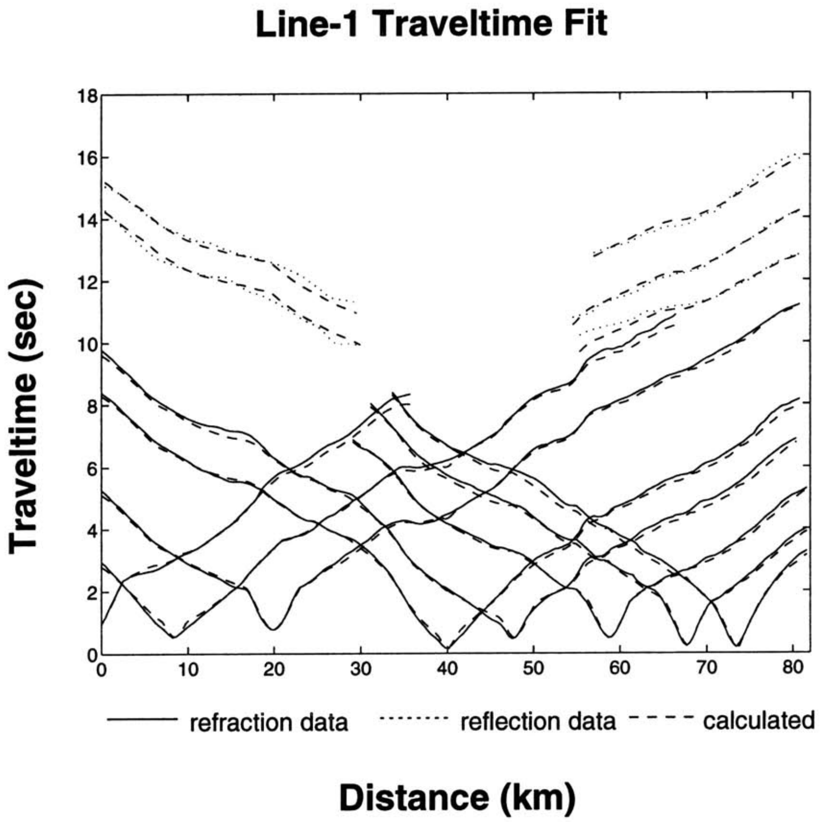

Figure 7-11: The first-arrival (Pg) and the reflection (PmP) traveltime fit for line 1 after 20 inversion iterations.

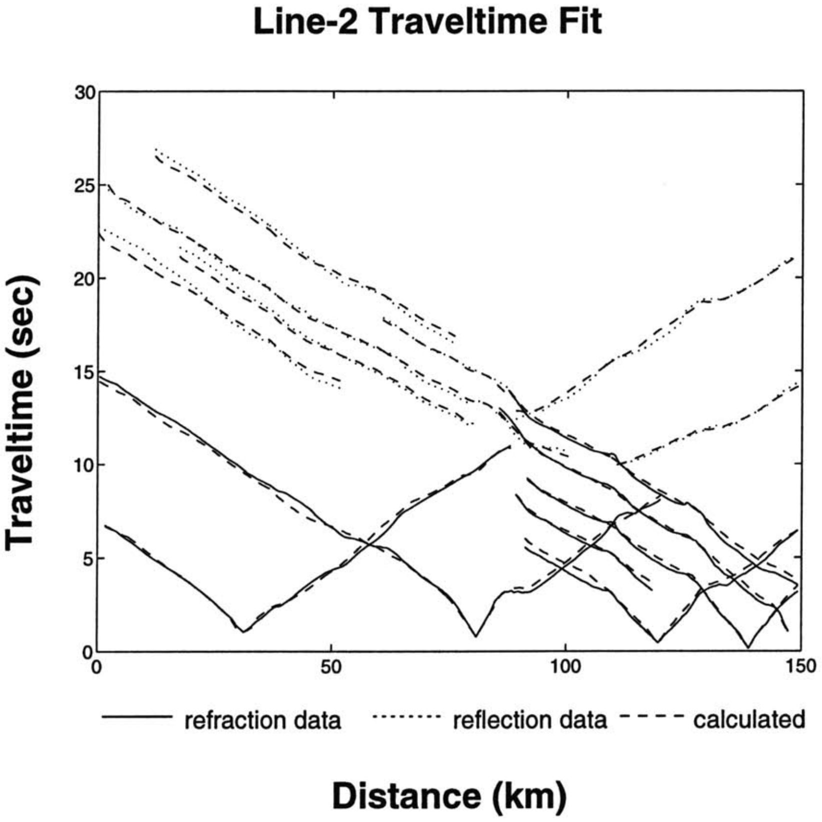

Figure 7-12: The first-arrival (Pg) and the reflection (PmP) traveltime fit for line 2 after 20 inversion iterations.

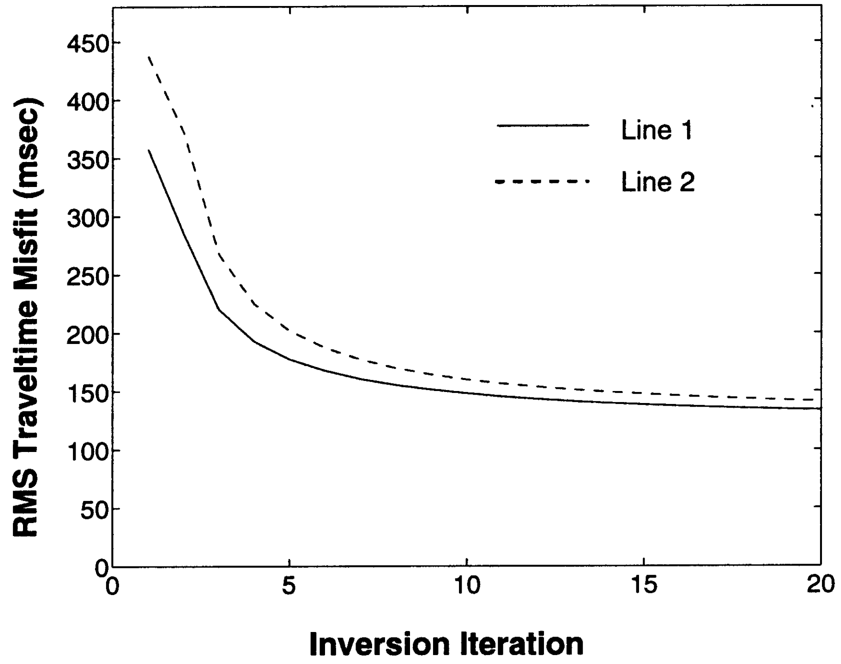

Figure 7-13: RMS traveltime misfits versus inversion iteration during the joint refraction and reflection traveltime tomography.

Chapter 8

Discussion and Conclusions

We have developed three imaging techniques for reconstructing the subsurface structure, i.e., nonlinear refraction traveltime tomography, joint refraction traveltime migration and tomography, and joint refraction and reflection traveltime tomography. These imaging techniques interpret traveltime data recorded on the surface and account for the nonlinearity of the traveltime problems in several ways. More importantly, we solve all these problems on a regular grid model which is capable of representing any complexity in the earth's structure. Solving a traveltime imaging problem on a regular grid is a challenge, because we must deal with a large number of model parameters, thereby requiring intensive computation and also sophisticated numerical techniques to handle large uncertainty. This thesis reports how we overcome these difficulties to implement these three imaging techniques. These methods are very efficient on a workstation.

We first developed a new raytracing technique that is applied to all three traveltime imaging methods in various ways, from a point source to expand the first-arrival refractions, from a point source and then a line source (reflector) to generate reflections, and from a line source to downward continue traveltimes for migration. The performance of the raytracing method is crucial in this thesis, because it determines the accuracy and efficiency of all three imaging methods, consequently, feasibility and applicability for solving the nonlinear traveltime problems. The approach that we proposed for the traveltime calculation seems well suited for the imaging purposes. It accounts for wave effects in various structures, and high efficiency is achieved by identifying minimum computational effort for certain particular structure prior to raytracing.

We characterized refraction traveltime problem and identified a few unique physical properties associated with refraction. Consequently, we posed a nonlinear inverse problem that minimizes the misfits of average-slowness data and apparent-slowness data. The tomography problem is regularized by the Tikhonov's method to obtain one stable and unique solution. We found that the errors in the refraction traveltimes are not distributed as random Gaussian type in general, only the errors in their gradients and their absolute shooting times are. Accounting for this pattern of errors, we performed uncertainty analysis by applying nonlinear Monte Carlo inversions. In fact, we believe this complete nonlinear traveltime method represents the first *nonlinear refraction traveltime tomography*, since all previous tomography methods applied to the refraction problems were designed for any survey geometry, they did not reflect the fact of "refraction" and account for its unique physics.

We combined refraction migration and tomography in one joint process by way of regularization. This method can resolve a high-resolution image and define a different concept of "smoothness" for the solution. We view the success of this joint process as a major breakthrough in seismic imaging. Conventionally, *migration* and *tomography* were defined as two different technical fields, and they were performed separately. It is apparent that migration needs accurate velocity information which tomography may help and tomography needs interface information which migration may be able to reconstruct, however, the lack of quantitative connection between the two methods makes it difficult to link them automatically. A few attempts were made to perform joint migration and tomography, but proposed methods are interactive rather than automatic, and need the user's decision during the process to correlate results of migration and tomography. We presented two algorithms to link migration and tomography in an automatic way, *i.e.*, constraining model interface or constraining model-derivative interface by migration image in the tomographic inversion. Because we conduct traveltime migration which requires computation time compatible to two forward traveltime problems only, the joint migration and tomography method is nearly as efficient as the nonlinear traveltime tomography. On the other hand, the method also demonstrates that regularization does not necessarily result in featureless structures in the entire model. Correlating model parameters within each geological zone defined by migration in the tomography inversions reconstructs more meaningful solution.

Our third approach for imaging the subsurface is to take both refraction and reflection traveltimes into a simultaneous tomographic inversion. The major difficulties of this problem include large numerical computation burden for calculating both refractions and reflections in a regular grid model and also the data ambiguity due to long rays and short rays. Because of these difficulties, previous joint refraction and reflection methods parameterized a model with some assumed functional and linearized the inverse problem in one way or another. In this thesis, however, we solved a nonlinear simultaneous inverse problem on a regular grid as it was posed without any additional assumptions about structure and data. This joint nonlinear imaging technique is feasible because of several approaches applied: the efficient raytracing method that we developed, the use of the Tikhonov's regularization method, and the input of refraction and reflection traveltimes in a physically meaningful way. Because the undetermined features of the slowness field in the reflection traveltime problem are physically inherent, one must provide additional physical constraints to obtain a more reliable solution. The inclusion of the refraction data for performing a joint traveltime tomography is one of the attempts for this purpose. From the data point of view, the identification of the first-arrival refractions is much more reliable than the reflections. Therefore, the availability of the refraction data is not an issue in general. Similar to the refraction traveltime tomography, we applied nonlinear Monte Carlo inversions to perform uncertainty analysis after obtaining a solution from the joint inversion.

All of the examples shown in this thesis were designed to explore the validity and usefulness of these methods. We have shown that the nonlinear refraction traveltime tomography method works well for a graben model if the second- or third-order derivative operator is applied for regularization and both the average-slowness and the apparent-slowness data are inverted. For the same model, we have also shown that the joint migration and tomography method can well reconstruct the velocities and the sharp interface. We applied joint refraction and reflection traveltime tomography method to an oceanic crustal model and showed its effectiveness. In principal, these three imaging techniques can be applied to the earth structure at different scales. In this thesis, for demonstration purpose, we applied nonlinear refraction traveltime tomography method and joint refraction traveltime migration and tomography method to two shallow imaging cases (South Boston, Massachusetts and Riley County, Kansas), and applied joint refraction and reflection traveltime tomography method to one crustal imaging case in southern California.

Imaging the shallow Earth's structure for two real cases implies great applicability of these techniques to the geological engineering problems. The first case in South Boston, Massachusetts was to image bedrock in a complex near-surface area. Determination of bedrock depth is often needed for various engineering projects. We demonstrate that the new techniques that we developed can deal with the difficult situation where the large velocity variations occur above the bedrock. It is obvious that correctly reconstructing the shallow velocity structure is crucial for imaging the bedrock topography. However, conventional methods for mapping a refractor all assume simple overburden velocity structure. More importantly, they cannot explore the validity of the assumption, but always obtain a solution in any case. For the field survey in South Boston, MA, our nonlinear refraction traveltime tomography technique automatically reconstructed the entire velocity structure that influences the data. Estimating the posterior model correlation at a point on the bedrock image for Line 1 gave an uncertainty measure for that particular point. When we performed joint migration and tomography for the same data set, migration image (refractor) and the largest velocity contrast reconstructed in the model tended to converge to the same locations, their final mismatch gave uncertainty estimate in another manner. The interest for the Bala Kimberlite survey was on the reconstruction of the entire shallow velocity structure. It is apparent that tomography is an ideal approach for this purpose. In this case, the anomalies in the traveltimes cannot be easily explained in any intuitive way. They show negative and infinite apparent velocities, and the traveltime curves are fairly nonlinear with respect to distance. Applying nonlinear traveltime tomography method quickly resolves the structure complexity. We repeated the tomography inversions for two different initial models, the solutions are consistent, both indicating the same features.

When we modeled the crustal structure off shore near southern California, it happens that PmP and Pg are the only two phases that can be identified on the recordings. In fact, the shallow earth from the seafloor to 3 km in depth shows strong lateral and vertical heterogeneity which can be constrained by the first-arrival refractions (Pg). Performing joint refraction and reflection traveltime tomography resulted in a model that contains much complexity in the shallow structure, smooth mid and lower crust, and a dipping Moho. Without the refraction data included, the complexity seen in the shallow earth would be mapped into the deep crust or the Moho geometry. For this particular case, we took the reflection from the Moho only because of availability, the technique can certaintly deal with many reflections as well.

8.1 Future Work

Starting from July, 1995, our initial goal for this thesis work was to develop a real nonlinear refraction traveltime tomography technique which should mostly depart from the existing methods that had not accounted for the characteristics of the seismic refraction yet. We first realized that the available raytracing techniques are not sophisticated enough for refraction calculation. Therefore, we developed a new raytracing method. Along the way, we also developed joint migration and tomography method when we attempted to enhance the inversion resolution. We inverted both refraction and reflection traveltimes for solving a joint tomography problem, because we thought that utilizing both the first and later arrivals should be the next step. There are certainly many other research issues which we have not explored yet. We will discuss only a few that have occurred to us during the development of this thesis.

Traveltime calculation is still a challenge in terms of efficiency and accuracy. It seems that developing wavefront methods will continue to be the future direction. However, one of the major problems is that the user often has no idea how accurate the calculated traveltimes are for a complex velocity model. Therefore, one may not be able to know if the model solution really corresponds to the data misfit residual. If the traveltime accuracy is higher than the noise level in the data, it will be difficut to verify if the solution is meaningful. Can we sufficiently increase the local rays in a graph template so that the accuracy is high enough for any model? We can hardly do that because of large computational burden. Even though we decide to do so, we still do not know how "high" the accuracy is when we deal with a complex model. Therefore, in the future, we must solve the problem of measuring the accuracy of the traveltime calculation during the tomography inversion. On the other hand, if the efficiency of the traveltime calculation can be greatly enhanced, it will be in turn very helpful for improving the accuracy and also allowing us to do more on measuring the accuracy. The forward traveltime calculation in our nonlinear refraction traveltime tomography takes about 92% CPU time of the whole imaging process, the further improvement of the approach is certainly important.

In this thesis we introduced the approach to invert "traveltime curves" rather than traveltimes. We minimized the misfits of the averge traveltimes and the first-order derivatives of the traveltimes as derived from the two nearby receivers. One direction that we could pursue further is to completely regularize the traveltime data for inversion. When we dealt with the ill-posedness of the inverse problem, we chose the Tikhonov method to regularize the model parameters. Similarly, we might apply a cubic spline interpolation method to the traveltimes and generate real curves from the data. There are physical reasons for doing this. Considering the seismic wave propagation through some sharp features in the subsurface, we can observe that the signature of the structure in terms of traveltime becomes smaller when the wave propagating longer distance. Smooth variations in traveltimes recorded on the surface are commonly seen, therefore, data interpolation is not unrealistic. In such a way with regularization applied to both data and model, we might eventually solve a continuum inverse problem which is independent of data and model discretization.

We showed two algorithms for conducting joint refraction traveltime migration and tomography. The approach can also be applied to the wavefield reflection recordings, which are often migrated for exploring oil and gas reservor. The fundamental problem in reflection migration is the lack of accurate velocity information. The methods that we proposed can link migration and tomography in an automatic manner. We might apply a cross-correlation technique to track the migrated events iteratively and perform a traveltime tomography while migrating wavefield. The procedure should be efficient for iterative prestack migration. If one applies Kirchhoff migration using rays, then the results of the traveltime calculation for the tomography purpose can also be used for migration.

References

Ackermann, H. D. , L. . W. Pankratz, and D. Dansereau, Resolution of ambiguities of seismic refraction traveltime curves, *Geophysics, 51,* 223–235, 1986.

Adams, R. D. , A. A. Hughes, and D. M. McGregor, Analysis procedures at the international seismological centre, *Phy. Earth Planet. Inter., 30,* 85–93, 1982.

Aki, K. and P. G. Richards, *Quantitative Seismology,* W. H. Freeman, New York, 1980.

Aki, K. , A. Christoffersson, and E. S. Huseby, Three-dimensional seismic-velocity anomalies in the crust and upper-mantle under the U.S.G.S. California seismic array, *EOS, Trans. Am. Geophys. Union, 56,* 1145, 1974.

Aldridge, B. and D. Oldenburg, Refractor imaging using an automated wavefront reconstruction method, *Geophysics, 57,* 223–235, 1992.

Ammon, C. J. and J. E. Vidale, Tomography without rays, *Bull. Seis. Soc. Am., 83,* 509–528, 1993.

Ammon, C. J. , G. E. Randall, and G. Zandt, On the nonuniqueness of receiver function inversions, *J. Geophys. Res., 95,* 15,303–15,318, 1990.

Backus, G. and F. Gilbert, The resolving power of gross earth data, *Geophys. J. R. Astr. Soc., 16,* 169–205, 1968.

Backus, G. and F. Gilbert, Uniqueness in the inversion of inaccurate gross Earth data, *Phil. Trans. R. Soc. Lond., A266,* 123–192, 1970.

Bishop, T. N. , K. P. Bube, R. T. Cutler, R. T. Langan, P. L. Love, J. R. Resnick, R. T. Shuey, D. A. Spindler, and H. W. Wyld, Tomographic determination of velocity and depth in laterally varying media, *Geophysics, 50,* 903–923, 1985.

Bohannon, R. G. and E. Geist, Upper crustal structure and neogenetectonic development of the California Continental Borderland, *Geol. Soc. Am. Spec., in press,* 1996.

Bolt, B. A. , The revision of earthquake hypocenters, focal depths and origin times using a high-speed computer, *J. Geophys. Res., 3,* 433–40, 1960.

Brookins, D. G. , The Kimberlites of Riley County, Kansas, *Kansas Geological Survey Bulletin, 200,* 1–27, 1970.

Bube, K. B. and R. T. Langan, Hybrid L1/L2 data fitting with applications to tomography, *Extended Abstracts, 1990 Ann. Internat. SEG Mtg.*, 69–73, 1989.

Bube, K. B. , R. T. Langan, and J. R. Resnick, Theoretical and numerical issues in the determination of reflector depths in seismic reflection tomography, *J. Geophys. Res., 100,* 12,449–12,458, 1995.

Cai, W. and F. H. Qin, Three-dimensional refraction imaging, *Extended Abstracts, 63rd Ann. Internat. SEG Mtg.,* 620–625, 1994.

Červený, V. , I. A. Molotkov, and I. Psencik, *Ray methods in seismology,* Univ. of Karlova Press, 1977.

Červený, V. , *Ray-tracing algorithms in three-dimensional laterally varying layered structures,* D. Reidel Publ. Co., 1987.

Chapman, C. H. , A new method for computing synthetic seismograms, *Geophys. J. R. Astr. Soc., 54,* 481–518, 1978.

Chiu, S. K. L. , E. R. Kanasewich, and S. Phadke, Three-dimensional determination of structure and velocity by seismic tomography, *Geophysics, 51,* 1559–71, 1986.

Claerbout, J. F. , Toward a unified theory of reflector mapping, *Geophysics, 36,* 467–481, 1971.

Clayton, R. W. and G. A. McMechan, Inversion of refraction data by wave-field continuation, *Geophysics, 46,* 860–868, 1981.

Constable, S. , R. Parker, and C. Constable, Occam's inversion: a practical algorithm for generating smooth models from electromagnetic sounding data, *Geophysics, 52,* 289–300, 1987.

Coultrip, R. L. , High-accuracy wavefront tracing traveltime calculation, *Geophysics, 58,* 284–292, 1993.

Dabas, M. , A. Tabbagh, and J. Tabbagh, 3-D inversion in subsurface electrical surveying -I. Theory, *Geophys. J. Int., 119,* 975–990, 1995.

Delprat-Jannaud, F. and P. Lailly, Ill-posed and well-posed formulations of the reflection travel time tomography problem, *J. Geophys. Res., 98,* 6589–6605, 1993.

Dijkstra, E. , A note on two problems in connection with graphs, *Numer. Math., 1,* 269–271, 1959.

Dobecki, T. L. and P. R. Romig, Geotechnical and groundwater geophysics, *Geophysics, 50,* 2621–2636, 1985.

Dreyer, R. M. , Magnetic survey of the Bala intrusive, Riley County, Kansas, *Kansas Geological Survey Bulletin, 70,* 21–28, 1972.

Farra, V. and R. Madariaga, Non-linear reflection tomography, *Geophys. J., 95,* 135–47, 1988.

Fischer, R. and J. M. Lees, Shortest path ray tracing with sparse graphs, *Geophysics, 58,* 987-996, 1993.

French, W. S. , Computer migration of oblique seismic reflection profiles, *Geophysics, 40,* 961–980, 1975.

Fuis, G. , D. A. Okaya, R. W. Clayton, W. J. Lutter, T. Ryberg, T. M. Brocher, T. M. Henyey, M. L. Benthien, P. M. Davis, J. Mori, R. D. Catchings, U. S. ten Brink, M. D. Kohler, K. D. Klitgord, and R. G. Bohannon, Images of crust beneath Southern California will aid study of earthquakes and their effects, *EOS, Trans. Am. Geophys. Union, 77,* 173–174, 1996.

Gardner, G. H. F. , W. S. French, and T. Matzuk, Elements of migration and velocity analysis, *Geophysics, 39,* 811–825, 1974.

Gazdag, J. , Wave equation migration with the phase-shift method, *Geophysics, 43,* 1342–1352, 1978.

Guillemin, E. A. , What is Nature's error criterion ?, *Trans. Inst. of Radio Eng., PG on Circuit Theory, CT-1,* 1–76, 1954.

Hagedoorn, J. G. , The plus-minus method of interpreting seismic refraction sections, *Geophys. Prosp., 7,* 158–182, 1959.

Hill, N. R. , Downward continuation of refracted arrivals to determine shallow structure, *Geophysics, 52,* 1188–1198, 1987.

Hole, J. A. and B. C. Zelt, 3-D finite-difference reflection traveltimes, *Geophys. J. Int., 121,* 427-434, 1995.

Hole, J. A. , Nonlinear high-resolution three-dimensional seismic travel time tomography, *J. Geophys. Res., 97,* 6553–6562, 1992.

Huang, H. , C. Spencer, and A. Green, A method for the inversion of refraction and reflection travel times for laterally varying velocity structure, *Bull. Seis. Soc. Am., 76,* 837–46, 1986.

Jackson, D. D. , Interpretation of inaccurate, insufficient, and inconsistent data, *Geophys. J. R. Astr. Soc., 28,* 97–109, 1973.

Julian, B. R. and D. Gubbins, Three-dimensional seismic raytracing, *J. Geophys., 43,* 95–113, 1977.

Kirkpatrick, S. , C. D. G. Jr., and M. P. Vecchi, Optimization by simulated annealing, *Science, 220,* 1001–1005, 1983.

Klimes, L. and M. Kvasnicka, 3-d network ray tracing, *Geophys. J. Int., 116,* 726–738, 1993.

Kutrubes, D. L. , J. Zhang, and J. Hager, Comparison of conventional processing techniques and nonlinear refraction traveltime tomography for surveys at eastern massachusetts coastal site, *Proceedings, SAGEEP, Keystone, Colorado, Environmental and Engineering Geophysical Society*, pp. 135–138, 1996.

Lankston, R. W. , The seismic refraction method: a viable tool for mapping shallow targets into the 1990s, *Geophysics, 54,* 1535–1542, 1989.

Lees, J. M. and E. Shalev, On the stability of P-wave tomography at Loma Prieta: a comparison of parametarizations, linear and nonlinear inversions, *Bull. Seis. Soc. Am., 82,* 1821–1839, 1992.

Lines, L. R. and S. Treitel, A review of least squares inversion and its application to geophysical problems, *Geophys. Prop., 32,* 159–186, 1984.

Lutter, W. J. and R. L. Nowack, Inversion for crustal structure using reflections from the PASSCAL Ouachita experiment, *J. Geophys. Res., 95,* 4633–46, 1990.

Mackie, R. L. and T. R. Madden, Three-dimensional magnetotelluric inversion using conjugate gradients, *Geophys. J. Int., 115,* 215–229, 1993.

Mandal, B. , Forward modeling for tomography: triangular grid-based huygens' principle method, *J. Seis. Exp., 1,* 239–250, 1992.

Marquardt, D. W. , An algorithm for least squares inversion and its application to geophysical problem, *SIAM J., 11,* 431–441, 1963.

Matarese, J. R. , *Nonlinear traveltime tomography,* PhD thesis, Massachusetts Institute of Technology, 1993.

McMechan, G. A. , J. M. Harris, and L. M. Anderson, Cross-hole tomography for strongly variable media with applications to scale model data, *Bull. Seis. Soc. Am., 77,* 1945–1960, 1992.

Moore, D. G. , Reflection profiling studies of the California Continental Borderland structure and quaternary turbidite basin, Technical report, GSA Special Paper, 1969.

Morgan, F. D. O. , *Electronics of sufide minerals: implications for induced polarization,* PhD thesis, Massachusetts Institute of Technology, 1981.

Moser, T. J. , T. van Eck, and G. Nolet, Hypocenter determination in strongly heterogeneous earth models using the shortest path method, *J. Geophys. Res., 97,* 6563–6572, 1992.

Moser, T. J. , Efficient seismic ray tracing using graph theory, *Extended Abstracts, Ann. Internat. SEG Mtg.,* 1106–1031, 1989.

Moser, T. J. , Shortest path calculation of seismic rays, *Geophysics, 56,* 59–67, 1991.

Moser, T. J. , Migration using the shortest-path method, *Geophysics, 59,* 1110–1120, 1994.

Nakanishi, I. and K. Yamaguchi, A numerical experiment on nonlinear image reconstruction from first-arrival times for two-dimensional island arc structure, *J. Phys. Earth, 34,* 195–201, 1986.

Nercessian, A. , A. Hirn, and A. Tarantola, Three-dimensional seismic prospecting of the Mont Dore volcano, France, *Geophys. J. R. Astr. Soc., 76,* 307–15, 1984.

Nolet, G. and T. J. Moser, Traveltimes in a 3-D earth and a new look at the S discrepancy, *EOS Trans. AGU, 72,* 316, 1991.

Nolet, G. , *Waveform Tomography,* D. Reidel Publishing Company, 1987.

Palmer, D. , *The generalized reciprocal method of seismic refraction interpretation,* SEG, Tulsa, 1980.

Parsons, T. , J. McCarthy, W. M. Kohler, C. J. Ammon, H. M. Benz, J. A. Hole, and E. E. Criley, Crustal structure of the Colorado Plateau, Arizona: application of new long-offset seismic data analysis techniques, *J. Geophys. Res., 101,* 11,173–194, 1996.

Podvin, P. and I. Lecomte, Finite difference computation of traveltimes in very contrasted velocity models: a massively parallel approach and its associated tools, *Geophys. J. Int., 105,* 271–284, 1991.

Press, W. H. , S. A. Teukolsky, W. T. Vetterling, and B. P. Flannery, *Numerical recipes in Fortran: the art of scientific computing,* Cambridge Univ., 1992.

Pullammanappallil, S. and J. Louie, Inversion of seismic reflection travel time using a nonlinear optimization scheme, *Geophysics, 58,* 1607–1620, 1993.

Pullammanappallil, S. , *Simulated annealing and Kirchhoff migration,* PhD thesis, University of Nevada, Reno, 1994.

Qin, F. , Y. Luo, K. B. Olsen, W. Cai, and G. T. Schuster, Finite-difference solution of the eikonal equation along expanding wavefronts, *Geophysics, 57,* 478–487, 1992.

Rockwell, D. W. , A general wavefront method, in Musgrave, A. W., Ed., Seismic refraction prospecting, *Soc. Expl. Geophys.,* pp. 363–415, 1967.

Rodi, W. L. , *Regularization and Backus-Gilbert estimation in nonlinear inverse problems: application to magnetotellurics and surface waves,* PhD thesis, Pennsylvania State University, University Park, PA, 1989.

Rothman, D. H. , Nonlinear inversion, statistical mechanics, and residual static estimation, *Geophysics, 50,* 2784–2796, 1985.

Saito, H. , Traveltimes and raypaths of first arrival seismic waves: computation method based upon Huygens' principle, in *Soc. Exploration Geophys. 1989 Meeting,* pp. 244–247, SEG, Tulsa, OK, 1989, Expanded abstracts.

Saito, H. , 3-D ray tracing method based on Huygens' principle, in *Soc. Exploration Geophys. 1990 Meeting,* pp. 1024–1027, SEG, Tulsa, OK, 1990, Expanded abstracts.

Saito, H. , Anisotropic traveltime tomography at the Buckhorn Test Facility in Illinois, in *Proc. Soc. Exploration Geophys., 1991 Meeting,* Tulsa, OK, 1991, SEG, Expanded abstracts.

Scales, J. , P. Docherty, and A. Gersztenkorn, Regularisation of nonlinear inverse problems: imaging the near-surface weathering layer, *Inverse Problems, 6,* 115–131, 1990.

Scales, J. , Tomographic inversion via the conjugate gradient method, *Geophysics, 52,* 179–185, 1987.

Schenk, F. L. , Refraction solutions and wavefront targeting, in Musgrave, A. W., Ed., Seismic refraction prospecting, *Soc. Expl. Geophys.,* pp. 416–425, 1967.

Schneider, W. A. , K. A. Ranzinger, A. H. Balch, and C. Kruse, A dynamic programming approach to first arrival traveltime computation in media with arbitrarily distributed velocities, *Geophysics, 57,* 39–50, 1992.

Shaw, P. R. and J. A. Orcutt, Waveform inversion of seismic refraction data and applications to young Pacific crust, *Geophys. J. R. Astr. Soc., 82,* 375–414, 1985.

Shepard, F. P. and K. O. Emery, Submarine topography off the California Coast-Canyons and tectonic interpretation, Technical report, GSA Special Paper, 1941.

Shima, H. , 2-D and 3-D resistivity image reconstruction using crosshole data, *Geophysics, 57,* 1270–1281, 1992.

Shor, G. G. and R. W. Raitt, Seismic studies in the southern California Continental Borderland, Technical report, International Geological Congress, Mexico City, 19581.

Steeples, D. W. , C. M. Schmeissner, and B. K. Macy, The evolution of shallow seismic exploration methods, *J. of Environmental & Engineering Geophys., 0,* 15–25, 1995.

Stefani, J. P. , Turning-ray tomography, *Geophysics, 60,* 1917–1929, 1995.

Stolt, R. H. , Migration by Fourier transform, *Geophysics, 43,* 23–48, 1978.

Stork, C. and R. W. Clayton, Analysis of the resolution between ambiguous velocity and reflector position for traveltime tomography, *Extended Abstracts, 56th Ann. Internat. SEG Mtg.,* 545–50, 1986.

Tarantola, A. , *Inverse Problem Theory,* Elsevier, 1987.

ten Brink, U. S. , R. M. Drury, G. K. Miller, T. M. Brocher, and D. Okaya, Los Angeles region seismic experiment (LARSE), California-off-shore seismic refraction data, Technical report, U.S. Geological Survey, open-file report, 1996.

Thompson, D. R. , *Nonlinear waveform tomography: theory and application to cross-hole seismic data,* PhD thesis, Massachusetts Institute of Technology, 1993.

Thornburgh, H. R. , Wave-front diagrams in seismic interpretation, *AAPG Bull., 14,* 185–200, 1930.

Tikhonov, A. N. and V. Y. Arsenin, *Solutions of ill-posed problems,* Wiley, 1977.

Um, J. and C. Thurber, A fast algorithm for two-point seismic ray tracing, *Bull. Seis. Soc. Am., 77,* 972–986, 1987.

van Trier, J. and W. W. Symes, Upwind finite-difference calculation of traveltimes, *Geophysics, 56,* 812–821, 1991.

Vedder, J. G. , *Regional geology and petroleum potential of the Southern California Borderland, in Geology and resource potential of the continental margin of western North America and adjacent ocean basins - Beaufort Sea to Baja California, edited by D. W. Scholl, A. Grantz, and J. G. Vedder,* Circum-Pacific Council of Energy and Mineral Resources, Earth Science Series, 1987.

Vera, E. E. , J. C. Mutter, P. Buhl, J. A. Harding, M. E. Kappus, R. S. Detrick, and T. M. Brocher, The structure of 0- to 0.20 m.y.-old oceanic crust at 9°n on the East Pacific Rise from expanded spread profiles, *J. Geophys. Res., 95,* 15,529–56, 1990.

Vidale, J. , Finite-difference calculation of travel times, *Bull. Seis. Soc. Am., 78,* 2062–2076, 1988.

Vidale, J. , Finite-difference calculation of traveltimes in three dimensions, *Geophysics, 55,* 521–526, 1990.

Vinje, V. , E. Iversen, and H. Gjoystdal, Traveltime and amplitude estimation using wavefront construction, *Geophysics, 58,* 1157–1166, 1993.

Wang, B. and L. W. Braile, Simultaneous inversion of reflection and refraction seismic data and application to field data from the northern rio grande rift, *Geophys. J. Int., 125,* 443–459, 1996.

Weber, Z. , *Some improvement of the shortest path ray tracing algorithm, in* Full field inversion methods in ocean and seismo-acoustics, *edt by O. Diachok, A. Caiti, P. Gerstoft and H. Schmidt,* Kluwer Academic Pulishers, 1995.

White, D. J. , Two-dimensional seismic refraction tomography, *Geophy. J., 97,* 223–245, 1989.

Wilcock, W. D. , M. E. Dougherty, S. C. Solomon, G. M. Purdy, and D. R. Toomey, Seismic propagation acorss the East Pacific Rise: finite difference experiments and implications for seismic tomography, *J. Geophys. Res., 98,* 19,913–32, 1993.

Zanzi, L. , Inversion of refracted arrivals: a few problems, *Geophys. Prosp., 38,* 339–364, 1990.

Zelt, C. A. and R. B. Smith, Seismic traveltime inversion for 2-d crustal velocity structure, *Geophys. J. Int., 108,* 16–34, 1992.

Zhang, J. and M. N. Toksöz, Nonlinear refraction traveltime tomography, *submitted to Geophysics,* 1996.

Zhang, J. , R. L. Mackie, and T. R. Madden, 3-D resistivity forward modeling and inversion using conjugate gradients, *Geophysics, 60,* 1313–25, 1995.

Zhang, J. , W. Rodi, R. L. Mackie, and W. Shi, Regularization in 3-D dc resistivity tomography, *Extended Abstracts, Proceedings, SAGEEP, Keystone, Colorado, Environmental and Engineering Geophysical Society,* 130–135, 1996.

Appendix A

Finite-Difference versus Minimum-Traveltime Method

A.1 Introduction

For the first arrival traveltime calculation on a regular velocity grid, wavefront raytracing methods appear more sophisticated than the conventional two-point raytracing methods. Wavefront raytracing methods can simulate many wave effects, such as diffraction, raypaths to shadow zone. For the purpose of traveltime tomography, they are also efficient, because one forward calculation gives the traveltimes throughout the model. The computation speed is independent to the number of receivers. Specifically, wavefront raytracing methods include the finite-difference solution of the eikonal equation (Vidale, 1988, 1990) and the minimum-traveltime raytracing method that applies graph theory or Huygens' principle to expand a wavefront (Saito, 1989, 1990; Moser, 1989, 1991). The latter was also called "shortest path raytracing method" by Moser (1989, 1991). However, in this thesis we used the name, "minimum traveltime raytracing method", which is more proper for the seismic traveltime problem. Further refinements of both approaches have been done by several authors (*finite-difference methods:* Podvin and Lecomte, 1991; Van Trier and Symes, 1991; Hole and Zelt, 1995; *minimum-traveltime methods:* Mandal, 1992; Fischer and Lees, 1993; Klimes and Kvasnicka, 1993; Weber, 1995). But the numerical comparison of the two approaches have not been made yet, and statements about their performance are often misleading. In the following, we shall point out several differences between the two methods. Particularly, we will discuss the advantages and disadvantages of each method for the refraction calculation.

A.2 Finite-Difference Eikonal Solvers

Vidale (1988, 1990) presented a method that solves for the first arrival traveltimes by a finite-difference solution to the eikonal equation

$$(\frac{\partial T}{\partial x})^2 + (\frac{\partial T}{\partial z})^2 = s(x,z)^2 \tag{A.1}$$

where $T(x,z)$ is the first arrival time for seismic energy propagating from a point source through a medium with a slowness distribution of $s(x,z)$. In Vidale's method, the solution region is developed along an expanding square, which introduces significant errors at interfaces where velocity contrasts are large. Briefly we review the finite-difference scheme that Vidale (1988) proposed to solve equation (A.1).

In Figure A-1, assuming a source point at A, the arrival times at the four points B_1, B_2, B_3, and B_4 can be computed by taking the product of the distance h and the average slowness between points A and B_i,

$$T_{B_i} = h\frac{s_{B_i} + s_A}{2} \tag{A.2}$$

Then the arrival times T_{C_i} at the four corner points can be computed with the following formulas:

$$T_{C_i} = T_A + \sqrt{2(h\bar{s}_i)^2 - (T_{B_{i+1}} - T_{B_i})^2} \tag{A.3}$$

$$\bar{s}_i = \frac{1}{4}(s_A + s_{C_i} + s_{B_i} + s_{B_{i+1}})$$

Using the above formulas, one can first time the open circles in Figure A-1, a total of 8 nodes surrounding the source point A. After we know the traveltimes at open circles, the next step is to time filled circles in next ring. To do so, we first need to find the minimum-time point along the previously timed ring. Adjacent points to the minimum-time point are timed first. Starting from the minimum-time point, the points are then sequentially timed along the edge using a finite-difference scheme. After all four edges are timed, the times of the four corner points are calculated. Therefore, the traveltimes are sequentially calculated along the "expanding squares" until the nodes in the whole model are timed.

Qin *et al.*(1992) carefully analyzed the problem with this "expanding square" approach. The schemes that Vidale (1988) proposed require "the time for the part of the raypath leading to a point must be known before the time of the point can be found" (Vidale, 1988). This can be violated for models with moderate to large velocity contrasts. Mathematically it may lead to negative values inside the square root in equation (A.3). Quantitatively, the "expanding square" scheme violates causality if the critical angle is less than $\sin^{-1}(V_1/V_2) = 45$ degrees, or $V_1/V_2 < \sqrt{2}/2$.

To preserve causality, Qin *et al.*(1992) attempted to improve the finite-difference approach by Vidale (1988) by solving the eikonal equation along an expanding wavefront. They described the approach that they presented, "we time the points (about a 5×5 grid of points) near the source region by a Huygens' principle method (Saito, 1990)." However, they did not realize that the approach is already much more than an eikonal solver, it is a minimum-traveltime method (or shortest path raytracing method) based on Dijkstra's algorithm (Dijkstra, 1959) or Huygens' principle, an approach adopted for seismic traveltime calculation by Saito (1989, 1990) and Moser (1989, 1991). In fact, the approach that Qin *et al.*(1992) showed is equivalent to a 5th-order graph template method described by Saito (1989, 1990) and Moser (1989, 1991).

In another effort to solve the problem in the finite-difference schemes for sharp velocity contrasts, Podvin and Lecomte (1991) proposed an approach that "relies on a systematic application of Huygens' principle in the finite difference approximation." Again, they identified the difficulties of Vidale's (1988) finite difference schemes for timing local nodes in different structures. Therefore, they explicitly add some more conditions for the proper use of finite-difference schemes in order to separate the propagation modes of transmission, diffraction and head waves. In addition, applying Huygens' principle is to ensure correct expansion of a local wavefront. Their approach turns to be a combination of finite-difference approach and a minimum-traveltime method. But it is apparently more complicated and expensive than a minimum-traveltime method. Podvin and Lecomte (1991) implemented the approach on a parallel computer.

Hole and Zelt (1995) presented an alternative algorithm to improve the problem in Vidale's finite-difference approach. They adopted part of the idea from Podvin and Lecomte (1991) and included a head-wave operator in the finite-difference propagation scheme. In order to maintain the high computation speed that Vidale's finite-difference approach achieves, Hole and Zelt (1995) did not apply Huygens' principle in every step when expanding the local wavefront. Instead, they chose to apply a posterior correction based on the Huygens' principle. After traveltimes have been computed throughout the entire model, the traveltime field is used as a starting point and times are recomputed starting with a "source" volume at the appropriate wall of the model and expanding perpendicular to that face. Traveltimes from the new calculations replace the previously computed times only if the new times are smaller. This approach is fast, and may enhance the accuracy of finite-difference calculation associated with the head waves. But it does not guarantee to be always effective. The authors suggested, "the reverse propagation step may need to be repeated multiple times in the presence of a sufficiently complex velocity model, although for most models one reversal is sufficient."

The finite-difference approach proposed by Vidale (1988, 1990) provides simplicity and savings in computation time. But its inaccurate calculation for refraction traveltime is a problem, becoming a major concern in the research community. Although a variety of corrections or new finite-difference operators are proposed to improve the solution, the fundamental issue is actually very simple, one must find a minimal time from one point to another. The minimum-traveltime methods that apply graph theory for searching the shortest traveltime paths from points to points are more straight-forward in this sense. In fact, all the proposed alternative algorithms for improving the finite-difference performance either completely or partially use the ideas behind the minimum-traveltime methods. In the following, we shall explain some details of the minimum-traveltime methods and compare their performance with the finite-difference approaches.

A.3 Minimum-Traveltime Methods

In Chapter 2, we have already introduced the minimum-traveltime methods (or shortest path ratracing methods) by Saito (1989, 1990) and Moser (1989, 1991). In this Appendix, we move one step further to show the original ideas that they adopted for the traveltime calculation. Once the ideas are understood, one can employ many different *graph templates* to expand a wavefront. It appears that eikonal solver is just one of the many ways to time the local nodes. An important issue is that a graph template must be sufficiently accurate for sampling a wavefront. It happens that Vidale's (1988, 1990) "graph template" (finite-difference schemes) is not a good one.

Moser (1989, 1991) clearly described graph theory using Dijkstra's (1959) algorithm. In Dijkstra's algorithm, one arranges an order of n nodes to be updated so that after exactly n iterations the shortest traveltime paths are found. The nodes are divided in a set P of nodes with known traveltimes and a set Q of nodes with not yet known traveltimes along shortest paths from s. Initially, P is empty and $Q = N$. The minimum traveltime node of Q is s, with a known traveltime $tt(s) = 0$, so that it can be transferred to P. Complete Dijkstra's algorithm can be formulated as follows,
(1) Initialization

$$\begin{aligned} Q := N \;\; tt(i) : &= \infty \quad for\ all\ i \in N \\ P := \phi \;\; tt(s) : &= 0 \end{aligned}$$

(2) Selection

$$Find\ i \in Q\ with\ minimal\ traveltime\ tt(i)$$

(3) Updating

$$\begin{aligned} &tt(j) := min(tt(j), tt(i) + d_{ij}) \quad for\ all\ j \\ &transfer\ from\ Q\ to\ P \end{aligned}$$

(4) Iteration check

$$\begin{aligned} &If\ P = N\ stop \\ &else\ go\ to\ 2. \end{aligned}$$

Step (2) turns out to be most time-consuming in the algorithm. Moser (1990) suggests to use "heap" sorting algorithm which requires $\log n$ operations for n nodes.

Recently, Klimes and Kvasnicka (1994) proposed an INTERVAL method for sorting, their approach is about 4-5 times faster than the heap sorting algorithm.

Dijkstra's algorithm presents an approach that guarantees to find global minimum traveltimes. However, there is always an accuracy issue involved for finite-grid modeling. One cannot obtain an exact solution by expanding a wavefront with a number of finite samples. Errors mainly occur in the updating stage, where a way of approximately timing local nodes needs to be defined. Timing local nodes in the minimum-traveltime method is conducted using a *graph template*. Nakanishi and Yamaguchi (1986) showed a template with straight rays only in a constant velocity cell. Then there is no error associated with a slowness integral along a local raypath. But there are other errors due to finite-angle sampling which lead to violation of Snell's law across cell interfaces. On the other hand, using straight rays within a constant velocity cell requires to place more traveltime nodes than the number of velocity cells on the graph network. This may introduce large computational burden in the second step when sorting for the minimum traveltime points is conducted. Saito (1989, 1990) and Moser (1989, 1991) illustrated a graph template that uses straight rays across several rings of nodes with a traveltime node placed at each corner of a cell. This graph template is practical for seismic traveltime calculation in terms of computation time. From a first look, using straight rays across cell interfaces may introduce large errors. However, its accuracy may be much better than one might thought. The graph template that Saito (1989) and Moser (1989) proposed allows us to sample wavefront curvature densely, and gives us choices for using long rays when necessary.

Matarese (1993) summarized Saito's and Moser's graph templates with a concept of *order*, i.e., the graph template that connects a source up to the first ring of nodes is called "first order", the one that connects a source up to the second ring of nodes is called "second order", so on. Higher-order graph template allows for better precision for traveltime calculation, usually a 5th-order graph template seems working well for a seismic traveltime problem (Saito, 1989; Fischer and Lees, 1993). The higher the order of a graph template is used, the more traveltime nodes are included for selecting a minimal time along the wavefront, requiring more computational time.

With these concepts in the minimum-traveltime methods, one can understand that the finite-difference approach by Vidale (1988, 1990) actually uses a somewhat 2nd-order graph template in a form of "square ring". Because of this low order, the computation is fast, but the results are inaccurate. Later improved approaches (Qin *et al.*1992; Podvin and Lecomte, 1991) are equivalent to the use of a higher-order graph template with more node connections and more directions sampled for wave propagation, and require longer computation time. Hole and Zelt (1995) added a head wave operator to the low-order "graph template" in Vidale's approach (1988, 1990), and conducted node connection check from one or more side walls for possible correction. Their approach may be useful for simple structures, which are often the cases in real problems. However, it does not guarantee an accurate solution for complex velocity model, as one can understand from the minimum-traveltime algorithm.

The accuracy issue is clear, we must well sample a wavefront during finite numerical expansion. This requires sufficient angle and node sampling. To do so, we need many node connections in a graph template, but we cannot afford large computational load which may occur when selecting a minimal time with too many nodes involved. Therefore, as introduced in Chapter 2, we proposed a new approach that a high-order graph template is in effect only in areas where velocity structures are complex. Before raytracing, the model gradients are calculated (they are also needed in tomography inversion). In areas where the velocity gradients are smaller than a given tolerance, traveltime nodes are eliminated and only connections using straight rays are applied. In addition, we place nodes on certain locations at the cell interfaces in a graph template so that a wavefront can be uniformly sampled. Numerical comparison will be illustrated in the next section.

A.4 Comparison of Numerical Accuracy

In this section, we shall compare numerical accuracy of traveltime calculation for four different wavefront raytracing methods. They include a finite-difference eikonal solver by Vidale (1988), an improved finite-difference method by Hole and Zelt (1995), 4th- and 5th-order minimum-traveltime methods by Saito (1989) and Moser (1989), and an optimized minimum-traveltime method proposed in this study. We choose a 2-layer model for which analytical traveltimes are available. From a source on the surface, direct wave, refracted waves, and transmitted wave all should be generated. We realized that few published papers showed error distribution for this simple model except for Podvin and Lecomte (1991), who showed errors up to about 0.15% using their approach for a two-layer model with a 1:2 velocity contrast. Vidale (1988) showed raypaths only for a two-layer model. Most models that were previously studied for accuracy comparison are either homogeneous, allowing a comparison with analytical traveltimes of direct waves only, or too complicated that one can only compare with results from another raytracing algorithm.

In the following experiments, we fix the top layer velocity to be 1000 m/s, but use two different velocities for the lower layer, 2500 m/s and 4000 m/s, respectively. Note the different error scale used in each figure. Figure A-2 shows the relative errors by using Vidale's (1988) finite-difference method. Clearly, large errors are generated due to high velocity contrast, where the algorithm fails to map a wavefront accurately. For the velocity contrast 1:2.5, the largest error is about 8.7% and it occurs near the critical refraction point, the errors in the refracted arrivals at the surface are about 1.32%. The latter directly affects traveltime accuracy in a refraction traveltime inversion problem, while the former influences raypath estimate for inversion in the subsurface. When the velocity contrast is 1:4, the relative errors increase to 32.4% and the refraction errors at the surface are about 5.7%. The occurence of these large errors when using Vidale's algorithm for models with sharp velocity interfaces can be well explained with the analysis given in the previous sections.

Figure A-3 shows the relative errors for the same models when using improved finite-difference algorithm by Hole and Zelt (1995). Because of a head-wave operator included and reverse propagation applied for necessary corrections, the errors are significantly reduced in comparison to Vidale's original algorithm. But the large errors are still associated with refractions and up to 3.2% for a velocity contrast 1:2.5, and 3.7% for a velocity contrast 1:4, again indicating imprecision for mapping a wavefront at the critical point. In addition, a constant error is added to the traveltimes whose paths are connected with the sharp velocity interface. This is because Hole and Zelt (195) used an average slowness of 4 neighbor nodes at each point for traveltime calculation (personal communication, 1996). Taking average slowness can avoid determining a smaller slowness along a cell interface, and make the computation slightly faster, and the results should be reasonably accurate for smooth velocity structures, but inaccurate across sharp interfaces.

For the same two models, we also apply the 4th- and 5th-order Saito's (1989) and Moser's (1989) minimum-traveltime methods and calculate their relative errors with respect to the analytical traveltimes. As shown in Figure A-4 and Figure A-5, the errors are nearly independent to the velocity contrasts. They are up to about 1.3% for the 4th-order method for both velocity models, and about 0.7% when a 5th-order method is applied. The largest errors occur only in the areas where the wavefront angle from a source is poorly sampled by the local ray legs. In the figures, these are the areas close to horizontal and vertical lines from the source. We finally apply an optimized minimum-traveltime method as described in Chapter 2. It involves optimizing angle sampling in a graph template with straight rays within each cell only, and eliminating traveltime nodes in the area where velocity structure is "smooth". For the two-layer models, this suggests that the traveltime network consists of nodes only at the model boundaries and velocity interface, the resulting traveltimes have errors only due to discrete points. Because this approach does not calculate traveltimes at locations where nodes are eliminated, we actually interpolate and map the times back into the entire model for accuracy comparison. Figure A-6 shows that the relative errors are negligible, less than 0.1% in both cases.

A.5 Conclusions

We studied some details in the wavefront raytracing methods for traveltime calculation, including finite-difference solution to the eikonal equation, and the minimum-traveltime method. We point out that it is fair to view the finite-difference eikonal solver as one particular minimum-traveltime method. Any finite-difference schemes only provide an approach for updating local traveltimes in a similar fashion as a graph template in the minimum-traveltime method, they may fail and lead to large errors if Huygens' principle is not well satisfied. In fact, the ideas behind the minimum-traveltime methods are more straight-forward, one can choose a variety of ways to time local nodes. For example, we present an optimized graph template that accounts for angle sampling as well as numerical efficiency. The approach is more meaningful than solving an eikonal equation with many required corrections or considerations for different wave modes. Numerical comparison also shows that minimum-traveltime methods are the most reliable and accurate. In terms of computation time, a 5th-order minimum-traveltime method can be four times slower than the finite-difference approach by Vidale (1988), but it should be faster than the finite-difference methods by Podvin and Lecomte (1991) and Qin *et al.*(1992) which require additional computational efforts. The computation time of an optimized minimum-traveltime method depends on the velocity structures, or the number of the remaining traveltime nodes after elimination. For a two-layer velocity model, its speed is comparable to the Vidale's finite-difference approach.

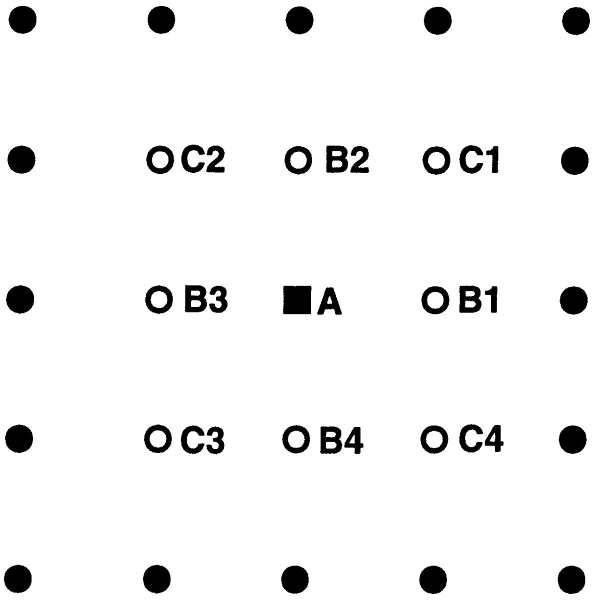

Figure A-1: Finite-difference mesh centered about source point A, where B_i and C_i for $i = 1, 2, 3, 4$ are to be timed first. Then using a finite-difference scheme to time filled circles with known traveltimes at open circles.

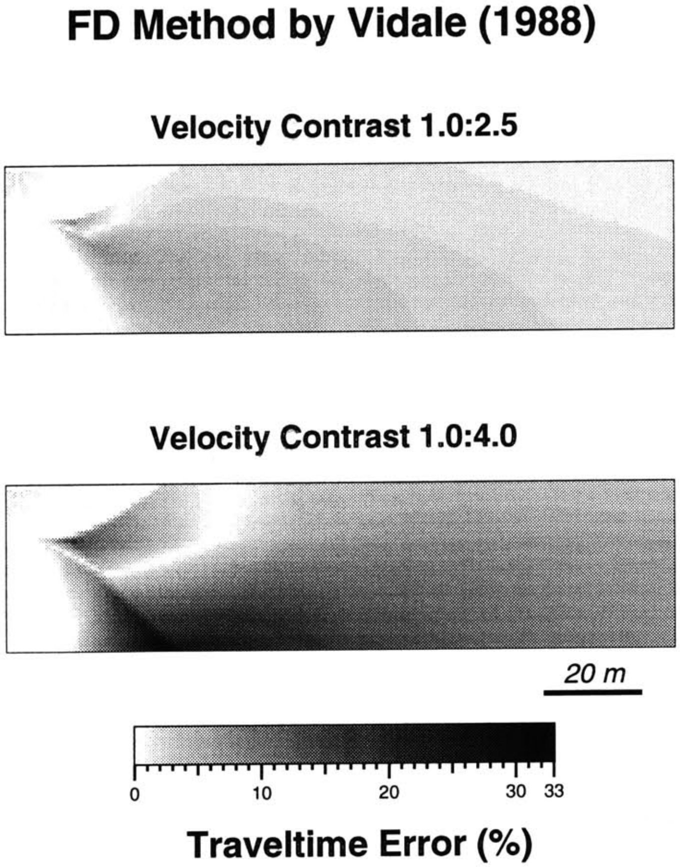

Figure A-2: Comparison with exact solution. The upper layer velocity is fixed to be 1000.0 m/s, the lower layer velocity is 2500 m/s in the top model, and 4000 m/s in the bottom model. Model dimensions are 200×50 meshes. Relative traveltime errors (percentage) due to a surface source by using Vidale's (1988) finite-difference method are displayed.

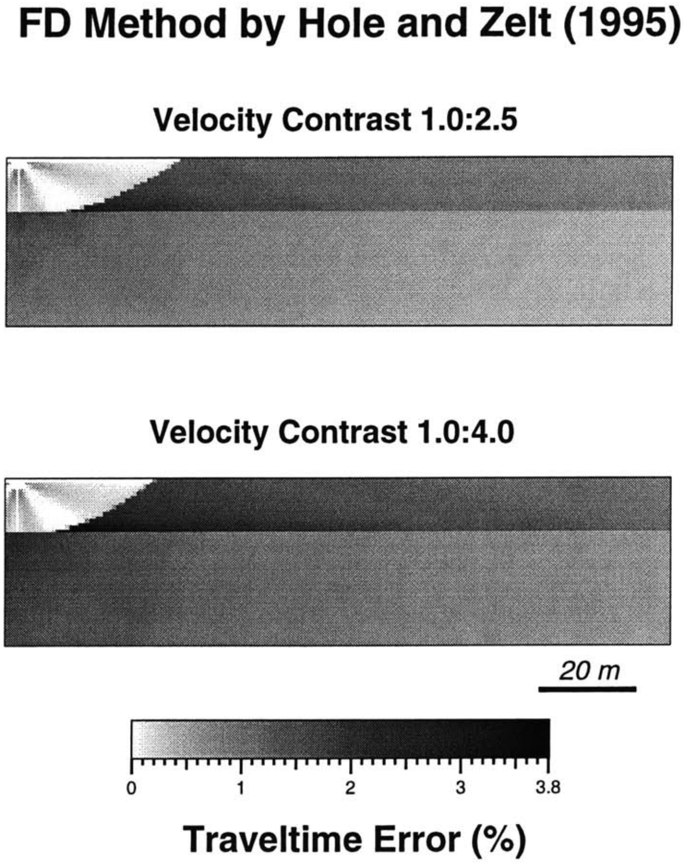

Figure A-3: Comparison with exact solution. The upper layer velocity is fixed to be 1000.0 m/s, the lower layer velocity is 2500 m/s in the top model, and 4000 m/s in the bottom model. Model dimensions are 200×50 meshes. Relative traveltime errors (percentage) due to a surface source by using Hole and Zelt's (1995) finite-difference method are displayed.

Fourth-Order Minimum-Traveltime Method

Velocity Contrast 1.0:2.5

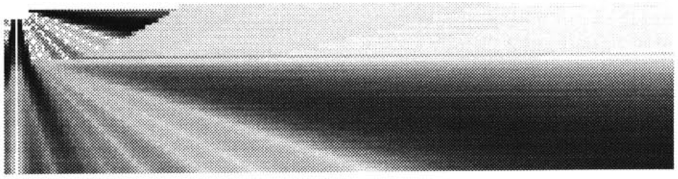

Velocity Contrast 1.0:4.0

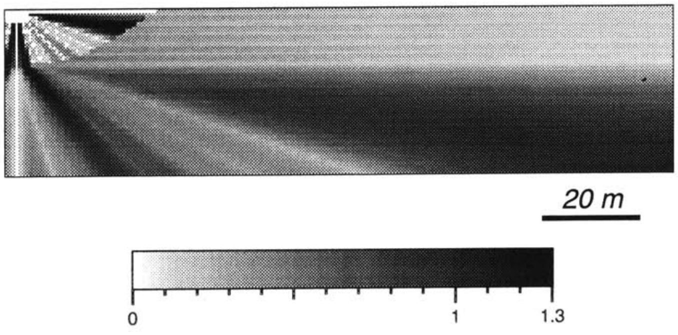

Figure A-4: Comparison with exact solution. The upper layer velocity is fixed to be 1000.0 m/s, the lower layer velocity is 2500 m/s in the top model, and 4000 m/s in the bottom model. Model dimensions are 200×50 meshes. Relative traveltime errors (percentage) due to a surface source by using a 4th-order Saito's (1989) and Moser's (1989) minimum-traveltime method are displayed.

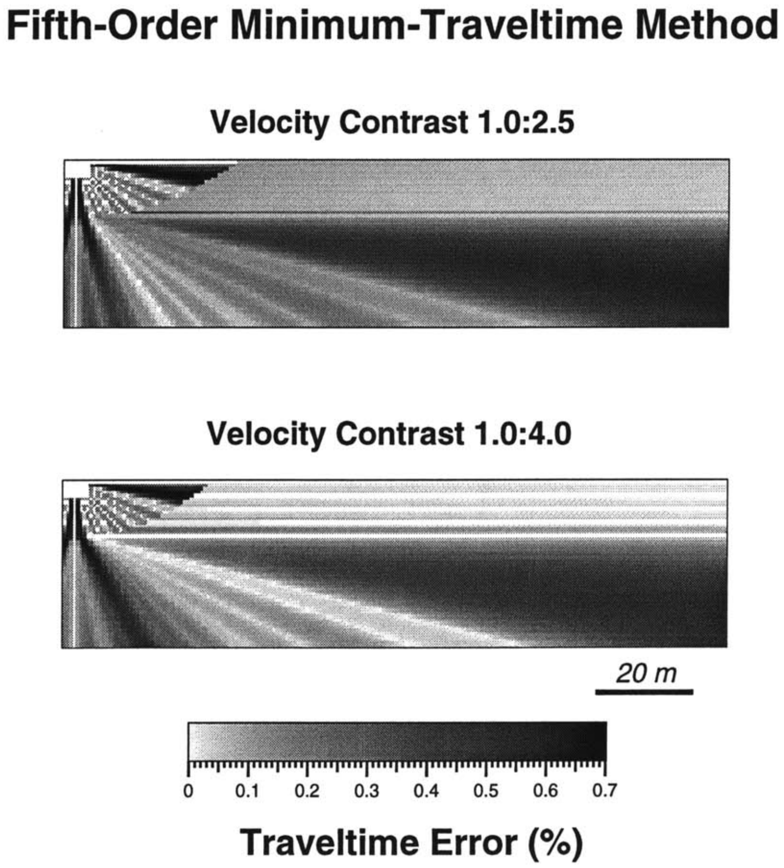

Figure A-5: Comparison with exact solution. The upper layer velocity is fixed to be 1000.0 m/s, the lower layer velocity is 2500 m/s in the top model, and 4000 m/s in the bottom model. Model dimensions are 200 × 50 meshes. Relative traveltime errors (percentage) due to a surface source by using a 5th-order Saito's (1989) and Moser's (1989) minimum-traveltime method are displayed.

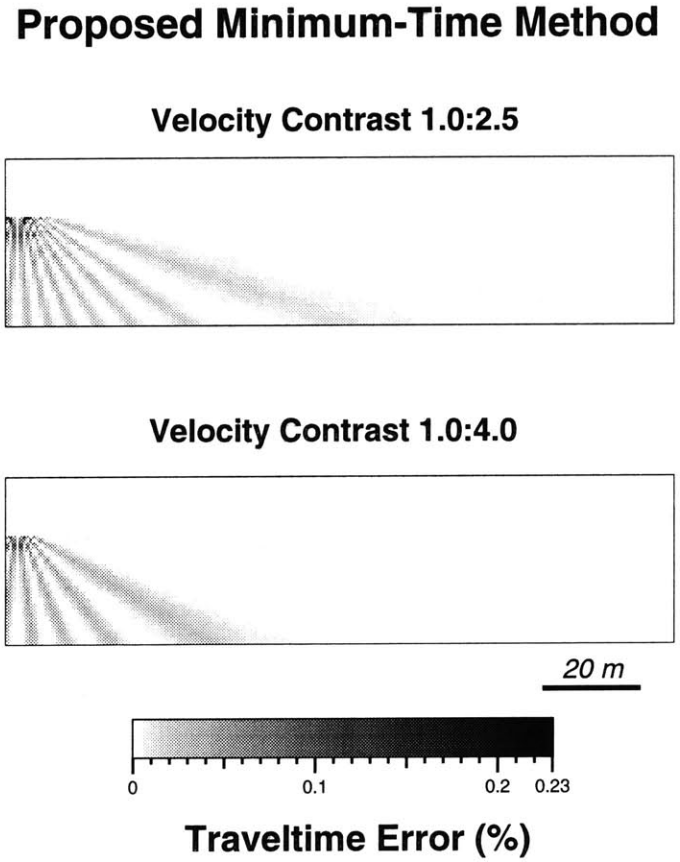

Figure A-6: Comparison with exact solution. The upper layer velocity is fixed to be 1000.0 m/s, the lower layer velocity is 2500 m/s in the top model, and 4000 m/s in the bottom model. Model dimensions are 200 × 50 meshes. Relative traveltime errors (percentage) due to a surface source by using an optimized minimum-traveltime method are displayed.

Appendix B

Creeping versus Jumping Inversions

B.1 Introduction

Regularization is a very specific term in the geophysical inversion techniques. It is mainly about *model regularization*, and typically this involves using a difference operator that connects neighbor slowness nodes in one way or another. The role of regularization can be very significant, and control the outcome of inversions ultimately. However, the understanding of regularization has not been very consistent. In Chapter 3, we have already discussed the criteria of smoothness needed for tomography inversions. Here we shall further address the issue as where to apply the regularization to, i.e., to regularize model stepsize or model itself? Smoothing model stepsize during inversion is regarded as "creeping", while smoothing model itself is called "jumping" method (Shaw and Orcutt, 1985; Constable *et al.*, 1987; Scales *et al.*, 1990, Zhang *et al.*, 1996). Both methods have been widely applied in the geophysical tomography problems, although in some cases authors are not aware of such differences. For examples, Shima (1992) (electrical tomography), Dabas *et al.*(1994) (electrical tomography), and White (1990) (seismic refraction tomography) actually applied creeping approaches, while Shaw and Orcutt (1985) (refraction inversion), Constable *et al.*, (1987) (MT inversion), Ammon *et al.*(1990) (receiver function inversion), and Zhang *et al.*(1996) (resistivity tomography) used jumping inversion methods.

In the following, we shall derive creeping and jumping algorithms in two ways which represent different views on the same ideas. Scales *et al.*(1990) commented that both methods should yield identical results whenever the initial model is smooth if the Tikhonov regularization is applied. However, we shall analytically and numerically illustrate that for a nonlinear and ill-posed inverse problem these two approaches produce two different solutions from any initial model. This is because these two inversion schemes simply minimize two different objective functions (creeping: data variance only; jumping: data variance and the stabilizing functional) and the regularization plays different role in each of these inversions. We conclude that only jumping inversion along with the second- or higher-order smoothing operator can effectively deal with ill-posedness in tomography inversion. In the following discussion, we shall refer data to a vector d for simplicity, although the tomography approaches that we present in this thesis invert two types of data related to the traveltimes (average and apparent slownesses). Our focus in this appendix is on the differences of the creeping and jumping inversion strategies.

B.2 Linearizing A Forward Problem

Following Shaw and Orcutt (1985) and Ammon (1990), we first start from the expansion of a forward calculation problem. A forward problem may be described by

$$d = G(m), \tag{B.1}$$

where d represents data and G represents the functional which operates on the model m to produce the traveltime. The relationship (B.1) is nonlinear, and represents the numerical calculation of traveltimes in our traveltime inversion. Assuming that an initial model m_0 is "close" to the true earth model m, then the problem may be linearized by expanding the observed traveltimes in a Taylor series about m_0,

$$G(m) = G(m_0) + A\Delta m + O\|(\Delta m^2)\| \tag{B.2}$$

where A is the partial derivative matrix of the functional G at m_0, Δm is the model correction vector. Discarding the nonlinear term $O\|(\Delta m^2)\|$, we complete the linearization,

$$A\Delta m \approx G(m) - G(m_0) = d - G(m_0) \tag{B.3}$$

The right-hand side of (B.3) is a data residual vector, the left-hand side is a simple matrix product. For a refraction traveltime inverse problem, equation (3) is an ill-conditioned system of equations which can be solved for Δm using standard least squares techniques.

Shaw and Orcutt (1985) described a simple algebraic modification of (B.3) due to R. L. Parker (unpublished manuscript, 1985) which consists of adding Am_0 to both sides of (B.3):

$$A\Delta m + Am_0 \approx d - G(m_0) + Am_0. \tag{B.4}$$

Considering $m = \Delta m + m_0$, equation (B.4) is simplified to

$$Am \approx d - G(m_0) + Am_0 \tag{B.5}$$

Equation (B.5) is of the same form as (B.3) and can be solved using the standard Singular-Value Decomposition (SVD) approach. The important difference between (B.5) and (B.3) is that in (B.5) we solve for the model m, not a correction vector Δm. This allows us to apply constraints on the model itself rather than the model stepsize. Solving equation (B.3) with smoothness constraints is to deal with the following inverse problem,

$$\begin{pmatrix} A \\ \tau R \end{pmatrix} \Delta m = \begin{pmatrix} d - G(m) \\ 0 \end{pmatrix} \tag{B.6}$$

where R is a regularization operator, and we have suggested to use a 2nd- or higher-order derivative operator in Chapter 3. Solving equation (B.5) with smoothness constraints is to deal with another one,

$$\begin{pmatrix} A \\ \tau R \end{pmatrix} m = \begin{pmatrix} d - G(m) \\ 0 \end{pmatrix} + \begin{pmatrix} Am_0 \\ 0 \end{pmatrix} \tag{B.7}$$

The regularized inverse problem that solves equation (B.6) is a *creeping* approach, in which we solve Δm and also constrain Δm during the inversion. Equation (B.7) indicates a different situation, where we directly solve m and place constraints on m. The second approach is a *jumping* method.

B.3 Roles of Tikhonov Regularization

Although equations (B.6) and (B.7) are frequently referred as *creeping* and *jumping* methods, the most important difference between the two methods is what the inversions actually minimize rather than the optimization approach itself. In this section, we shall show that Tikhonov regularization plays different role in each inversion scheme and inversions minimize two different objective functions. To be more specific, we shall study the minimization of the following objective functions,

$$Creeping: \quad \Phi(m) = ||d - G(m)||^2 + \tau ||R(\Delta m)||^2, \tag{B.8}$$

$$Jumping: \quad \Phi(m) = \|d - G(m)\|^2 + \tau\|R(m)\|^2. \tag{B.9}$$

Solving equation (B.6) with a least-squares method is equivalent to the minimization of the objective function (B.8). This is what a creeping approach actually does when we apply constraints on the model stepsize. On the other hand, a jumping approach minimizes the objective function as shown in expression (B.9). At this point, we have already generalized the inverse problems. Any approach that minimizes the objective function (B.8) is a creeping method, and any inversion that minimizes the objective function (B.9) is a jumping method. One may see that, in equation (B.8), when $\Delta m \rightarrow 0$, the objective function becomes,

$$\Phi(m) = \|d - G(m)\|^2 \tag{B.10}$$

Therefore, a creeping method inverts data only. Because of ill-posedness which occurs in many tomography problems, creeping methods are greatly challenged by the nonuniqueness of the solutions. There may be too many solutions that fit the data equally well, and the solutions depend on the initial models. On the other hand, jumping inversion minimizes misfit of data as well as the curvature roughness of the model. A trade-off parameter τ is used to weight between data misfit and model roughness. For each selected τ, the inversion converges to one unique data rms residual and model curvature roughness norm (R is an Laplacian operator), even though different initial models may be chosen to repeat the experiment. This behavior has been demonstrated by a few authors (Ammon *et al.*, 1990, Zhang *et al.*, 1996). However, it by no means suggests that jumping inversion should always produce one unique solution. Unique model curvature roughness does not necessarily correspond to one single unique model. It depends on the inherent physical constraints of the tomography problems. For example, for a medical survey geometry where a sufficient ray coverage is available, Matarese (1993) demonstrates that jumping inversion can reconstruct one unique solution no matter what initial model is used. For refraction traveltime tomography, this can rarely be true due to poor constraints on the deep structure. Because of some undetermined features in the slowness field, the nonuniqueness of the solutions may be also physically posed in the reflection traveltime tomography. Nevertheless, the use of a jumping inversion approach can remove nonphysical solutions, i.e., those with nonphysical curvature roughness in the model. This constraint appears to be very important, making inversions much more friendly.

In the following, we shall derive equations and verify that jumping and creeping inversions may produce different solutions for any initial models. As we addressed early, one can minimize the objective functions in (8) and (9) with any optimization approaches, leading to the two types of inversions, creeping and jumping. We apply Gauss-Newton method to minimize the two objective functions, resulting in two iterative schemes,

$$Creeping: \quad (A^T A + \tau L^T L)\Delta m_k^c = A^T(d - G(m_{k-1}^c)), \tag{B.11}$$

$$Jumping: \quad (A^T A + \tau L^T L) m_k^j = A^T(d - G(m_{k-1}^j) + A(m_{k-1}^j)). \tag{B.12}$$

where k is the inversion iteration. Assuming an initial model m_0, the difference of model solutions using creeping and jumping schemes after the first iteration can be derived from (B.11) and (B.12),

$$m_1^j - m_1^c = -(A^T A + \tau L^T L)^{-1}(\tau L^T L m_0). \tag{B.13}$$

Based on a similar derivation, Scales *et al.*(1990) incorrectly concluded that for a smooth initial model, jumping and creeping will give the same results if the Tikhonov regularization is applied. However, we argue that their conclusion only applies to the result for the first inversion iteration as shown by equation (B.13). As inversions proceed further, the creeping and jumping solutions at iteration $k-1$ ($k \geq 2$) will both have somewhat roughness, and the difference of the solutions at iteration k becomes,

$$m_k^j - m_k^c = -(A^T A + \tau L^T L)^{-1}(A^T A(m_{k-1}^j - m_{k-1}^c) - \tau L^T L m_{k-1}^c). \tag{B.14}$$

It appears that the Tikhonov regularization does not necessarily guarantee creeping and jumping solutions to be same at iteration after one even if the initial model is smooth. In creeping, the Laplacian operator plays a role as a "procedure control" and regularizes the curvature of each model stepsize but ignoring the entire model curvature roughness, consequently, only data misfit norm has been minimized. While in jumping the role of the Laplacian is to minimize the model curvature roughness. As the result, both data misfit and model curvature roughness have been minimized. A lesson that we have learned from these derivations is the importance of an objective function that one should correctly pose. Different optimization techniques may or may not converge fast under certain conditions, but what is minimized will ultimately determine whether the solutions are reliable for a strongly ill-posed inverse problem.

B.4 Numerical Examples

We shall perform numerical experiments using creeping and jumping inversion methods as described by equations (B.11) and (B.12). A 2D velocity model consisting of a dipping boundary and a high velocity zone is grided by 50 cells. We assume 9 shots and 24 receivers at the surface. The velocity contrast in the model is fairly large, with velocity varying from 600 m/s to 3000 m/s. Figure B-1 shows the model and the raypaths. One can see that the ray coverage is quite sparse in the subsurface. This situation often occurs in the refraction traveltime problem. However, we shall show that the subsurface structure can be fairly well reconstructed from this limited information if the inversion strategy is proper.

We construct two different initial models for tomography inversions. One is homogeneous, with a velocity of 2000 m/s. The other consists of two layers with a dipping interface. One may make an initial model like the second one on the basis of a first look at the data, and include certain features. Figure B-2 illustrates progressive development of inversions from the two initial models by regularizing the model stepsize. We should mention that all the inversions performed here minimize the misfits of traveltime curves, which is a new approach introduced in Chapter 3. For the homogeneous initial model, we found that the creeping method is unable to change local incorrect features in the subsurface once they are somehow generated. As shown in this example, the high velocities on the left at depth of about 25 m are over estimated after the first iteration, but remain unchanged over the later iterations. For the second starting model, the convergence is faster because of the partial features that are accounted for. However, the updated model fairly depends on the initial model over all of the iterations, and the final solution keeps the pattern of the initial model with some nonphysical roughness. In both cases, creeping method successfully finds a model that fits data, but the solution is unrealistic, containing unnecessary features for fitting the data. This is because the approach only regularizes the model stepsize, but ignores the overall structures in the solution. In contrast, Figure B-3 shows that jumping inversions find a consistent solution from both initial models, which contains minimum structures needed for fitting the data. Therefore, the solution is stable and unique, although most likely it is not exact same with the true model. The uniqueness that we posed here is regarding the uniqueness of the minimum-structure solution on the basis of the available data information. It is still likely that there are two or more minimum-structure solutions due to poorly constrained physical problem.

We should point out that the first-arrival rays in the above example only constrain the top of the high-velocity anomaly. However, the solution seems also showing some deep features of the anomaly, which are simply the results of regularization for a minimum structure.

B.5 Conclusions

We derived *creeping* and *jumping* inversion algorithms, and pointed out that their real differences are in the objective functions that they minimize. For an inverse problem that the number of grids is approximately equal or close to the rank of the least-squares matrix, both inversion methods may be able to solve the problem well. In fact, in earthquake traveltime tomography in which a large number of data points are used, creeping methods are often applied (Bolt, 1960; Adams *et al.*1982). However, it is important to understand that a jumping inversion method should potentially work better than a creeping method in a generally ill-posed inverse problem. It is also important to understand the potential risk that one may have to deal with when applying a creeping method, i.e., the solution depending on an initial model and overlooking the global structures. We demonstrate these issues in numerical experiments.

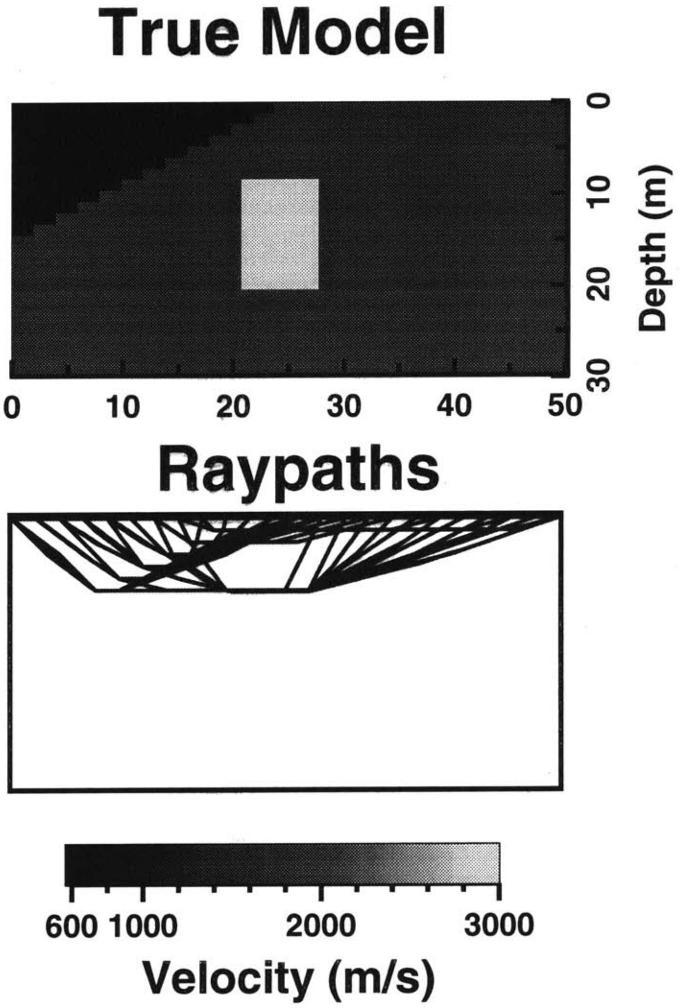

Figure B-1: A velocity model consisting of a high-velocity zone and large dipping velocity interface. We assume 9 sources and 24 receivers on the surface. The corresponding raypaths are also displayed.

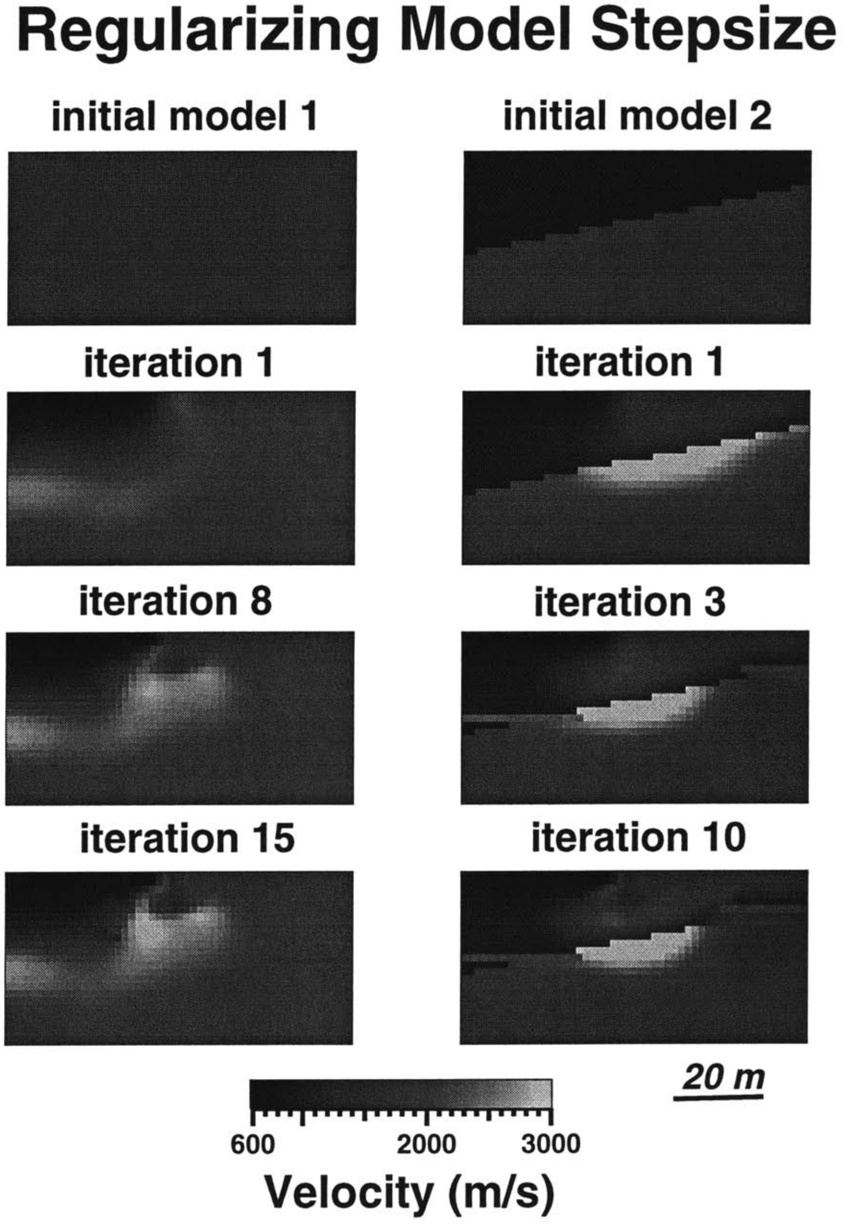

Figure B-2: From two different initial models, a creeping inversion method is applied to invert velocity structures. The solutions are dependent to the initial models.

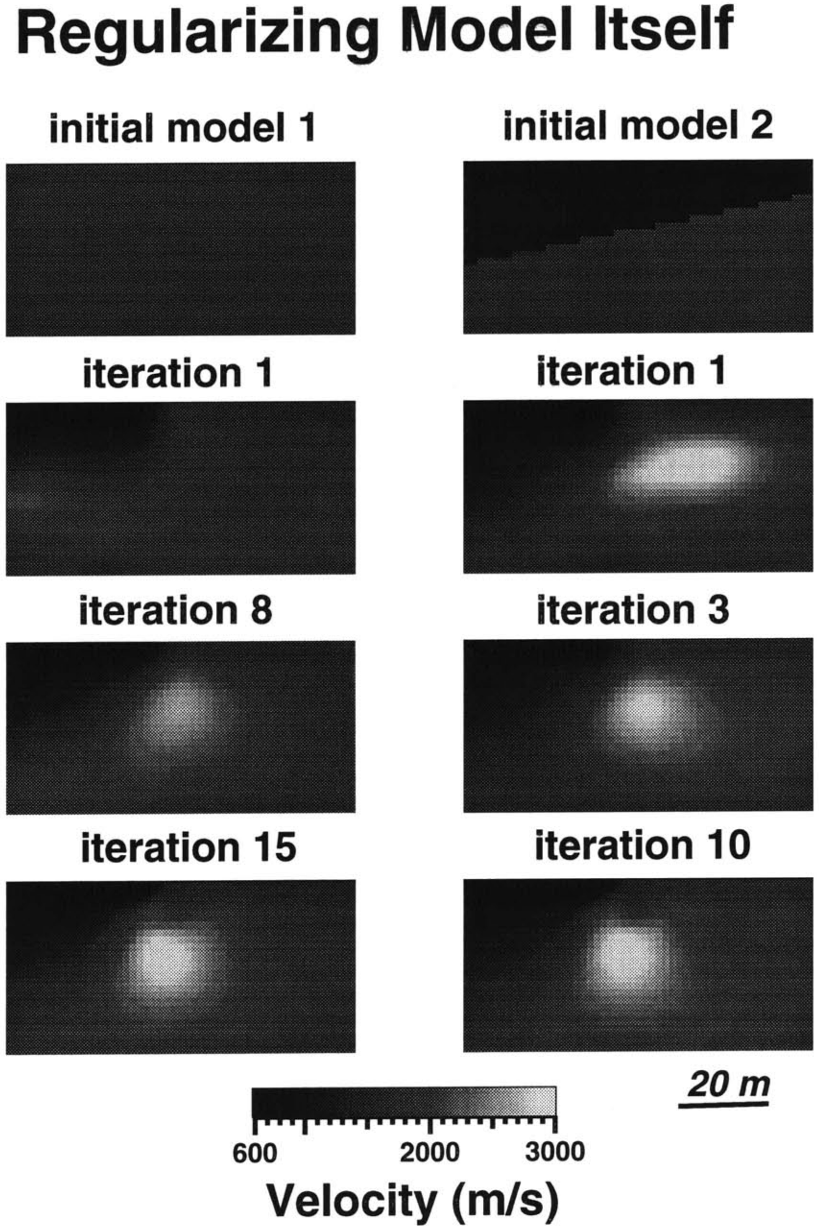

Figure B-3: From two different initial models, a jumping inversion method is applied to invert velocity structures. The solutions are independent to the initial models.

Appendix C

Data Misfits versus Model Roughnesses

C.1 Introduction

As we introduced in Chapter 3, our nonlinear traveltime tomography inversion minimizes an objective function that consists of the misfits of the average and apparent slownesses as well as the model roughnesses. The model roughnesses are defined by the application of a regularization operator R on the slowness model. A trade-off parameter τ is applied to determine a proper ratio between data misfits and model roughnesses for certain problem. The selection of τ is somewhat subjective, although with real data, one can find a τ that allows the data misfits to converge to the predetermined residuals as derived from noise level. If there is no additional information available, one can always check the errors in the reciprocal times from refraction and reflection data and obtain an estimate. Several authors discussed the selection of a trade-off parameter τ in a regularized inversion. These include Smith and Booker

(1988) for magnetotelluric inversion, Ammon *et al.*(1990) for teleseismic receiver function inversion, Matarese (1993) for cross-well traveltime tomography inversion, Zhang *et al.*(1996) for 3D d.c. resistivity tomography inversion. In this Appendix, we show the influence of τ on the refraction traveltime tomographic solution. The conclusions are also applicable to the joint refraction and reflection traveltime tomography that we described in Chapter 5, because the joint tomography is implemented in the same way as in the refraction traveltime tomography inversion.

C.2 Numerical Experiments

As shown in equation (3.1), we define the model roughness norm as the following,

$$S_3 = mR^T Rm, \tag{C.1}$$

where R is a regularization operator, and m is the slowness model. We chose R to be a Laplacian operator in this study, which calculates slowness differences with a three-point formula in each dimension. Because R is symmetric, the calculation of S_3 involves applying R twice on the model m. There are two separate data terms in the objective function. One is the misfit of average-slowness data (S_1), the other is the misfit of apparent-slowness data (S_2). A weighting parameter ω is needed between the two terms. We found that an optimal weighting parameter is between 0.4 and 0.5 in general.

We repeat the numerical experiments shown in Chapter 3 with a number of different τs. The inversion reconstructs a graben model from refraction data with 12 sources and 48 receivers. These τs are, 0.5, 1.0, 3.0, 5.0, 10.0, 20.0, 30.0, 40.0, and 50.0. The starting model consists of 2 layers with constant velocities as shown in Figure 3-2. The inversion results are obtained when the objective function converges and approximately remains constant.

Figure C-1 shows the misfits of average and apparent slownesses versus the trade-off parameter τ. As the trade-off parameter increases, both average-slowness and apparent-slowness residuals increase. The figure shows that relatively large gradients in the curves appear if τ is less than 10.0. For large τ, the increase of the data misfit residuals is nearly linear to the trade-off parameter.

Although we do not directly minimize the misfit of traveltimes by the least-squares criterion, it is important to understand how the traveltime residual varies with the trade-off parameter. We use the following formula to calculate the traveltime residual,

$$\sqrt{\frac{\sum_{i=1}^{N}(d_i - G_i(m))^2}{N}} \tag{C.2}$$

where d is data, $G(m)$ is the calculated data, N is the total number of data points. Figure C-2 (top) shows the data residual versus the trade-off parameter. As the trade-off parameter increases, the traveltime residual also increases. The variations are smooth and continuous. Therefore, one can easily interpolate the points and obtain a continuous curve. The curve is very important for selecting an optimal τ that corresponds to an allowed *rms* data residual. When we reconstruct a model, we must know how much we want to fit data. Conducting nonlinear inversions, we nearly do not have much difficulties to fit data to any level. However, fitting noise introduces large uncertainty in the solution. Figure C-2 (bottom) presents an important feature of the regularized inversion. As the trade-off parameter increases, the data residual sum $((1-\omega)S_1 + \omega S_2)$ increases and the model roughness decreases.

It is also interesting to observe the inversion process. Our inversions include two stages in terms of fitting data, one, inverting the average-slowness data only before the 6th iteration, the other, simultaneously inverting average and apparent slownesses from the 6th iteration. As shown in Figure C-3, a sudden decrease in the traveltime residual takes place when the apparent-slowness data are inverted. Meanwhile, an increase in the slowness roughness norm occurs due to deep structures that are reconstructed from inverting the apparent-slowness data. During these inversions, the trade-off parameter uniquely controls the convergence.

Regularized nonlinear inversion with a jumping scheme enables us to reconstruct a stable solution. With a trade-off parameter $\tau = 5.0$, we conduct an inversion for 100 iterations. We found that the model remains nearly unchanged (260 m/s) after the first 10 iterations. Figure C-4 shows the calculated velocity residuals with the following formula,

$$\sqrt{\frac{\sum_{i=1}^{n}(m_i^k - m_i^{true})^2}{n}} \tag{C.3}$$

where m^k is an iterative solution, m^{true} is the true model, n is the number of the model parameters. After 10 inversion iterations, variations in the velocity residuals are less than 5 m/s.

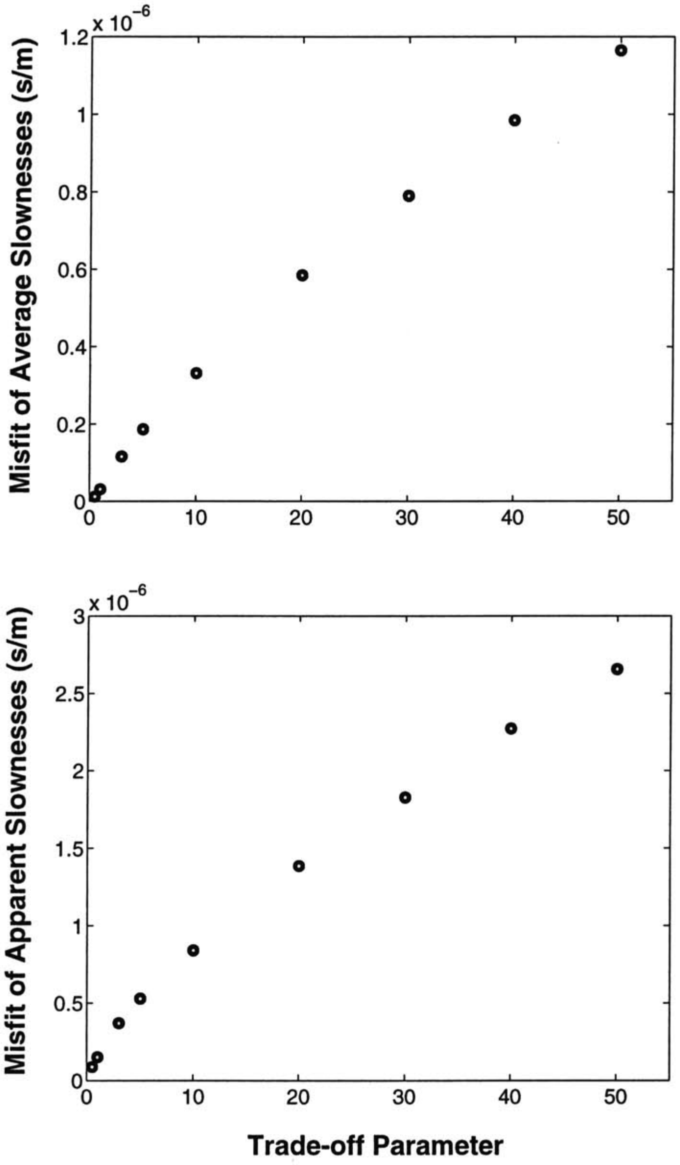

Figure C-1: RMS Misfits of the average and apparent slownesses versus the trade-off parameter varying from 0.5 to 50.0.

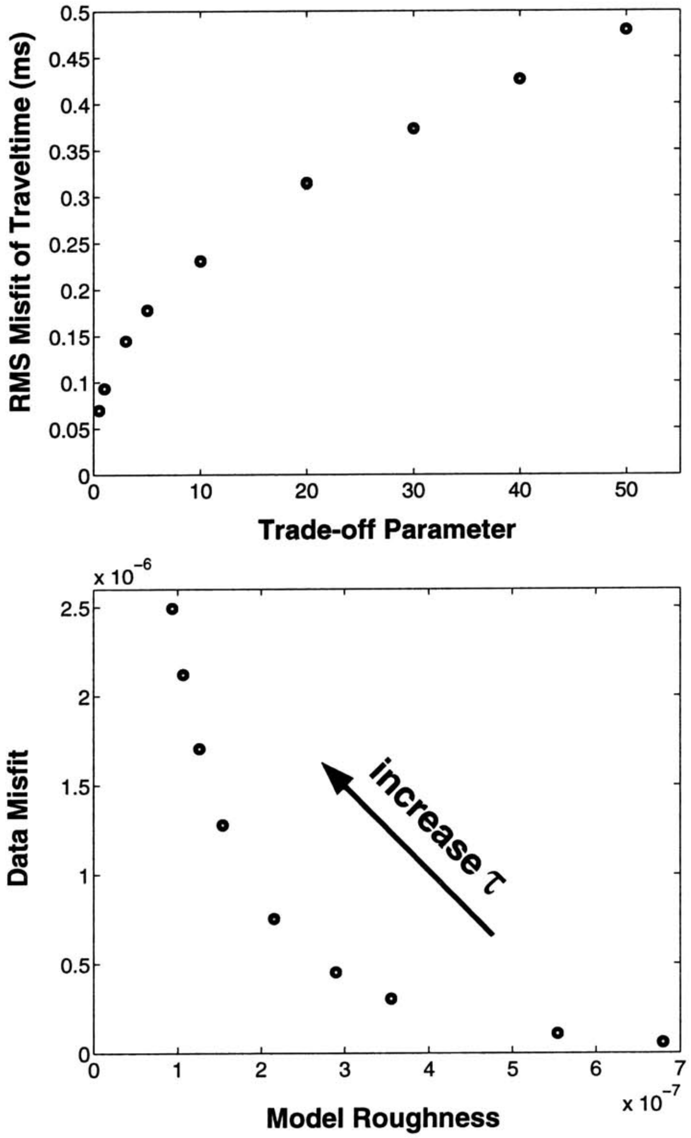

Figure C-2: RMS traveltime residual versus the trade-off parameter varying from 0.5 to 50.0 (top), and the data misfit sum versus model roughness (bottom). As the trade-off parameter increases, the model roughness decreases and the traveltime residual increases.

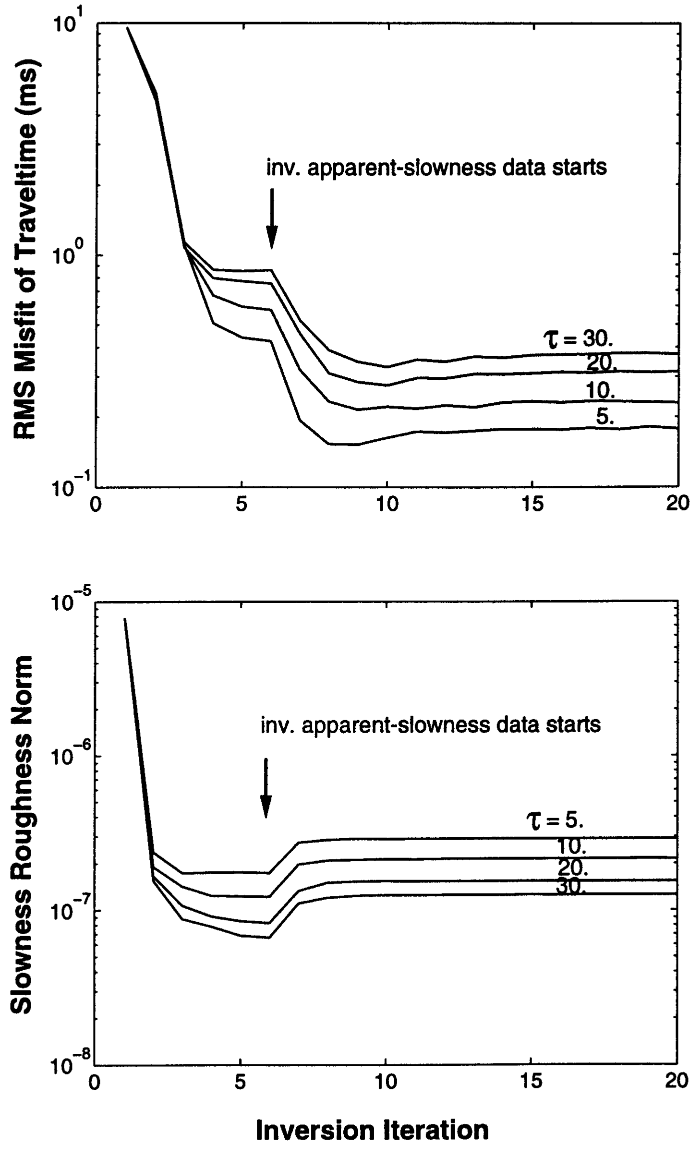

Figure C-3: RMS misfit of traveltimes and the slowness roughness versus inversion iteration for four different trade-off parameters. Inverting apparent-slowness data is included from the 6th iteration.

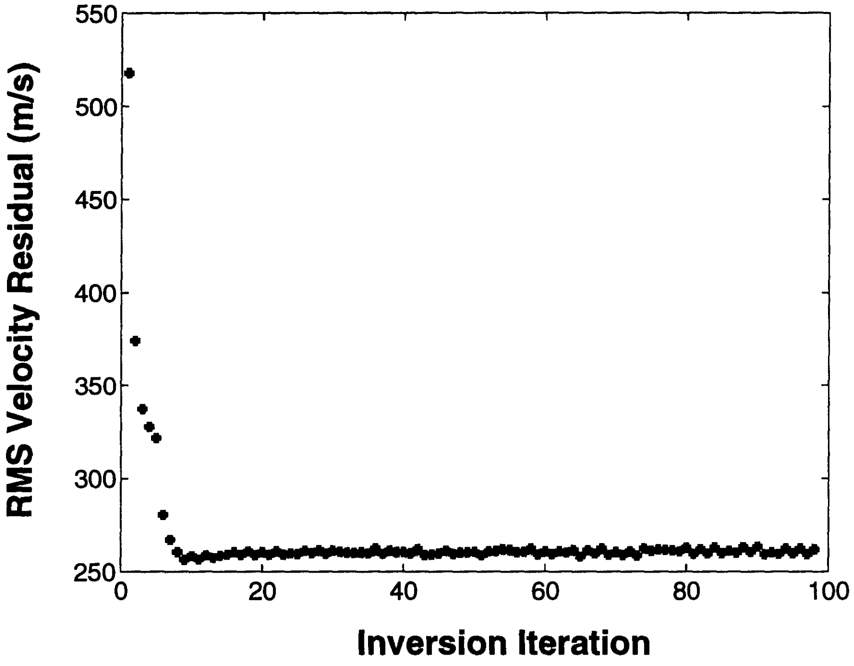

Figure C-4: RMS velocity residual versus inversion iteration. A trade-off parameter 5.0 is selected. After the first 10 iterations, the velocity residual remains nearly unchanged.

5646 - 96